Exploring the Potential of Antibody Mimetics for Detecting Environmental Contaminants

Eleni Koutsoumpeli

Ph.D.

University of York

Electronic Engineering

June 2017

Abstract

Over the past 15-20 years, there has been growing interest and concern from the scientific and regulatory communities over the potential risks of emerging environmental contaminants (ECs). State-of-the-art techniques used for monitoring ECs do not provide the high spatial and temporal resolution measurements required to better understand and mitigate the risks. Immunoassays, which use antibodies to detect a target compound with high affinity, specificity and selectivity, partly address these limitations. However, the use of antibodies for the detection of small-sized, non-immunogenic environmental contaminants, presents a number of challenges. Recent advances in protein engineering have led to the emergence of antibody mimetics that offer the high affinity and specificity associated with antibodies, but with reduced batch-to-batch variability, increased stability, and *in vitro* selection to ensure rapid discovery of binders against a wide range of targets. This study explores the potential of Affimers, a recent example of antibody mimetics, as suitable bioreceptors for the detection of small organic molecules. Methylene blue (MB), a redox-active molecule used as a fabric dye and diclofenac (DCF), an important environmental contaminant, were selected as the target compounds and Affimers against MB and DCF were developed by the BioScreening Technology Group, University of Leeds. The objectives of this project were to a) demonstrate that the developed Affimers can bind to the selected targets with very high affinity, b) assess their performance in the complexity of environmental water samples (selectivity), and c) investigate the potential of an Affimer-based assay for small molecule detection.

Target immobilisation for Affimer characterisation was achieved using long-chained alkanethiol linkers coupled with oligoethylene glycol (LCAT–OEG) and the immobilisation approach was evaluated through electrochemical measurements and infrared spectroscopy. Subsequently, binding between the immobilised targets and target-specific Affimers was quantified using quartz crystal microbalance with dissipation monitoring (QCM-D). Affimer affinity studies revealed Affimer dissociation constants (K_D=13.7 nM and 73 nm for MB and DCF Affimers respectively) was comparable to that of high affinity antibodies. Furthermore, the high selectivity of MB-Affimers was demonstrated using limnetic water samples. Finally, an Affimer-based competition ELISA was demonstrated (LOD=75 nM), illustrating the potential of Affimers as bioreceptors in immunoassays for the detection of small-sized, non-immunogenic compounds. These findings are very promising, encouraging further research into Affimer-based assays and biosensors in order to introduce a novel, alternative path for rapid, on-site monitoring of contaminants in the environment.

Table of Contents

List of Figures

List of Tables

Acknowledgements

Firstly, I would like to express my sincere and deep gratitude to my supervisors Steve Johnson and Jane Thomas-Oates for their continuous support throughout this PhD. Thank you for your guidance, encouragement, enthusiasm and inspiring mentorship.

I would also like to thank my examiners Michael McPherson and Thomas Krauss for the inspiring discussion during the viva and their invaluable comments on my thesis.

I am deeply thankful to Darren Tomlinson and the BioScreening Technology Group at the University of Leeds (Christian, Lia, Anna, Thomas) for their help and advice, and, critically, for the development of MB- and DCF-Affimers. In addition, I would like to express my thanks to Robin Bon and his research group (James, Elliot, Sjors, Hester, Aisling) for hosting me at the School of Chemistry, University of Leeds, where I spent the first months of my project, and for being so kind and helpful towards a 'rusty' synthetic chemist. Particularly, I am especially grateful to Robin for his kind help and insightful advice throughout my PhD. I am also very thankful to Jacob Hauser, for kindly offering to do synthetic work for me.

I would like to thank all members of the Bioinspired Technologies Group (Pepe, Katherine, Ahmed, Steve) for their support and for making every day in the lab more enjoyable and fun. I would also like to thank the entire CAPACITIE project crew (Alistair, Lorraine, Prado, Emily, Xiu, Gabor, Fady, Magda, Mayank, Michelle, Xinwei, Rina, Kyle, Julen). Thank you guys for all the wonderful memories, the laughs, the tears, the adventures, the travels, the support; I will always keep all of these dear in my heart.

I am very thankful to Patrick Phillips and Michael Meyer for hosting me at the US Geological Survey during my placement, and to Dana Kolpin for arranging this opportunity. I am particularly grateful to Patrick and Patricia Phillips for the amazing hikes in the wilds of Vermont, the cider 'sampling', the great company and their wonderful friendship.

I am also thankful to my best friends Alexandra and Sandy, and to dear George for their support.

Nick, words cannot express the entirety of my gratitude for being by my side, not only throughout this PhD, but for all these years we have been sharing a life together. Thank you for your love, for always backing my choices and for your endless support. Also, I am very glad that, not only you

resisted the urge to drown me into a pond while I was writing up this thesis, but you kindly and patiently helped me in all ways possible.

The biggest acknowledgements go to my parents, Maria and Gilbert, to whom I am eternally grateful for their unconditional love, support and guidance; I owe everything to them. I am also grateful to my loving brother, Vasilis.

Finally, Suki (the dog) must be thanked for generously offering comic relief moments that were much needed during the last leg of my thesis write-up.

Author's Declaration

All work presented in this thesis is original to the best knowledge of the author, except where otherwise acknowledged. All sources have been listed as References. This work has not previously been presented for an award at this, or any other, institution. Parts of the research presented in this thesis have been published as research articles in scientific journals, listed below in chronological order.

Journal Articles

E. Koutsoumpeli, J. Murray, D. Langford, R. Bon and S. Johnson, 'Probing molecular interactions with methylene blue derivatized self-assembled monolayers', *Sens. BioSens. Res.*, vol. 6, pp. 1-6, 2015.

E. Koutsoumpeli, C. Tiede, J. Murray, A. Tang, R. Bon, D. Tomlinson and S. Johnson, 'Antibody Mimetics for the Detection of Small Organic Compounds Using a Quartz Crystal Microbalance', *Anal. Chem.*, vol. 89, no. 5, pp. 3051-3058, 2017.

Chapter 1

Overview

1.1 Emerging Environmental Contaminants

The exponentially growing world population and the subsequent urbanisation has led to the development of large and densely populated cities, which, social and economic impacts aside, have a number of detrimental impacts on public health and the ecosystem [1]. Rapid technological and social advances (e.g. transportation, industrialization, health care, communication) have improved life quality, but have also induced a major shift in the urban lifestyle that results in an increased concentration of energy use and product consumption which consequently lead to increased waste production. Additionally, diseases associated with the modern urban way of life such as obesity, diabetes and mental illnesses along with an increasingly aging population have led to a huge increase in the use of pharmaceuticals [2] [3]. Therefore, in addition to the pollution caused by industrial activity in the city outskirts, urban dwellers contribute to a heightened discharge of compounds, such as personal care products (PCPs), cleaning agents, pharmaceuticals, microplastics and engineered nanoparticles (ENPs). All of the above contribute to the complex lattice of urban pollution sources that threaten human and ecosystem health. For example, ethinyl estradiol, typically administered with contraceptive pills, is not fully metabolised by the human body and the greatest part of it (~60%) is excreted and released to the environment in wastewater discharges [4]. Many studies have linked this xenostrogen with endocrine disruption or other adverse effects to aquatic organisms, most notably the feminisation of several species of fish in surface waters [5].

Just like ethinyl estradiol, the plethora of newly introduced compounds found in PCPs, pharmaceuticals, microplastics and ENPs are not well characterised regarding their environmental fate and effects [6]. However, through a number of pathways, these compounds are discharged to a variety of environmental compartments potentially causing harm to the ecosystem. A characteristic example of the complexity of exposure to these recently identified environmental contaminants is diclofenac (DCF) and its fatal effects on vulture populations of the Indian subcontinent. Diclofenac, or 2-(2, 6-dichloranilino) phenylacetic acid, is a widely consumed, over-the-counter nonsteroidal anti-inflammatory drug (NSAID), used to treat inflammatory diseases or as an analgesic. Although a number of studies have reported potential adverse effects of diclofenac on

aquatic organisms [7], its disastrous ecological impact was identified in South Asia in what came to be known as the Indian vulture crisis. Diclofenac was extensively used in this area as a veterinary drug to treat inflammation or other symptoms of disease in cattle. The vultures scavenging on livestock carcasses would be exposed to diclofenac, which was extremely toxic to these birds, particularly those of the *Gyps* genus, causing extensive visceral gout, kidney failure and death. This resulted in a critical decline of their population bringing them to the brink of extinction. The eradication of vultures across the Indian continent caused additional ecological consequences that threatened human health, such as the rapid increase in the number of feral dogs that benefited from the absence of scavenging birds, and the subsequent rise in cases of rabies in humans [8] [9].

Such case-studies demonstrate that these classes of compounds, collectively called emerging contaminants (ECs), pose a complex challenge, not only due to the generally limited knowledge base, but also due to their usually very low concentrations in the environment which may render them difficult to detect [10]. The concern and awareness of ECs was raised due to recent technological advances in analytical methods, which allowed detection of these compounds in very low concentrations. These methods, however, are often time-consuming, specialist, complex and expensive and thus can limit the spatial and temporal resolution with which the presence of ECs can be mapped. These challenges need to be properly addressed by the scientific community and the regulatory authorities; it is imperative to understand the factors and processes affecting urban pollution as well as the effects and potential threats to human health and the ecosystem. This knowledge is necessary in order to support well-informed decision making for developing improved and effective approaches to mitigate current pollution, and proactively address potential future urban environmental problems. The introduction of novel, cost- and time-effective tools for assessing pollution is essential for reaching these objectives. Aiming to contribute to such efforts, an approach using novel biomolecular technologies is presented in this work.

1.2 Current Methods for Detection of ECs in Water

Currently, the major approach for monitoring water quality involves the periodic collection of aquatic samples (grab or composite samples), followed by extraction and purification steps and analysis using laboratory-based instruments. The state of the art techniques for analysing ECs in aquatic samples are primarily based on liquid (LC) or gas (GC) chromatography coupled with mass spectrometry (MS). In general, chromatographic techniques are used to separate mixtures ahead of infusing them into the mass spectrometer for analysis. GC or LC use a separation column containing material, called the stationary phase, and the sample is carried through the column by an appropriate solvent or gas, called the mobile phase. Depending on their different interactions with the stationary phase, each of the substances in a sample may be eluted by the mobile phase at a different rate from the others and so exit the column at different times, before reaching the mass spectrometer [11]. Mass spectrometry is a technique to identify compounds in a sample. The molecules of the analyte are ionised and the resulting ions are separated by a mass analyser and detected according to their mass-to-charge ratio. This technique measures the molecular weight of the compounds present in the mixture while fragmentation of the molecular species provides structural information. Mass spectrometry coupled with gas or liquid chromatography is a powerful analytical approach; its high selectivity and exceptional detection limits rank it as what is considered the "gold standard" in sample analysis and is routinely used in research, diagnostics, forensics and many other fields and applications [12].

In regard to emerging contaminants, the US-EPA standard analytical method for determining pharmaceuticals and personal care products is based on high performance liquid chromatography combined with tandem mass spectrometry (HPLC/MS/MS) in a multiple reaction monitoring (MRM) acquisition mode, which is a highly sensitive and selective technique. Steroids and hormones, which belong to another subclass of ECs, are routinely analysed by high resolution gas chromatography combined with high resolution mass spectrometry (HRGC/HRMS). Both techniques are highly sensitive and the limits of detection (LOD) can reach levels of ng/L and in some cases even pg/L [13] [14]. For example, the standard methods for analysing diclofenac in aquatic samples involves solid phase extraction (SPE) followed by LC-MS methods, such as LC-ion-trap-MS-MS and the LODs of these techniques range from 1-7 ng/L [15]. In addition, the US Geological Survey recently introduced a novel method for the detection of 110 pharmaceuticals by injection of the water sample without prior SPE (solid phase extraction) onto HPLC-MRM, where detection limits ranged from 0.45 to 94.1 ng/L [16].

These techniques are powerful and their excellent LODs have allowed the detection of previously unnoticed substances in environmental samples. They are, however, bound by a certain number of limitations. Firstly, since measurements cannot be taken *in situ*, they mainly rely on grab samples, which provide only a 'snapshot' of the presence of specific compounds at the point and time of sampling. Additionally, as with most analytical techniques, these approaches do not give further information about bioavailability. Increasing the temporal and spatial resolution of spot sampling would be impractical, since these methods are labour-intensive and can be expensive (including transport and analytical costs). Composite samples using automatic samplers set at a high sampling rate can generate samples that are more representative than grab samples, but are still limited by costs, time and manual effort. Moreover, there are many cases, such as in drinking water quality monitoring, where analytical results are required rapidly, but the overall spot sampling, transport and laboratory based analysis process is time-consuming and often does not meet that need [17].

Apart from spot samples and automated samplers, passive samplers are often used, which sequester, accumulate and retain the pollutants until collection and analysis, providing time-weighted average (TWA) concentrations of the analyte(s). Notable examples include Chemcatcher, used for organic compounds and heavy metals, and Polar Organic Chemical Integrative Sampler (POCIS), which is able to mimic bioaccumulation of pollutants in organisms. These approaches have been shown to be very reliable and sensitive, however, they still rely on laboratory-based analytical methods, such as those introduced earlier. The analytical instruments used for such methods are usually large, complex and expensive, and involve labour-intensive techniques to handle, purify and analyse environmental samples, and require highly skilled and trained operators, factors that greatly impede the development of a rapid, cost-efficient environmental monitoring scheme [17-20].

Alternative approaches to assess contaminant levels and exposure include the use of biomarkers or whole-organism bioassays which are based on the biological response or reaction of organisms to the presence of specific substances, providing acute toxicity indicators. Similarly, biological early warning systems (BEWS) can provide real-time measurements of health levels of organisms (such as fish, daphnia, algae or microorganisms) based on physiological or behavioural changes in the environment. These approaches are very useful as preliminary screening methods and allow the early detection of the environmental impact of contaminants, but have limitations (e.g., being time-consuming, labour-intensive) and often require validation from standard analytical techniques [17].

1.3 Emerging Alternatives for Detection of Environmental Contaminants

An analytical tool that has been increasingly gaining ground is based on immunoassays, which are a type of bioassay. In general, a bioassay is an assay using living organisms (*in vivo*) or biological elements (*in vitro*) for measuring and assessing the biological activity of a specific substance, or a group of substances. *In vitro* bioassays use a biological recognition element, such as antibodies, DNA, enzymes or whole cells which are able to detect a specific analyte coupled to a transducer element that converts this recognition event into a readable and quantifiable output signal (Figure 1.1) [20].
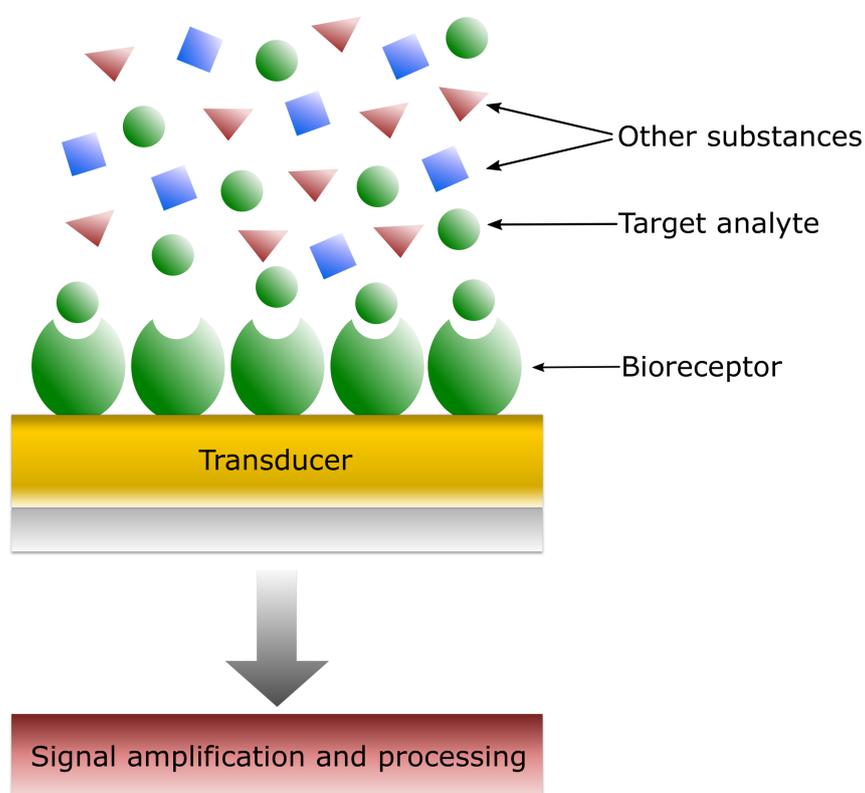
Figure 1.1: Schematic of the basic elements of a bioassay or biosensor (adapted from [21]).

Many enzyme-based biosensors have been used for detection of pesticides, based on the inhibition reaction or catalytic activity of enzymes in the presence of the target analytes. Given that many pesticides have a similar mode of action, most of these methods are used for screening purposes, since they can only detect the total concentration of a certain class of pesticides, and do not provide information for an individual compound [20]. In contrast, immunoassays can be very specific to a

target compound. Immunoassays are bioassays that use antibodies as biorecognition elements. Critically, antibodies offer very high specificity and affinity for their respective antigen, which can be exploited in immnoassays. Such assays are fast, simple and fairly inexpensive if employed broadly following antibody development. Antibodies are highly selective and can recognise the target antigen even in complex matrices, such as blood or urine, and thus require little to no sample pre-treatment. Moreover, depending on the assay format, immunoassays do not usually require large, laboratory-bound instruments, thus allowing operation in the field and reducing the time delays and expenses associated with sample transport. There are several EU projects, such as the River ANAlyser (RIANA) and the Automated Water Analyser Computer Supported System (AWACSS), that employ immunosensors for the multiplexed detection of organic contaminants such as pesticides, polycyclic aromatic hydrocarbons (PAHs), or endocrine disruptors (EDCs). These approaches provide a rapid, cost-effective, multiplexed screening of pollutants in water samples that can substantially enhance pollution monitoring [22].

However, the biorecognition mechanism of antibody-antigen binding can be sensitive to the surrounding environmental parameters, such as temperature, pH or ionic strength, since antibodies are biomolecules that naturally function within the narrow range of conditions inside organisms [23]. In environmental samples, these parameters can vary significantly from these conditions, which can consequently affect the binding abilities or stability of antibodies. It is possible to optimise experimental design in order to improve the performance of the assay, but this can be a challenging and time-consuming procedure which, in the complexity of environmental matrices, may still not always guarantee reliability [23]. Another important limitation of antibodies for environmental applications is development, since raising antibodies against a target compound requires the immunisation of animals. Most environmental contaminants are small-sized molecules that are potentially toxic or non-immunogenic. Therefore, the development of antibodies against such targets can prove to be a challenging, expensive and time-consuming process, if not unfeasible [25]. As a result, despite their numerous advantages, antibody-based assays often fail to meet the demand of regulatory and routine environmental monitoring for cheaper, faster, reliable and robust methods.

Recent advances in protein engineering technologies and synthetic chemistry have enabled the development of alternative affinity receptors with improved characteristics, in order to address the limitations of antibodies. Notable examples of such reagents include antibody fragments (Fabs), DNA or RNA aptamers, molecularly imprinted polymers (MIPs) and antibody mimetics [26]. This study is focused on antibody mimetics, which are synthetic binders that can mimic the highly specific binding of antibodies, but with increased stability, whilst addressing the limitations of *in vivo* development, exhibiting high versatility and reduced costs and time of development,. Affimers

(previously described as Adhirons) are a recent example of antibody mimetics [27]. The development of Affimers against a specific target is achieved by *in vitro* selection instead of *in vivo*, which enables the production of Affimers against a wide range of conventional and unconventional targets, including small, organic compounds such as environmental contaminants. Moreover, the size of the Affimer protein scaffold is ~12-15 kDa, which is almost ten times smaller than that of a typical antibody (~150 kDa), and is significantly more stable, exhibiting very high thermostability (melting temperature is over 100 °C).

The increased stability of the scaffold permits surface immobilisation free of conformational changes, and thus integration of the receptors with biosensors. The scaffold is also largely pH resistant, therefore (in contrast to conventional antibodies) allowing for Affimer development against a target in a wider range of conditions.

Several recent studies have demonstrated the selection of Affimers against over 350 different proteins, as well as peptides, cells, organic molecules and even inorganic metallic nanoparticles, illustrating the versatility of this technology. However, the main aim of these studies, including Affimer characterisation and assay development, has been primarily focused towards applications in clinical diagnostics and therapeutics, where, in most cases, the target antigens are proteins. Proteins are large and complex molecules, with several epitopes, which permit the use of a variety of approaches for the development of Affimer-based bioassays, based on conventional immunoassay methods. However, assay development for small-sized organic compounds, such as environmental contaminants, can be more challenging. In addition, the complexity of environmental matrices, such as surface water, can significantly impede the sensitivity of the assay. These are critical issues for the future development of assays for monitoring emerging contaminants in the environment or even for quantifying the concentration of pharmaceuticals in a patient sample [27-31].

Considering the improved characteristics of synthetic binders over conventional antibodies and the versatility of Affimer technology, it is worth exploring the potential of these protein-engineered antibody mimetics as alternative bioreceptors in bioassays for the detection of contaminants in the environment. This project aims to investigate the ability of Affimers to bind to small organic compounds in surface water samples, aspiring to provide the groundwork for novel, sensitive and reliable bioanalytical tools that would contribute to the increasing efforts to optimise pollution monitoring.

1.4 Project Description and Summary of Thesis

Methylene blue (MB) and diclofenac (DCF) were selected as the target compounds for this study and Affimers against these two targets were developed by the BioScreening Technology Group (BSTG group, Biomedical and Health Research Centre, University of Leeds), and named MB-Affimers and DCF-Affimers respectively, in this study. The main aims of this project were to a) demonstrate that the developed Affimers can bind to the selected targets with very high affinity, b) assess their performance in the complexity of environmental water samples (selectivity), and c) investigate the potential to develop an Affimer-based assay for small molecule detection.
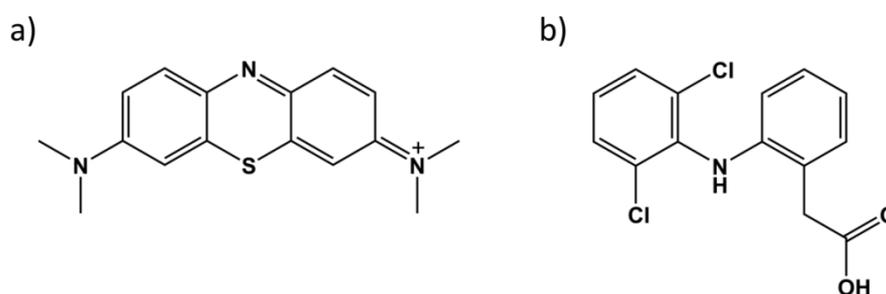
Figure 1.2: Chemical structure of a) methylene blue and b) diclofenac

MB (Figure 1.2a) is a water-soluble dye belonging to the phenothiazine class of heterocyclic compounds and is the most commonly used substance for dying cotton, wood and silk [32]. In addition, it is widely used as a therapeutic agent, most notably for the treatment of methemoglobinemia and malaria, and is also a common stain used in biochemical research [33]. MB has a size comparable to that of many classes of environmental contaminants, and although not highly toxic, its widespread release in the aquatic environment renders it an important environmental contaminant [32]. However, the reason to select MB as a target contaminant in this study was its well-characterised redox properties [34]. Considering the small molecular mass of most environmental contaminants, such as MB, immunosensors for environmental monitoring are typically operated in a competition assay format, which requires the immobilisation of the target molecule on the sensing surface. Therefore, it is of key importance that the properties of the target compound are not altered by the immobilisation process. Here, the small-molecule target was immobilised using a self-assembled monolayer (SAM) of long-chained alkanethiols (LCAT) containing an MB-labelled oligoethylene glycol component (OEG) and by using MB, it is possible to monitor its redox behaviour when immobilised on the surface. For these reasons, MB was selected as the proof-of-principle target for the purposes of this study.

Electrochemical (cyclic voltammetry, electrochemical impedance spectroscopy) and spectroscopic (polarisation modulation-infrared reflection-absorption spectroscopy or PM-IRRAS) techniques were employed for the assessment of MB immobilisation protocols and the characterisation of the MB-terminated molecular layer on the gold surface of sensors. Next, quartz crystal microbalance with dissipation monitoring (QCM-D) was used to monitor the interactions between MB-Affimers and the surface-immobilised MB in order to estimate affinity. QCM-D was also used to evaluate the performance of MB-Affimers in surface water samples, here a limnetic[1] sample. Finally, the potential for Affimer-based assays in a competition format was investigated by QCM-D.

Given its well-reported adverse ecotoxicological impacts and the increasing need to monitor its presence in the environment, diclofenac (DCF) was selected as the second target compound for this study (Figure 1.2b). Using the knowledge and information acquired by studying MB-Affimers, the same approaches (QCM-D; target-derivatised LCAT-OEG SAMs) were applied to assess the performance of DCF-Affimers. Finally, considering its widespread use as a monitoring tool, enzyme-linked immunosorbent assays (ELISA) were used to further assess DCF-Affimer binding affinity and demonstrate a competition assay. The ELISA protocol was developed and adapted for DCF by the BioScreening Technology Group and was replicated at the University of York.

This thesis is divided into two main segments, namely, the introduction (Chapters 1-3) and the experimental section (Chapters 4 and 5). Chapter 2 provides an overview of immunoassays, antibodies and the main principles of antibody binding, as well as a literature review of alternative affinity receptors, including Affimers, and a brief description of the Affimer selection process.

Chapter 3 provides a background to the techniques used in this work for the assessment of Affimer affinity selectivity and assay development.

Chapter 4 is focused on MB-Affimers and presents the experimental results of:
a) Assessing and characterising the protocol used for immobilisation of MB on gold surfaces through MB-terminated LCAT-OEG SAMs using cyclic voltammetry (CV), electrochemical impedance spectroscopy (EIS), PM-IRRAS and QCM-D.
b) Investigating the binding interaction between MB-Affimers and surface immobilised MB using QCM-D, estimating Affimer affinity through saturation binding and kinetics studies, demonstrating its selectivity for MB in limnetic samples and presenting an Affimer-based competition assay with QCM-D.

---

[1] Limnetic: 'pertaining to or living in the open water of a freshwater pond or lake down to the depth of light penetration' [35]. Here, limnetic refers to limnetic water samples.

Chapter 5 explores the binding interactions of DCF-Affimers with DCF, building on the experience obtained by studying MB-Affimers. Similarly to MB, DCF was immobilised on gold surfaces using DCF-terminated LCAT-OEG SAMs and the molecular film was characterised using EIS and PM-IRRAS. Next, QCM-D sensors functionalised with LCAT-OEG-DCF SAMs were used to investigate the interactions with DCF-Affimers. The affinity of DCF-Affimers was estimated through saturation binding measurements using ELISA. Finally, preliminary work on the development of an Affimer-based competition ELISA is presented.

Lastly, in Chapter 6, the findings of this study are summarised and discussed, as well as the potential future directions of this research and the focus of the corresponding further work.

Chapter 2

Alternative Receptors for Immunoassays

2.1 Overview

Conventional immunoassays rely on the use of antibodies as biorecognition elements, which are typically developed through the immunogenic response of infected mammals. This approach not only involves significant effort, time and costs but also poses a number of challenges and limitations, particularly where antibodies are required against non-immunogenic targets. Advances in recombinant technologies and protein engineering have enabled the development of artificial binding agents that are selected *in vitro*. The relative simplicity of selection coupled with the robustness of these synthetic biorecognition elements have led to significant interest in their use in bioassays. This chapter presents an overview of immunoassays, antibodies and the underlying principles behind antigen-antibody interactions, as well as an introduction to synthetic affinity receptors, including Affimers, which are the main focus in this project.

2.2 Immunoassays

Immunochemical analytical methods are bioassays that rely on the specific interaction between an antibody and its antigen. Immunoassays have found widespread use in several areas, such as clinical diagnostics, food safety and environmental monitoring. The immunoassay depends on two key processes: i) biorecognition of the antigen which is provided by the selectivity of the antigen-antibody binding reaction, and ii) the signal transfer process, where the biorecognition event is translated into a quantifiable signal through a change in the electrochemical, optical, mechanical or thermal properties of the system. In general, immunoassays can be divided into two broad categories, label-based or label-free, depending whether the detection is dependent on use of signalling labels [20].

2.2.1 Labelled immunoassays; enzyme-linked immunosorbent assay (ELISA)

In labelled immunoassay formats, a label is used to quantify the amount of bound target analyte. Widely used labels are enzymatic, fluorescent, chemiluminescent, redox probes or radioactive isotopes (radioimmunoassay). The most extensively used and established immunoassay in medical diagnostics, food and environmental analysis is the enzyme-linked immunosorbent assay (ELISA), where enzymatic labels, typically horseradish peroxidase (HRP), alkaline phosphatase, β-galactoxidase or glucose oxidase are used to enable transduction of the biorecognition event. In the presence of its substrate, the enzyme label produces a measurable signal, such as colour change, fluorescence or chemiluminescence and the intensity of the optical signal is measured to quantify the amount of analyte. A source generates a light beam of known characteristics (wavelength, intensity) which passes through the sample and, following Beer's law, the intensity of the absorbed light is proportional to the amount of the analyte solution [36]. For example, in colourimetric assays that use horseradish peroxidase, the enzyme reacts with the substrate 3,3',5,5'-tetramethylbenzidine (TMB) in the presence of hydrogen peroxide which results in a blue colour, and the intensity of the colour is measured by a spectrophotometer at ~650 nm [37]. In a similar manner, immunoassays based on fluorescent or chemiluminescent labels quantify the amount of bound analyte by measuring the light emitted by the label [38]. Most colourimetric, chemiluminescent or fluorescent assays are highly sensitive and have found numerous applications as diagnostic tools.
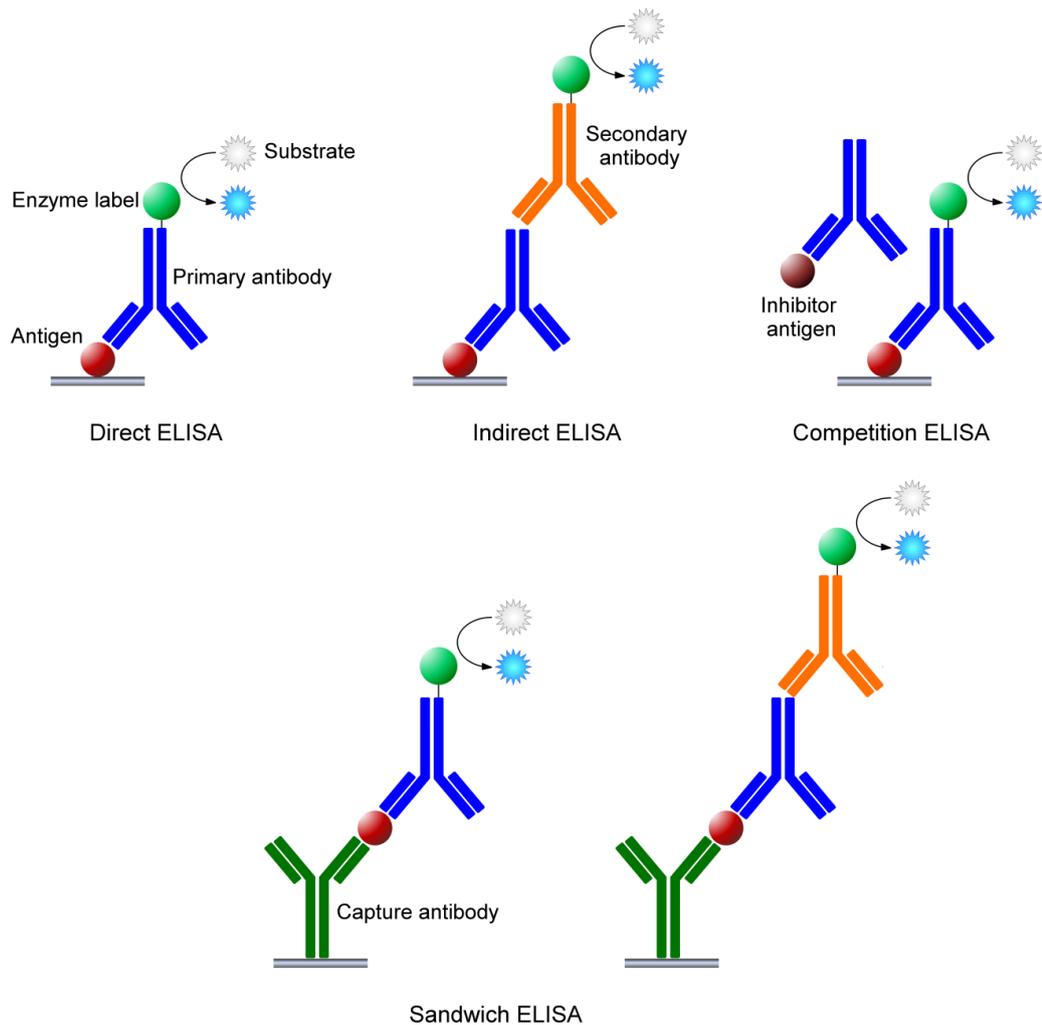
Figure 2.1: Schematic of the most common ELISA formats: direct, indirect, competition and sandwich. The sandwich ELISA is shown in two configurations: direct (left) or indirect (right) detection (adapted from [39]).

There are four principal ELISA formats: direct, indirect, sandwich and competitive (Figure 2.1). Sandwich ELISAs consist of two steps where a primary and secondary antibody are used. The primary antibody (Ab_1) is immobilised on a surface and is used to capture the target analyte. Then, the enzyme-labelled, secondary antibody (labelledAb_2) is introduced into the system and binds to a different region of the captured analyte, forming an immunocomplex (Ab_1-analyte-labelledAb_2). The intensity of the enzymatically-generated signal is then proportional to the amount of the target analyte. This format involves the development of at least two antibodies against different regions of the target, and is consequently more suitable for large antigens, such as proteins. Perhaps the most well-known example of a sandwich ELISAs is associated with the pregnancy test, where monoclonal antibodies are used to detect the presence of the established pregnancy biomarker, human chorionic gonadotropin (hCG). It is a rapid (1-3 min) test where hCG detection is determined by visual evaluation of the colour change at the test lines of a lateral flow strip or by

measuring the reflectance or transmittance of light. Here, hCG is captured by immobilised anti-hCG antibodies and detected by secondary, anti-hCG antibodies labelled with enzymes (or directly with blue-coloured latex particles for detection via reflectance). Today, a vast array of technologies for over-the-counter home pregnancy tests have been developed with the latest advance being the digital, "one-step" home pregnancy test, launched by Clearblue [37].

ELISAs can be further characterised as 'direct' or 'indirect' depending on the detection approach. In direct assays, the target antigen is adsorbed on a solid support, such as polystyrene well plates, and an enzyme-labelled antibody is used for the direct detection of the target. In indirect detection, the signal is transduced by a secondary, labelled antibody that binds to the primary antibody (Figure 2.1).

In competition (or inhibition) ELISAs, a sample containing the antigen is first incubated with antibodies before the mixture is added to antigen-coated wells. Sample and immobilised antigens compete for a limited number of antibody binding sites, so after washing, the amount of the analyte in the sample is inversely proportional to the signal generated by the antibodies bound to immobilised antigens (through direct or indirect detection; Figure 2.1 shows direct detection). This format is commonly used for small sized antigens that usually have limited epitopes [40] [41].

The main advantages of ELISA compared to instrumental analytical techniques are the low cost and shorter analysis time and its simplicity of use. 96-well plate formats are ordinarily used, and coupled with the rapid analysis provided by an absorbance microplate photometer (also known as plate reader), it is possible to screen more than 100 samples a day. The use of 384- and 1356- well plates can increase assay productivity ten-fold, if not higher, without significantly increasing the costs or man power. The throughput can be further increased with automation of several steps of the process. An additional advantage of ELISA is that very small volumes of reagents are required for each assay. Finally, depending on the assay development and optimisation, ELISAs can analyse samples from complex matrices with minimum (or no) purification requirements, such as gravity filtration, solid-phase extraction or ultrasonic extraction [40].

Although ELISAs were developed for basic and applied biological and clinical research, immunoassays have been used increasingly for the detection of environmental contaminants, primarily pesticides or endocrine disruptors. ELISA test kits that package all the required reagents and sample preparation equipment are available commercially in various formats, enabling the acquisition of field measurements [42]. For example, ELISA tests for atrazine, a widely used and highly toxic pesticide, have been available for many years and demonstrate detection limits in the range 0.01-0.3 µg/L and show good correlation with GC-MS comparisons [43-45]. Most field

immunoassays use colourimetric analysis, because even though fluorescent and radioactive assays are more sensitive, the portability of associated measurement systems is difficult to achieve.

ELISA assays have also been developed for detecting pharmaceuticals, such as diclofenac [9] [46]. Deng et al. [46] demonstrated an indirect competitive ELISA for detection of diclofenac in surface, drinking and waste water, using HRP-labelled antibodies and a plate reader to measure absorbance. The LOD was found to be 6 ng/L in pure water, while the analytical working range was about 20 to 400 ng/L and showed a good correlation with data from LC-MS. To note, the European Quality Standards for diclofenac in surface waters have been defined as 100 ng/L [47]. In a further study, the same research group modified the ELISA for analysis of diclofenac in animal tissue extracts, again with a good correlation with ESI-LC-MS data [9]. In 2015, an ELISA using of monoclonal antibodies for the detection of diclofenac in freshwater and wastewater samples was demonstrated. The LOD was 7.8 ng/L, while the antibody used in the assay remained stable over a wide pH range (5.2 – 9.2 pH), increased levels of salinity or humic acids and showed minimum cross-reactivity for major diclofenac metabolites or structurally similar NSAIDs [48].

Although diclofenac ELISA test kits are not yet available commercially, anti-diclofenac antibodies for use in ELISAs are sold by several companies [49]. In view of the urgent need for constant monitoring of diclofenac levels, ELISAs offer a reliable and sensitive yet cost effective alternative to conventional instrumental techniques, especially considering the limited availability of the latter in countries like India or Nepal, where the ecotoxicological impact of diclofenac has been significant [9].

Immunoassays provide a rapid, low-cost, simple-to-use alternative to standard instrumental analysis such as LC- or GC-MS. While most ELISAs do not offer as low detection limits as these analytical techniques, they remain a useful tool for routine screening of contaminants in the field [20]. However, conventional ELISAs present a number of technological and analytical challenges. ELISAs consist of several stages, including multiple incubation and washing steps, which can increase time, costs and the complexity of the assay. Moreover, it can often be difficult to develop a pair of antibodies (primary and secondary) that bind to different epitopes of the antigen, and the development of monoclonal antibodies, which are usually required for sandwich assays, need greater development time and so incur increased costs over polyclonal antibodies. Finally, ELISAs do not permit real-time monitoring of the antigen-antibody interactions, thus little information is provided regarding the kinetics of the process, if that is desirable in an assay. These limitations have led to the development of label-free immunoassays, where the biochemical interaction between the antibody and antigen is measured directly (i.e. label-free) by an underlying transducer that generates a signal proportional to the amount of antigen [20, 50].

2.2.2 Label-free immunoassays

There are two basic types of label-free immunoassays, direct and indirect. In direct assays, the signal is directly proportional to the amount of target analyte captured by antibodies immobilised on a sensor surface. Indirect assays function similarly to competitive assays, and are essentially a binding inhibition test. Here, the target compound is immobilised on the transducer surface, while a mixture of the sample, containing the target analyte, and antibodies are preincubated in solution and introduced onto the sensor. The presence of the target analyte inhibits the binding of antibodies to the immobilised target. The signal due to bound antibodies is thus inversely proportional to the amount of the sample analyte [20].

In general, there are three main elements that constitute a label-free immunoassay or immunosensor: a bioreceptor, a transducer and a signal processing and amplification system (Figure 1.1) [50]. The transducer is a device capable of translating a physical, chemical or biological signal into an electric response, which enables the generation of a readable, electronic signal. Ideally, this conversion is performed with minimum disruption to the biological complex in the measured system [51]. Essentially, the sensitivity and LOD of the biosensor is highly dependent on the transducer and the affinity of the bioreceptor, whereas the selectivity and specificity is mainly determined by the bioreceptor [52]. Several transduction mechanisms have been investigated, notably transducers that are sensitive to changes in electrochemical, optical or mechanical properties, that can easily be developed into portable devices for field measurements.

Electrochemical transduction is perhaps the most widely used method in immunosensors. Here, the biochemical reaction occurs at the surface of an electrode that measures the local changes in the electrochemical properties of the analytical system. The resulting electrical signal is associated with the number of biorecognition events and is thus directly related to the amount of the target analyte. The main advantages identified with electrochemical biosensors are their speed, high sensitivity and low LODs, low cost, ease of use, the simplicity of the system and their potential for miniaturisation which can allow *in situ* analysis [20] [38] [50].

There are several types of electrochemical transduction, depending on the nature of the electrochemical changes to be detected during a biorecognition event. Electrical impedance spectroscopy (EIS) has been increasingly gaining ground as an approach for biosensing. In EIS, changes in the capacitance or conductance of the system following formation of the antigen-antibody complex are detected through the impedimetric response. EIS is a powerful tool demonstrating high sensitivity and can provide real-time, label-free monitoring of molecular interactions [50]. For instance, a label-free impedimetric immunosensor for the detection of

bisphenol A in human serum has been reported with a detection limit of 0.3 ng/mL [20]. A second type of electrochemical sensor relies on amperometric methods, where the measured property is the change in current when an electroactive species is either reduced or oxidised as a result of the antigen-antibody interaction [20]. As an example, Deng and Yang [53] reported the detection of the herbicide 2, 4-dichlorophenoxyacetic acid through an amperometric ELISA, which reached a detection limit of 0.072 ng/mL, with high stability[2] and sample throughput.

Label-free sensors based on optical transduction of a molecular binding event have also been established in many areas including medicine, security, food safety and environmental health. Optical immunosensors measure changes in the optical properties (including absorption, luminescence and refractive index) of the sample or the transducer's surface when biochemical reactions occur. As with electrochemical sensors, optical approaches are able to provide rapid and real-time detection, require small amounts of reagents and, in some cases, miniaturisation is possible to achieve. Several types of optical transducers have been demonstrated, such as Mach-Zehnder interferometry (MZI) and reflectometric interference spectroscopy (RIfS), with surface plasmon resonance (SPR) being the most established [20].

Surface plasmon resonance (SPR) is a highly sensitive, versatile and powerful technique capable of real-time, label-free detection of biomolecular interactions. Briefly, in SPR, the bioreceptors are immobilised on a thin gold film deposited on a glass prism. A polarised beam of light hits the metal film and upon reaching a certain angle, the incident light resonates with the surface plasmons of the metal, resulting in absorbance, which appears as a dark line in the spectrum of the reflected beam (Figure 2.2). The adsorption or desorption of mass due to biomolecular interactions changes the refractive index local to the sensor surface, resulting in a shift of the incident angle where surface plasmon resonance occurs. Thus, the observed shifts are directly related to the amount of the analyte [54]. SPR has been used extensively in health science research and has demonstrated a great miniaturisation, portability and automation potential. These attributes render it an excellent tool in immunosensing and has found numerous applications in drug discovery, clinical trials and environmental monitoring [55]. For example, Mauriz et al. demonstrated a portable SPR immunosensor for the detection of the pesticide chlorpyrifos in aquatic samples through a competitive assay [56].

---

[2] In this report, stability was referred to the number of precise and accurate measurements without cleaning and recalibration of electrodes [53].
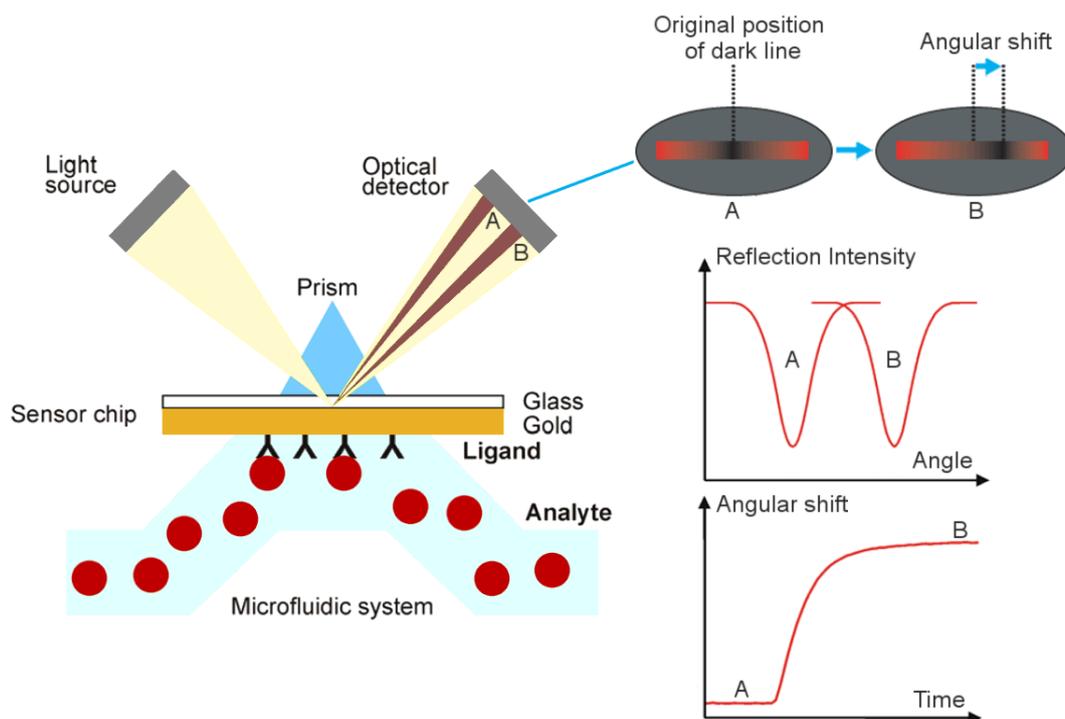
Figure 2.2: Schematic of surface plasmon resonance. The polarised light beam hits the metal film, and at a certain angle the surface plasmons resonate and absorb light which appears as a dark line in the reflected spectrum. Changes to the refractive index of the sensor surface due to biomolecular interactions causes an angular shift. The angular shift is monitored over time to study binding kinetics (adapted from [57] [58]).

Although optical and electrochemical approaches have found widespread applications in biosensors, the potential of acoustic wave sensors has also been increasingly investigated for immunosensing. The principle is based on the use of piezoelectric materials, such as quartz crystals. The application of an external, alternating electric field to the crystal incurs deformation, resulting in a mechanical wave that propagates through or along the surface of the sensor (depending on the shape and size of the crystal or the electric field). The wave is subsequently transduced back to an output electrical signal. The acoustic wave is sensitive to changes in the properties of the crystal (such as thickness, mass, viscosity) due to physical, chemical or biological phenomena occurring at its surface. Therefore, the differences between the input and output electrical signal provide a measure of the interactions on the sensor surface [59].

A widely used acoustic wave sensing technique is the quartz crystal microbalance (QCM). A quartz crystal is sandwiched between two electrodes, and a surface coating (such as gold) is used to immobilise the molecular components, such as antibodies or antigens. The application of an external alternating electric field forces the crystal to oscillate at its resonant frequency (in a shear vibrational mode). The adsorption of molecules on the surface increases the mass loading on the sensor, resulting in a decrease in the measured resonant frequency. The resonant frequency is measured over time, and thus, QCM provides real-time monitoring of molecular interactions

without the need for hazardous (e.g radioactive) or expensive labels. More recently, dissipation monitoring has been incorporated in QCM (called QCM-D), where the dissipation of the energy of the oscillation is monitored simultaneously with the frequency. This approach enables the viscoelastic properties of molecular films to be studied, and thus the detection of conformational changes occurring during biomolecular interactions [60] [61]. Label-free immunosensors based on QCM have been employed for a number of environmental applications. For example, QCM in both a competitive and a direct assay format has been used to detect atrazine with very low LODs (25 pg/mL and 1.5 ng/mL, respectively) [62]. As with SPR, QCM enables label-free detection and real-time monitoring, allowing the study of the kinetics of biomolecular interactions.

Acoustic sensors offer high versatility, since a wide choice of materials can be used for surface coating of the piezoelectric crystals, whilst a wide range of targets can be analysed, such as proteins, nucleic acids, whole cells, nanoparticles or small molecules, making them excellent tools for biosensing [63]. QCM (or QCM-D) is a bulk acoustic wave (BAW) sensor, since the acoustic wave propagates through the bulk of the crystal. However, besides BAW sensors, another type of acoustic wave sensors is surface acoustic wave (SAW) sensors, where the acoustic wave travels across the surface of the piezoelectric material. SAW sensors, notably Love wave type sensors, have been used in numerous bioanalytical and diagnostic applications. SAW biosensors can be integrated with microfluidics systems and miniaturised to produce lab-on-chip devices. For instance, SAW biochips for diagnostic applications have been reported, demonstrating label-free, sensitive detection of protein and DNA biomarkers [64] [65].

2.3 Antibodies
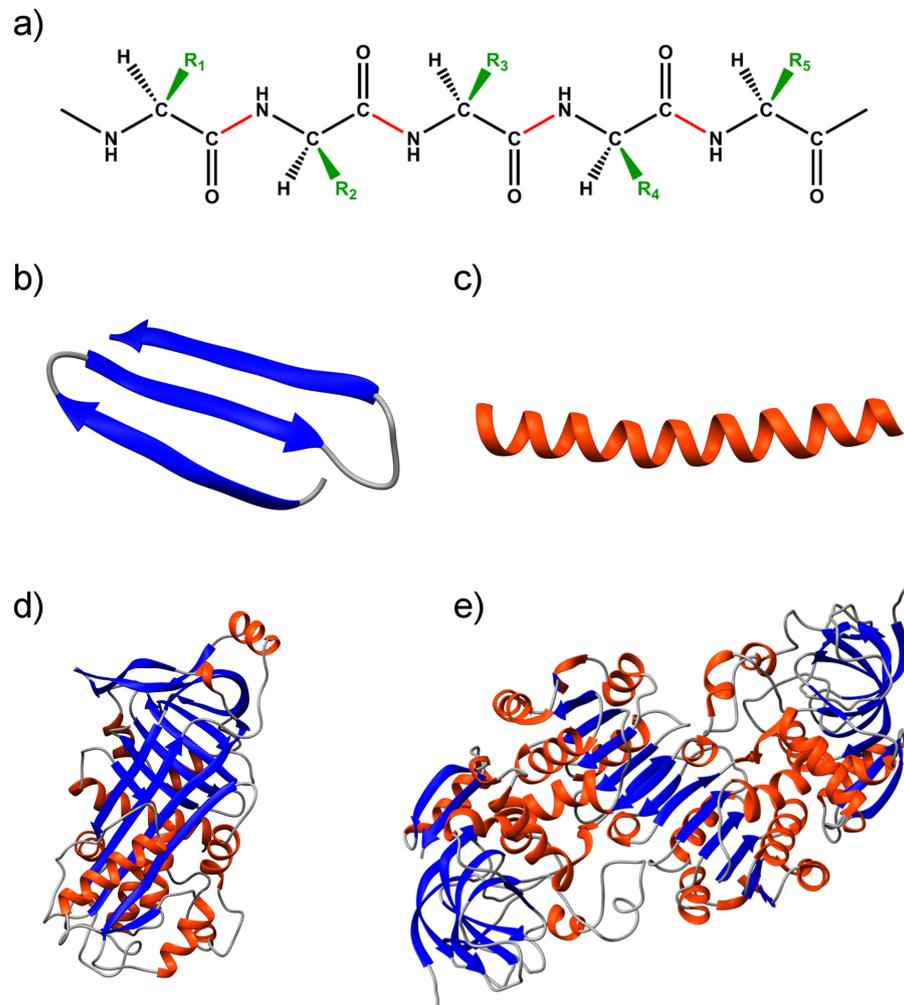
Figure 2.3: a) Primary protein structure consisting of a backbone of amino acids (black) linked together by peptide bonds (red) and variable side chains (green); secondary structure: b) β-sheets (blue) and c) α-helix (orange); d) tertiary structure (ovalbumin, PDB ID: 1OVA); e) quaternary structure (human alcohol dehydrogenase, PBD ID: 1M6H).

Proteins, including antibodies, are long sequences of amino acids folded into a specific 3-dimensional structure. Protein structure is classified as primary, secondary, tertiary or quaternary (Figure 2.3). The primary structure is essentially the sequence of linked amino acids, following translation of the DNA (or RNA) sequence and post-translational modifications (including disulfide bonds). The carboxyl group of one amino acid and the amine group of the next amino acid form a stable covalent bond, called a peptide bond. The chain of linked amino acids is called a peptide or polypeptide and consists of a backbone of repeating units connected by peptide bonds and variable side chains. The C-terminal amino acid has no further amino acids attached to its

carboxyl group, while the N-terminal amino acid, conventionally considered to be the beginning of the polypeptide chain, is not linked to any further amino acids through its α-amino group.

Hydrogen bonds between amine and carboxyl groups of adjacent amino acids in the backbone cause the polypeptide to fold into its secondary structure, which consists mainly of β-sheets and α-helices (Figures 2.3b and 2.3c), while the remaining sections of the chain adopt simpler structures, such as β-turns or ω-loops. The tertiary structure is the three-dimensional conformation of the entire polypeptide chain, as the secondary structural elements fold together governed by covalent (disulfide bonds) and non-covalent (hydrophobic, Van der Waals and ionic) interactions (Figure 2.3d). For multimeric proteins, two or more polypeptides (subunits) are combined through the same forces so that the protein attains its quaternary structure (Figure 2.3e) [66].

Antibodies belong in a class of proteins called immunoglobulins, which are soluble glycoproteins produced in the B-lymphocytes (B-cells), a type of white blood cells of vertebrates and are one of the many elements of an organism's immune system. Immunoglobulins are present in the serum and tissue fluids as soluble proteins or as membrane-bound receptors on the surface of B-cells, and are responsible for recognising and specifically binding to a certain epitope (the antigenic determinant) of an antigen in order to either mark the antigen and activate other mechanisms of the immune system or neutralise the antigen by blocking a functional moiety. In humans, antibodies are divided into five different classes of immunoglobulins, IgG, IgA, IgM, IgD and IgE, which differ in size, amino acid sequence and carbohydrate content. IgG, weighing around 150-170 kDa, is the predominant immunoglobulin protein (~80%) in human serum and is the type of antibody principally used in immunoassays [67].

An IgG molecule consists of four polypeptide chains, two light chains (L), ~25 kDa each, and two heavy chains, (H), ~55 kDa each. Each heavy chain forms a dimer with a light chain (H-L) through disulfide bonds and multiple non-covalent interactions, and the two H-L dimers are similarly bound to form the complete immunoglobulin molecule (Figure 2.4). Both the heavy and light chains consist of variable and constant regions. The variable regions are located at the N-terminus domain of each chain and the amino acid sequence of these regions vary greatly among different antibodies, while the remaining region is constant and characteristic of each antibody. V_H and V_L refer to the variable domains of the heavy and light chains respectively, while C_H and C_L are used for the constant domains of the immunoglobulin, which have very limited variations between different IgG antibodies. Enzymatic proteolytic cleavage of IgG produces three fragments: two identical Fab fragments that demonstrate antigen binding activity and one Fc fragment that is not involved with antigen binding and consists of heavy chain components (Figure 2.4). The oligosaccharides of the antibody are attached to the Fc fragment, and although they play no role in

antigen binding, they affect interaction with Fc-receptors that are present on the B-cell surface and recognition of the antibody by the immune system [68].
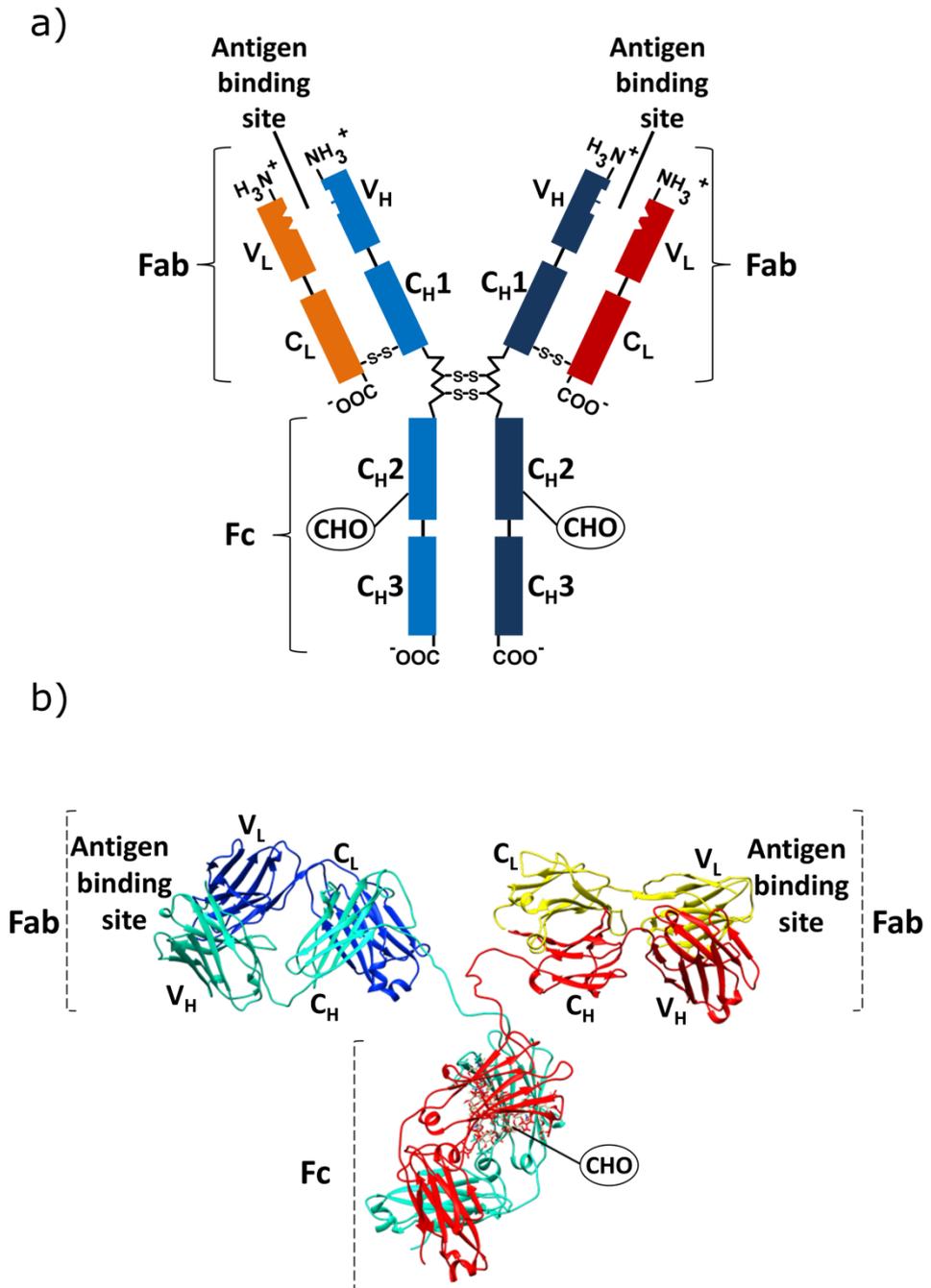
Figure 2.4: a) Schematic of the main elements of an IgG antibody, consisting of two heavy (H) and two light (L) chains; enzymatic cleavage separates the molecule into Fab and Fc regions. In the Fab fragments, the antigen binding site is formed by the combination of the variable domains, V_L and V_H, of the light and heavy chain respectively. The Fc fragment consists of only constant regions of the heavy chains and contains carbohydrates (CHO) that interact with Fc-receptors of B-cells (adapted from [69]), b) 3-D representation of IgG protein structure (PDB ID: 1IGT; visualised using Chimera).

Both heavy and light chains in a Fab fragment consist of a variable domain (~110 amino acids in the N-terminal region) and a constant domain (~110 residues in the C-terminal region), called V_H, V_L, C_H1 and C_L respectively. Constant and variable domains in both heavy and light chain consist of a similar double β-sheet structure, called the *immunoglobulin fold*, (Figure 2.5) which comprises antiparallel β-strands connected by peptide loops of varying length. The two β-sheets are folded and held together mainly by hydrophobic interactions and a disulfide bond [67] [68] [70].

The antigen-binding site is formed by six peptide loops, three from the V_L domain and three from the V_H domain, which are called *hypervariable regions* or *complementarity determining* regions (CDRs) while the double β-sheet regions, called the *framework region*s (FRs) exhibit much less variation and serve as a scaffold where the antigen-binding site is presented. An IgG molecule has two identical binding regions, one from each pair of H-L chains, which enables bivalent binding [23]. Other immunoglobulin molecules, such as IgM, that have several binding sites, exhibit multivalent binding [68].
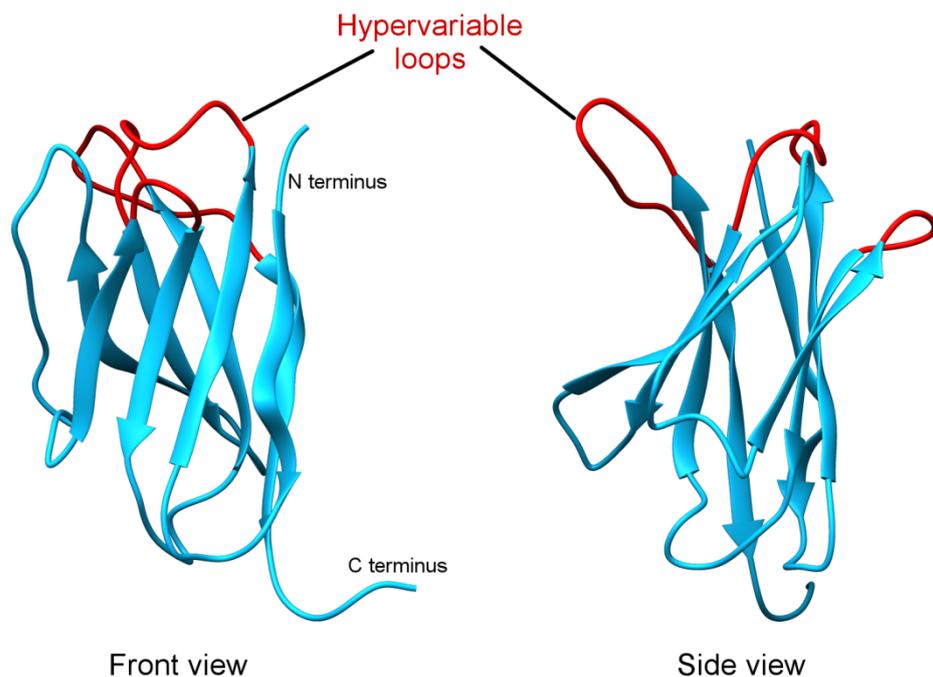
Figure 2.5: Front and side view of the 3D structure of the immunoglobulin fold. Antiparallel β-sheets are held together by hydrophobic interactions and a disulfide bond, while three hypervariable loops are presented at one end of the structure (adapted from [66]; PDB ID: 7FAB, visualised using Chimera).

Since most antigens consist of multiple epitopes, B-cells produce a variety of antibodies against an antigen, each binding to a different epitope. The antiserum, i.e. the serum of an immunised organism, thus contains a heterogeneous mixture of antibodies, called polyclonal antibodies. This heterogeneity increases the effectiveness of the immune response *in vivo*. However, it can be

disadvantageous for *in vitro* applications that require consistency in the antibodies developed for the recognition or caption of antigens through specific epitopes. This batch-to-batch variability can be overcome using monoclonal antibodies. Monoclonal antibodies are derived from a single B-cell clone hybridised with a myeloma cell, to form hybridoma. All antibodies produced by the same hybridoma are specific to the same epitope of the antigen. In addition, the clones of the hybridoma cells can be cultured indefinitely and produce monoclonal antibodies with consistent specificity for research, diagnostic and therapeutic purposes [68].

2.4 Antibody-Antigen Interactions

The antigen-antibody complex is formed through the bimolecular association between the antigen's epitope and the binding site (CDR regions) of the antibody. The antigen-antibody binding depends on a range of non-covalent interactions which include:

- Hydrogen bonds between electronegative atoms of the amino acid residues.
- Ionic bonds (salt bridges) between oppositely charged groups.
- Hydrophobic interactions between non-polar residues.
- van der Waals interactions [68].

Hydrophobic interactions force the non-polar groups of the amino acids to aggregate so as to avoid contact with water molecules and they play a key role in the stability of the antigen-antibody complex. The hydrogen bonds and the salt bridges contribute largely to the specificity of the interaction. Compared to a covalent bond, each type of the above interactions is individually weak, so a large number is necessary for high affinity binding. These interactions only occur over very short distances, so the formation of the antigen-antibody complex depends on their proximity [71].

The association between a single epitope of an antigen and the binding site of an antibody is based on the complementarity of the interacting sites, a characteristic that defines the specificity of the antigen-antibody interactions. A measure of the strength of this non-covalent interaction is the binding *affinity,* and high affinity antibodies bind strongly to the antigen's epitope to form a stable complex. Equation 2.1 describes the association between one of the binding sites of the antibody (Ab) and the epitope of a monovalent antigen (Ag) in order to form the antigen-antibody complex (Ag-Ab):

$$Ag + Ab \underset{k_{off}}{\overset{k_{on}}{\rightleftharpoons}} Ag\text{-}Ab \qquad (2.1)$$
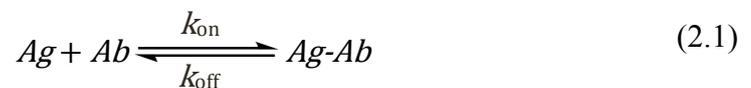
Here, k_{on} refers to the second order association rate constant and is expressed in units of $M^{-1}s^{-1}$, while k_{off} is the first order dissociation rate constant expressed in s^{-1} [71].

The affinity constant, K_A, (with unit M^{-1}) is the ratio of the rate constants,

$$K_A = \frac{k_{on}}{k_{off}} = \frac{[Ag-Ab]}{[Ag][Ab]} \qquad (2.2)$$

and is a measure of the antibody's affinity for the specific antigen at equilibrium, where [*Ag-Ab*] is the concentration of the bound Ag-Ab complex and [*Ag*], [*Ab*] are the concentrations of free antigen and antibody, respectively. While K_A is used to quantify the affinity of the antibody, the dissociation constant, K_D, is used to express the stability of the Ag-Ab complex (in M). It is based on the reverse reaction of Equation 2.1 and is the reciprocal of K_A so that,

$$K_D = \frac{1}{K_A} = \frac{k_{off}}{k_{on}} = \frac{[Ag][Ab]}{[Ag-Ab]} \qquad (2.3)$$

Stable complexes thus have low values of K_D. For immunoassays, high affinity is required for a low limit of detection, but the stability of antigen-antibody complex is also crucial to the performance of the assay, since dissociation during washing steps is undesirable. Using biosensor technology, such as SPR or QCM, it is possible to study the antigen-antibody binding kinetics in real time. Here, an antibody is immobilised on the sensor surface and as the analyte is introduced into the system, the interaction between the antibody and antigen is monitored in real time. The more analyte that is bound to the surface immobilised antibody, the greater the response signal until it reaches a plateau, which corresponds to saturation. The resulting association part of the response curve (Figure 2.6) can be used to calculate the association rate, k_{on}. In a typical experiment, the analyte solution is then replaced by running buffer, which shifts the equilibrium conditions ([Ag] is now reduced), leading to dissociation of antigen from the surface-immobilised antibodies. The dissociation phase is again monitored in real time in order to estimate the dissociation rate, k_{off}.

Figure 2.6 illustrates three hypothetical assays for three different antibodies against the same antigen. An antibody with high association and high dissociation rates forms the antigen-antibody complex rapidly but also dissociates quickly in a washing step (Ab3), while little dissociation is observed for an antibody with a low dissociation rate (Ab1). Thus, the lower the k_{off} is, the more suitable the antibody will be for most immunoassay formats. For this reason, the affinity of bioreceptors is typically expressed using the dissociation constant, K_D, and high affinity antibodies are expected to have K_D values between 10^{-12} and 10^{-8} M [37].

The experimental determination of affinity is based on a number of assumptions. 1) The antibodies are assumed to be homogeneous (e.g. monoclonal antibody) and only one species of the analyte/antigen is present in the solution. 2) The reaction is assumed to proceed to equilibrium and the separation of bound and unbound antigen is complete. 3) There is no non-specific binding or allosteric effects [37]. In practice, it is not possible to meet all of these conditions, but the above

above equations provide a theoretical framework for studying the antigen-antibody interactions and understanding the underlying processes.
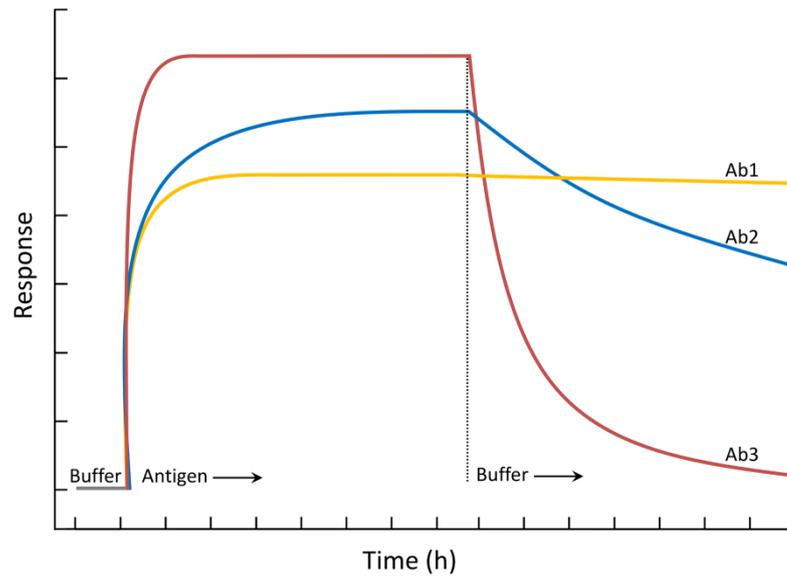
Figure 2.6: Example of responses curves (using real-time monitoring techniques such as SPR or QCM) of antigen binding with three different antibodies. Ab1 and Ab3 both have a high rate of association (k_{on}) but the dissociation rate (k_{off}) for Ab3 is faster than that of Ab1. Ab2 represents the response curve for a typical antibody (adapted from [37])

Since most antigens have more than one epitope, and antibodies can have multiple binding sites, there can be several interactions that affect the strength of the overall antigen-antibody binding. The overall strength of the interactions between a multivalent antibody and the epitopes of a multivalent antigen is called *avidity*. Therefore, even if an interaction at a single site has low affinity, higher valence can result in high avidity and thus stronger antigen-antibody binding [68].

2.5 Parameters Affecting Antigen-Antibody Interactions

Several types of molecular interactions are responsible for the antigen-antibody interactions, and these interactions are dependent on the local conditions and may thus influence protein stability and antigen binding.

The main parameters that can affect the stability of the proteins or the antigen-antibody complex are the temperature, pH and ionic strength of the solution. One of the main non-covalent interactions that drive protein folding and protein interactions is hydrogen bonding. The thermal energy provided by increasing temperature can break these hydrogen bonds leading to antigen dissociation and protein unfolding (denaturation). In contrast, decreasing the temperature can affect hydrophobic interactions in aqueous solutions, as a result of change in the interactions between water molecules around non-polar residues, which consequently weakens the hydrophobic effect that drives the folding of the protein (cold denaturation) [72].

The pH of the solution can also affect protein structure and function, by changing the charge of residues that participate in hydrogen bonding or salt bridges. At neutral pH, acidic side chains are negatively charged, but will become neutral in a pH lower than their pK_a. In contrast, basic residues are positively charged at neutral pH, becoming neutral at a pH greater than their pK_a [67]. Additionally, changes in the ionic strength of the solution, that is the concentrations of anions and cations, may also affect electrostatic interactions between charged residues.

The change in the overall charge of a protein or the screening of charge interactions that occurs at high ionic strength not only affects the structure and function of a protein, but also the way it interacts with the surrounding environment. For example, when the pH of the solution reaches the isoelectric point, the protein becomes neutral and thus less soluble in water and may form aggregates. Furthermore, changes in the net charge can influence interaction of a protein with surfaces, depending on the properties of the solid material, either by increasing its affinity for the material to the point of denaturation or changing its orientation so that the binding site becomes inaccessible [37].

2.6 Challenges and Limitations of Antibodies for Environmental Applications

The dependence of antigen-antibody binding on local environmental conditions has the potential to compromise the specificity or reliability of an immunoassay. Antibodies are a product of the immune response system and have evolved to function within the well-defined conditions maintained in an organism [23]. The use of antibodies in environments where the pH, temperature or ionic strength differ from physiological conditions can affect their binding abilities and stability. This presents a significant challenge for the application of immunosensors for use with environmental samples, where samples with a wide range of matrix properties (including pH and ionic strength) have to be analysed. Moreover, antibodies are large proteins with multiple domains, thus surface immobilisation, as is required for application in immunosensors, can often be challenging as it may lead to conformational changes that affect the antigen-antibody interaction, induce variations in antibody orientation or lead to steric hindrance between proteins [30].

Furthermore, monoclonal antibodies are preferred over polyclonal as they not only reduce batch-to-batch variability but are also homogeneous, ensuring the antibodies bind to only one epitope in an assay. However, the time, efforts and costs of hybridoma development are significantly higher than for polyclonal antibodies [68]. In addition, *in vivo* development of antibodies can be challenging or impossible when the targets are small-sized molecules, non-immunogenic or potentially toxic, which can be the case for environmental contaminants [73]. As a result, antibody-based assays for small molecule environmental contaminants often fail to meet the demands of regulatory and routine environmental monitoring for cheaper, faster, reliable and robust methods.

2.7 Alternative Affinity Receptors

Recent advances in protein engineering and materials chemistry, have led to the emergence of synthetic affinity receptors as replacements for antibodies in immunoassays. For example, recombinant technologies enable the production of large libraries of potential bioreceptor molecules containing randomly generated sequences from which bioreceptors with the highest affinity for the target compound are selected. These biological approaches, as well as bio-inspired chemical synthesis approaches, have led to a variety of receptors with improved characteristics compared to antibodies, such as increased specificity and selectivity, higher stability and reduced costs and time of development [40].

Antibody fragments

Antibody fragments, which only contain those regions of an antibody associated with antigen binding, have been introduced as alternative bioreceptors that are easier and less expensive to manufacture. The most common types include Fab fragments and single chain variable fragments (scFv), which are both significantly smaller than antibodies. This enables optimisation of surface coverage in biosensors and reduction of steric hindrance. Their reduced size also allows tissue penetration, which is an important property for therapeutic applications. However, antibody fragments tend to degrade more quickly than antibodies, and although methods to extend their half-life have been developed, these can significantly increase the production costs [74]. In addition, their tendency to aggregate makes purification challenging, while immobilisation on solid surfaces can often cause conformational changes and, as a result, reduction in affinity or specificity [30].

Molecularly imprinted polymers

A non-biological approach to generate affinity receptors is template-directed chemical synthesis for the production of *molecularly imprinted polymers* (MIPs). Inspired by the lock-key mechanism of enzyme activity, MIPs are polymers containing cavities that are complementary to a target compound. The molecular imprinting process involves the co-polymerisation of functional monomers and a cross-linker in the presence of a template molecule that resembles the target (Figure 2.7). The monomers form a complex with the template and their functional groups are held in position by the cross-linked polymer. Although a wide range of materials can be employed, the most common functional monomers used in molecular imprinting are vinyl and acrylic monomers, such as methacrylic acid or vinylpyridine. Following polymerisation, the template molecule is removed leaving complementary cavities behind that serve as binding sites for molecular

recognition [38] [75]. This approach enables the development of artificial, non-biological receptors that can mimic the molecular recognition properties of biological receptors, such as antibodies and enzymes. In comparison to bioreceptors, MIP production can be much faster and more cost-effective. Due to their synthetic nature, MIPs are also very stable and robust, with high thermal and pH resistance and very long shelf-life [26]. MIPs can function as excellent receptors for small molecules, which has led to their increasing use in sample purification techniques, such as solid-phase extraction (SPE). A vast array of MIPs targeting toxins, pesticides, antibiotics and pharmaceuticals have been developed over the years and have become available commercially as highly selective SPE phases [26] [76].
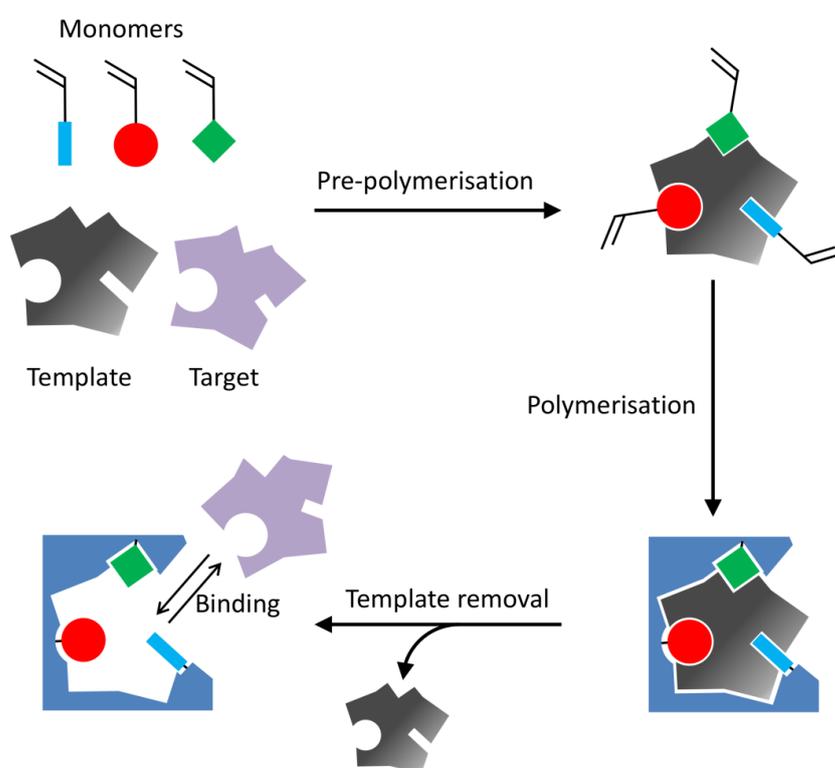
Figure 2.7 Schematic of the molecular imprinting process (adapted from [26]).

Other uses of MIPs have been focused on molecularly imprinted bioassays (analogous to immunoassays) and, to a lesser extent, *in vivo* applications. Notable examples include the development of MIP-based immunoassays for the detection of the pharmaceuticals theophylline and diazepam [77] and the antibiotic vancomycin [78]. Furthermore, melittin, a small, toxic peptide was successfully removed from mice using MIPs [79]. However, despite their advantages, MIPs exhibit much lower affinities than antibodies, slow binding kinetics, poor reproducibility and quite often poor site accessibility. [38] [79]. In addition, MIPs for protein capture and recognition are severely limited; typically organic solvents are used for the molecular imprinting process and MIPs

31

are thus more effective in non-aqueous environments. Moreover, the synthetic nature of MIPs poses increased risks of immunogenicity or toxicity in live organisms, which greatly restricts their use in therapeutics and *in vivo* diagnostics [26]. Although efforts to overcome such challenges are increasing, including development of water-compatible MIPs or the use of molecularly imprinted polymer nanoparticles (MIP NPs) [75] [79], these limitations need to be comprehensively addressed in order to fully exploit the potential of MIPs as alternative receptors.

Aptamers

A class of non-protein biorecognition elements that has received significant interest is nucleic acid affinity probes, called *aptamers*. Aptamers, which is a portmanteau word derived from the Latin *aptus* (to 'fit') and the Greek *meros* ('part') [81] , are artificial, *in vitro* selected, single stranded DNA or RNA sequences that bind to a target compound with very high affinity and specificity. The concept of this technology relies on that of natural selection; here, from a large pool of binders, a binder's 'fitness' over that of others is determined by its ability to bind strongly to a target molecule [82]. Aptamers that bind to a specific target are developed using systematic evolution of ligands by exponential enrichment (SELEX), a method firstly presented in 1990 that enabled the selection of high affinity, non-antibody binders *in vitro* (Figure 2.8).
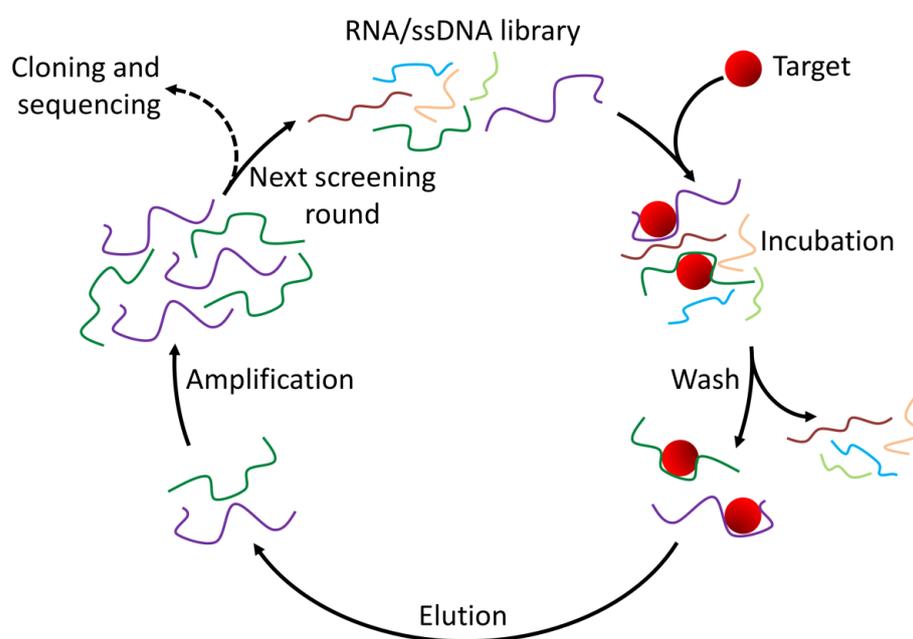
Figure 2.8: Brief schematic of the SELEX process for aptamer development. The library of oligonucleotides is incubated with the target, washed to remove unbound sequences and eluted to select the target-binding sequences. The eluted oligonucleotides are amplified and can be either subjected to subsequent screening rounds or isolated for sequencing (adapted from [80]).

SELEX starts with a large library of oligonucleotides (10^{14} – 10^{15} distinct sequences). The first selection round begins by mixing this library with the target antigen. Following incubation, low-affinity molecules are washed away, after which strong binders are eluted and amplified by polymerase chain reaction (PCR). The reduced oligonucleotide pool is then used in the following round of selection. This selection process is repeated several times, resulting in high affinity probes that are then isolated, sequenced and characterised. Aptamers are smaller and more stable than antibodies, have longer shelf-life and can demonstrate high binding affinity. An interesting trait of aptamers is that they often undergo a conformational change upon binding to the target. This is a very useful feature for biosensing, where, by adding fluorescent or redox labels on specific regions of the aptamer, target binding can be detected by the shifts in the electrochemical or optical signal due to such conformational changes.

These advantages, along with the versatile, cost- and time-efficient *in vitro* development, has encouraged researchers to intensify their efforts in producing aptamers, and numerous sequences have found use in basic and applied research, diagnostics or even therapeutics [26] [50]. However, while aptamers are more stable than antibodies, they can be easily degraded in complex matrices, such as blood serum or cell environments. More importantly for application in environmental monitoring, they can become unstable over a range of pHs or temperatures, and are sensitive to cation concentration and nuclease digestion. DNA aptamers are more stable than RNA, but are still not fully resistant to degradation. In addition, the charged backbone of the oligonucleotides is self-repelling which can lead to conformational instability or unfolding during surface immobilisation. Efforts to overcome such challenges have been focused on chemical modifications to increase their stability and functionality. Still, aptamers are limited to the types of chemical bonds they can form for target capture due to their short range of building blocks, which consequently narrows their range of targets [83-85].

Antibody mimetics

A promising alternative to aptamers are protein-based synthetic binders called protein scaffolds or non-IgG scaffolds (or peptide aptamers, due to their similarities in function and development with DNA or RNA aptamers). Protein scaffolds mimic the high binding affinity and specificity of antibodies, and for this reason they are also termed *antibody mimetics* [73] [86]. Although not based on immunoglobulins, they mimic many of the features associated with antibodies: a constant protein backbone and variable antigen-binding domains, similar to the complementarity determining regions (CDRs) of antibodies. However, antibody mimetics are considerably smaller than antibodies (between 6-20 kDa compared to 150 kDa), and highly stable and robust against local environmental conditions. The selection of protein scaffolds proceeds through a process

similar to SELEX in the sense that they both follow a repetitive cycle of selection and amplification until the strongest binders are identified. The majority of selection methods employ phage display technologies, although several other approaches have been used, such as cell, yeast or ribosomal display [87].

A number of different protein scaffolds derived from a range of organisms (including viruses, bacteria, fungi, plants, animals and humans) have been selected for antibody mimetics development, and modified by inserting variable peptide sequences at specific sites using recombinant technologies. In addition, similar to aptamers, their small size allows tissue penetration, an important trait for therapeutic applications. Furthermore, due to their synthetic nature, they can readily be modified chemically, depending on the desired properties. For example, cysteine residues can be engineered at specific sites either for orientation-specific surface immobilisation or for conjugation of functional molecules, such as biotin, radionuclides, fluorescent labels or polyethylene glycol. This allows the properties of the binders to be engineered for the intended application, such as tailoring their pharmacokinetic characteristics, e.g. extended half-life for therapeutics or rapid clearance for diagnostics such as medical imaging [88] [89].

The flexibility of antibody mimetics is not limited to their enhanced physicochemical properties. The *in vitro* nature of their selection entirely bypasses the use of animal immunisation, which permits the selection of binders against a vast range of targets, including those which would normally be challenging or impossible for conventional antibodies, due to their small size, toxicity or low immunogenicity. The variable domains which form the binding sites of antibody mimetics, are typically peptide loops anchored at both ends within the protein scaffold. This enables the peptide loop to adopt different conformations and recognise targets of different shape, charge or hydrophobicity while being embedded in a rigid and biologically inert protein scaffold [73]. The peptide sequences of the variable loops are randomised in order to construct large pools (libraries) of different variants of the binding protein. A gene encoding each antibody mimetic is inserted into the DNA of a microorganism or an expression vector, so that when the gene is expressed the binding protein is displayed on the outer surface or compartment of the carrier. This approach enables the creation of large and diverse libraries of carriers, each displaying a different variant of the protein scaffold.

The display library is screened for the selection of high affinity target-binding proteins, using a process similar to SELEX screening, called *biopanning* (Section 2.8; Figure 2.13) [87] [90]. This process has been shown to enable the selection of antibody mimetics against a wide range of conventional or unconventional targets, and that exhibit very high affinities, comparable to that of antibodies. Furthermore, while the development of antibodies against new targets is time-

34

consuming, usually requiring several months, the production of antibody mimetics typically only takes a few weeks. In addition, protein display library screening technologies are substantially less expensive, consume far less material than *in vivo* development strategies and thus enable low cost production with high yields [26] [73] [84] [89].

The first antibody mimetic introduced as an antibody alternative was reported in 1996 by the Roger Brent group; they demonstrated the selection of protein engineered affinity proteins against human cyclin-dependent protein kinase 2 (CDK-2) using thioredoxin (TrxA), a modified *E. coli* enzyme, as a scaffold (Figure 2.9f). The binders demonstrated dissociation constants for CDK-2 in the nanomolar range which is comparable to those for high affinity antibodies [91]. Since then, numerous studies have reported the use of thioredoxin-based antibody mimetics that bind to a variety of clinically important protein targets [26]. During the past 15-20 years, over 50 different antibody mimetics of variable origin have been introduced, with the number of reports of novel scaffolds as well as research and development on potential applications growing constantly [92]. Notable examples of antibody mimetics are presented below.
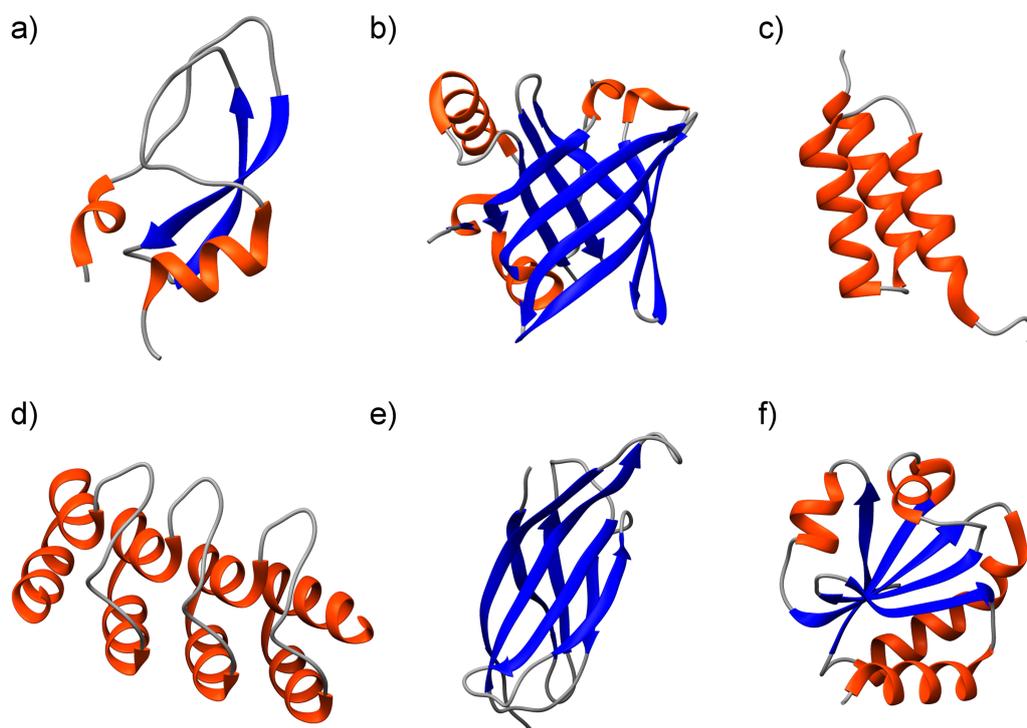
Figure 2.9: Protein structures of a) Kunitz domain (PDB ID: 1KTH), b) Anticalin (PDB ID: 1LPN), c) Affibody (PDB ID: 2B88), d) DARPin (PDB ID: 2JAB), e) Adnectin (PDB ID: 2QWQ) and f) Thioredoxin (PDB ID: 2TRX). All structures were visualised using Chimera (here, β-sheets are highlighted in blue, α-helices in orange, while peptide loops are shown in grey).

Monobodies (Adnectins)

Monobodies are an antibody mimetic that has been used extensively in clinical studies. The scaffold is based on the tenth domain of human fibronectin, a small (~10 kDa) protein consisting of a stable backbone of seven β-sheets and three accessible loops with randomised sequences that serve as binding sites (Figure 2.9e). Several approaches have been reported for library screening, including phage display, mRNA display and yeast-two hybrid. Monobodies demonstrate high thermal and chemical stability as well as remarkable K_D values reaching picomolar levels. A wide variety of proteins have been targeted by monobodies, including SARS viral proteins, rabbit and goat IgG, yeast small-ubiquitin-like modifier (SUMO), green fluorescent protein (GFP) and various cytokines, growth factors, enzymes and signalling proteins. Monobodies are available commercially as Adnectins[TM] from Adnexus Therapeutics (currently owned by Bristol-Myers Squibb) [26] [89] .

Anticalins

Anticalins are based on lipocalins, which are extracellular proteins found in both prokaryotes and eukaryotes and are responsible for storage or transport of hydrophobic molecules such as vitamins, lipids or various secondary metabolites. Anticalins consist of eight anti-parallel β-strands that form a barrel like structure (a β-barrel), four connecting variable loops and an α-helix at the C-terminus. The variable loops and the adjacent residues of the β-barrel form a ligand pocket that binds tightly to small molecules or peptides (Figure 2.9b). Anticalins are small (160-180 residues) proteins, that lack disulfide bonds and exhibit high thermal stability, while demonstrating very high binding affinities of nano and picomolar levels [26] [89] [92]. The Anticalin technology has been commercialised by Pieris Pharmaceuticals and is focused on therapeutic applications, focusing to date on anemia, respiratory and cardiovascular diseases, and immuno-oncology applications, some of which have advanced to human Phase I clinical trials. An Anticalin for anemia treatment has already moved to Phase II trials [93].

Kunitz domains

Kunitz domains are based on serine protease inhibitors, usually of human origin. They are small (~60 residue), stable proteins, consisting of disulfide-cross-linked α-helices and β-sheets and one or two (Figure 2.9a) variable loops that can be randomised to yield high affinity binders via phage display library screening. Kunitz domain scaffolds have been primarily used for the development of therapeutic agents [26]. The most notable example is the FDA-approved drug Kalbitor (ecallantide)

for the treatment of hereditary angioedema or blood loss prevention during cardiothoracic surgery and functions as an inhibitor to plasma protease kallikrein [94].

Affibodies

Affibodies are derived from the artificially mutated B-domain of the immunoglobulin-binding region of staphylococcal protein-A, called the Z-domain. These are small (6.5 kDa; 58 residues), single domain proteins containing only three α- helices and no disulfide bridges (Figure 2.9c). The target-binding regions are developed by randomisation of 13 residues in two of the protein's helices and selection is achieved using phage display [95]. The applications of Affibody technology have been explored for diagnostic, therapeutic and research purposes, such as molecular imaging, targeted therapy, protein purification or biosensors. For instance, Affibodies targeting HER2 proteins have been tested in clinical trials for *in vivo* imaging of malignant tumours on breast cancer patients, while Affibodies against Taq DNA polymerase and human IgA have been used as capture agents in microarrays [89].

DARPins

Designed ankyrin repeat proteins (DARPins) are based on ankyrin repeat (AR) proteins, which are binding proteins ubiquitous in eukaryotic organisms. AR proteins are assemblies of repeated motifs, each motif containing 33 residues shaped into two α-helices linked by a short β-turn. DARPins (14-22 kDa) are consensus designed AR proteins with 7-8 randomised residues in each repeat and usually consist of four, five or six AR repeats (Figure 2.9d). Selection of DARPins through ribosomal display yields high affinity binders with K_Ds in the picomolar range. DARPins demonstrate very high stability owing to a hydrophobic interface in the interior, while the N-terminal and C-terminal repeats are hydrophilic, and thus can be readily expressed in *E. coli* as soluble proteins. DARPins can be designed to exhibit avidity since their repeat structure enables the insertion of different binding sites on a single DARPin molecule, so that it can target multiple epitopes on the same antigen or capture several targets [26]. The DARPin approach was further extended to synthesise LoopDARPins, where elongated loops (19 residues) were inserted in the β-turn position of each repeat, aiming to increase the interaction surface on the proteins [96]. DARPins are currently a registered trademark of Molecular Partners AG. The main focus of research has been on their use as therapeutic agents in immuno-oncology, where DARPins targeting cancer-related proteins have currently entered phase I and II clinical trials, as well as ophthalmology, where phase III trials on treatment of retinal diseases have already been initiated [97]. DARPins have also been used in biosensors for the detection of MalE, a maltose binding protein, demonstrating nanomolar range affinities and 0.3 nM LOD [98].

The range of unique and novel antibody mimetics is growing constantly and these are steadily gaining ground as useful tools in therapeutics, diagnostics and basic or applied research. Other noteworthy antibody mimetics include Affilins, Avimers, Fynomers, Knottins, Atrimers, Alphabodies, Repebodies, Centyrins, Pronectins and Obodies. For a more detailed discussion on established antibody mimetics see recent review articles [26] [86-89] [92].

2.8 Affimers

This study is focused on Affimers, a class of antibody mimetics based on cystatins, which are a large family of cysteine protease inhibitors, all sharing sequence homology and a common tertiary structure consisting of a single α-helix and an anti-parallel β-sheet. Affimer is a registered trademark of Avacta Life Sciences Ltd, which has developed two Affimer scaffolds of different origin, each aimed at different applications. For therapeutic purposes, a protein scaffold of human origin, based on the human cystatin Stefin A (SteA), is used to reduce the risk of immunogenicity. For research and diagnostic applications, phytocystatin, a plant-derived cystatin, was used to develop a second Affimer scaffold that was initially called Adhiron; currently, the term Affimer is used by Avacta for both scaffolds [85] [89].
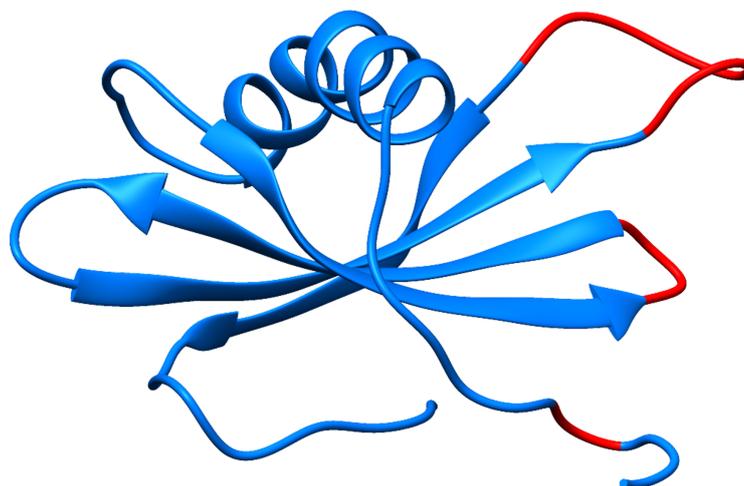
Figure 2.10: Structure of the Affimer scaffold based on human stefin A (STM). Antigen-binding peptide inserts are highlighted in red (adapted from [99]; PDB ID: 1NB5).

The concept of the cystatin scaffold was first introduced in 2005 by researchers at the Medical Research Council Cancer Unit in Cambridge, where they used a rational approach to design a protein scaffold that would meet the requirements for an 'ideal' peptide aptamer [99]. Here, an ideal scaffold was defined as being: a) of known structure; b) stable enough to hold a wide variety of inserted antigen-binding peptides; c) flexible enough to retain its folding following peptide insertion; d) biologically inert so as to limit interactions with cellular proteins and e) expressed identically in both prokaryotic and eukaryotic systems. By comparing a number of different protein scaffold candidates, the authors identified Stefin A as most closely meeting all the defined criteria. SteA is a small (98 residue), monomeric, single-domain protein that requires no post-translational

modifications or disulfide bridges, is well-expressed in different biological systems and is not toxic to human cells whilst exhibiting high thermal stability. Mutations by amino acid replacements in three positions in the protein yielded the biologically inert Stefin A triple mutant scaffold (STM) (Figure 2.10). The STM scaffold retained high thermal stability (~81 °C melting temperature), was well-expressed in bacterial, yeast and mammalian cells and contained two regions suitable for peptide insertions without affecting the protein's folding. The same group also modified the STM scaffold with a cysteine residue for site-specific oriented immobilisation on gold, and were able to demonstrate successful label-free detection of target proteins using SPR [100]. This approach of oriented immobilisation of the STM scaffold was implemented in later studies in order to demonstrate electrochemical detection of cyclin-dependent kinases (CDK), even in complex matrices such as yeast cell lysates [101]. Since then, the use of this antibody mimetic has been demonstrated with a variety of label-free transducers including open circuit potential measurements [102], field-effect transistors [103], SPR [104], dual-polarization interferometry, [105] QCM-D and microcantilever sensors [106]. In addition, Johnson et al. [83] reported the highly sensitive Affimer-based impedimetric assay for the detection of C-reactive protein, an important inflammatory biomarker. The latest variant of the Affimer scaffold, termed Stefin A quadruple mutant-Tracy (SQT), has been developed against biomarkers of fibrosis [107], HPV16 oncoproteins [108] and CDK2 [109].
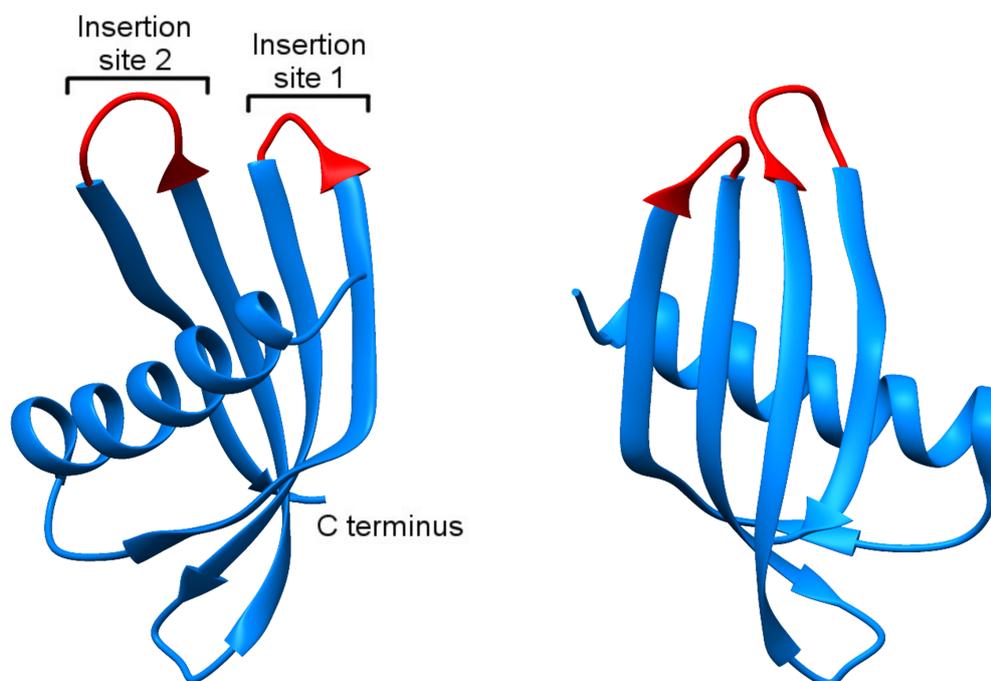
Figure 2.11: Structure of the Adhiron scaffold, showing a single α-helix and four antiparallel β-sheets (blue) and two antigen-binding peptide inserts (red) (Adapted from [27]; PDB ID: 4N6U).

A similar cystatin scaffold, but based on plant-derived cystatins (phytocystatins) and called Adhiron (Figure 2.11), was designed and presented by the BioScreening Technology Group (BSTG) at the University of Leeds [27]. Here, 57 phytocystatin sequences were aligned in order to derive a consensus phytocystatin sequence by identifying the most common residues at each site of the aligned sequences. Consensus protein design is based on the hypothesis that regions in the protein sequence that are most instrumental for protein stability and functionality are expected to show a high degree of conservation among homologous proteins in different organisms [110]. The consensus sequence derived from the sequence alignment consists of a four-stranded antiparallel β-sheet and one α-helix. The scaffold was further modified by replacing the two peptide loops responsible for protease inhibitor activity with randomised peptide sequences of nine amino acid residues at each loop (excluding cysteine) to create antigen-binding peptides. This randomisation yielded a large (~10^{10}) and highly diverse library of Adhiron variants that, through phage display, can be screened for the selection of high affinity binders against a particular target. The Adhiron scaffold is a small (92 residues, 12-14 kDa), monomeric, single-domain protein, that lacks disulfide bridges and glycosylation sites, demonstrates high stability (melting temperature up to 101 °C) and high solubility, while it is readily expressed in microbial hosts. These features satisfy the criteria proposed for protein engineered therapeutic proteins [111] as well as the requirements defined by the designers of the STM Affimer scaffold [112]. The scaffold is also largely pH resistant, thus, allowing target selection in alkaline or acidic conditions. Moreover, as with the STM scaffold, the insertion of a cysteine residue enables covalent and oriented immobilisation of Adhirons on gold surfaces [105]. These traits (high scaffold stability, site-directed immobilisation free of conformation changes) make Adhirons ideal for integration in biosensors.
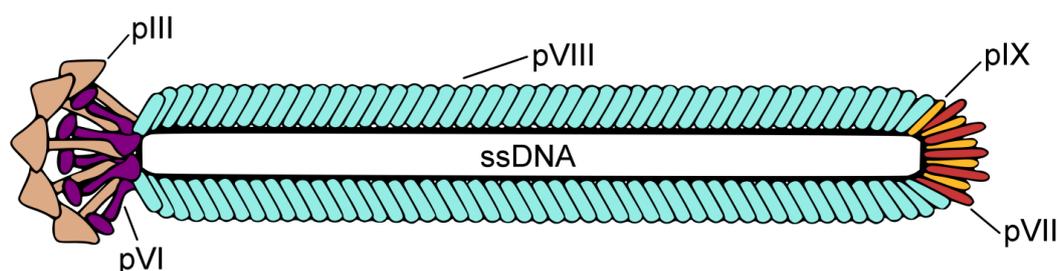
Figure 2.12: Schematic of the basic structure of an M13 filamentous bacteriophage. The ssDNA is encapsulated by a cylindrical protein coat, which consists of about 2700 copies of the major coat protein (pVII) and five copies of each of the minor coat proteins (pIII, pVI, pVII and pIX). The Adhiron protein is displayed at one of the pIII coat proteins (adapted from [114]).

The selection of Adhiron molecules is achieved using phage display libraries and an affinity selection process called biopanning. Phage display relies on the use of bacteriophages (or simply phages), which are DNA-containing viruses that infect bacteria (typically *Escherichia coli*) and use

the host machinery to replicate. Phages are valuable tools in biotechnology and are extensively used in protein engineering processes [82]. Different types of bacteriophage (such as M13, f1, fd, T7, T4 and λ) are used depending on the application; for Adhiron development, the M13 filamentous phage is employed. These are long (900 nm), rod-shaped viruses that encapsulate a closed, circular single-stranded DNA molecule (ssDNA) inside a cylindrical protein coat, that consists of about 2700 copies of a major coat protein and five copies of four different minor coat proteins (Figure 2.12) [112]. To create phage display libraries, the gene that encodes the phage coat major (pVIII) or minor (pIII) protein is modified in order to carry a foreign sequence, which is expressed as a 'fusion' (hybrid) coat protein. [113].
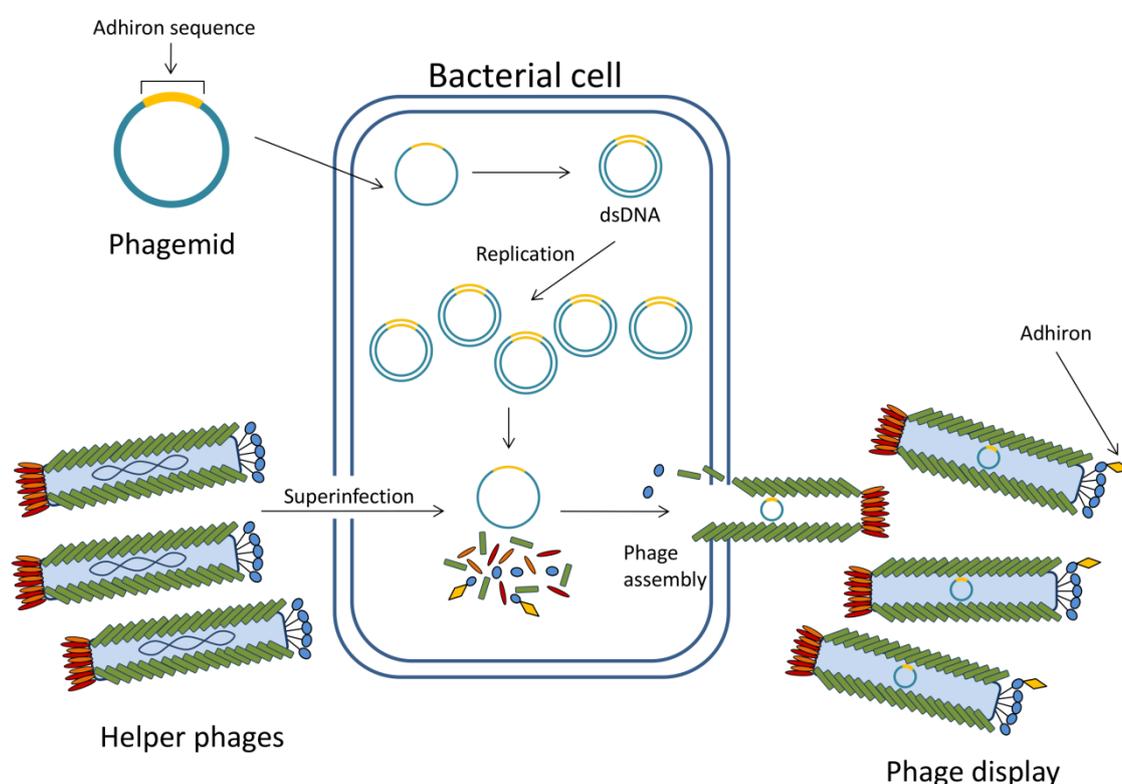
Figure 2.13: Brief schematic of phage display construction. Here, the coding region of an Adhiron protein is inserted into the pIII minor coat protein gene and the recombinant phage DNA is incorporated into a phagemid[3]. The recombinant phagemid is inserted into *E. coli* and replicated using the host machinery. Phage assembly is initiated by superinfection of the host bacteria with helper phages, followed by excretion of phage particles that display the Adhiron protein as a fusion pIII coat protein.

---

[3] A phagemid is a plasmid that carries a plasmid origin of replication (so as to normally replicate in bacterial host cells), an antibiotic resistance gene (for selection of plasmid-bearing host cells) and a filamentous phage origin of replication. A plasmid is a small, circular, double-stranded DNA molecule, typically of bacterial origin. Plasmids (or phagemids) containing foreign DNA (recombinant DNA) are extensively used in protein engineering as cloning vectors to carry the recombinant DNA into host cells for replication and expression; phagemids can also be packaged into viral particles as ssDNA [82].

In order to construct the Adhiron phage display library, the coding region of the Adhiron protein was inserted into the pIII minor coat protein gene and the recombinant phage DNA was incorporated into a phagemid vector (called pBSTG1) that was subsequently introduced into *E. coli* through electroporation (Figure 2.13). In the Adhiron coding region, the scaffold sequence remains constant, whereas the antigen-binding peptide sequences are randomised, resulting in a large pool of sequence variants of the Adhiron coding region, each incorporated into pBSTG1 phagemids (called pBSTG1-Adh). Following electroporation, each *E. coli* cell carries a phagemid with a different sequence variant. The ssDNA of each phagemid is replicated inside the host but its phage assembly mechanism is inactive. Virion assembly is initiated by infection of the phagemid-rich bacteria with helper phage particles (here M13KO7) that carry all necessary phage assembly genes. The secreted phage particles are hybrids (or mosaics) of the phagemid and helper phage, which contain both the recombinant (fusion) and wild-type of the pIII coat proteins. Therefore, inside the protein coat, the DNA of the virion carries the Adhiron protein coding region, whilst the Adhiron protein is exposed to the environment where it can interact with other proteins or molecules. As a result, the pool of pBSTG1-Adh phagemids is now a large library of phage particles (phage display library), each displaying a different Adhiron variant as a pIII fusion coat protein [27] [82] [113].
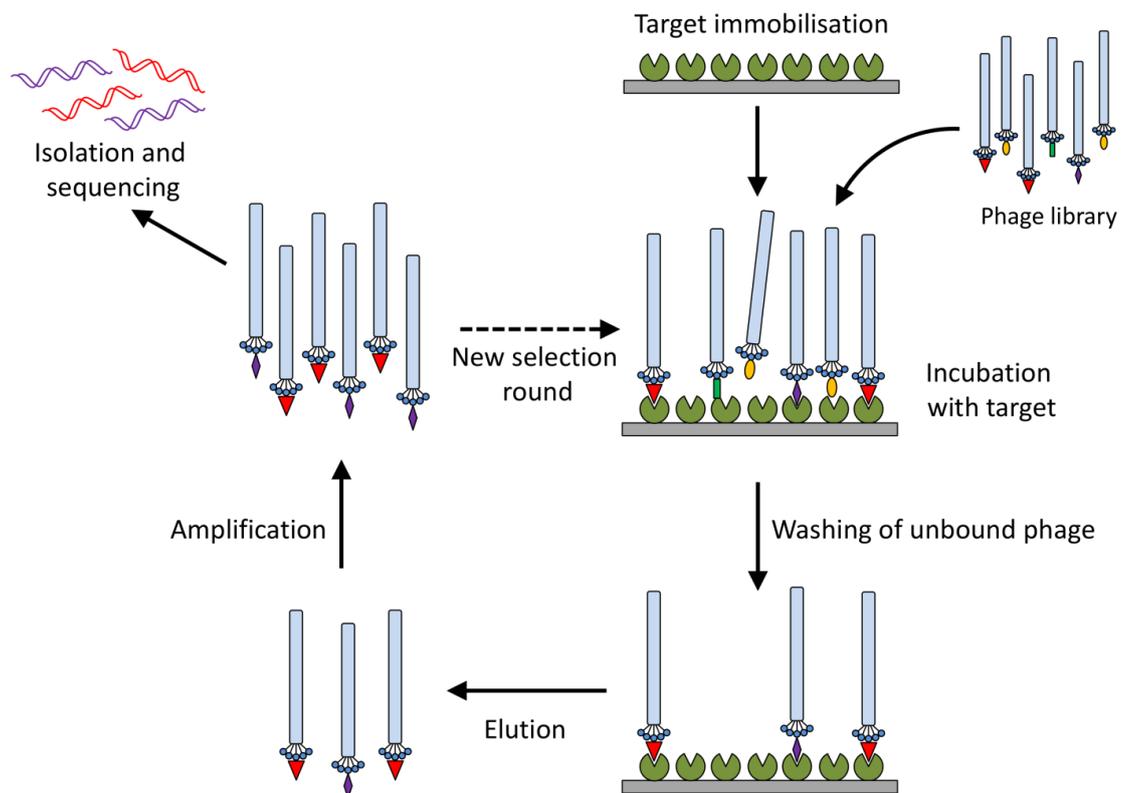
Figure 2.14: Schematic of the affinity-based protein selection process (biopanning) from phage display libraries. In the first screening round, the phage library is incubated with the target and then washed to remove non-specifically bound phages. The specifically bound phages are eluted and amplified by infecting bacteria. The amplified phages are subjected to additional selection rounds or are isolated and sequenced for further characterisation (adapted from [26]).

The biopanning process starts with the immobilisation of the target on a solid substrate and the incubation with the Adhiron library (Figure 2.14). Typically, the immobilisation method is based on the remarkably high binding affinity between biotin and streptavidin. Initially, the target molecule is labelled with a biotin linker. Then, the biotin-labelled target is immobilised onto streptavidin-coated substrates through the biotin. Notably, to reduce binding of non-specific Adhirons, prior to the first selection round (incubation with target), the Adhiron phage library is pre-panned against wells containing only the biotin linker (no target). This pre-panning step helps removing phages that bind to the biotin linker and streptavidin-coated surfaces. The unbound phages are then used for the first selection round, where following incubation with immobilised target, those that did not bind to the target are washed away, so that only target-interacting phages remain. The specifically bound phages are eluted, usually by low or high pH buffers. Unlike the antigen-binding peptides, the Adhiron scaffold and the M13 phage are resistant to extreme pH values, enabling them to withstand these harsh conditions and remain stable, whilst the Adhiron binding site is destabilised and dissociates from the target. Here, elution was achieved by adding glycine-HCl (pH 2.2) followed by Tris-HCl (pH 9.1) for neutralisation and further eluting with triethylamine (neutralised with Tris-HCl pH 7). The eluted phages are then amplified by infecting bacterial cells, facilitated by M13KO7 helper phages. The enriched and amplified phage library aliquot is used for the second screening round, where the biotinylated target is now immobilised on streptavidin-coated magnetic beads. The phage library aliquot is incubated with target, washed to remove unbound phages, whilst bound phages are eluted and amplified as in the first round. In the final round, the phage pool is now incubated with immobilised target on NeutrAvidin-coated plates (so as to further reduce non-specific binding). For selection of Adhirons against small targets, such as short peptides or small molecules, additional screening rounds are required [27] [82]. Following amplification of the phages selected in the final round, the ability of the displayed Adhirons to bind the target is typically demonstrated by phage ELISA. In this assay, the phages are incubated with biotinylated target on streptavidin-coated wells and, following washing, bound phages are detected by an HRP-labelled, anti-phage antibody with TMB as substrate [27]. The phages that demonstrate binding to the target are then isolated and sequenced to identify and compare the antigen-binding peptide sequences of each Adhiron protein in order to reveal common occurring binding motifs (i.e. clones of the same Adhiron variant). Adhirons with unique binding motifs are then selected for further characterisation, such as thermal stability, structure determination or binding affinity [113]. Adhiron binders against yeast SUMO have been demonstrated with nanomolar range affinities for their target protein, whilst showing minimum cross-reactivity with the closely related human SUMO proteins [27]. High affinity Adhiron binders have since been selected against numerous molecules, including fibroblast growth factor (FGF1), cell adhesion molecule CD31, SH2 domains as well as a 12-amino acid peptide. The latter, as a small-sized target, required additional screening rounds to ensure high affinity and specificity. More recently, Adhirons have been selected against

fibrinogen, hypoxia-inducible factor 1 (HIF-1) and even magnetite nanoparticles [28] [29] [115] and today Affimers targeting over 350 different targets have been reported, illustrating the versatility of this technology.

Adhirons have also been demonstrated as important binding agents for use in immunoassays. For example, an Adhiron-based impedimetric biosensor for the detection of anti-myc tag antibodies was shown to have picomolar sensitivity [30]. More recently, an impedance biosensor with 90 fg/mL LOD has been demonstrated for the detection of interleukin-8, an important biomarker of acute inflammation [31]. The Affimer (human stefin A) and Adhiron (phytocystatin) scaffolds have been commercialised by Avacta and both are currently marketed under the Affimer brand (as Type I and Type II Affimer corresponding to the STM and the Adhiron scaffold, respectively). Recently, Avacta announced the selection of high affinity and specific Affimers against the NS1 protein of the Zika virus and the development of three independent assays for rapid diagnostics of Zika infection; notably, selection, characterisation and immunoassay development together required approximately 16 weeks, a very short period compared to conventional antibody development [116].

The main focus of Affimer research has been orientated towards clinical diagnostic and therapeutic applications that are largely involved with targeting specific proteins. Proteins are large, complex molecules with several epitopes. This increases the probability of selecting Affimers with high affinity. However, detection of small-sized molecules by bioreceptors, including Affimers, is significantly more challenging and has received far less attention. Indeed, to date, only the single use of Affimers in competitive ELISAs for the detection of a small molecule (the antifungal drug posaconazole), has been reported. Critically, the posaconazole Affimers exhibited high specificity and insignificant cross-reactivity with the closely related drug voriconazole, illustrating the potential for Affimers for small-molecule detection [117].

Considering the versatility of Affimers and their enhanced properties and benefits compared to conventional antibodies, it is worth exploring their potential as alternative bioreceptors in bioassays for the detection of contaminants in the environment. This project aimed to evaluate Affimers as synthetic binders of small organic compounds, focusing on the environmental contaminants methylene blue and diclofenac. Affimers based on the Adhiron scaffold were selected against the two targets (Appendix A) and their affinity was evaluated using a variety of techniques. For methylene blue, the performance of Affimers in the complexity of surface water samples was also assessed. Finally, Affimer-based assays in competition format were developed for both targets, in order to demonstrate the potential for environmental applications (Chapters 4 and 5). It should be

noted that, hereinafter, the term Affimer will be used to refer to the Adhiron scaffold and the Adhirons selected against the targets of this study.

Chapter 3

Description of Techniques for Studying Affimer-Target Interactions

3.1 Overview

Immobilisation of the target analyte is critical for Affimer selection; for streptavidin-coated surfaces this was achieved by coupling the target to a long-chained biotinylated linker (Appendix A). In this work, however, the analytical techniques used to study Affimer-target interactions involved the use of gold-coated sensors (with the exception of ELISAs), and the most widely used approach for target immobilisation on gold surfaces is through *self-assembled monolayers* (SAMs) of alkanethiols. Both diclofenac (DCF) and methylene blue (MB) were thus attached to long-chain alkanethiols (LCAT) coupled with oligoethyleneglycol components (OEG). The LCAT component ensured the formation of dense and well-ordered molecular monolayers assembled on gold, whereas the OEG region enhanced the protein resistance of the molecular film [118]. The synthesis of target-derivatised LCAT-OEGs for this study is an adaptation of the synthetic protocol reported in Murray et al. [119], which makes use of the versatility of solid-phase chemistry to synthesise functionalised LCAT-OEGs. The MB- or DCF-derivatised LCAT-OEGs (referred to as LCAT-OEG-MB and LCAT-OEG-DCF respectively) were synthesised following this approach and were then used to form SAMs on the gold surfaces of sensors, in order to study the interaction of the immobilised target with Affimers (synthesis of LCAT-OEG-MB and LCAT-OEG-DCF are described in Chapters 4 and 5, respectively).

Biomolecular interactions between the target-derivatised SAMs and Affimers were studied through quartz-crystal microbalance with dissipation monitoring (QCM-D), where the target was immobilised on the gold surface of QCM-D sensors. However, before using LCAT-OEG-DCF and LCAT-OEG-MB to study the Affimer-target interactions, it was important to ensure that the SAM has assembled correctly and that surface immobilisation did not affect the properties of the target. This was achieved using cyclic voltammetry (CV), to study the redox properties of the methylene blue in the LCAT-OEG-MB SAMs. In addition, the conformation and structure of both the LCAT-OEG-DCF and LCAT-OEG-MB SAMs was characterised through electrochemical impedance spectroscopy (EIS) and infrared-spectroscopy (polarisation modulated – reflection absorption

infrared spectroscopy, PM-IRRAS), to determine whether through this immobilisation approach the target was efficiently presented on the surface for studying Affimer-target interactions.

The LCAT-OEG SAM characterisation and Affimer binding studies are reported in Chapters 4 and 5. This chapter provides a brief overview of SAMs and the above mentioned analytical techniques.

3.2 Self-assembled Monolayers

In general, the term SAM refers to the well-structured molecular assemblies that form spontaneously when organic molecules chemisorb onto the surface of solids (and sometimes liquids, such as mercury). The organic adsorbates contain a 'headgroup' (Figure 3.1), which has a high affinity for the substrate's surface and is responsible for the spontaneous adsorption of the molecules, which in effect lowers the free energy of the substrate [120]. Inter-molecular interactions between neighbouring organic backbones drives ordering of the SAM, leading to the formation of a well-structured 2D monolayer which alters the interfacial properties of the substrate, as determined by the nature of the 'tailgroup'. SAMs thus offer a highly versatile approach to tailor the physical and chemical properties of a material's surface according to the intended use, such as conductivity, wettability, chemical functionality or thermostability. As a result, macroscopic or microscopic phenomena occurring at the interface can be studied through SAMs, which enable coupling the external conditions to the electronic and optical properties of the substrate. An additional advantage of SAMs is that they are easily prepared in ambient atmospheric conditions and can assemble on objects of any size or shape [120] [121].
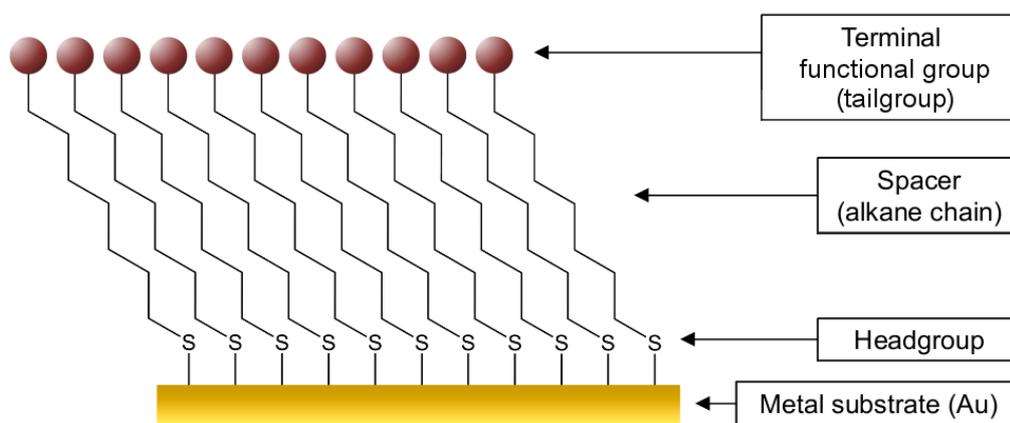
Figure 3.1: Schematic of self-assembled monolayers main components. The head groups (such as thiol groups) are chemisorbed to the metal substrate (e.g. gold) and separated by a spacer (alkane chain); the terminal (tail) groups interact with the species in the solution (adapted from [120]).

The solid substrates used for preparing SAMs are usually metals, and preferably noble metals such as Au, Ag, Pt, Pd or Hg. Other materials, such as silicon, carbonaceous materials and metal nanoparticles, have also been used for assembling SAMs. The most commonly used material, and of particular interest to this project, is gold. As a fairly inert metal, gold does not react with most chemicals and is resistant to oxidation, which makes it ideal to handle and use under atmospheric conditions and in combination with complex biological matrices. Additionally, thin gold films can

easily be deposited onto silicon wafers, glass slides or other silicon-based materials, and subsequently patterned through various lithographic and etching methods. Gold nanoparticles can be also used as SAM substrates. Moreover, the inert and robust nature of gold allows the removal of deposited impurities or residues through UV-ozonation critical for the assembly of well-structured SAMs; in fact, gold can withstand even more aggressive cleaning methods such as piranha cleaning. Another important characteristic is gold's biocompatibility, which enables the adhesion of cells or viruses to its surface without toxic effects, thus enabling analysis of whole cell systems or bacteriophages. Finally, thin gold planar surfaces are compatible with a number of established analytical and characterisation methods such as SPR, QCM-D, PM-IRRAS or electrochemical techniques [120] [121].

The first reported SAMs were based on alkylsilanes, but today a wide variety of monolayers and substrates have been introduced and investigated. The most widely studied and extensively used class of monolayers are those based on organosulfur compounds on gold, which depend on a stable bond formed between the thiolic groups and the substrate's surface [122]. More specifically, *n*-alkanethiols on gold are of particular interest to this study, since they form a strong S-Au bond, enabling the formation of densely packed and highly ordered SAMs [123]. This bond (which is considered a type of covalent or semi-covalent bond [120]) is energetically favourable and displaces other adventitiously adsorbed organic materials.

$$RSH + Au(0)_n \longrightarrow RS - Au(I) \cdot Au(0)_{n-1} + \frac{1}{2}H_2 \qquad (3.1)$$
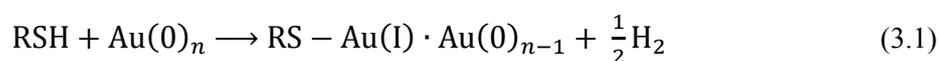
It is worth noting that this mechanism of alkanethiol-SAM formation on gold can be also applied for site-directed immobilisation of bioreceptors (antibodies, peptide aptamers, etc.), where the self-assembly is enabled through cysteine residues [122]. Figure 3.1 illustrates the typical structure of a thiol-based SAM on a gold substrate. Each alkane chain (spacer) has a thiol head group that is chemically linked to the gold surface. A terminal (or "tail") group is on the opposite end of the alkane chain, and consists of a functional group. Alkanethiols have been synthesized with a wide variety of terminal groups (including amine, carboxylic acid, hydroxyl, methyl and redox-active groups) which can alter the interfacial properties of the substrate, for example hydrophobicity and surface charge, and provide chemical functionality such as electron transfer or chemical reactivity. The composition of the SAM determines its functionality which can vary depending on the application [122].

50
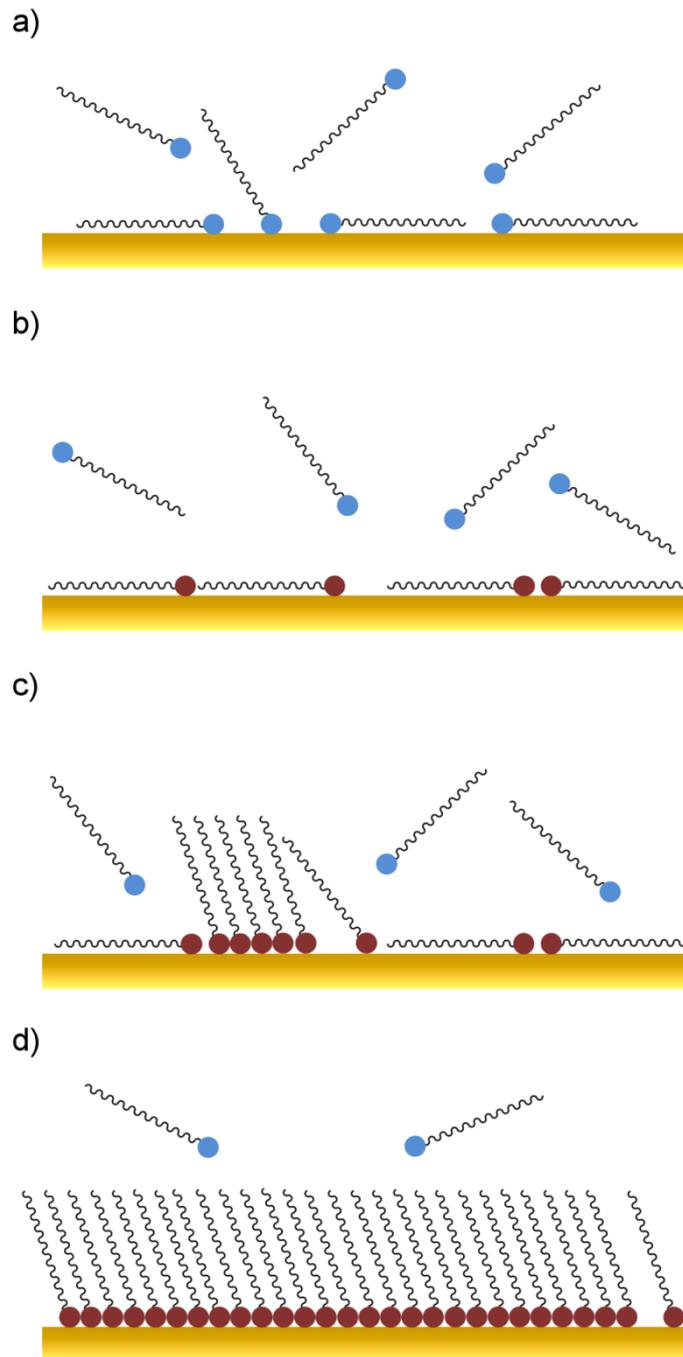
Figure 3.2: Scheme of the different phases of self-assembly of alkanethiols on gold: a) physisorption, b) 'lying-down' phase, c) gradual formation of the 'standing-up' phase, d) completion of the final, 'standing-up' phase (adapted from [124])

The mechanism of alkanethiol-SAM assembly consists of separate, progressive phases. Initially, more than 90% of the alkanethiols that make up the fully assembled SAM, assemble rapidly (within minutes) on the surface (Figure 3.2a). In the second phase, a more dense and well-ordered monolayer is formed at a slower rate (over hours). It is presumed that in the initial stage, the alkanethiols instantaneously interact with the gold substrate, primarily through physisorption rather

than chemisorption and are mainly in a 'lying-down' position (or 'striped'). Gradually, chemisorption starts taking place so that more alkanethiols become alkanethiolates as time passes (Figure 3.2b). The resulting monolayer in this initial phase, although ordered to a certain degree, has a low coverage and contains defects. However, chemisorption (in this case, the formation of Au-S bonds) is more energetically favoured than physisorption, so, over the course of hours, the alkanethiols undergo reorganisation that increases the number of chemisorbed molecules (Figure 3.2c). Specifically, the alkanethiols slowly adopt a more upright position ('standing-up' phase) so as to attain the highest possible number of S-Au bonds and thus maximise density while the defects are filled with alkanethiols from the solution. Finally, the SAM adopts its final structure (Figure 3.2d), as the alkanethiols reorganise and orientate through chain-chain interactions in order to become a well-packed, dense and highly crystalline monolayer [121] [122]. Figures 3.1 and 3.2d depict the SAM as composed of uniformly aligned molecules; in reality however, the monolayer exhibits a variety of defects such as pinholes, islands, domains or collapsed sites. The metallic surface of the substrate is not flat and free of defects, but contains several features in its polycrystalline structure, such as terraces, steps or impurities, that can affect the uniform packing of the monolayer. In addition, variations in the tilt angles or molecular vacancies from alkanethiols that have remained in the 'lying-down' phase will influence the homogeneity of the SAM packing.

SAMs modified with redox molecules have drawn increasing interest, since they can be used to study electron transfer kinetics on functionalised electrodes or provide label-free platforms for electrochemical sensing of biomolecular interactions. The most widely studied redox species on SAMs are metal complexes such as Fe, Ru or Os complexes [122]. For example, ferrocene-terminated SAMs have been used to probe molecular interactions [125]. Here, label-free detection of biotin–streptavidin interactions was demonstrated using mixed-SAMs of hydroxyl-, ferrocene- and biotin-terminated alkanethiols (the hydroxyl chains were used as dilutants). The ferrocene complexes showed sensitivity to the changes in the local electrostatic environment caused by the binding of streptavidin to biotin. This type of interaction, which affects the electron transfer, can be detected by simple electrochemical methods, such as cyclic voltammetry. It should be noted that for such applications, the redox potential of the electroactive species should be within a certain potential range, which is limited by the stability of the SAM and the characteristics of both the electrolyte and the analyte [126]. The electrochemical desorption potential for alkanethiolates on gold (Equation 3.2) is typically around -1.0 V (vs Ag/AgCl reference electrode), although this value can vary depending on the electrolyte, SAM chain length, the degree of order or the number of intermolecular interactions (such as hydrogen bonding) [120].

$$RS - Au + e^- \longrightarrow RS^- + Au^0 \qquad\qquad (3.2)$$

There are two main approaches for modifying SAMs with redox groups, either via attachment of ligand after SAM formation (post-assembly) or, as used in this work, through synthesis of alkanethiols modified before SAM formation (pre-assembly) [119]. In many cases, the bulky, charged redox species result in steric hindrance or interactions between the redox centres that can affect the ordered packing of the monolayer and often cause defects in the SAM. The most common solution to such issues is using mixed-SAMs where a dilutant alkanethiol with inert tail groups is incorporated in the SAM in order to separate the redox molecules (Figure 3.3) [126].
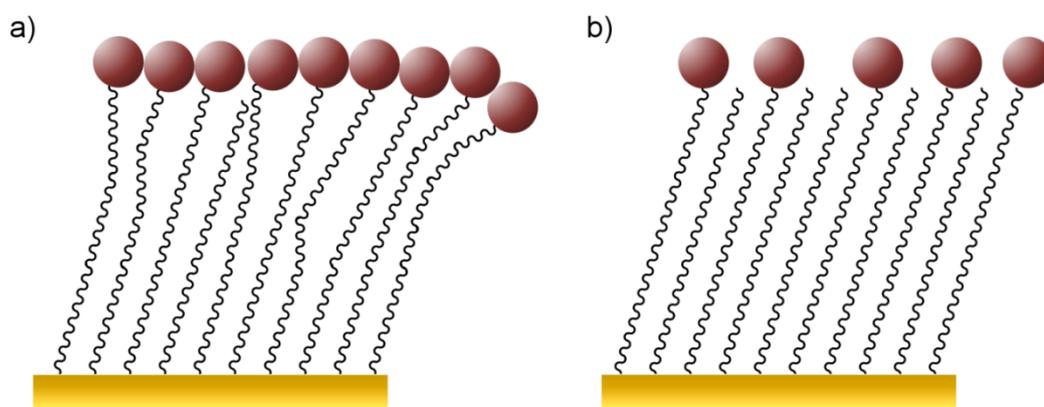
Figure 3.3: Schematic of alkanethiol SAMs on gold illustrating a) the SAM disorder caused by steric hindrance of bulky terminal groups and b) the increased order by separating the terminal groups with a dilutant to form mixed SAMs.

For the purposes of this study, long-chained alkanethiols (LCAT) were combined with oligoethyleneglycol units (OEG) and were then crosslinked with the target molecules (MB or DCF). This approach enables the formation of dense and well-packed SAMs where the presence of the OEG region increases the hydrophilicity of the monolayer and enhances its resistance to non-specific adsorption of proteins or other organic material [120]. Water molecules bind to the oxygen atoms of the oligomer through hydrogen bonding and form a stable solvation shell, so the proteins cannot easily displace the bound water to adsorb on the surface [127].

3.3 Brief Description of Electrochemical Techniques

Electrochemistry is the area of chemistry that studies the interrelation of electrical and chemical processes in a system. Specifically, it is interested in the transport of charge (electrons or ions) across the interface between two chemical phases, such as an ionic conductor (the electrolyte) and an electronic conductor (the electrode). The main focus in this study is the interactions and events that occur at the electrode/electrolyte interface when a potential difference is applied and a current flow occurs by the movement of electrons to/from a redox-active group attached to the electrode.

The simplest form of an electrochemical system consists of two electrodes separated by at least one electrolyte phase. This system is called an electrochemical cell, and the potential difference between the two electrodes, the cell potential, corresponds to the relative energies of the charge carriers in the two different phases of the interface, and controls the direction and rate of electron transfer. The electrode where electrons are released to the electrolyte phase, and is thus oxidised, is called the anode, whereas the electrode where reduction is occurring by the gain of electrons is called the cathode. This movement of electrons allows the flow of current through the system, which functions as an electrical circuit [128].
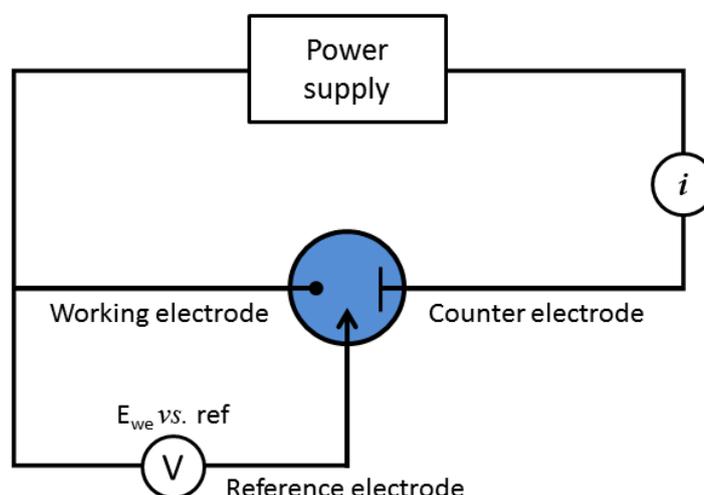
Figure 3.4: Diagram depicting a three-electrode system, where the electrochemical cell is connected to an external power supply. Current flows between the working and counter electrodes while the potential of the working electrode is measured with respect to the reference electrode (which has a fixed potential); adapted from [128].

According to Faraday's laws for electrochemical systems, the current passing through an electrode is directly proportional to the amount of a substance reduced or oxidised at the electrode's surface.

Voltammetric techniques, such as cyclic voltammetry, are used to study the chemical reactions occurring in the cell by measuring the flow of electrons moving across the interface (i.e. the rate of electron transfer). These methods use a three-electrode system (Figure 3.4), since it is necessary to control the potential on one of the electrodes, which is not possible using a two-electrode cell. A three-electrode system consists of the working (or indicator) electrode, the reference electrode and the counter (or auxiliary electrode). One is usually interested in studying only one of the redox reactions occurring in the cell; the electrode where this reaction takes place is the working electrode, and it is usually made of an inert material such as gold, platinum or carbon. The potential of the working electrode is always measured and reported with respect to that of the reference electrode. The composition of the reference electrode is such that its potential remains essentially constant and is not affected by changes in the cell. The standard (or normal) hydrogen electrode, SHE (or NHE) is the internationally accepted reference electrode and all other potentials are reported with respect to the NHE. Another very commonly used reference electrode, as used in this study, is the *silver-silver chloride electrode* (Ag/AgCl/KCl) which has a potential of +0.197 *vs*. NHE. Finally, the counter electrode, which is typically made of graphite or platinum, is responsible for facilitating the current flow and completing the circuit, so that current is not run through the reference electrode, which would alter its potential [128].

In this work, the working electrode is a planar gold surface deposited on a silicon wafer, while a platinum electrode functions as the counter electrode. At the electrode surface, the array of charged species and oriented dipoles at the metal-solution interface form a double layer (Figure 3.5), which, within a certain potential range, can approach the behaviour of an ideal polarised electrode (IPE), where no charge transfer is occurring across the interface, so only non-faradaic[4] processes are happening (accumulation of charges on both sides of the interface, also called charging current). This structure, where charge cannot cross the interface, is analogous to a capacitor, and the structure of the double-layer will affect the rate of charge transfer processes occurring at the electrode.

The inner layer of the solution side of the double layer is called the compact Helmholtz or Stern layer and is the one closest to the electrode (Figure 3.5). The compact layer includes solvent molecules and other species (ions or molecules) that are specifically adsorbed (through short range, non-coulombic interactions) on the electrode and, as described by IUPAC [129], "the locus of the electrical centres of the specifically adsorbed ions" is called the inner Helmholtz plane (IHP). The

---

[4] Faradaic processes involve charge (e.g. electrons) transfer across the electrolyte/electrode interface, causing oxidation or reduction to occur. In contrast, no charge transfer takes place during non-faradaic process and the observed current flow occurs due to accumulation (or removal) of charges on the electrode owing to changes in the potential of the electrode [128].

nearest non-specifically adsorbed ions (solvated ions) form the outer Helmholtz plane (OHP), while the solvated ions further away and extending to the bulk of the solution form the diffuse layer, whose thickness depends on the total concentration of ions in the solution [128].
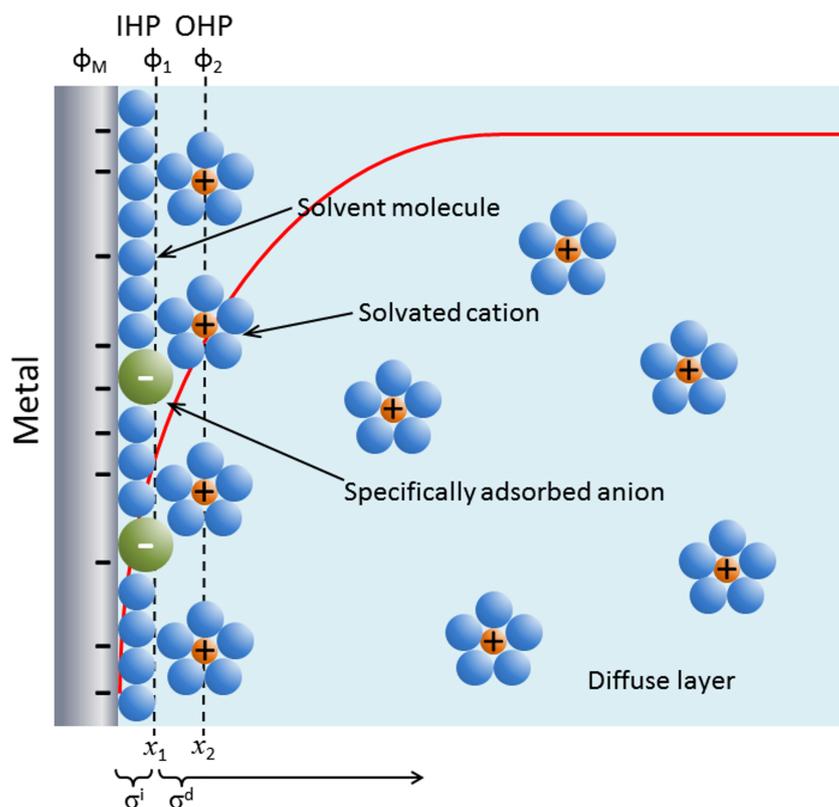
Figure 3.5: Schematic of the Helmholtz model of the electrical double layer. IHP is the inner Helmholtz plane where the specifically adsorbed anions are located, OHP the outer Helmholtz plane of the solvated cations. φ_1, φ_2 are the electrochemical potential of the IHP and OHP respectively, while φ_M corresponds to the potential of the working electrode. The solvated cations further from the OHP form the diffuse layer. Finally, x_1 and x_2 refer to the distance of each plane and σ^i, σ^d refer to the charge density of the IHP or the diffuse layer respectively. The red line illustrates the trend of the electrical potential developed at the IHP, OHP and diffuse layer (adapted from [128]).

When a molecular monolayer, such as that formed by alkanethiol SAMs through the covalent bonding of the thiol group with the gold surface, is assembled on the electrode surface, the capacitance of the interface is decreased, since the thickness of the monolayer reduces the proximity of the outer sphere species (outer Helmholtz plane) to the metallic surface. Thus, the monolayer acts like a blocking film and behaves like an IPE, and therefore, provided that the monolayer is free of pinholes or defects which would allow penetration of the solution species, essentially, no electron transfer will occur. If, however, the layer is thin enough (less than 1.5 nm), electrons can tunnel through the molecular film. For example, the incorporation of the redox species into a SAM assembled on the working electrode surface, such as the LCAT-OEG-MB SAMs used in this study, locates the redox centres close to the electrode surface and, consequently,

enables tunnelling of electrons through the molecular film. The electroactive terminated molecules are often diluted with non-electroactive molecular chains within the film to form mixed SAMs (Figure 3.3), so that the bulky redox groups are kept apart [121] [126] [128].

3.3.1 Cyclic Voltammetry (CV)

Cyclic voltammetry is a widely used amperometric method for interrogating interfacial electron transfer processes. In general, voltammetry is a potential sweep method, where the potential of the working electrode is varied linearly over time and the current is observed as a function of the applied potential; such a plot is called a voltammogram. In CV, the potential is applied within a specified range, and upon reaching one of the extremes, it is reversed so that it moves in the opposite direction, until it reaches the initial potential, thus completing a full cycle (Figure 3.6a).
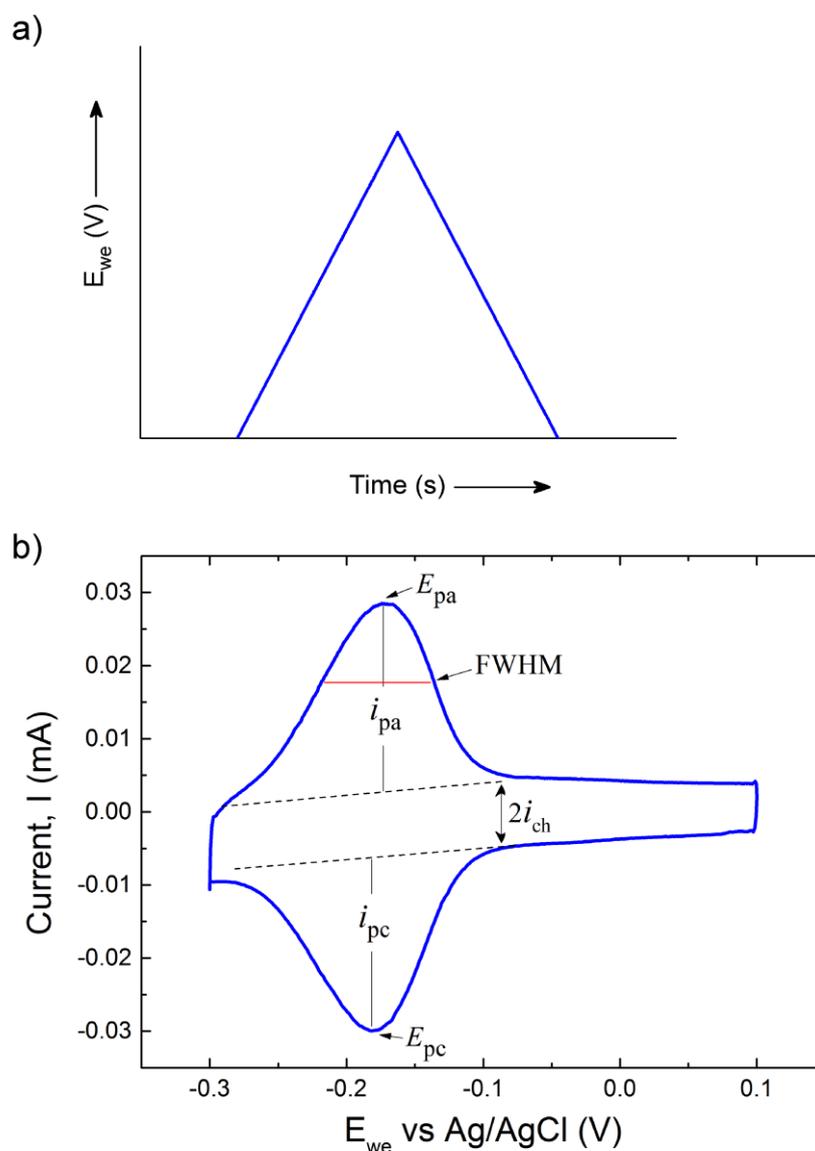
Figure 3.6: a) Working electrode potential (E_{we} Ag/AgCl reference electrode) as a function of time during a CV cycle, b) cyclic voltammogram (current *vs.* E_{we} of an LCAT-OEG-MB SAM in McIlvaine buffer pH 7 at 100 mV/s scan rate. The main parameters shown in a CV plot are the peak current (i_{pa} for oxidation and i_{pc} for reduction), the peak potential (E_{pa} and E_{pc}), the full-width at half of the peak maximum height (FWHM) and the charging or capacitive current i_{ch}. [126]

Initially, only non-faradaic current flows in the cell. As the potential becomes more positive and approaches the formal potential of the redox groups, a gradually increasing electron flow towards the electrode occurs, causing a faradaic current which corresponds to the oxidation of the redox species (Figure 3.6b) [128]. For an ideal, surface-immobilised reversible redox reaction, the peak potentials, E_{pa} and E_{pc}, are independent of the scan rate (the rate at which the applied voltage is scanned, v in mV/s) and concentration of redox moieties, and the peak separation $\Delta E_p = E_{pa} - E_{pc}$ equals zero at low scan rates. The formal potential, E^0, is centred between the two peak potentials so that $E^0 = E_{pa} + E_{pc}/2$. For an ideal reversible system, where there are no other processes that affect the charge transfer reaction, the peak oxidation, i_{pa}, and peak reduction current, i_{pc}, are equal such that $i_{pa} / i_{pc} \approx 1$, and both exhibit a linear relationship with scan rate [126] [128]. This linear relationship between the faradaic current, i_p, and the scan rate, v, can be used to calculate the surface coverage, Γ (mol/cm^2), of redox-immobilised moieties using Equation 3.3 [126].

$$i_p = \frac{n^2 F^2}{4RT} \, vA\Gamma \qquad\qquad (3.3)$$

Here, n is the number of electrons involved in the reaction and F the Faraday constant (96,485.3365 s A/mol), R is the universal gas constant (8.314472 J/K mol), T is the absolute temperature (K) and A the surface area of the substrate (cm^2).

At low scan rates, redox SAM-functionalised electrodes, such as the LCAT-OEG-MB SAM used in the following experiments, behave like a reversible system, with symmetrical peaks and the peak current is directly proportional to the scan rate. Increasing the scan rate can cause peak separation so that $\Delta E_p \neq 0$, and the higher the rate the more the peaks separate. Here, the potential is swept faster than species involved in the redox reaction (such as protons) can diffuse to the layer, so that electron transfer appears sluggish and thus, larger potentials are required to motivate charge transfer. By plotting the peak potential vs. $\log(v)$ it is possible to calculate the rate of electron transfer (k_{ET}) of the species absorbed to the electrode by following the Laviron method (Figure 3.7) [126]. To determine k_{ET}, one must first find the transfer coefficient, α, which ideally should be 0.5 for all overpotentials[5], but very often deviates from this value. To calculate α, the peak potentials, E_{pa} and E_{pc}, are plotted separately against the logarithm of the scan rate, so that

---

[5] The overpotential (η) is the difference between the applied potential, E_p, and the formal potential, E^0, and can be determined by the difference in the peak and formal potential ($\eta = E_p - E^0$) [126].

they give two branches (Figure 3.7). As the scan rate increases the data form a straight line where the gradient of this line is given by Equation 3.4,

$$slope = -\frac{2.3RT}{\alpha nF}$$

(3.4)

The electron transfer rate, k_{ET}, can be calculated from Equation 3.5 [126] which assumes that $\eta=0$. Here, ν_a and ν_c are determined from the x-intercepts of the lines fit to E_{pa} and E_{pc}, respectively.

$$k_{ET} = \frac{\alpha nF\nu_c}{RT} = (1-\alpha)\frac{nF\nu_a}{RT}$$

(3.5)
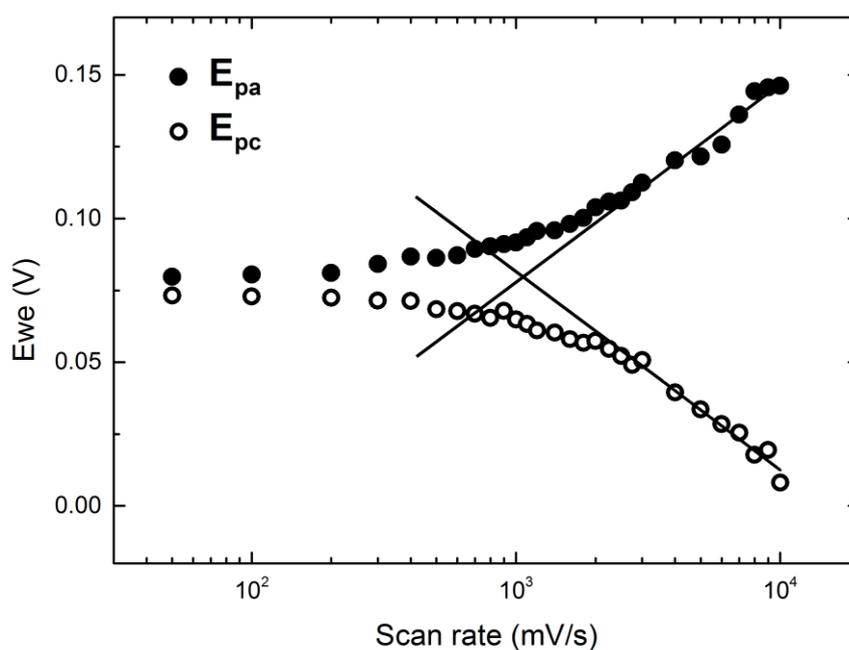
Figure 3.7: Laviron (trumpet) plot of an LCAT-OEG-MB SAM in 100 mM phosphate buffer at pH 7. Peak potentials, Epa and Epc are plotted against the logarithm of the scan rate. The linear regions at higher scan rates have been fitted to calculate the rate of electron transfer, k_{ET}.

Finally, a cyclic voltammogram can provide additional information about the characteristics of the monolayer. The background current (i_{ch}), also called the *charging* or *capacitive* current, can be used to calculate the capacitance of the SAM, as shown in Equation 3.6.

$$i_{ch} = C_{DL}v$$

(3.6)

Here, C_{DL} is the capacitance of the SAM in Farad (1 F = 1 s^4 A^2/m^2 kg) and v is the scan rate (mV/s). Subsequently, the capacitance can be used to calculate the thickness of the monolayer, d (nm),

$$C_{DL} = \varepsilon_0 \varepsilon_r \frac{A}{d} \tag{3.7}$$

where ε_0 is the permittivity of the vacuum (8.85419×10^{-12} F/m), ε_r the relative permittivity (dimensionless) and A the surface area of the substrate (cm^2) [123] [130].

3.3.2 Electrochemical Impedance Spectroscopy

Information regarding the structural characteristics of a self-assembled monolayer can be obtained through electrochemical impedance spectroscopy (EIS). In this method, a small sinusoidal potential (AC excitation signal) is applied on a DC bias over a range of frequencies, and the resulting current signal is measured at each frequency. The current flowing through the electrochemical cell is determined by the electrochemical impedance of the system. For an ideal resistor, the Ohmic resistance is independent of frequency and the AC current signal is in phase with the AC potential. In contrast, for an ideal capacitor, the AC current is -90º out of phase with the applied potential. For more complex systems, such as electrochemical cells which are modelled typically by a series of resistors and capacitors, the phase and magnitude of the current vary continuously with frequency [131].
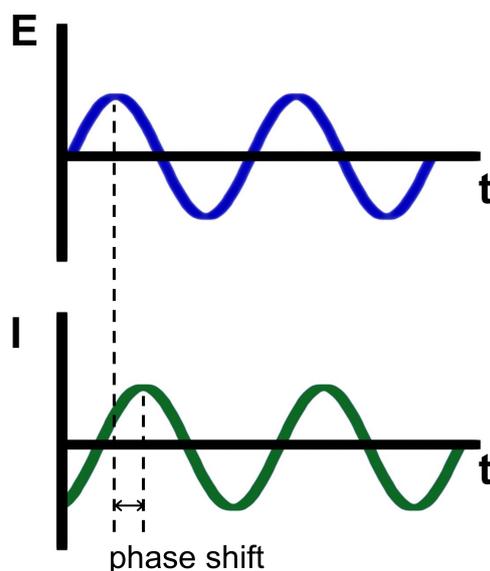
Figure 3.8: The sinusoidal AC excitation potential, *E*, as a function of time and the out-of-phase AC current response (adapted from [131]).

Mathematically, the applied sinusoidal excitation potential is expressed as a function of time (Equation 3.8).

$$E_t = E_0 \sin(\omega t) \tag{3.8}$$

Here, E_t is the potential[6] at time t, E_0 is the amplitude of the excitation signal and ω is the radial frequency (where $\omega=2\pi f$). The resulting AC current signal, I_t, is given by Equation 3.9 where ϕ is the phase difference (Figure 3.8):

$$I_t = I_0\sin(\omega t + \phi) \tag{3.9}$$

As defined by Ohm's law, the resistance (R) of a resistor is the ratio of voltage and current (Equation 3.10).

$$R = E/I \tag{3.10}$$

Analogously, the impedance, Z, of the system is calculated as a ratio of E_t and I_t (Equation 3.11). However, this is only true in a linear system, where the AC current response to the sinusoidal AC excitation potential is also a sinusoid function over time at the same frequency (but out-of-phase). Therefore, in EIS, the applied AC excitation signals are very small (1-10 mV), so as to approach a pseudo-linear system so that,

$$Z = E_t/I_t \tag{3.11}$$

Through Equations 3.9-3.11, the impedance can thus be expressed as:

$$Z = \frac{E_0 \sin(\omega t)}{I_0\sin(\omega t+\phi)} = Z_0 \frac{\sin(\omega t)}{\sin(\omega t+\phi)} \tag{3.12}$$

The relationship between frequency, phase and impedance can be visualised using a Bode plot, where the logarithm of the magnitude of the impedance, $\log(|Z|)$, and the phase, ϕ, are plotted as a function of frequency, $\log(\omega)$, as shown in Figure 3.9a. Considering that the impedance of a SAM-functionalised electrode is dependent on the structural characteristics of the organic coating, valuable information regarding the properties of the monolayer can be obtained by studying its capacitive and resistive behaviour through EIS. The Randles circuit shown in Figure 3.9b is often used as a simple model of the impedance of an electrode coated with a SAM. Here, R_{SOL} refers to the solution resistance, C_{DL} is the double-layer capacitance formed at the electrode-electrolyte interface, R_{CT} the charge-transfer resistance and C_{AD} the capacitance of the adsorbed layer [126] [131] [132].

---

[6] The symbol V is used extensively in the literature for voltage or potential, but here (and in section 3.3.1), in order to avoid confusion with the symbol for volume, V, the symbol E is used instead, following the nomenclature often used in electrochemistry [128]

In order to study the impedance of a redox-active SAM, the applied potential is selected to be far from the redox potential of the electroactive species, so that no electron transfer occurs. In this case, electron transfer associated with the redox reaction need not be considered and only R_{SOL} and C_{DL} contribute to the impedance.
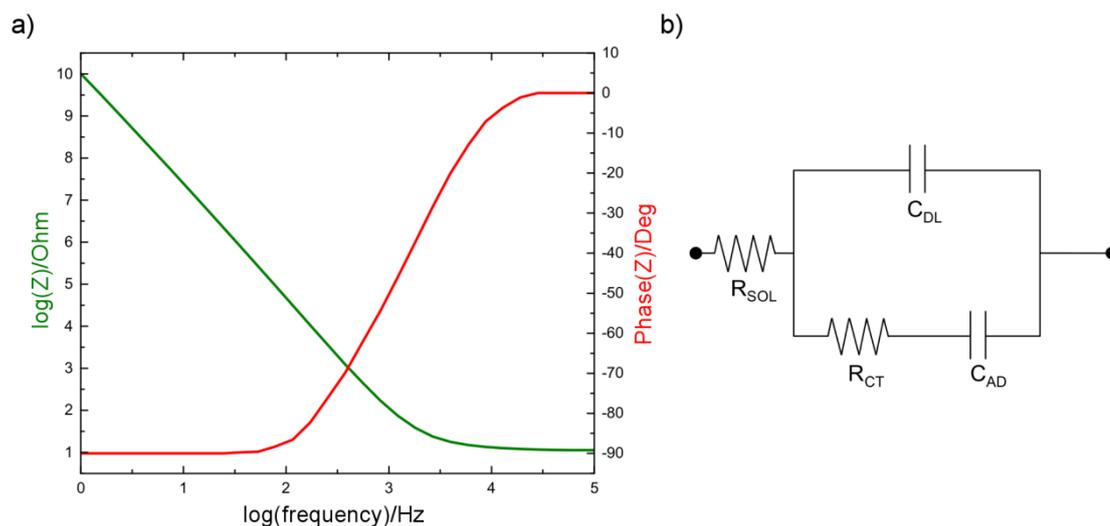
Figure 3.9: a) Example of a Bode plot, where the impedance magnitude (log(Z)) and the phase angle, ϕ, are plotted as a function of frequency; b) Randles circuit model for a redox-species coupled to a monolayer [132].

The magnitude of the impedance of a capacitor reduces with frequency, thus at high frequencies the resistive components of the Randles circuit (R_{CT} and R_{SOL}) dominate and the current and potential are thus in phase. As the frequency decreases, the impedance of the capacitive components increases, thus the overall impedance of the system also increases and the current and potential are no longer in phase. If the capacitive component of the impedance is dominant, then the phase shift will approach -90º, characteristic of a pure, ideal capacitor. When studying SAMs, this capacitive behaviour is associated with the insulating properties of the organic film, which in turn is related to the order and packing density of the monolayer. A dense, well-packed SAM with few pinholes and defects is expected to approach the behaviour of an ideal capacitor, which is translated as a phase value close to -90º in a Bode plot [126] [131].

3.4 Quartz Crystal Microbalance with Dissipation Monitoring (QCM-D)

QCM is an interfacial acoustic sensing technique that enables real-time monitoring of molecular interactions. The working principle of QCM relies on the piezoelectric property of quartz. In 1880, Pierre and Jacques Curie observed that the application of external pressure to a quartz crystal induced an electrical potential across the deformed crystal, generating an electric field; this is the piezoelectric effect [133]. One year later, the converse piezoelectric effect was predicted mathematically by Gabriel Lippmann and demonstrated by the Curie brothers, who showed that the application of an external electric field caused mechanical deformation of a quartz crystal [59][134]. The mode of deformation depends on the cut of the crystal with respect to its crystallographic axes, whilst the direction and extent of deformation depends on the direction and amplitude of the applied electric field. At equilibrium, all dipoles in the quartz crystal are randomly orientated and thus have zero net dipole moment. Upon the application of an electric field, the dipoles are orientated parallel to the field, causing a lattice strain and an overall deformation of the crystal (Figure 3.10a). By applying an alternating electric field, the direction of the crystal deformation alternates at the frequency of the field (Figure 3.10b) [135] [136].
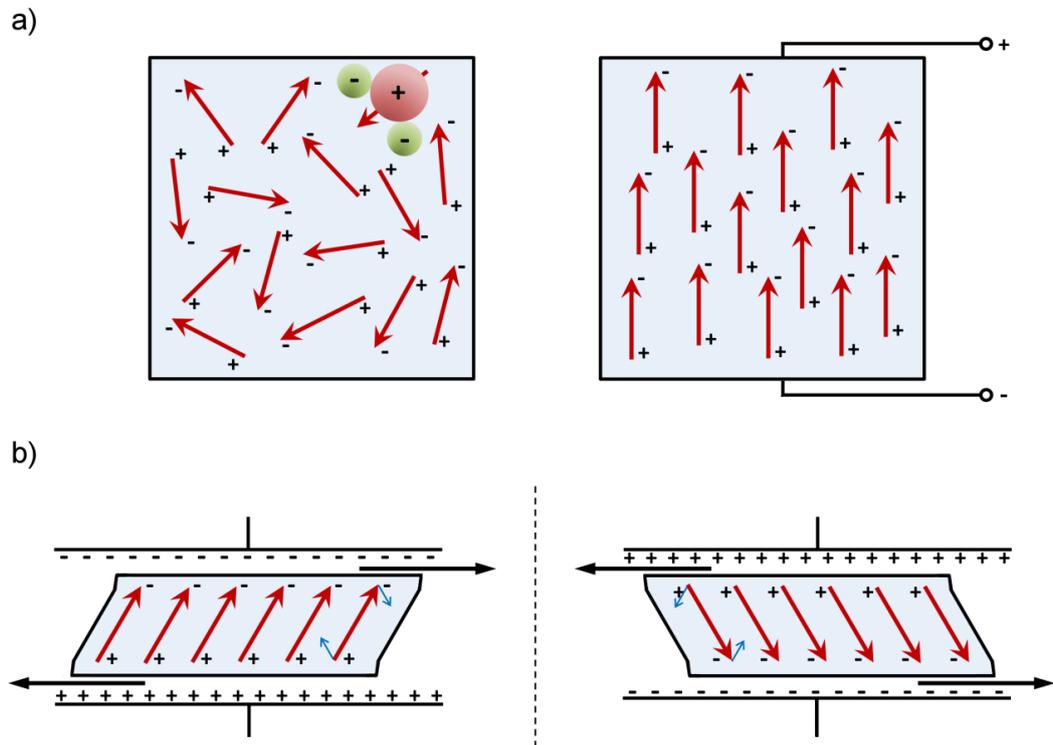
Figure 3.10: a) Converse piezoelectric effect: Upon application of an electric field, the randomly orientated dipoles (SiO$_2$) in a quartz crystal (left) align their direction with that of the applied field (right), resulting in b) a lattice strain and a deformation of the crystal (here, a shear strain), where the direction of applied field affects the direction of the shear stress (adapted from [135-137]).

A QCM sensor consists of a very thin quartz crystal sandwiched between two electrodes, so that upon application of AC voltage, the oscillation of the crystal deformation occurs in a thickness-shear mode, where a transverse wave propagates through the crystal (Figure 3.11a). When the frequency of the applied voltage reaches the resonant frequency of the crystal, the amplitude of vibration reaches its maximum [133]. Resonance occurs when a system oscillates at its natural frequency driven by an external force (such as an alternating electric field). An oscillating system can vibrate in a series of distinct modes, called normal modes. For each mode (here, the shear vibrational mode), the lowest frequency is called the fundamental frequency (f_0). For instance, the quartz crystals used in commercial QCM devices have a fundamental frequency between 5-10 MHz [138]. Any frequency higher than the fundamental frequency is called an overtone, and integer multiples of the fundamental frequency are called harmonics (n) [139]. Here, the quartz crystal plate oscillates at its fundamental frequency (in the thickness-shear mode) when its thickness, t_Q, is half the wavelength of the acoustic wave, λ_Q, so that $t_Q = \lambda_Q/2$, which creates a standing wave that propagates across the crystal and reflects back into the crystal at the surface [133].
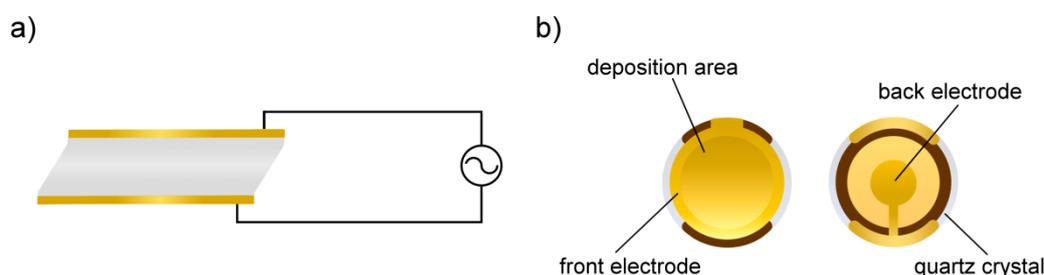
Figure 3.11: a) shear deformation of the QCM sensor due to the applied AC voltage; b) schematic of a typical QCM sensor (adapted from [61], [133] and [140])

A typical QCM sensor consists of a thin-cut quartz wafer, where two gold electrodes are plated on each side (typically through vapour deposition), whilst one side is covered with a surface coating, usually gold (Figure 3.11b). Adsorption processes, such as the formation of self-assembled monolayers of alkanethiols, occur on this coated surface. Depending on the application, other surface coatings can be used, such as Ti, Pt, Cr, Co, SiO_2, polystyrene, graphene oxide, etc. [140]. In a typical experimental set-up, the QCM sensor chip is loaded into a flow cell, as seen in Figure 3.12. The sensor is connected to an oscillator through the gold electrodes from both sides. Once the circuit is closed, the oscillator drives the sensor to shear vibrational mode at its resonant frequency, by applying an AC voltage. A frequency counter is used to measure the frequency output of the oscillator, and is recorded and processed by a computer [61] [133] [141]. The resonant frequency of the quartz plate is temperature-dependent, so a temperature-controlled chamber is often used.
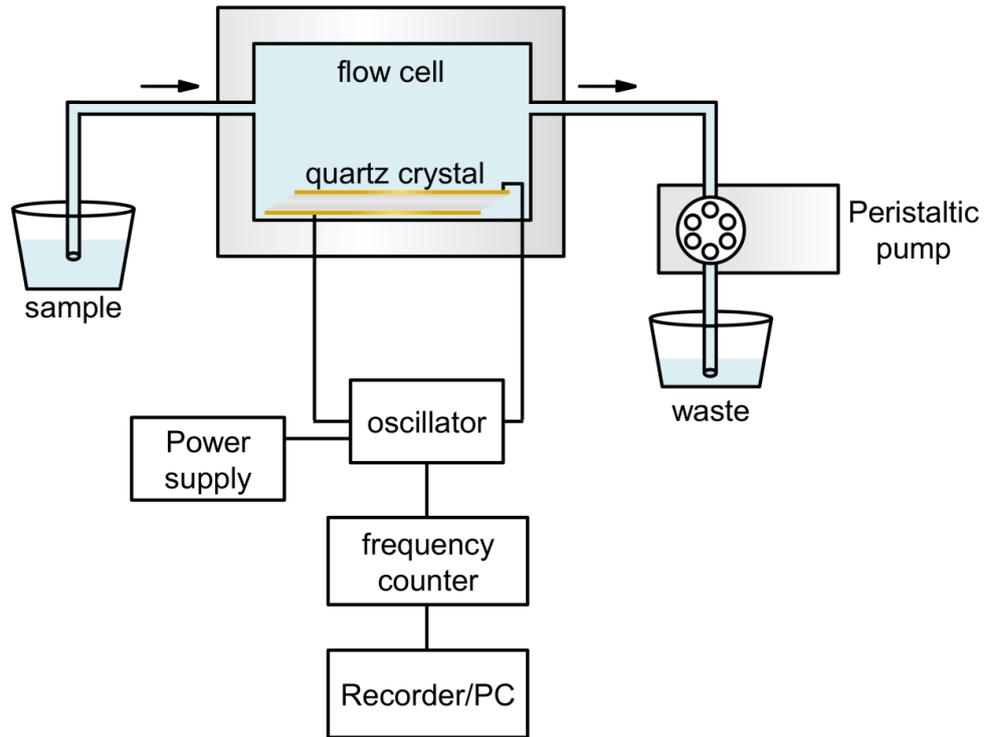
Figure 3.12: Schematic of the basic experimental set-up of a quartz crystal microbalance (here, using liquid samples); adapted from [142-144].

Critically, the resonant frequency of the crystal depends on its structure, thickness, shape and mass [144]. In 1959, Günter Sauerbrey showed that shifts in the resonance frequency of the sensor in vacuum are related to changes in the mass of the crystal. Mass deposited on the sensor due to adsorption or desorption processes on the surface results in a proportional shift in the resonant frequency. This relationship between frequency and mass is described by the Sauerbrey model, which states that under vacuum and for a thin, rigid and homogeneous surface film, the measured frequency shift is linearly related to the adsorbed or desorbed mass, as described in Equation 3.13,

$$\Delta f = -C_f \Delta m \qquad (3.13)$$

where Δm is the deposited mass (in ng/cm^2), $\Delta f = f_f - f_i$ (f_f is the frequency measured after mass deposition and f_i is the initial frequency), while C_f is the mass sensitivity constant:

$$C_f = \frac{\rho_Q v_Q}{2f_0} \text{ or } \frac{\rho_Q d_Q}{f_0} \qquad (\text{since } v_Q = d_Q f_0) \qquad (3.14)$$

Here, ρ_Q and d_Q refer to the density and thickness[7] of the quartz crystal, respectively, whilst v_Q is the shear wave velocity. For a quartz crystal with f_o=5 MHz (such as the one used in this study), v_Q=3340 m/s, 330 μm thickness and 2650 kg /m³ density, the mass sensitivity constant is 5.65 MHz·m²/kg. Consequently, a frequency shift of 1 Hz, corresponds to a shift in mass of 17.7 ng/cm². Thus, when using Equation 3.13 to estimate the deposited mass from the measured frequency shift, C_f is often expressed as C (1/ C_f ; 17.7 ng/cm²·Hz), and the Sauerbrey equation takes the following form:

$$\Delta m = -C \frac{\Delta f}{n} \tag{3.15}$$

where n (n = 1, 3, 5, 7…) refers to each harmonic [60] [61] [133]. The calculated mass may be used to determine the surface coverage (Γ, $molecules/cm^2$) and the deposited film thickness (d_f, nm) through Equations 3.16 and 3.17 respectively.

$$\Gamma = \frac{\Delta m \, N_A}{MW} \tag{3.16}$$

$$d_f = \frac{\Delta m}{\rho_f} \tag{3.17}$$

Here, N_A is Avogadro's constant (6.02214 × 10²³ molecules/mol), while *MW* refers to the average molecular weight of the deposited compounds. ρ_f refers to the density of the film, which, for hydrated biomolecules, is considered to be close to that of water (1 g/cm³) [145].
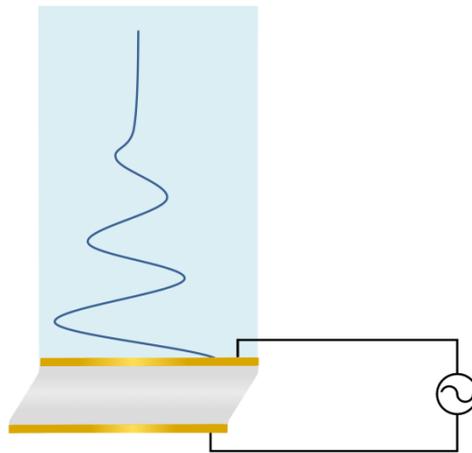
Figure 3.13: Propagation of the shear wave from the quartz crystal into the liquid above (adapted from [146]).

---

[7] The symbol t is often also used for thickness; here, to avoid confusion with the time symbol, t, thickness is symbolised by d.

The Sauerbrey model refers to QCM measurements under vacuum; however, most biomolecular systems are studied in the liquid phase, where the acoustic wave travels into the bulk fluid. Consequently, the properties of the liquid, such as density and viscosity, affect the resonant frequency, as the shear motion of the oscillating crystal couples with the damped propagation of the shear wave in the liquid (Figure 3.13) [146]. As a result, the mass loading can differ from that estimated by Sauerbrey. Kanazawa and Gordon presented a simple physical model to predict the changes of frequency for a quartz sensor immersed in liquid:

$$\Delta f = f_0^{\frac{3}{2}} \left(\frac{\eta \rho}{\pi \mu_Q \rho_Q} \right)^{\frac{1}{2}} \tag{3.18}$$

where ρ is the density and η the viscosity of the liquid, while μ_Q and ρ_Q are the shear modulus and density of quartz, respectively [147].
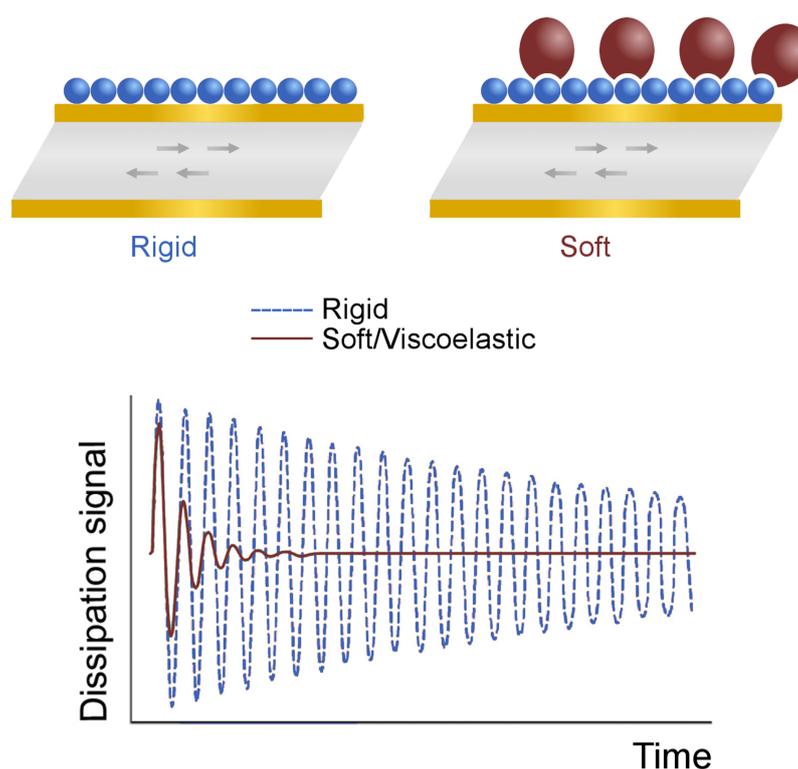
Figure 3.14: Differences in the dissipation signal over time for a rigid (blue) and soft/viscoelastic (maroon) molecular film on a quartz crystal (adapted from [60]).

The mass-frequency relation described by Sauerbrey refers to the deposition of a thin, rigid and homogeneous film. However, when measuring biomolecular systems in the liquid phase, viscous

69

and elastic contributions are often added to the frequency shift. Dissipation monitoring within the QCM (QCM-D) provides an approach to account for such contributions, and Q-sense was the first to commercialise this technology, in 1996 [60] [61]. In QCM-D, the applied AC voltage is momentarily shut off (~20 ms every second), and the decay of the oscillation of the quartz crystal is recorded [61] [141] [142]. The oscillation decay over time depends on the properties of the sensor, the surface coating and the liquid in contact, thus changes in the viscoelastic properties of the sensor surface are reflected as changes in the decay rate of the oscillation, which is related to the dissipation of the oscillating energy (Figure 3.14). The amplitude of oscillation, A, decays as an exponentially damped sinusoidal:

$$A(t) = A_0 e^{-t/\tau} \sin(2\pi f + \phi), \ t \geq 0 \qquad (3.19)$$

where, A_0 is the amplitude at $t=0$, τ is the decay time constant and ϕ is the phase. Thus, f and τ can be calculated through this equation by recording the amplitude of oscillation over time. The dissipation factor, D, which is dimensionless and calculated using Equation 3.20, reflects the viscoelastic characteristics of the sensor surface and changes in viscoelasticity are expressed by a shift in energy dissipation, ΔD, (in 10^{-6}).Simultaneous monitoring of frequency and dissipation thus enables the mechanical nature of the deposited film, i.e. rigid or soft to be determined, as well revealing structural changes of an adsorbed layer, for example, as a result of conformational shifts of absorbed antibodies, enzymes or DNA due to molecular binding or changes in the pH of the buffer.

$$D = \frac{1}{\pi f \tau} \qquad (3.20)$$

A thin, rigid film couples to the oscillation of the sensor and the shear wave exhibits low energy dissipation, whereas a softer, more elastic film will not completely follow the oscillation of the crystal, but experiences further deformation, resulting in increased dissipation (Figures 3.14 and 3.15) [61]. Consequently, considering that the Sauerbrey model does not account for viscoelasticity or adsorbed water, when $\Delta D > 0$ the measured frequency shift is not directly proportional to the change in mass, leading to misestimates of the deposited mass [148]. Several investigators have presented models to quantify mass changes with respect to the viscoelastic properties of soft and thick layers [149]. However, for very small dissipation shifts ($\Delta D < 1$-2×10^{-6}), the molecular film can still be considered a hard, non-elastic layer, and a D/f ratio greater than 1/30 is commonly used as practical rule of thumb for deciding when the Sauerbrey model is suitable for estimating the adsorbed mass [145] [150].

70
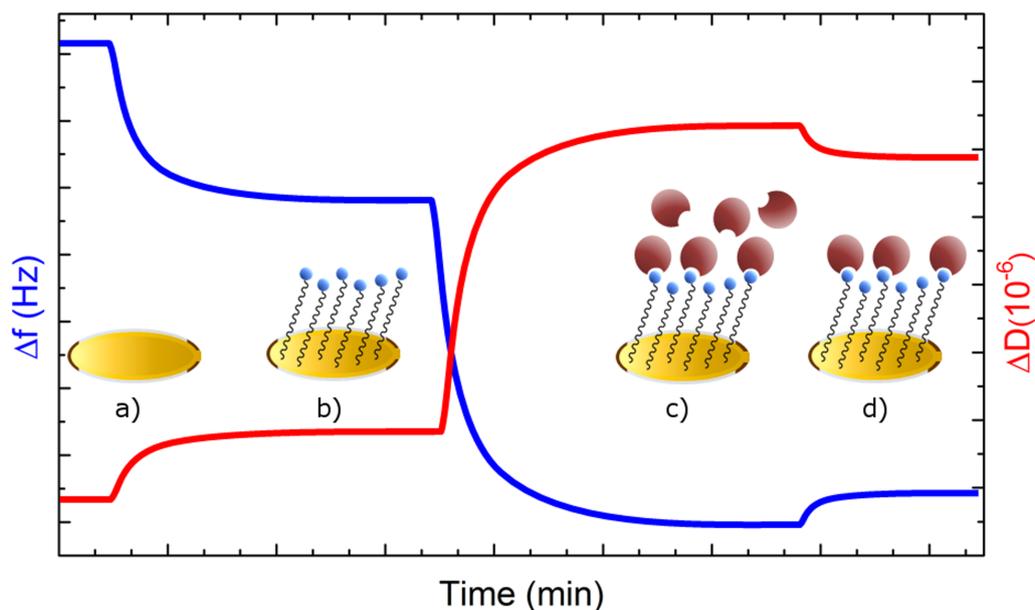
Figure 3.15: Example of real-time data of a QCM-D measurement of a direct biomolecular assay, where the bioreceptors bind to the surface-immobilised target molecules: a) resonant frequency and dissipation baseline for a clean QCM-D sensor in running buffer, b) the adsorption of target molecules on the surface induces a decrease in the resonant frequency and a dissipation increase that is dependent on the viscoelasticity of the molecular film, c) the interaction of the adsorbed molecules with the bioreceptors results in further frequency decrease and a corresponding dissipation increase, d) washing with running buffer removes non-specifically adsorbed (physisorbed) binders which can cause a conformational change of the adsorbed layer (adapted from [61]).

One additional feature of QCM-D technology is the ability to monitor all frequency and dissipation overtones simultaneously. Q-Sense instruments measure seven frequency overtones (n = 1, 3, 5, 7, 9, 11, 13) and seven corresponding dissipation overtones, which provide information regarding the homogeneity of the adsorbed layer [145]. The decay length, δ, is the distance from the sensor surface that the acoustic wave propagates until it decays. This distance depends on the bulk properties of the liquid (density, viscosity) above the sensor, and is inversely proportional to the frequency. Higher overtones (i.e. higher frequencies) exhibit shorter decay lengths i.e. do not travel far from the surface. Thus, for high overtones, the observed f and D shifts correspond to the characteristics of the layer closer to the surface, whilst lower overtones reflect the properties of the upper parts of the layer (or multilayer) and the fluid above [146] [151]. For instance, for a deposited film, high ΔD in the first and third overtone may correspond to a soft and viscous phase in the upper part of the film, whilst lower ΔD values for higher overtones reveals a rigid layer closer to the surface.

QCM-D is a highly versatile technique, and depending on the instrument design can combine piezoelectric measurements of mass and viscoelasticity with other techniques, such as electrochemistry, ellipsometry or surface plasmon resonance [152] [153]. For instance, in this work, QCM-D was combined with electrochemistry (EQCM-D) by coupling the instrument with a

potentiostat and using a specially designed electrochemical flow cell, where the gold surface of the electrode facing the solution is used as the working electrode [154]. The combination of these techniques enables several parameters in the same molecular system to be studied in one instrument, such as mass and structure of deposited films by QCM-D and interfacial charge transfer and electrostatic interactions between adsorbed molecules by electrochemical measurements, such as cyclic voltammetry.

QCM-D has been used in a wide range of applications in several areas, such as food, environmental and clinical analysis, and for a broad spectrum of analytes, from large biomolecules (e.g. DNA, antibodies, enzymes) to smaller molecules (such as pharmaceuticals or contaminants), lipids or even whole cells [142]. Critically, it is a valuable tool for immunosensing as it provides real-time, label-free, *in situ* monitoring of biomolecular interactions, thus allowing kinetics analysis of binding reactions. It has also been used widely to characterise and optimise antibody immobilisation approaches, which is a key element to the development of immunosensors [144]. However, QCM-D's accuracy and application for analytical purposes is limited by a few factors. Firstly, as the resonant frequency depends on density and viscosity, it can be significantly affected by temperature variations. While a temperature-controlled QCM-D measurement chamber is simple to implement in a laboratory instrument, the temperature sensitivity can be challenging for portable QCM-D based biosensors for environmental monitoring in the field. Other limiting factors are mounting stresses on the sensor or pressure waves caused by the fluidic pumps. These, however, can be overcome by careful handling and selection of an appropriate pump and tubing [145]. Moreover, the application of this technology in routine analysis is faced with cost limitations, since instrument, accessories and sensors are expensive, whilst the re-usability of sensors is limited and usually decreases the accuracy of the measurement [144]. Finally, the accuracy in mass determination can be affected by the model used to convert frequency changes to mass [133]. Further research on instrument design and materials can potentially improve performance and overcome most limitations, so as to incorporate this technique in biosensor technology for faster, rapid and on site monitoring. Nonetheless, QCM-D is a very useful tool for immunosensing and studying antigen-antibody binding reactions and is thus increasingly used by researchers.

3.5 Introduction to FT-IR Spectroscopy (PM-IRRAS)

IR spectroscopy is used widely for structural determination of compounds by measuring the absorption of light in the infrared region. A beam of IR light passing through a sample causes vibrational excitations of covalently bonded atoms in a molecule (Figure 3.16). Each type of bond in the molecule vibrates at different frequencies and will thus absorb electromagnetic energy at this specific frequency, resulting in an absorbance spectrum that is characteristic of the studied molecule [155].
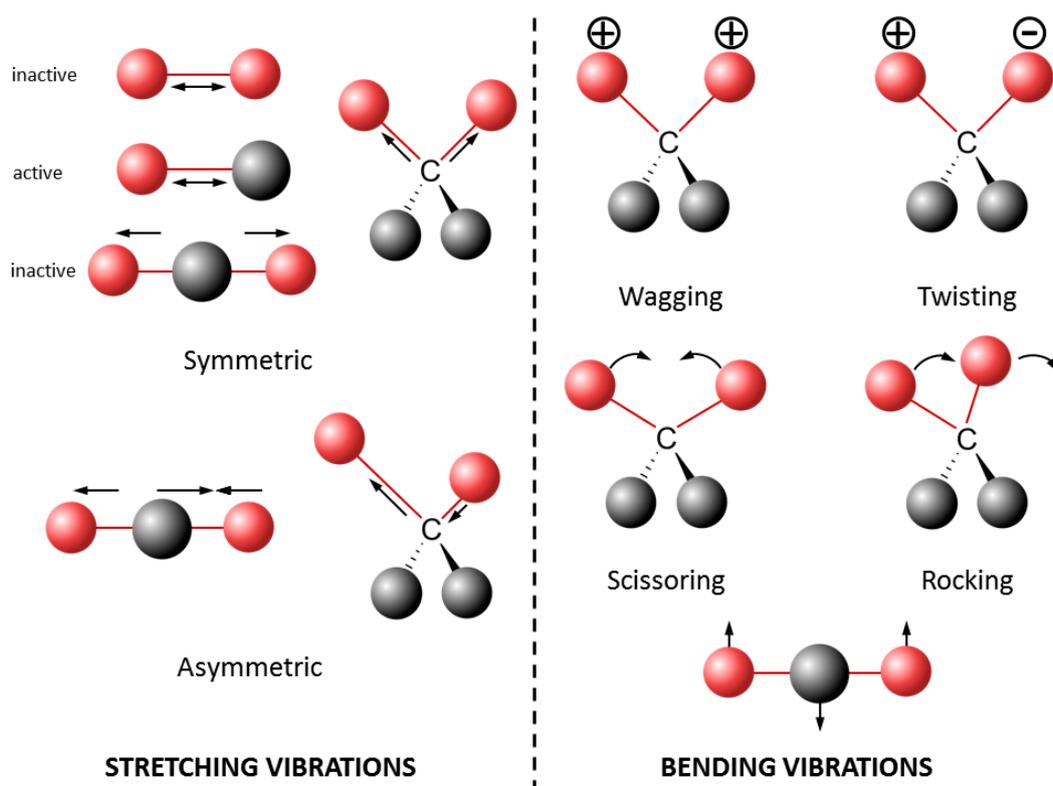
Figure 3.16: Examples of vibrational modes for linear and non-linear molecules (adapted from [11] [155] [156].

FT-IR spectrometers are used routinely for compound identification and are preferred over the conventional, double-beam dispersive IR spectrometers, due to their higher speed and signal-to-noise ratio. The main feature of an FT-IR instrument is the interferometer, typically in the Michelson configuration, which consists of a beamsplitter, a fixed mirror and a moving mirror (Figure 3.17). The energy generated by an IR source (usually a SiC element heated above 1000 K) reaches the beamsplitter and is split into two beams. One beam is reflected towards the fixed mirror and the other one is transmitted to the moving mirror. The latter moves back and forth with a constant velocity, so that the reflected light has a variable path length. The two beams reflected from each mirror are recombined at the beamsplitter, where they interfere either constructively or

destructively with each other due to the difference in path length, creating an interferogram. The recombined beam passes through the sample, where a portion of energy is absorbed while the transmitted light is sent to the detector. A computer connected to the detector transforms the interferogram to an IR spectrum by applying a mathematical function called a Fourier transform. The sample spectrum is ratioed to a background spectrum by measuring a reference sample in order to produce a transmittance spectrum (%T) as a function of frequency in wavenumbers (cm^{-1}). An absorbance spectrum can be also obtained by taking the log_{10} of the reciprocal of transmittance [157]. Typically, FT-IR measurements are performed under vacuum, so as to eliminate spectral contributions from atmospheric background, such as water vapour or carbon dioxide.
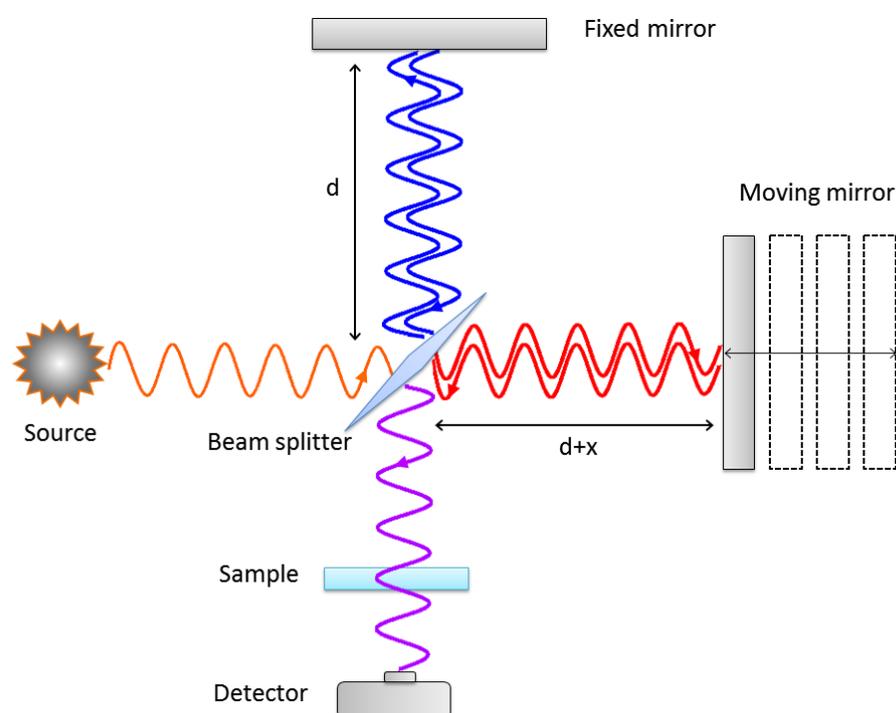
Figure 3.17: Layout of the Michelson interferomeneter (adapted from [36] [158] and [159]).

Infrared Reflection-Absorption Spectroscopy (IRRAS) is an application of FT-IR to characterise the chemical composition and conformation of molecular layers adsorbed onto metallic surfaces. In IRRAS, the light beam impinges onto the surface at a grazing angle of incidence and the reflected light is detected at the same angle. At this angle, the incident light interacts with the adsorbed molecules on the surface causing vibrational excitations that absorb energy at certain, characteristic frequencies. The transmitted beam is then reflected by the metal substrate and directed into the detector and, following Fourier transformation, presented as reflectance vs frequency. The main advantages of this approach are that measurements can be made at ambient pressure, instead of under vacuum, and also, a wide variety of substrates can be used. However, the thin-layered sample has significantly fewer molecules compared to a sample in a conventional FT-IR transmittance

measurement, which can severely affect the signal-to-noise ratio. In addition, the weak signal can be often suppressed by the vibrational bands of atmospheric water vapour, resulting in a poor signal-to-noise ratio. Moreover, a background spectrum requires an absolutely clean substrate, but the purity of the surface can be often compromised by interaction with the ambient atmosphere. Furthermore, alignment sensitivity and instrument drift can make it challenging to obtain a sample spectrum free of baseline artefacts [160].
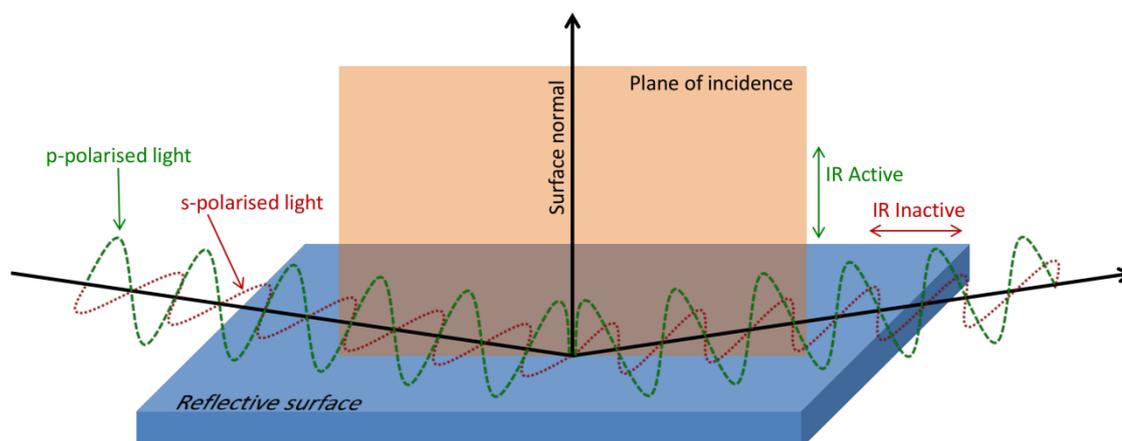
Figure 3.18: Schematic illustration of s- and p- polarised light on a reflective surface, where the electric field is wave is perpendicular or parallel to the plane of incidence, respectively. IR active vibrational modes are only those that produce electric dipole shifts parallel to the surface normal, so that only p-polarised light is effectively interacting with the surface molecules, in contrast to the s-polarised light (adapted from [159] and [161]).

Polarisation modulation-infrared reflection-absorption spectroscopy (PM-IRRAS) is an alternative approach that can overcome these challenges. This method relies on the selective interaction of different polarisation states of light with the thin film on the metal surface (Figure 3.18). The IR beam generated by an FT-IR spectrometer is passed through a polariser and a photoelastic modulator (PEM) that generates alternating states of s- and p-polarised light. At a high grazing incidence angle (~80º), the intensity of the electric field of p-polarised IR light is enhanced, due to constructive interference of the waves of the incident and reflected rays at the interface. Consequently, the interaction with the thin film is enhanced, and so is the IR absorption by the molecular layer on the surface, which allows the p-polarised IR reflectance spectrum of very thin layers of adsorbed species to be observed. In contrast, the electric field of s-polarised light at this incident angle is practically cancelled so that the interaction with the sample is negligible and essentially no absorption occurs. Thus, the reflected s-polarised light can provide the IR reflectance spectrum of the metal surface. By exploiting this simple selection rule for absorption of IR radiation at the surface (p-polarised light is enhanced, s-polarised light is cancelled) and switching

from one polarisation state to another, the spectrum of the molecular layer and the background can be obtained in a single measurement of the same sample. Hence, the issues concerning signal intensity and suppression by atmospheric interferences can be easily overcome and the sensitivity is significantly increased [159] [160].
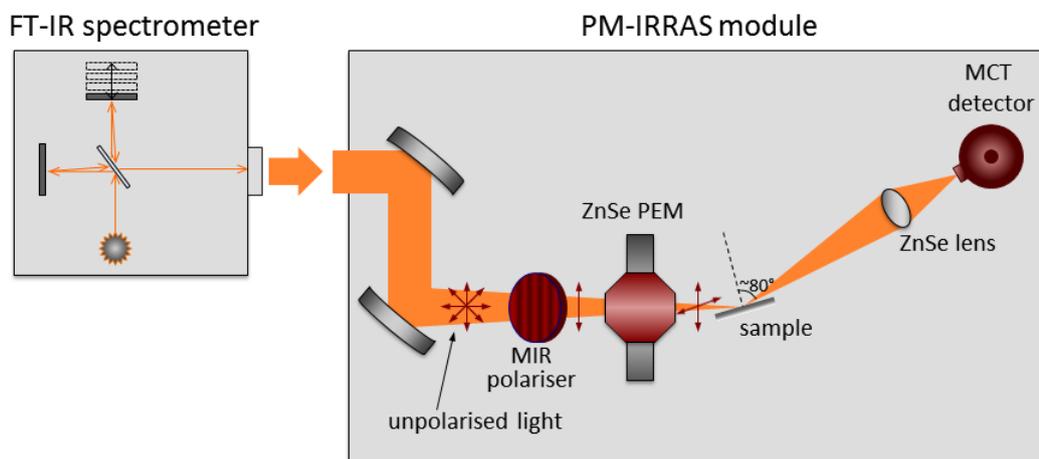
Figure 3.19: PM-IRRAS optical setup (adapted from [160] and [162]).

For a PM-IRRAS measurement, an IR beam is generated by an FT-IR spectrometer and, as shown in Figure 3.19 is focused by a parabolic mirror so that it impinges on the sample surface at a high incidence angle (~75º-80º). Before reaching the sample, the beam is polarised by a mid-infrared (MIR) wire grid polariser which consists of a closely spaced grid of metal wires on a ZnSe substrate. Next, the polarised light reaches the PEM, which is tilted at an angle of 45° to the transmission axis of the polariser. The PEM consists of a ZnSe crystal attached to a piezoelectric transducer (PZET) which is forced to oscillate at its resonant frequency (usually at 37 or 50 KHz) by an applied voltage. The oscillation of the piezoelectric transducer alternately stretches or compresses the ZnSe crystal, which induces birefringence shifts of the material. The alternating birefringence of the crystal refracts the incoming polarised light at different speeds so that during each PEM cycle the refracted light alternates polarisation states from parallel to perpendicular to the transmission axis. These polarisation states shift at a frequency twice that of the PEM oscillation. Finally, the polarisation modulated IR beam reaches the metallic surface of the sample, where the s- and p-polarised light interact with the surface and adsorbed molecules, and the reflected light is focused onto the detector by an MIR lens (usually a ZnSe lens). The detector is a mercury-cadmium-telluride (MCT) type detector, that is typically used for detection in the mid-IR region [160-163].

Chapter 4

Investigating Affimer Interactions with Small Molecules: Methylene Blue Exemplar

4.1 Overview

Affimer selection required the target to be immobilised by crosslinking the target with a long oligoethyleneglycol-biotin linker (Appendix A). Similarly, the study of Affimer-target interactions and the development of a competition binding assay required the immobilisation of the target on a sensor surface. This was achieved through self-assembled monolayers (SAMs) of long-chained alkanethiols (LCAT) containing an analyte-labelled oligoethylene glycol component (OEG). Methylene blue (Figure 4.1a) was selected as a proof-of-principle analyte for this study and the solid-phase synthesis of LCAT−OEG−MB, also referred to as MB SAM (Figure 4.1b), was performed following the protocol described by Murray et al. [119].

Prior to proceeding with Affimer-target binding studies, it is essential to 1) demonstrate that the LCAT−OEG−MB assembles into a stable, well-ordered molecular monolayer and 2) assess whether the attachment of a long-chained linker and the subsequent surface immobilisation affects the properties and behaviour of the target. The redox properties of MB were exploited in order to answer these questions. For this purpose, gold electrodes were functionalised with MB SAM and the redox activity characterised using cyclic voltammetry as a function of pH (the redox activity of MB is dependent on local proton concentration).

Furthermore, electrochemical measurements (both CV and EIS) were used to provide insight into the structure of the MB SAM. This was complemented by spectroscopic characterisation (PM-IRRAS) which revealed details of molecular structuring within the MB SAM. Critically, the bulky MB terminal groups of the MB SAM were found to influence the structure of the SAM. Additional monolayers formed by co-immobilisation of LCAT−OEG−MB with a dilutant were thus also investigated. Here, an OH-terminated LCAT-OEG (also referred to as OH SAM) was used to form mixed SAMs of LCAT-OEG-MB and LCAT-OEG-OH (also referred to as MB:OH SAM). Both mixed and pure MB SAMs were compared and characterised through CV, EIS and PM-IRRAS.

Finally, interactions between MB-Affimers and surface immobilised MB were studied using QCM-D. The use of QCM-D also enabled the effect of Affimer binding on the redox activity of MB to be investigated *in situ* through electrochemical QCM-D (EQCM-D). The affinity constant, K_D, of MB-Affimers was measured through both saturation binding and kinetics measurements in the QCM-D, while the selectivity of the Affimers for its target in complex matrixes was demonstrated using limnetic samples. Finally, the potential of Affimers as bioreceptors in immunoassays for the detection of small-sized, non-immunogenic compounds was demonstrated by an Affimer-based competition assay in the QCM-D.

4.2 Characterisation of LCAT-OEG-MB SAMs

4.2.1 Materials

LCAT-OEG-MB and LCAT-OEG-NH$_2$ (Figure 4.1b and 4.1c) were synthesised using solid-phase synthesis as described in Murray et al. [119] (Figure 4.2 and Appendix B) and stored in ethanol at 1 mM concentration (-18 ^{o}C). All chemicals for LCAT-OEG-MB synthesis were purchased from Sigma-Aldrich (Gillingham, UK), unless noted otherwise. 29-mercapto-3,6,9,12,15,18-hexaoxanonacosan-1-ol, referred to here as LCAT-OEG-OH (Figure 4.1d), was purchased from Prochimia Surfaces (Gdansk, Poland). Methylene blue chloride was purchased from Acros Organics (Geel, Belgium) and 1-dodecanethiol 98% (Figure 4.1e) was purchased from Sigma-Aldrich (Gillingham, UK). All buffers and solutions were prepared using ultrapure water (18.2 MΩ·cm, Milli-Q systems, Millipore) and the pH was measured using a pH meter (Mettler-Toledo, Switzerland).
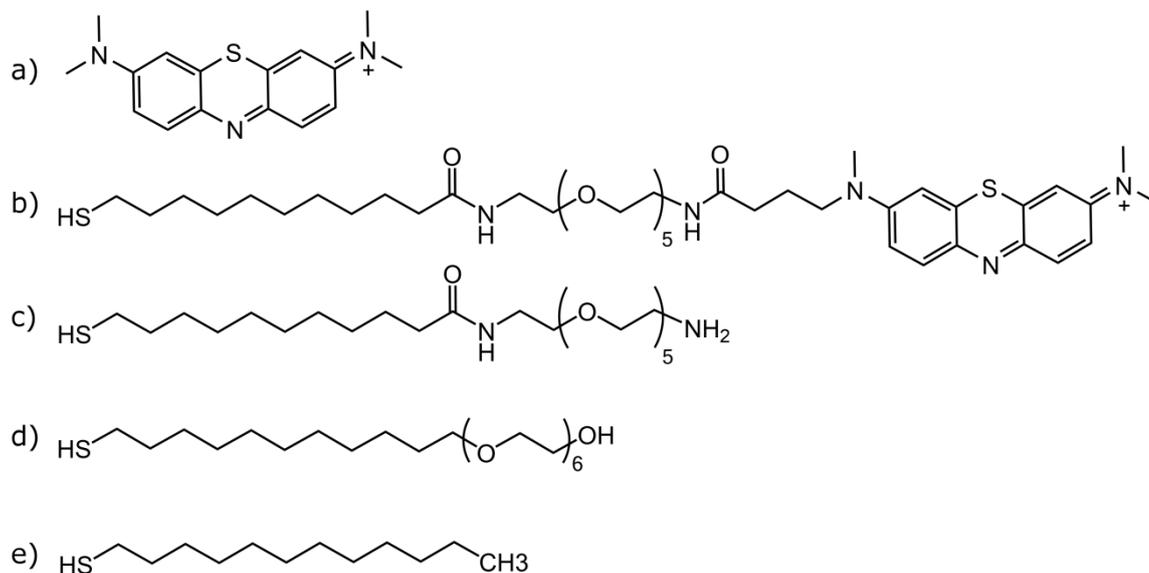
Figure 4.1: a) methylene blue, b) LCAT-OEG-MB c) LCAT-OEG-NH$_2$, d) LCAT-OEG-OH and e) 1-dodecanethiol.
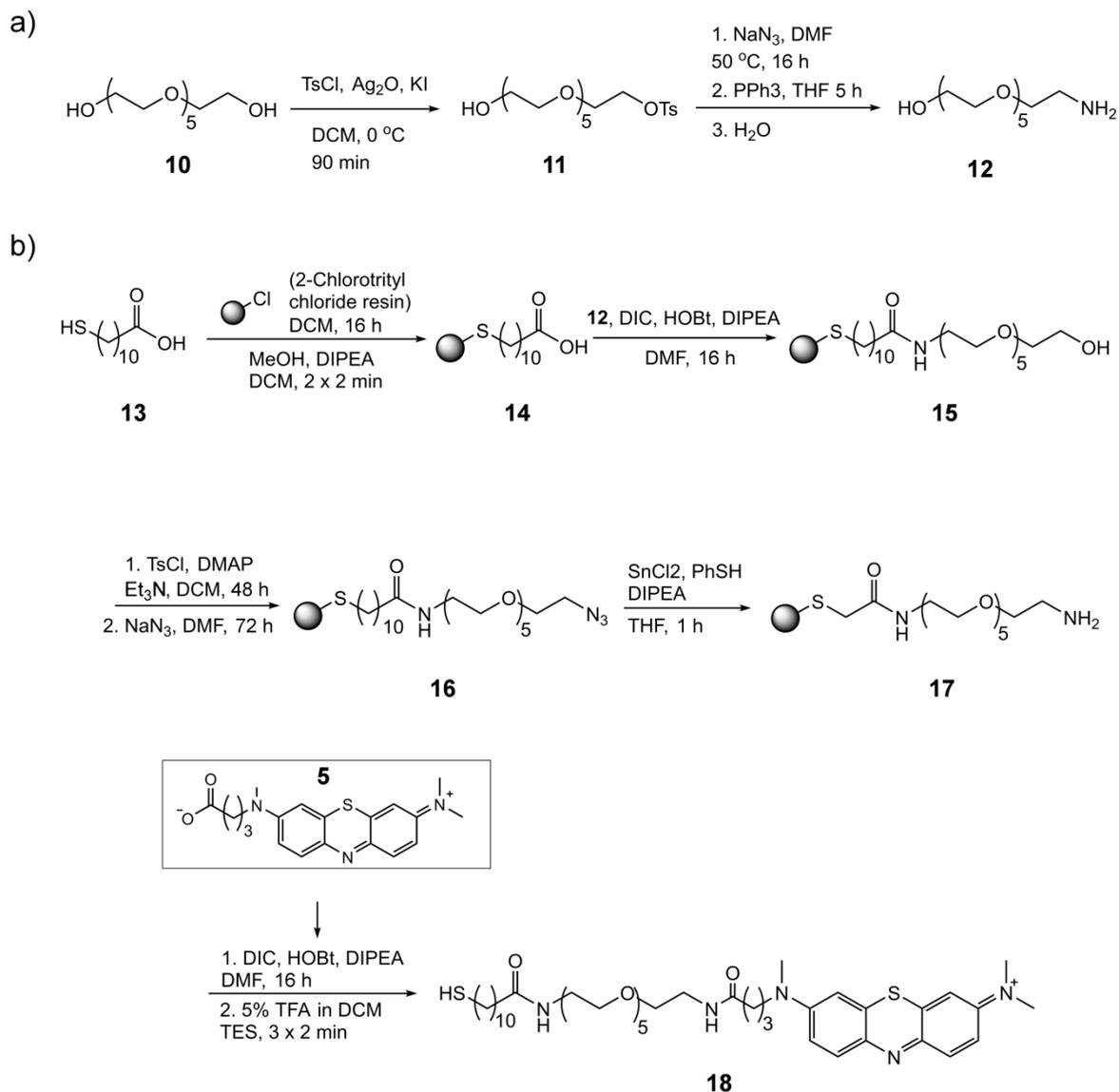
Figure 4.2: Schematic of the solid phase synthesis of LCAT-OEG-MB adapted from Murray et al. [119]: a) preparation of amino-OEG (12), b) Solid phase synthesis of MB-terminated LCAT–OEG on 2-chlorotrityl chloride resin, using N-(carboxypropyl)methylene blue (5), (Appendix A). Abbreviations: DCM=dichloromethane; DIC=diisopropylcarbodiimide; DIPEA=N,N-diisopropylethylamine; DMAP=4-dimethylaminopyridine; DMF=N,N-dimethylformamide; HOBt=1-hydroxybenzotriazole; TES=triethylsilane; TFA=trifluoroacetic acid; Ts=4-toluenesulfonyl.

4.2.2 Target immobilisation on Au-coated substrates

Planar gold surfaces, fabricated by electron beam evaporation of 25 nm Ti/100 nm Au onto a cleaned Si wafer (IDB technologies, Wiltshire, UK), were functionalised with single-species or mixed LCAT-OEG monolayers. Prior to functionalisation, the wafers were cleaved to approximately 10 by 20 mm and cleaned by immersion in piranha solution ($H_2SO_4:H_2O_2$ 70:30) for 10 min, followed by sonication in water, then ethanol for 10 min each and finally, dried with N_2 gas. (Note: Extreme caution must be taken when handling piranha solution, since it is strongly acidic and a strong oxidiser).

Pure LCAT-OEG SAMs were formed by immersion of the gold surfaces in a 0.1 mM ethanolic solution of the corresponding compound for 48 hours. The mixed MB:OH SAM was prepared using a mixture of 0.1 mM LCAT-OEG-MB and 0.1 mM LCAT-OEG-OH in ethanol at a 1:3 ratio (v/v). Pure LCAT-OEG-OH (Figure 4.1d) and 1-dodecanethiol (Figure 4.1e) SAMs were formed following the same approach and were used as references in PM-IRRAS (referred to as OH SAM and C_{12} SAM respectively). After incubation, the functionalised substrates were gently rinsed with ethanol and dried with N_2 gas.

4.2.3 Cyclic voltammetry and electrochemical impedance spectroscopy

The SAM-functionalised, gold-coated substrates were used as the working electrode and mounted in a three electrode electrochemical cell that included a Pt counter electrode and a Ag/AgCl (saturated KCl) reference electrode. Contact to the working electrode was achieved using a spring loaded pin connector. A Viton O-ring defined the surface area exposed to the electrolyte which was equal to 9.1 mm^2. EIS and CV measurements were performed using a Bio Logic SP-300 potentiostat (Berkshire, UK). All measurements, excluding those for pH dependency studies, were performed in 100 mM sodium phosphate buffer pH 7 (PB 7).

For pH dependency studies, McIlvaine buffers ranging from pH 2.2 to 8.0 were prepared by mixing different ratios of 0.1 M citric acid and 0.2 M Na_2HPO_4, as described by McIlvaine [164]. Moreover, a series of electrolytes covering a pH range from 4 to 12 were prepared, by mixing appropriate quantities of 0.04 M CH_3COOH, 0.04 M H_3PO_4, 0.04 M H_3BO_3, and adjusting with 0.2 M NaOH, as described in Britton and Robinson [165]. Each buffer was introduced to the SAM-functionalised gold electrode by pipetting 400 μL of it into the electrochemical cell. Following each measurement, the electrode was rinsed with ultrapure water and dried with N_2 gas. The order of CV measurements began at neutral solutions and moved gradually to higher, and then lower pH values,

since highly acidic or alkaline conditions can potentially cause the SAMs to deteriorate. The voltage range of the measurements was kept within -0.3V to +0.1V, again to minimise damage to the SAM via desorption of the thiol group or damage to the electrode surface. CV measurements were performed at different scan rates, ranging from 50 mV/s to 10,000 mV/s.

For EIS measurements, the impedance and phase angle were measured over the frequency range of 200 kHz to 0.1 Hz at a 10 mV DC potential *vs* reference electrode Ag/AgCl and an AC potential of 10 mV.

4.2.4 Polarisation modulated - infrared reflection absorption spectroscopy

For PM-IRRAS measurements, Au-coated Si wafers were cleaved to 20 by 30 mm and functionalised with SAMs analogously to Section 4.2.2. Infrared spectra of the LCAT-OEG SAMs assembled on the gold surfaces were acquired using a Bruker Vertex70 spectrometer (Bruker UK Ltd, Coventry, UK) coupled with a PMA50 polarisation modulation unit. The incident angle was set at 80° with a 4 cm^{-1} spectral resolution, while the PEM controller operated at 1000 cm^{-1}. Average measurement time was 15 min, collecting 1000 scans. As reference, 1-dodecanethiol SAMs (referred to as C_{12} SAM) were prepared using the same immobilisation approach as for LCAT-OEG SAMs.

4.2.5 Quartz crystal microbalance with dissipation monitoring coupled with electrochemicstry (EQCM-D)

Frequency and dissipation were measured in McIlvaine buffers of different pH, initially on a bare gold QCM-D sensor surface and then on an MB-LCAT-OEG SAM-functionalised sensor. The QCM-D measurements were combined with cyclic voltammetry (EQCM-D), in order to demonstrate that the pH dependency was due to the redox activity of the MB SAM rather than conformational changes in the monolayer. The pH dependency of the MB SAM redox reaction was investigated by comparing the shifts in frequency and dissipation as a function of pH before and after functionalisation of the MB SAM.

Gold coated QCM-D sensors (QSX 301, Biolin Scientific, Stockholm, Sweden) were cleaned by sonication in a 2% Hellmanex III solution (Hellma Analytics, Müllheim, Germany) and thorough rinsing in ultrapure water, followed by UV-ozone treatment (30 min) and immersion in EtOH (30 min). McIlvaine buffers ranging from pH 5 to pH 8 were prepared as described by McIlvaine [164].

A broader pH range was avoided to ensure the integrity of the SAM and the QCM-D sensors and fluidics.

The cleaned sensors were mounted into the QCM-D flow modules (QSense E4, QFM 401, Biolin Scientific, Stockholm, Sweden). The surface area exposed to solution was equal to 0.95 cm^2 as defined by a Viton O-ring (inner diameter 1.11 cm). EQCM-D was performed using a QEM 401 electrochemistry module (Biolin Scientific, Stockholm, Sweden) which includes a stainless steel counter electrode, a low leak Ag/AgCl reference electrode and a contact to the working electrode, here a gold coated electrochemical QCM-D sensor (QSX-338, Biolin Scientific, Stockholm, Sweden). Electrochemical measurements were performed using a Bio Logic SP-200 potentiostat (Berkshire, UK).

The resonant frequency (F) and dissipation (D) were monitored while ultrapure water was passed over the sensors using a peristaltic pump at a flow rate of 20 μL/min, until a steady baseline was achieved (defined by a frequency shift of less than 1 Hz over 10 minutes). Next, the frequency and dissipation were monitored over time as the sensors were exposed to the pH buffers using ultrapure water for the intermediate washing steps. Then, a 0.02 mM solution of LCAT-OEG-MB in ultrapure water was injected at a 20 μL/min flow rate for approximately 45 min until the frequency reached a plateau. The sensors were then washed with ultrapure water for approximately 20 mins and then exposed to each pH buffer solution in turn for approximately 25 mins. Before switching to the next pH buffer, the peristaltic pump was paused for 5 min and cyclic voltammetry was performed at a low scan rate of 100 mV/s and over a [-0.3V; +0.1V] voltage range.

4.3 Results

4.3.1 Redox activity of MB in LCAT-OEG-MB SAMs on Au surfaces

In Sections 4.3.1 and 4.3.2, the LCAT-OEG-MB SAM on Au surfaces was studied through CV and QCM-D in order to characterise the molecular monolayer structure and properties, and investigate whether the attachment of a long-chained linker and the subsequent surface immobilisation affects the properties and behaviour of the target (here, the redox activity of MB).
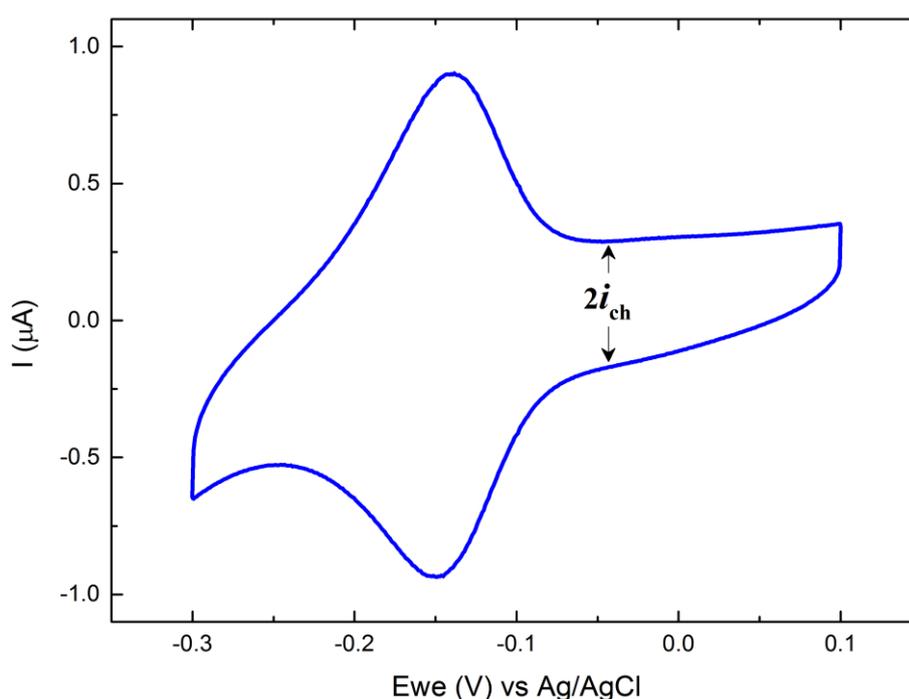
Figure 4.3: Cyclic voltamogramm of 0.2 mM MB SAM at 100 mV/s scan rate in McIlvaine buffer pH 7. Arrows indicate the charging (or capacitive) current, i_{ch}.

Figure 4.3 shows a cyclic voltammogram of the MB SAM in McIlvaine buffer pH 7 at 100 mV/s scan rate. Both peaks are fairly symmetric, (i_{pa}/i_{pc} = 1.24), and show minimum peak separation, ΔE_p = 1.90 mV, which is typical of an ideal and reversible redox active monolayer that is well tethered to the surface (Section 3.3.1). In addition, the formal potential, E^o, was found to be -144.35 mV, (E^0= E_{pa}+E_{pc} / 2), which is consistent with previous studies of MB electrochemistry with alkanethiol-SAMs or DNA monolayers [119] [130] [166]. The full width at half maximum (FWHM)[8] of the oxidation and reduction peaks was found to be 81.36 mV and 76.55 mV respectively. Both values are larger than the theoretical ideal (45.3 mV) for a two electron process

---

[8] The full-width at half of the peak maximum height (Chapter 3, Figure 3.6)

(Figure 4.5), but such deviations are often observed in redox active monolayers and are attributed to electrostatic interactions between neighbouring charged species [126]. The charging (or capacitive) current was extracted from the cyclic voltammogram (Figure 4.3) and used to determine the capacitance of the SAM through Equation 3.7. Specifically, the i_{ch} of the MB SAM is found to be 0.845×10^{-4} mA, leading to a capacitance of:

$$C_{DL} = \frac{i_{ch}}{v} = \frac{0.845 \times 10^{-4} \, mA}{100 \, mVs^{-1}} = 0.845 \times 10^{-6} \, F$$

The capacitance per unit area is often used for comparison to other SAMs. Here, the surface area of the electrode was 0.091 cm^2., thus, the capacitance per unit area was equal to 9.3×10^{-6} F/cm^2, which compares well with previous reports on alkanethiol SAMs, suggesting that the SAM forms a dense, well-packed monolayer [132] [167]. The calculated capacitance was used to estimate the thickness of the monolayer using Equation 3.8. The relative permittivity of molecular monolayers is typically assumed to be in the range 2-20 [168] and a value of 10 was used here.

$$d = \varepsilon_0 \varepsilon_r \frac{A}{C_{DL}} = 8.85419 F/m \times 10^{-12} \cdot 10 \frac{0.091 \, cm^2}{0.845 \times 10^{-6} \, F} = 0.95 \, nm$$

This value is slightly lower than the typical theoretical range of 1-3 nm [120]; however, it should be noted that due to the unknown true value of the relative permittivity, an arbitrary value has been used. Such deviations are not uncommon for monolayers with very long chains [126], especially considering the interference of the hydrophilic OEG layer that affects the ordered and dense packing of the monolayers.

The surface coverage of the MB SAM was calculated by plotting the peak anodic and cathodic current, i_{pa} and i_{pc}, against the scan rate (Figure 4.4a), and fitting the slope in Equation 3.3 (Section 3.3.1). The slope $\frac{i_{pa}}{v}$ was found to be 5.21×10^{-6} sA/V, so by rearranging Equation 3.3, the surface coverage, Γ, is:

$$\Gamma = \frac{i_{pa}}{v} \frac{4RT}{n^2 F^2 A} = 5.21 \times 10^{-6} A \, s/V \cdot \frac{4 \cdot 8.314472 \, J \, /K \, mol \cdot 293.15 \, K}{2^2 \cdot (96,485.3365 \, sA/mol)^2 \cdot 0.0908 cm^2}$$

$$\Gamma = 1.5 \times 10^{-11} \, moles/cm^2$$

$$\Gamma = 9.05 \times 10^{12} \, molecules/cm^2$$

85

This value is lower than the predicted theoretical density for an ideal LCAT SAM (4.5×10^{14} molecules/cm^2). This difference is attributed to the amorphous structure of the OEG layer and the steric hindrance caused by the bulky MB groups that affect packing of the monolayer [121][126]. Nonetheless, the peak current exhibits an approximately linear relationship with increasing scan rate, which is typical of an ideal, reversible process of a surface-immobilised redox system and demonstrates that MB is well-tethered to the gold substrate [126].
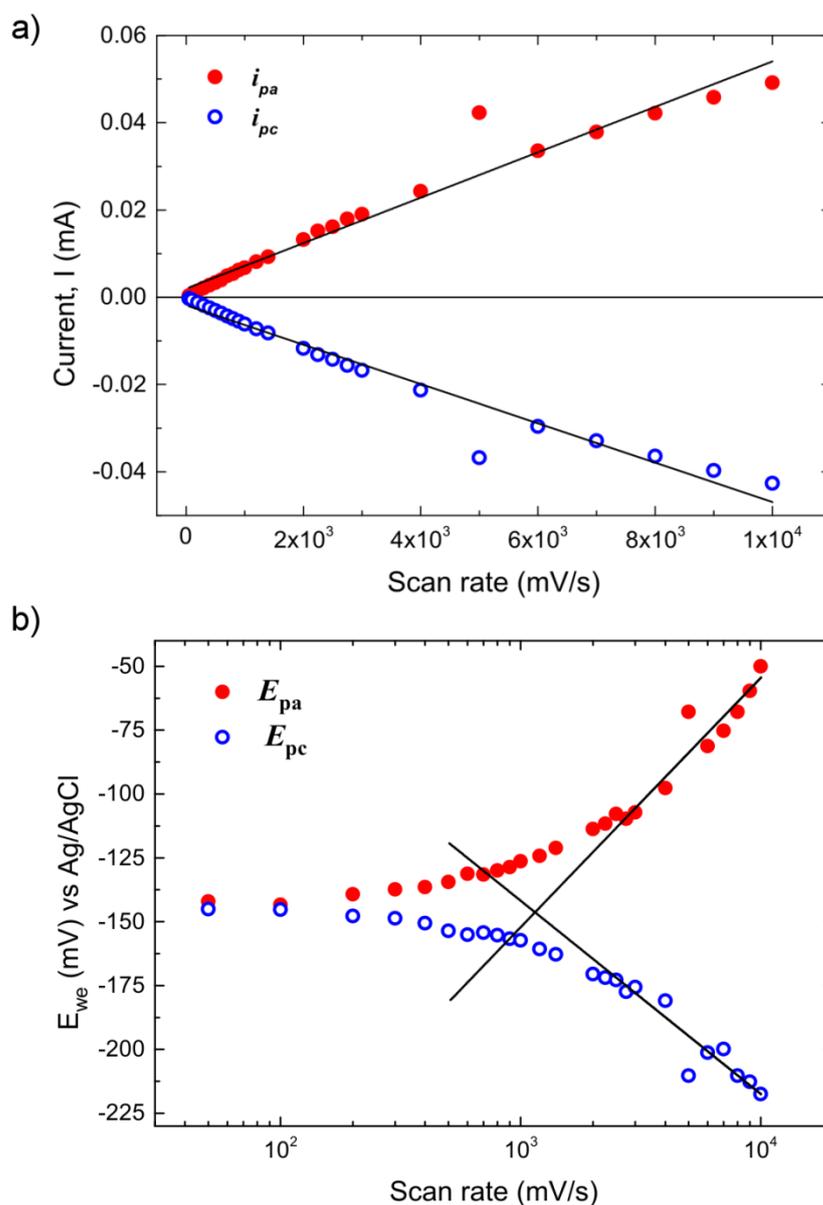
Figure 4.4: a) Peak current *vs* scan rate from CVs of 0.2 mM MB SAM in McIlvaine buffer pH 7. The slope of the fitted plot is used to determine the surface coverage of the monolayer; b) Laviron plot of the same MB SAM in McIlvaine buffer at pH 7. The linear regions at higher scan rates have been fitted to calculate the rate of electron transfer, k_{ET}.

As shown in Figure 4.4b, the oxidation and reduction peak potentials, E_{pa} and E_{pc}, have similar values at low scan rates. However, as the scan rate increases, diffusion of ions and protons to the MB groups affects the rate of the redox reaction so that larger overpotentials are required for charge transfer, and as a result, peak separation is observed. The kinetics of the redox reaction can be assessed by plotting E_{pa} and E_{pc} against the logarithm of the scan rate and the Laviron method is used to determine the rate of electron transfer, k_{ET}, as described in Section 3.3.1.

The slope and intercept of each branch (corresponding to the oxidation and reduction reactions) were determined by fitting the linear regions observed at high scan rates. These values allow calculation of the transfer coefficient, α, and the rate of electron transfer, k_{ET}. The calculated values, summarised in Table 4.1, are consistent with previous studies on redox-coupled long-chained alkanethiol monolayers on gold surfaces [169]. It should be noted that the accuracy of the Laviron method is reduced for densely packed monolayers, such as those studied here. Nevertheless these findings demonstrate that MB retains its redox activity when labelled and immobilised on a gold surface through an LCAT-OEG SAM. The symmetry and shape of the peaks, the very low peak splitting, the linear relationship between peak current and scan rate, as well as the thickness and surface coverage demonstrate that the LCAT-OEG-MB SAMs were well tethered to the surface, formed a dense and well-packed monolayer and the MB groups exhibited an ideal and reversible electrochemical behaviour of a two electron process.

	E_{pa}	E_{pc}
Slope (mV)	90.035	-69.552
Intercept (mV)	-410.074	57.13292
α	0.323	-0.42
k_{ET} **(s^{-1})**	10.501	-1.889

Table 4.1: Fitting data from Laviron plots, the estimated transfer coefficient, a, and the rate of electron transfer, k_{ET}

4.3.2 Investigating pH dependency of LCAT-OEG-MB SAM (CV, EQCM-D)

The two electron redox reaction of MB is proton dependent (Figure 4.5), therefore pH changes are expected to affect this process [34] [170]. To explore whether this pH dependency is retained in the surface-immobilised MB, the redox response of LCAT-OEG-MB SAM at different pHs was measured through cyclic voltammetry and QCM-D.
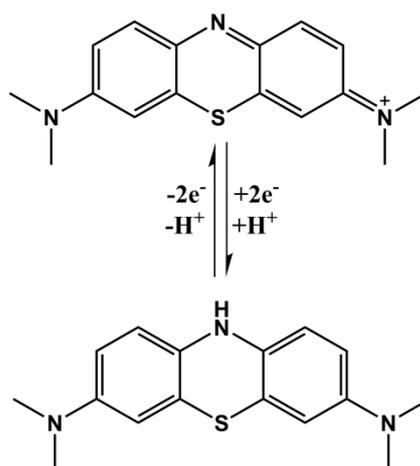
Figure 4.5: Redox reaction of methylene blue in solution [119]

Cyclic voltammogramms of LCAT-OEG-MB SAMs (on Au-coated silicon wafers) in McIlvaine buffers ranging from pH 5 to pH 8 revealed a decreasing shift in potential with increasing pH (Figure 4.6a), as expected for a proton-dependent redox reaction. This effect was also examined over a broader pH range using Britton-Robinson buffers ranging from pH 4 to pH 12. The rate of potential shift with proton concentration was determined by plotting the peak potential as a function of pH (Figure 4.6b). Both E_{pa} and E_{pc} were found to shift by around -33 mV/pH, which is very close to the predicted value of -29 mV/pH for a 2e⁻, 1H⁺ process [171]. It should be noted that highly acidic or alkaline conditions were found to affect the reversibility of the MB redox process and had a damaging impact on the SAM.

In near-neutral pH conditions, the peak current exhibited an approximately linear relationship with scan rate (Figure 4.7a), as expected for surface-immobilised redox systems (Equation 3.3). This linearity is based on the assumption that, since the electroactive species are adsorbed on the electrode surface (via SAMs), diffusion is not a limiting parameter of the redox reaction. This is true for slow scan rates, where the solution species involved in the redox reaction (here, electrons and protons) have enough time to diffuse to the SAM-modified electrode surface [126] [128]. In

faster scan rates, however, the potential is swept faster than the solution species can reach the electrode surface, thus diffusion becomes a rate-limiting step. This is reflected in the peak potential splitting observed with higher scan rates (Figure 4.7b). Diffusion is also dependent on the concentration of the solution species, and, therefore, is dependent on the proton concentration of the solution. Consequently, at extremes of pH, a deviation from the expected linearity between peak current and scan rate is observed.
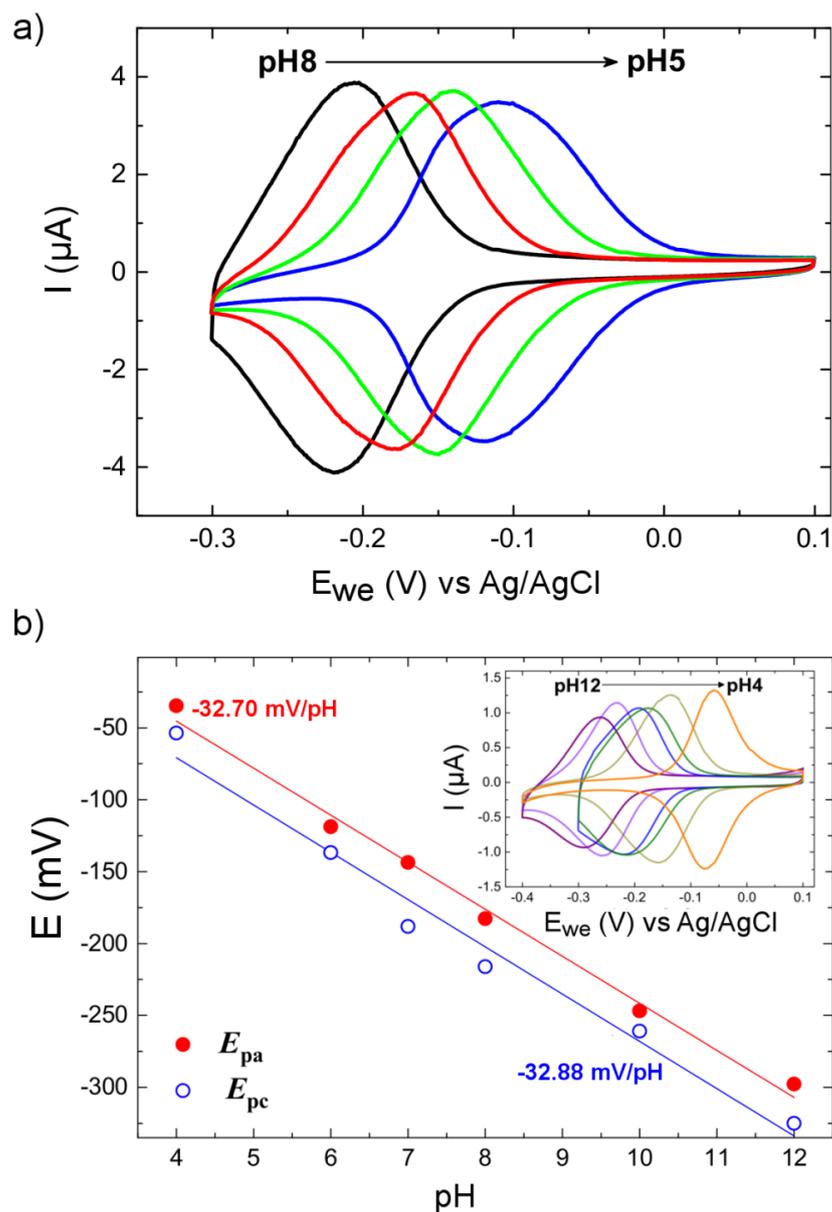
Figure 4.6: a) Cyclic voltamogramms of 0.2 mM MB SAM at 100 mV/s scan rate in different pH values of McIlvaine buffer; b) peak potential plotted as a function of pH of 0.2 mM MB SAM using Britton-Robinson buffers from pH 4 to pH 12. The slope of the fitted lines are used to determine the rate of potential shifts with pH. Insert shows the corresponding cyclic voltammograms for each pH.
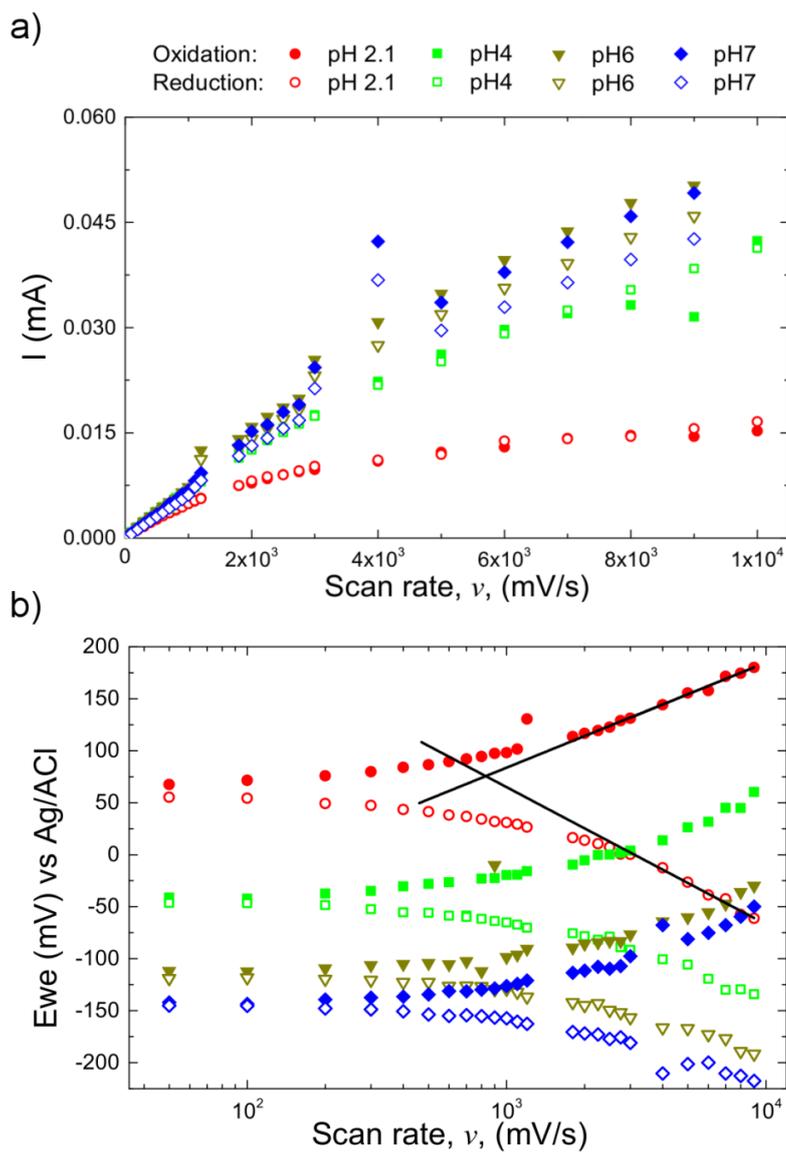
Figure 4.7: Oxidation and reduction peak current plotted against the scan rate and b) Laviron plots of CVs of 0.2 mM MB SAM in different pH values of McIlvaine buffer. The linear regions at higher scan rates of the Laviron plots have been fitted to calculate the rate of electron transfer, k_{ET}, for each pH (here shown only for the pH 2.1 plot).

The rate of electron transfer as a function of pH, calculated using the Laviron method (Figure 4.7b), was found to decrease at lower pH (Figure 4.8a), indicating that the rate of protonation and de-protonation of the redox group affect the kinetics of the reaction. In a proton-coupled electron transfer process (PCET), electron transfer occurs separately from proton transfer [171] [172], and consequently, intermediate forms exist between the fully oxidised or reduced forms (Figure 4.8b). At low pH, however, proton transfer is expected to precede electron transfer. As a result, the protonated intermediate will prevail, especially at fast scan rates, and the increased concentration of protons will impede the complete re-oxidation of the molecule. This sluggishness of the electron transfer rate with decreasing pH was indeed observed here, as seen in (Figure 4.8a). These findings

demonstrate that the redox reaction of the MB-terminal groups of the LCAT-OEG SAM follows a proton-coupled electron transfer process, thus demonstrating that MB retains its redox behaviour following immobilisation.
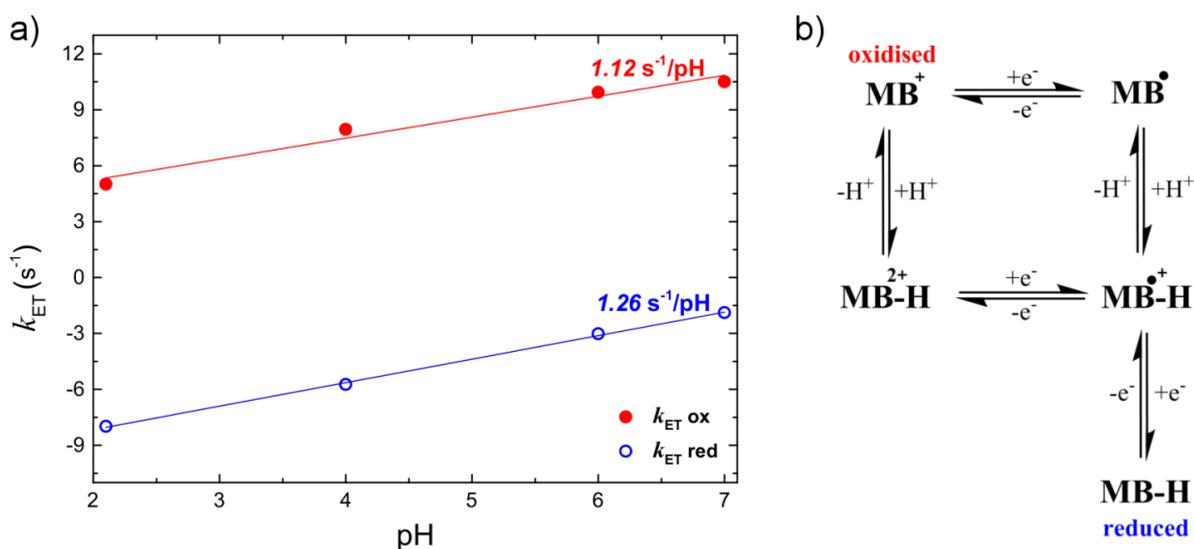
Figure 4. 8: a) Rate of electron transfer as a function of pH for the oxidation and reduction of MB SAM; b) schematic of the redox forms of MB for a 2e⁻/1H⁺ process, including intermediate forms of the partially oxidised molecule [170].

While the electrochemical studies are indicative of a proton dependent redox-reaction, it is important to demonstrate that the observed pH dependency is indeed a result of the change in the electron transfer kinetics rather than conformational changes of the monolayer caused by shifts in pH. EQCM-D was thus used to study the structural properties of the MB SAM by comparing the frequency and dissipation shifts as a function of pH before and after functionalisation of the MB SAM, while performing electrochemical measurements.

Figure 4.9a illustrates the changes in frequency and dissipation as a gold-coated QCM-D sensor is challenged with different pH buffers (McIlvaine buffers pH 5-8). D3, D5 and D7 represent the third, fifth and seventh dissipation overtones respectively, while F3 corresponds to the third frequency overtone. The introduction of a pH 5 McIlvaine buffer resulted in a decrease in frequency from the ultrapure water baseline and a corresponding increase in dissipation. When the sensor was washed with ultrapure water both frequency and dissipation returned to their original values. As the buffer pH increased, the frequency shifts became larger, as seen in Figures 4.9a and 4.9d, where the frequency shifts in each buffer were normalised to that of pH 7. Both D5 and D7 exhibited a stepwise increase with rising pH, whereas D3 showed a less linear pattern (Figures 4.9e-g).
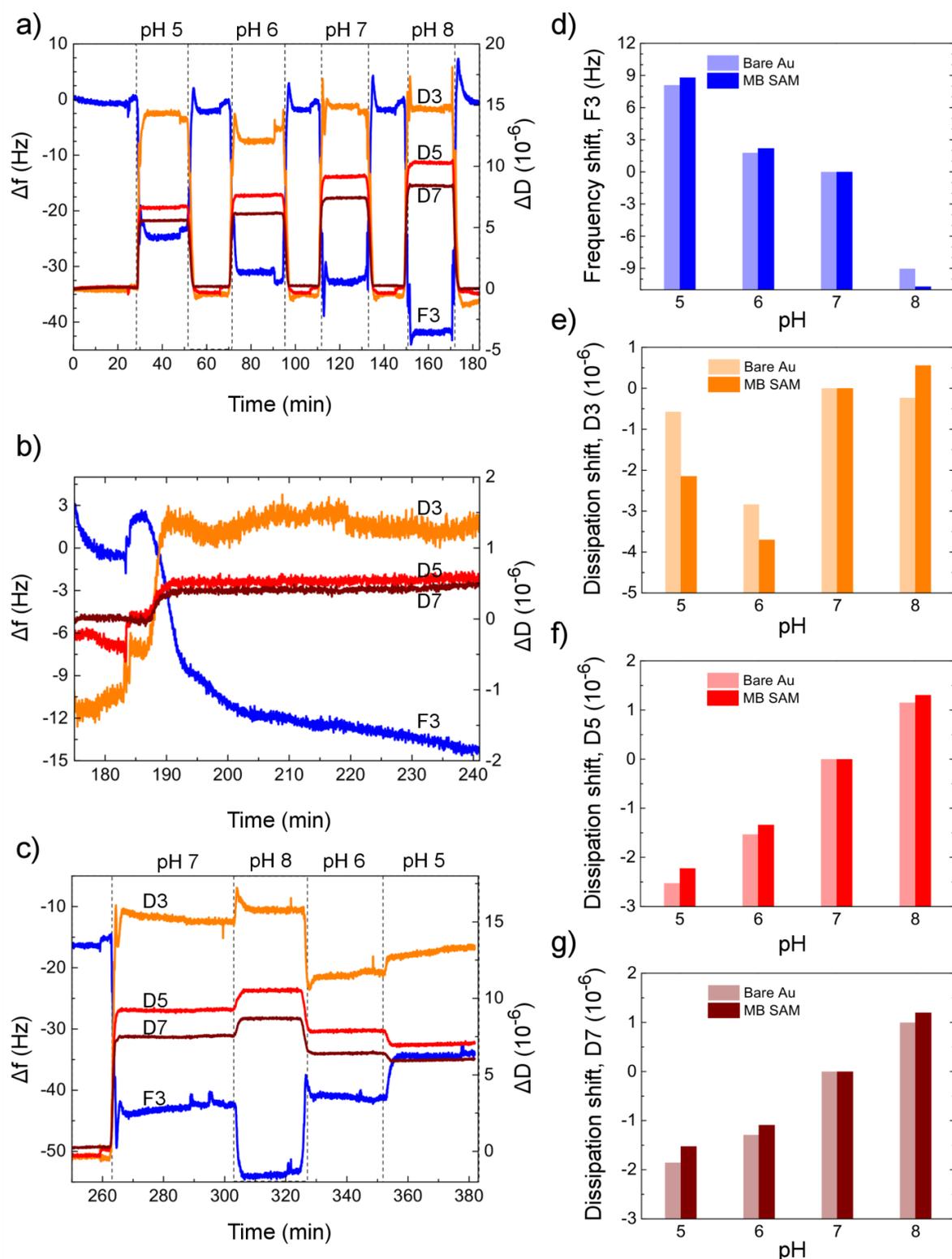
Figure 4.9: Shifts in frequency, Δ*f*, and dissipation, Δ*D*, over time as a result of a) injection of 100 mM McIlvaine buffers pH 5-8 over the bare gold surface of the QCM-D sensor, b) functionalisation of QCM-D sensor with 0.02 mM MB SAM in ultrapure water and c) injection of 100 mM McIlvaine buffers pH 5-8 over the SAM-functionalised sensor; (blue: F3, third frequency overtone); (orange: D3, red: D5, burgundy: D7 third, fifth and seventh dissipation overtone, respectively). Shifts in d) F3, e) D3, f) D5 and g) D7 as a function of buffer pH. Each shift was normalised to the shift corresponding to McIlvaine buffer pH 7.

92

The characteristics of the solution, such as density, viscosity or conductivity, have a significant effect on the oscillating frequency of a quartz crystal in contact with liquid [144] [147]. Consequently, the introduction of each pH buffer will induce a frequency shift and a corresponding change in the dissipation of the oscillating energy, according to the properties of each solution. Here, for instance, the increasing density of the McIlvaine buffers (in order of rising pH), caused a corresponding increase in dissipation, as seen in Figures 4.9a and 4.9e-g.

Following exposure to the pH buffers, the sensor was then challenged with a 0.1 M aqueous solution of LCAT-OEG-MB. Figure 4.8b shows the gradual decrease in frequency as the MB-SAM assembled onto the QCM-D sensor, while dissipation increased over time as the viscoelastic properties of the crystal changed due to formation of the monolayer.

The distance above the surface where the energy of the oscillation dissipates is inversely dependent on the frequency [148]. Therefore, dissipation shifts for the higher order frequency harmonics, D5 and D7, are expected to be more sensitive to the viscoelasticity of the near surface region of the layer (here, the rigid LCAT region), while the energy of the lower order harmonic, D3, dissipates further away from the surface and thus describes the viscoelastic properties of the upper parts of the layer (amorphous OEG phase).

Following SAM assembly, each pH buffer was again introduced into the QCM-D flow cell (Figure 4.9c). Both frequency and dissipation follow a similar trend to that of the sensor before functionalisation, as seen in Figures 4.9d-g, which indicates that the conformation of the monolayer is not affected significantly by different pH conditions.

Cyclic voltammograms (100 mV/s) of the MB SAM-functionalised EQMC-D sensor are shown as a function of buffer pH in Figure 4.10. Similarly to the CVs of the MB SAM on Au-Si substrates (Section 4.3.1), the peaks are highly symmetric with minimum peak separation, which correspond to the reversibility of the redox system. The peak potential decreased with changing pH and the potential shift rates were close to the predicted value of -29 mV/pH for a $2e^-$, $1H^+$ process (insert, Figure 4.10).

By linking the findings from QCM-D measurements with CV data of the MB SAM, it can be concluded that the pH dependency of the MB SAM redox response is due to the influence of the local proton concentration on the redox reaction kinetics, rather than conformational changes of the monolayer. Therefore, the redox process of the MB attached to the LCAT-OEG SAM is indeed dependent on the pH conditions and follows a $2e^-$, $1H^+$ process.
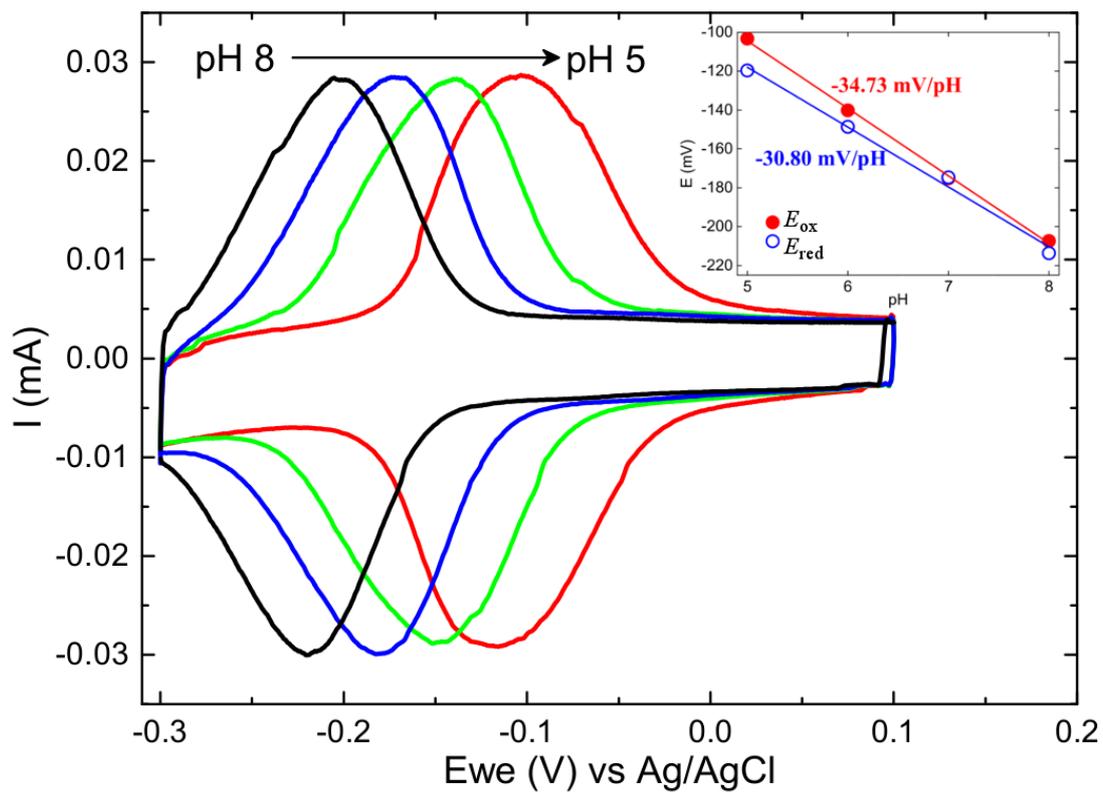
Figure 4.10: Cyclic voltamogramms of 0.02 mM MB SAM at 100 mV/s scan rate in different pH values of 100 mM McIlvaine buffer. Insert shows the CV peak potentials plotted as a function of pH. The slopes of the fitted lines correspond to the potential shift rates with increasing pH.

4.3.3 Mixed and pure MB SAMs: comparison by CV, EIS and PM-IRRAS

In this section, electrochemical (CV, EIS) and spectroscopic (PM-IRRAS) techniques were used to assess the differences between pure and mixed MB SAMs. In the previous sections (4.3.1, 4.3.2), CV and QCM-D measurements of the MB SAM showed that MB retains its redox properties after immobilisation through a long-chained OEG linker. The observed redox activity showed a pH dependency, which demonstrates that the redox reaction is a $2e^-$, $1H^+$ redox process, as expected of MB. These findings support the use of LCAT-OEG-MB SAMs for studying biomolecular interactions of MB-Affimers with surface-immobilised MB. However, the redox-active and bulky MB groups can interfere with the orderly packing of the monolayer and potentially inhibit access of the Affimer to the MB. Co-immobilisation with an appropriate SAM dilutant can reduce these effects. It is important, however, that the selected SAM dilutant does not exhibit non-specific binding with Affimers or other reagents present in a sample. An OH-terminated LCAT-OEG was selected for this purpose (Figure 4.1d), due to its excellent protein resistance properties [118] [127] [173].
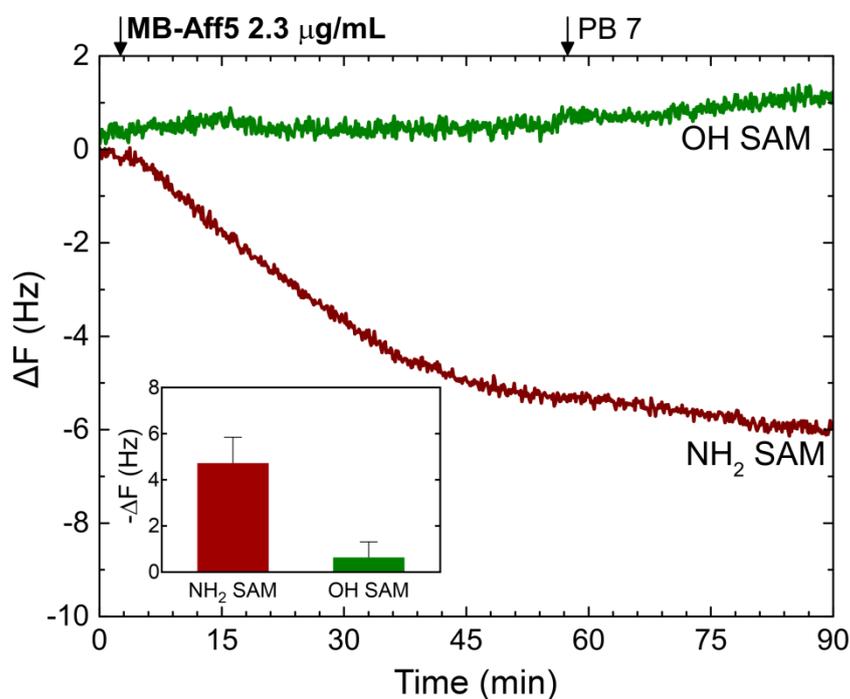
Figure 4.11: Real-time QCM-D showing shifts in the resonant frequency (third harmonic, F3) as a function of time; here, the sensors were functionalised with OH or NH₂ SAM and challenged with 2.3 µg/mL MB−Aff5 in PB 7. Inset shows bar charts of frequency shifts of OH and NH2 SAM vs MB-Aff5 (four nominally identical QCM-D measurements for each SAM).

To verify the reduced bio-fouling property of LCAT-OEG-OH SAMs (referred to as OH SAM), its QCM-D response to Affimers was compared to that of a NH$_2$-terminated LCAT-OEG SAM (referred to as NH$_2$ SAM). Figure 4.11 shows the frequency shifts of OH and NH$_2$ SAM-functionalised QCM-D sensors challenged with 2.3 µg/mL Affimer solutions in PB 7. The OH SAM exhibits considerably lower non-specific binding than the NH$_2$ SAM, thus demonstrating its suitability as a dilutant of the MB SAM.
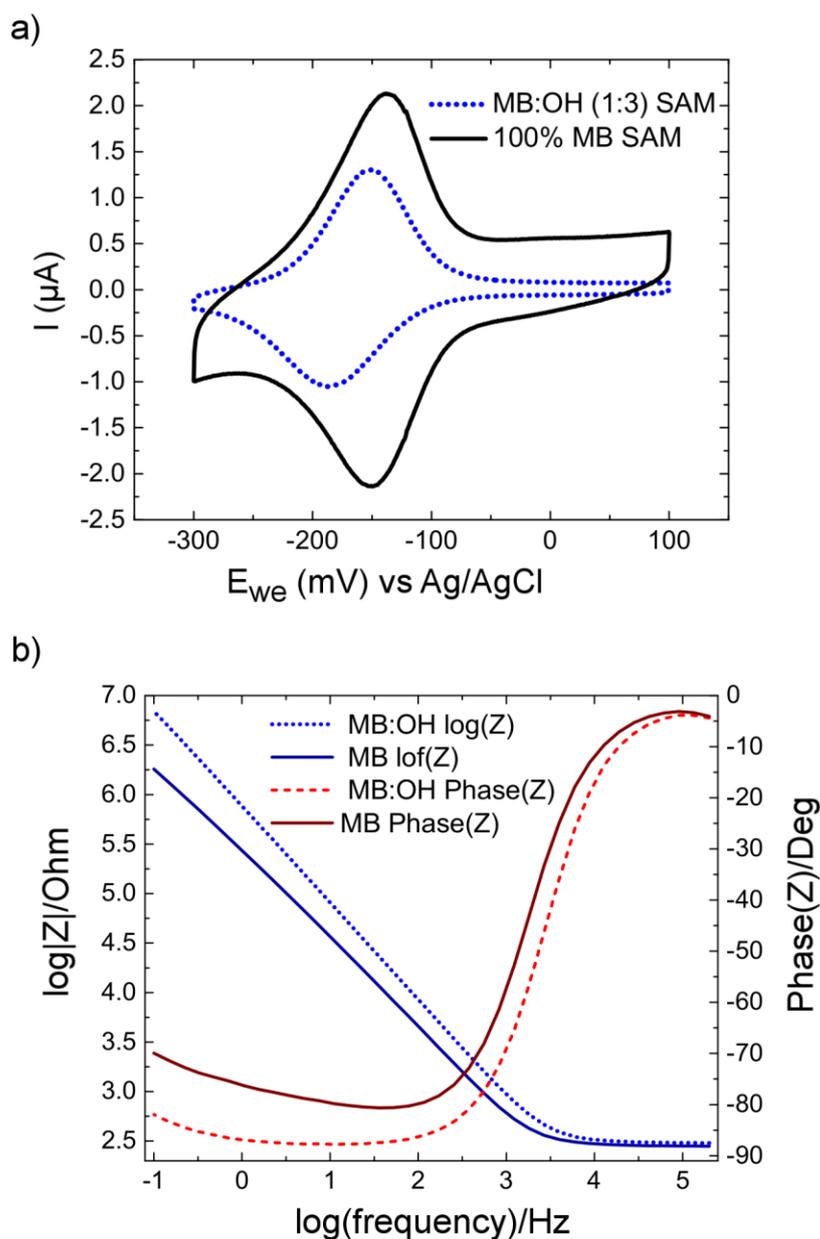
Figure 4.12: a) Cyclic voltammograms (250 mV/s) and b) Bode impedance of MB and mixed MB:OH (1:3) SAMs in PB 7.

Mixed MB:OH SAMs were formed by co-immobilisation of LCAT-OEG-MB and mixed with LCAT-OEG-OH at a 1:3 ratio and CV, EIS and PM-IRRAS were used to compare the resulting

monolayers to undiluted MB SAMs . Cyclic voltammograms of MB and mixed MB:OH SAMs at 250 mV/s scan rate in 100 mM sodium phosphate buffer pH 7 are shown in Figure 4.12a. As expected for ideal and reversible surface-immobilised redox systems, both monolayers exhibit highly symmetric oxidation and reduction peaks with very little peak splitting. The oxidation and reduction peak current of the mixed SAM is lower than that of the pure LCAT-OEG-MB SAM, which is attributed to the dilution of redox groups in the mixed monolayer.

When assessed by EIS, both SAMs seem to form well-packed films, as demonstrated by Bode plots in Figure 4.12b. Here, the slope of $log|Z|$ vs log(frequency) at low frequencies was close to -1 (MB:OH: -0.975, R^2=0.999; DCF: -0.883, R^2=0.999), thus approaching ideal capacitor behaviour. This behaviour is associated with densely-packed monolayers with good insulating properties [174]. At 0.1 Hz, the minimum phase angle for the MB SAM was -69.95°. In constrast, the phase angle of the mixed MB:OH SAM (-81.93°) approached closer to the phase angle of an ideal capacitor (-90°). The lower phase angle of the mixed SAM corresponds to a dense, highly insulating monolayer that is almost free of pinholes and defects [126], signifying that dilution of the bulky redox centres improved the orderly packing of the monolayer.

Both MB SAM and MB:OH SAM were further characterised using PM-IRRAS which provides deeper insight into the conformation differences between the two monolayers. A pure OH SAM (100% LCAT-OEG-OH) and a 1-dodecanethiol SAM (referred to as C_{12} SAM) were also used and acted as references. Figure 4.13a shows the IR absorption spectra of the four SAMs. The C_{12} SAM exhibited well-defined IR absorption peaks at 2919 cm^{-1}, 2851 cm^{-1}, 2963 cm^{-1} and 2877 cm^{-1}. These are associated with the CH$_3$ and CH$_2$ symmetric (v_s) and asymmetric stretch (v_a) bands and are typical for a tightly-packed, highly crystalline alkanethiol SAM with all-trans alkyl chains and very little gauche defects (v_a CH$_2$ 2919 cm^{-1} , v_s CH$_2$ 2851 cm^{-1}, v_a CH$_3$ 2963 cm^{-1}, v_s CH$_3$ 2877 cm^{-1}) [127] [175] [176]. The v_a CH$_2$ stretch in particular, is an indicator of the crystallinity of the molecular film [175-178]. This peak (at 2919 cm^{-1}) was also present in the data from all the LCAT-OEG SAMs which shows the existence of a well-packed, all-trans LCAT component under the OEG layer.

Absorption peaks associated with the conformation of the OEG component are contained within the fingerprint region between 900-1800 cm^{-1} (Figure 4.13b). Specifically, the peaks at 1348, 1244, 1114 and 964 cm^{-1} which were observed for both the OH and MB:OH SAMs, are distinctive of a helical conformation of the OEG component [176]. The band at 1114 cm^{-1} in particular, appeared as an intense and sharp peak for the OH SAM and MB:OH SAM. This peak is characteristic of asymmetric C-O-C stretching and the high intensity reveals the high degree of crystallinity of the OEG layer where the OEG helices are orientated almost parallel to the surface normal [127] [178].

Moreover, the sharp, intense peak at 1348 cm^{-1} is typical of the CH$_2$ wagging mode of a helical OEG. It is worth noting that the detection of several short peaks and/or shoulders (such as ~1124 or ~1080 cm^{-1}) indicates the existence of regions with less ordered, amorphous-like OEG domains. This suggests that while both the OH and MB:OH SAMs are mostly ordered with a high degree of helical OEG conformation, regions of amorphous OEG occur.
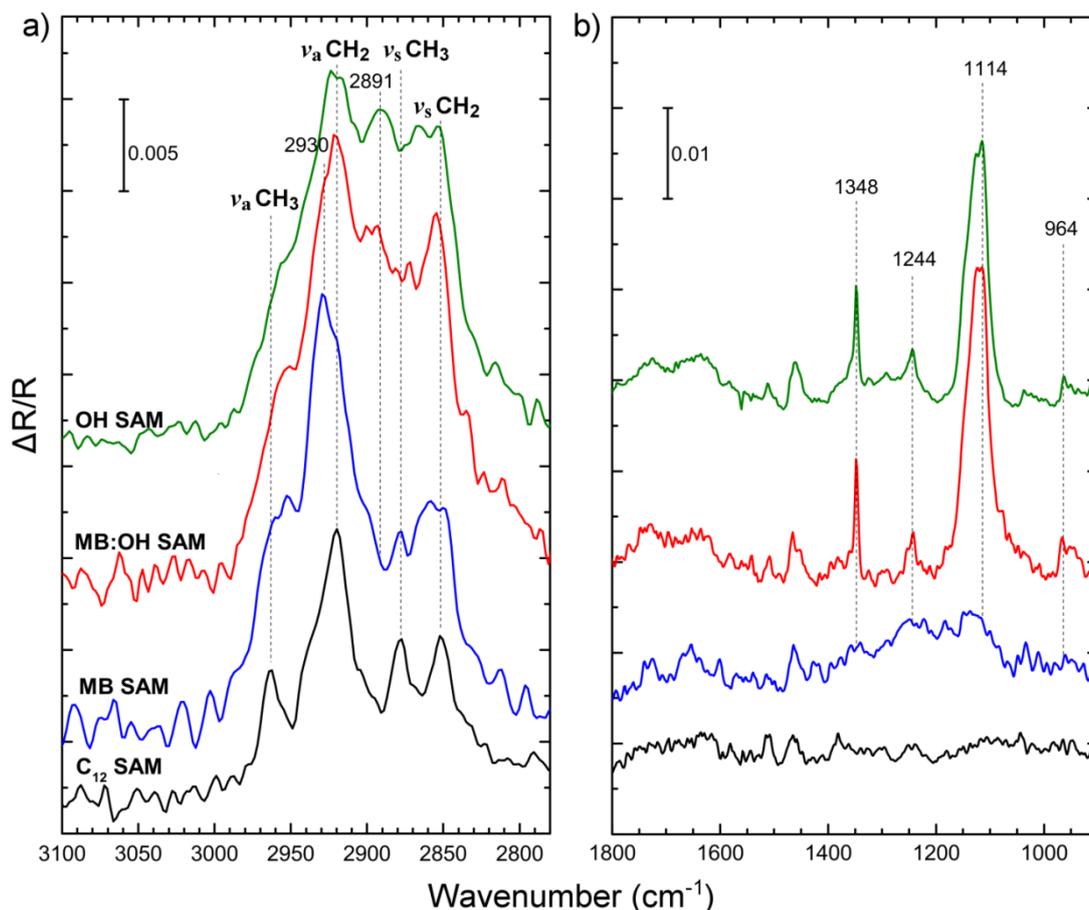
Figure 4.13: PM-IRRAS spectra of LCAT-OEG and alkanethiol SAMs on gold, showing a) the CH stretch region (2750-3100 cm^{-1}) and b) the fingerprint region (900-1800 cm^{-1}). The spectra have been stacked and presented with the y-axis expanded, to make it easier to see the relevant peaks.

In contrast, the C-O-C stretch region for the MB SAM appears as a broad band with short peaks in the IR spectrum (at 1080, 1100, 1148, and 1137 cm^{-1}) corresponding to a mainly amorphous OEG conformation that is less ordered than the OH and MB:OH SAMs [127] [177]. Moreover, the CH$_2$ wagging mode characteristic of helical OEG (at 1348 cm^{-1}), appeared as a weak doublet at ~1360 and 1340 cm^{-1}, indicative of a more amorphous conformation. In addition, unlike the MB and MB:OH SAMs, the IR absorption peak of the CH$_2$ twisting mode of a helical OEG layer (at 1244 cm^{-1}) was weak for the MB SAM [176] [179]. The reduced ordering of the OEG phase in MB-terminated SAMs can also be observed in the CH$_2$ stretch region (Figure 4.13a). Here, a 2930 cm^{-1} shoulder (ν_a CH$_2$ stretch of an amorphous OEG phase) was seen in the IR spectra of MB and

MB:OH SAMs, indicating a higher ratio of amorphous to helical OEG conformation in these MB-terminated SAMs compared to the pure OH SAM. Moreover, the band associated with the v_s CH$_2$ stretch of helical OEG chains (2891 cm^{-1}) was clearly observed for the OH SAM, but was less intense for the MB:OH SAM and absent for the MB SAM. The fact that the amorphous phase is more dominant in SAMs containing a component of LCAT-OEG-MB is attributed to the steric hindrance caused by the bulky MB units that interfere with the ordered packing of the OEG layer. The differences in helical to amorphous OEG ratio between the MB SAM and the mixed MB:OH SAM accounts for the differences in the EIS spectra of these molecular monolayers shown in Figure 4.12b.

These findings suggest that dilution of the MB SAM with LCAT-OEG-OH can improve the order and packing of the SAM by reducing the steric hindrance effects of the redox-active MB tail groups. Consequently, by forming mixed MB:OH SAMs, the target is immobilised through a well-ordered monolayer that enables efficient access by the Affimers. Therefore, this immobilisation approach was followed for studying biomolecular interactions of MB-Affimers with surface immobilised MB.

4.4 QCM-D monitoring of MB-Affimer interactions with surface-immobilised MB

The previous section showed that a) MB retains its redox activity when immobilised on a surface through self-assembled monolayers on gold and b) dilution of the LCAT-OEG-MB with LCAT-OEG-OH improved the structure of the monolayer. This approach to analyte immobilisation was thus employed to study biomolecular interactions of surface-immobilised MB with MB-Affimers. LCAT-OEG-OH was used as a control SAM to monitor potential non-specific interaction of Affimers with the surface and as a SAM dilutant to separate the bulky redox MB tail groups. Here, QCM-D was used to investigate the kinetics, affinity and selectivity of MB-Affimers for their target and demonstrate the possibility of operation in a competition assay format.

4.4.1 Methods

Gold coated QCM-D sensors (QSX 301, Biolin Scientific, Stockholm, Sweden) were cleaned by sonication in a 2% Hellmanex III solution (Hellma Analytics, Müllheim, Germany) and thorough rinsing in ultrapure water, followed by UV-ozone treatment (30 min) and immersion in EtOH (30 min). Cleaned sensors were functionalised with LCAT-OEG SAMs (mixed MB:OH 1:3 ratio or OH SAM) by immersion in 0.1 mM ethanolic solutions for 48 hours.

Following fuctionalisation, the sensors were rinsed in EtOH, dried with N_2 gas and loaded into the QCM-D flow modules (QSense E4, QFM 401, Biolin Scientific, Stockholm, Sweden). The surface area exposed to solution was equal to 0.95 cm^2 as defined by a Viton O-ring. Resonant frequency (F) and dissipation (D) were monitored while ultrapure water was passed over the sensors using a peristaltic pump at a flow rate of 20 μL/min, until a steady baseline was achieved (defined by a frequency shift of less than 1 Hz over 10 minutes), followed by injection of PB 7 to establish a running buffer baseline. Next, MB-Affimer solutions (either MB-Aff1 or MB-Aff5) in PB 7 were introduced at 20 μL/min flow rate until the frequency saturated. Affimers raised against green fluorescent protein (GFP) were used as controls (referred to as GFP-Aff). Finally, the sensors were washed with PB 7. For binding kinetics measurements, the flow rate was set at 10 μL/min.

Affimer binding was also interrogated electrochemically (EQCM-D). Cyclic voltammetry was performed at a scan rate of 100 mV/s and over a [-0.3V; +0.1V] voltage range.

To study the selectivity of MB-Affimers (that is, the ability to recognise MB among the interferences in a complex sample), limnetic water samples were collected (Heslington, York, UK), syringe-filtered through a 0.22 µM sterile filter unit (Millex, Millipore, Cork, Ireland) and used as a running solvent in QCM-D measurements (measured pH 8.17 ± 0.01). The limnetic samples were spiked with MB-Aff5 (or GFP-Aff as control) and injected over a MB SAM-functionalised QCM-D sensor.

4.5 Results

4.5.1 Interactions of MB-Affimer with MB (QCM-D/EQCM-D)

QCM-D and EQCM-D were used to explore molecular interactions between MB-Affimers and MB immobilised on the surface via the mixed MB:OH SAM. MB-Aff5 demonstrated significantly higher levels of expression than MB-Aff1 (Appendix A) and was thus taken forward for in-depth analysis. However, the affinity of MB-Aff1 was also investigated through kinetics and saturation binding measurements using QCM-D (Section 4.5.2).
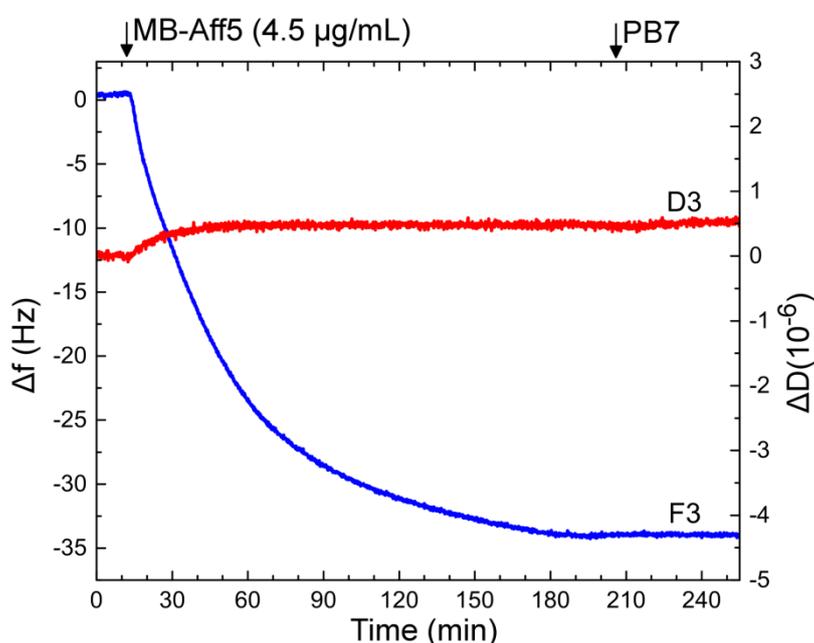
Figure 4.14: Real-time QCM-D showing shifts in the resonant frequency (third harmonic, F3) and dissipation (D3) as a function of time; here, the sensors were functionalised with MB:OH SAM and challenged with 4.5 μg/mL MB−Aff5 in PB 7

Real-time QCM-D data following exposure of a mixed MB:OH SAM (1:3) to a 4.5 μg/mL MB−Aff5 solution are shown in Figure 4.14. The interaction of MB−Aff5 with MB lead to a significant decrease in the resonant frequency of the quartz sensor as a result of the increase in the mass deposited on the surface (the third harmonic (F3) is shown here). The average frequency shift due to MB−Aff5 binding was −29.54 ± 2.11 Hz (from six nominally identical measurements). These ΔF values indicate a strong interaction between MB-Aff5 and the MB immobilised on the sensor surface. In vacuum, the resonant frequency of QCM-D is related to the mass loading of the crystal according to the Sauerbrey model, $\Delta m = -C\Delta f/n$, (Section 3.4, Equation 3.15 [61]). This

corresponds to an estimated deposited mass of 174.31 ± 12.44 ng/cm^2 and translates to a surface coverage of (8.47 ± 0.6) × 10^{12} molecules/cm^2 for a 12.4 kDa Affimer. Although, the Sauerbrey model does not account for the viscoelasticity of the layer, here the dissipation shift was sufficiently low (ΔD < 0.5 × 10^{-6}) to assume a dense, rigid film that couples to the oscillation of the quartz crystal. However, it should be noted that, in the liquid phase, the resonant frequency is sensitive to a number of solution and interfacial factors, as described by Kanazawa and Gordon [147] so the actual mass loading can differ from that estimated by Sauerbrey.
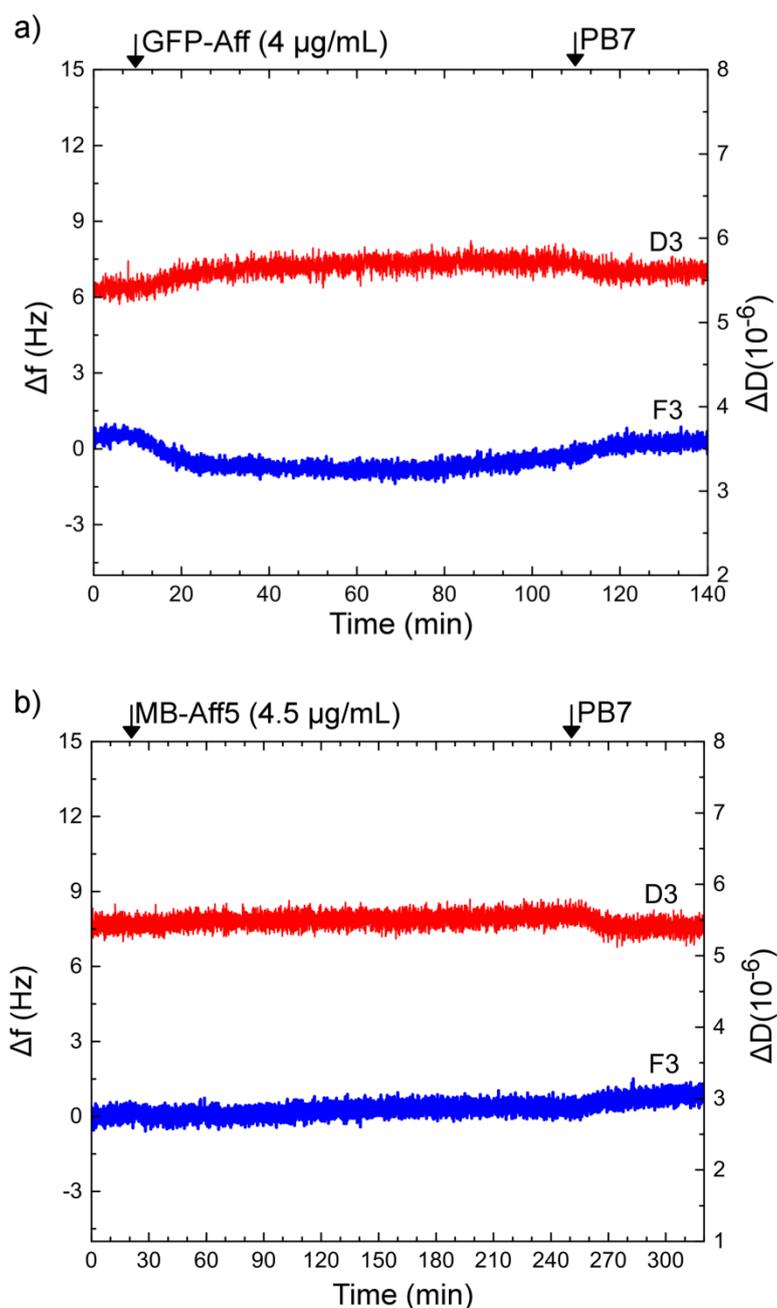
Figure 4.15: Real-time QCM-D showing changes in the resonant frequency (third harmonic, F3) and dissipation (D3) as a function of time. QCM-D sensors functionalised with (a) mixed MB:OH SAM and challenged with 4 µg/mL GFP−Aff in PB 7 and (b) 100% OH SAM and challenged with 4.5 µg/mL MB−Aff5.

To account for non-specific interactions of Affimers with the monolayer or the sensor surface, the mixed MB:OH SAM was also challenged with to GFP-Aff (control Affimer). As seen in Figure 4.15a, the frequency shift in the presence of GFP-Aff was insignificant compared to that of MB-Aff5 (Figure 4.14) and quickly recovered following rinsing in PB 7, thus demonstrating that MB-Aff5 showed specific binding to MB. The specificity of the interaction between MB and MB-Aff5 was further investigated by exposure of a 100% OH SAM to MB-Aff5 solution. As shown in Figure 4.15b, the resonant frequency remained constant. The absence of interaction between MB−Aff5 and the OH SAM is consistent with the demonstrated antifouling properties of the OEG region (Section 4.3.3).

Interactions between MB-Aff5 and the surface-immobilised MB were also observed by monitoring the redox activity of MB in the monolayer. Figure 4.16 shows cyclic voltammograms of an MB:OH SAM-functionalised EQCM-D sensor before and after exposure to MB-Aff5. Here, binding of Affimers on the SAM limits the access of ions and/or protons from solution to the electrode, resulting in a reduction in the peak oxidation and reduction currents (i_{pa} and i_{pc}). The reduction in peak current was found to be dependent on MB-Aff5 concentration, suggesting the potential for electrochemical detection and quantification of Affimer binding to redox-active targets.
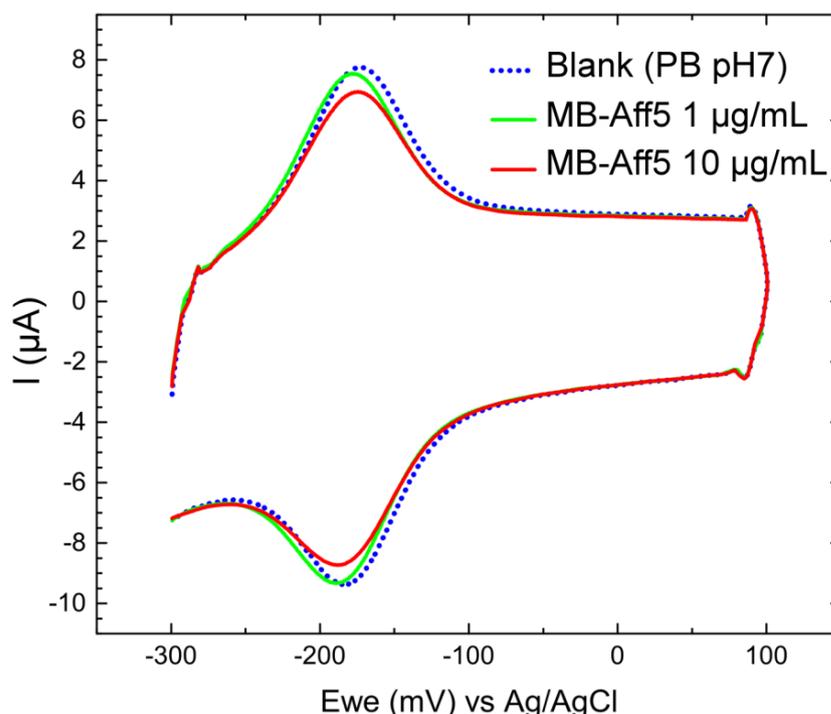
Figure 4.16: Cyclic voltammograms (100 mV/s) of a MB:OH SAM-functionalised EQCM-D sensor challenged with 0, 1, and 10 μg/mL MB−Aff5 in PB 7.

4.5.2 MB-Affimer affinity: saturation binding and binding kinetics

An MB:OH SAM-functionalised QCM-D sensor was exposed to increasing concentrations of MB−Aff5 or MB-Aff1 and monitored by QCM-D in order to calculate the Affimer binding affinity. Figures 4.17a and 4.18a show the third harmonic of the sensor resonant frequency as a function of time during exposure to MB-Aff1 or MB-Aff5 respectively from 1 to 10 μg/mL (PB 7 was injected between samples to remove non-specifically bound material). As the Affimer concentration increased, the frequency shifts became larger, peaking around 4 μg/mL for MB-Aff5 and 6 μg/mL for MB-Aff1. The response then saturated at a concentration around 8 μg/mL. The frequency shift was plotted as a function of concentration (Figures 4.17b and 4.18b) and fitted to a Hill-Langmuir isotherm, (Equation 4.1).

$$Y = \frac{B_{max} \cdot C^h}{K_D^h + C^h} \tag{4.1}$$

Here, B_{max} is the maximum response, C is the Affimer concentration (nM), h is the Hill slope, and K_D is the dissociation constant [180]. The value of the Hill slope reveals information regarding the number of binding sites of the receptor, so that a Hill slope of ~1 corresponds to monomeric (one-site) binding, whereas a slope of ~2 to dimeric binding (cooperative). Here, the Hill slope was found to be 1.36 for MB-Aff1 and 2.36 for MB-Aff5 (Table 4.2); the latter implies the possibility of two-site binding. It should be noted, however, that the Hill model assumes that the binding reaction under investigation has reached equilibrium, which in these QCM-D experiments was not attained within the injection time of reagent at each Affimer concentration. Consequently, the Hill slope values estimated here cannot provide an accurate determination of the number of sites used in Affimer binding.

The saturation binding data were also fitted using a standard Langmuir isotherm (Equation 4.2), but due to its poor fitting (Figures 4.17b and 4.18b), the Hill-Langmuir model was preferred for estimating the dissociation constant, K_D. For MB-Aff5, the K_D was found to be 216.4 nM, comparable to previously reported values for antibodies of small molecules (10^{-10}-10^{-7} M) [48] [181] [182]. The K_D of MB-Aff1 was 444.4 nM.

$$Y = \frac{B_{max} \cdot C}{K_D + C} \tag{4.2}$$
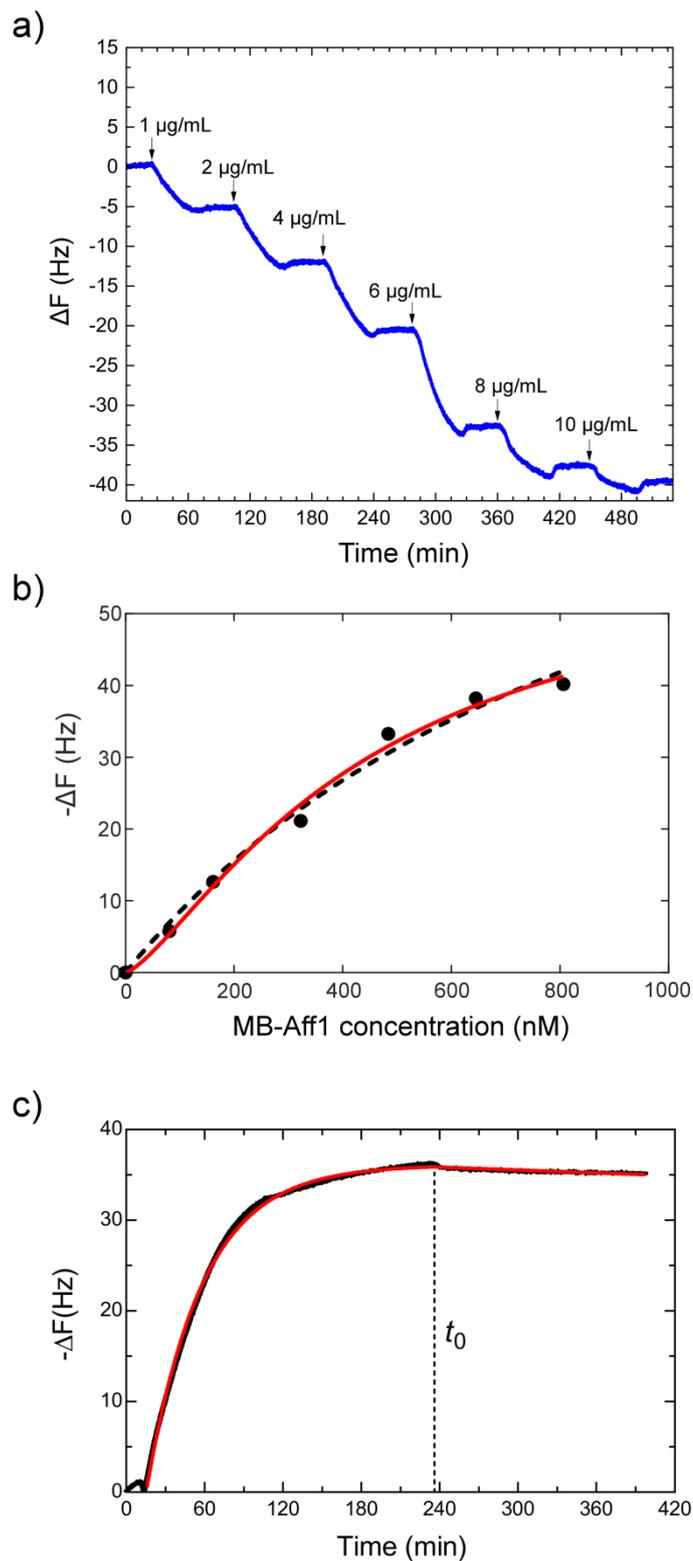
Figure 4.17: a) MB-Aff1 saturation binding: real-time QCM-D of resonant frequency shifts Δf (third harmonic) of MB:OH SAM-functionalised sensors during introduction of increasing concentrations of MB-Aff1 (in PB7); b) Frequency shifts plotted against Affimer concentration (red line shows Hill-Langmuir fit, dotted line shows Langmuir fit); c) MB-Aff1 binding kinetics: real-time QCM-D of frequency shift of MB:OH SAM-functionalised sensors during injection of 4 µg/mL (322 nM) MB−Aff1 at 10 µL/min flow rate. Red line shows association-dissociation fitting curves.
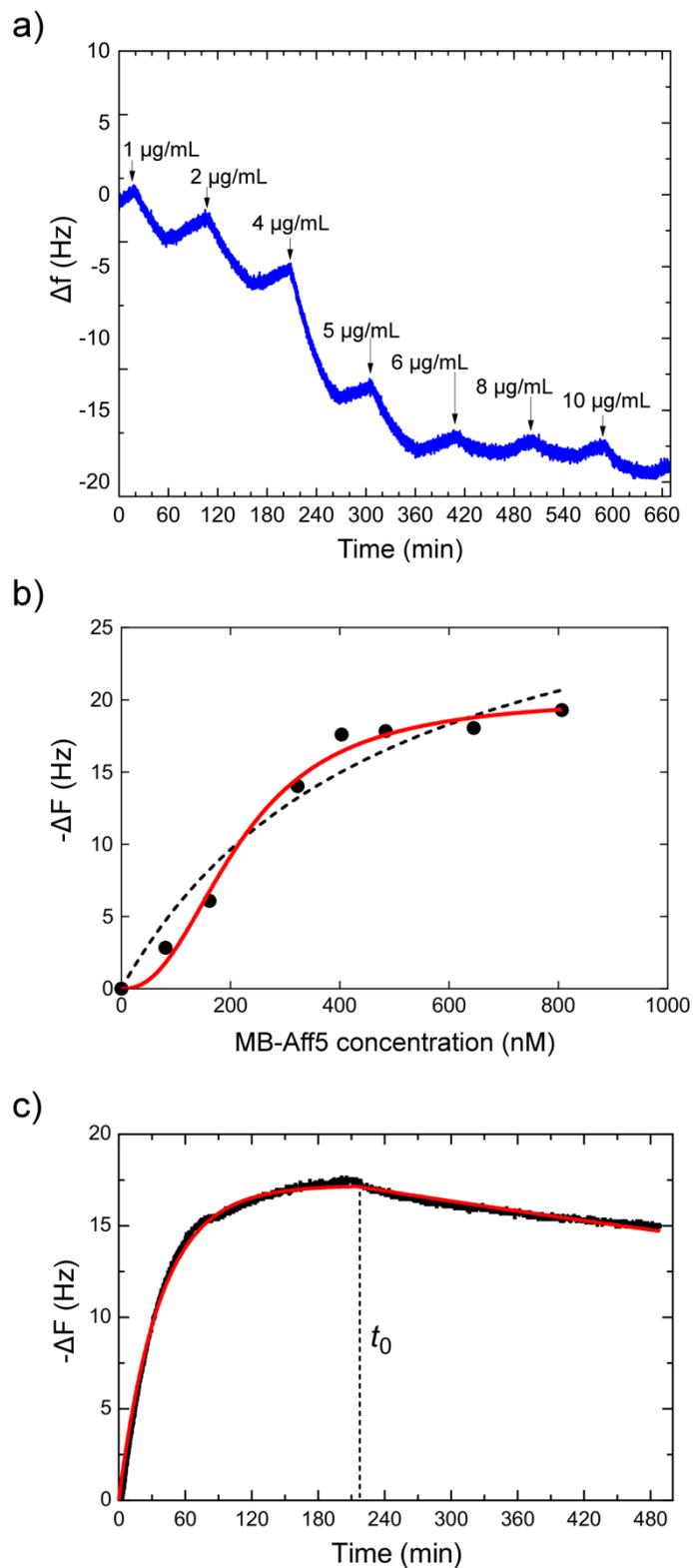
Figure 4.18: a) MB-Aff5 saturation binding: real-time QCM-D of resonant frequency shifts Δf (third harmonic) of MB:OH SAM-functionalised sensors during introduction of increasing concentrations of MB-Aff5 (in PB7); b) Frequency shifts plotted against Affimer concentration (red line shows Hill-Langmuir fit, dotted line shows Langmuir fit); c) MB-Aff5 binding kinetics: real-time QCM-D of frequency shift of MB:OH SAM-functionalised sensors during injection of 8 μg/mL (645 nM) MB−Aff5 at 10 μL/min flow rate. Red line shows association-dissociation fitting curves.

Affinity parameter	MB-Aff1	MB-Aff5
K_{Dsat} (nM)	444.4 (R^2=0.993)	216.4 (R^2=0.991)
$B_{max-sat}$ (Hz)	59.65	20.20
h	1.36	2.36
K_{Dkin} (nM)	1.41 (R^2=0.998)	13.70 (R^2=0.989)
k_{on} ($M^{-1}min^{-1}$)	7.2×10^4	4.1×10^4
k_{off} (min^{-1})	1.0×10^{-4}	5.6×10^{-4}
$B_{max-kin}$ (Hz)	52.00	17.50

Table 4.2: Affinity parameters of MB-Aff1 and MB-Aff5, as estimated by saturation binding (Hill-Langmuir model) and binding kinetics measurements using QCM-D (Figures 4.17 and 4.18).

To study the kinetics of the binding reaction, MB-Aff1 or MB-Aff5 were injected over an MB:OH SAM-functionalised QCM-D sensor at a flow rate of 10 µL/min and the frequency shift was measured as a function of time (Figure 4.17c and 4.18c respectively). The data were fitted using Equations 4.3 and 4.4. The rates of association (k_{on}) and dissociation (k_{off}) for MB-Aff5 were found to be 4.1×10^4 M^{-1} min^{-1} and 4.6×10^{-4} min^{-1}, respectively (Table 4.2). Since $K_D = k_{off}/k_{on}$, this yielded a dissociation constant of 13.7 nM for MB-Aff5, which is one order of magnitude lower than that calculated by saturation binding analysis. This discrepancy between kinetic and saturation binding analysis is not uncommon, since, in the latter case, equilibrium is usually not reached within the injection time of reagent at each concentration, which leads to overestimates of the K_D. Thus, the dissociation constant calculated by kinetic analysis is expected to be closer to the true affinity of the binder than the dissociation constant estimated by saturation binding measurements [180]. The K_D of MB-Aff1 was found to be one order of magnitude lower than MB-Aff5 (1.41 nM). However, considering the significantly higher expression levels of MB-Aff5, the latter was selected for the remaining study of MB Affimers.

$$\text{Association} = \left(\frac{B_{max} \cdot C}{K_D + C}\right)(1 - e^{-k_{obs} \cdot t}) \qquad (4.3)$$

Where k_{obs} is the observed rate constant of the association reaction: $K_{obs} = k_{on} \cdot C + k_{off}$

$$\text{Dissociation} = Y_0 \cdot e^{-k_{off} \cdot (t - t_0)} \qquad (4.4)$$

Where B_{max} is the maximum binding at equilibrium with maximum concentration of Affimer, C is the Affimer concentration, t_0 is the time at which dissociation was initiated and Y_0 is Y at time=t_0 (Y corresponds to response signal, here ΔF) [180] [183].

4.5.3 Selectivity of MB-Affimers in a complex matrix
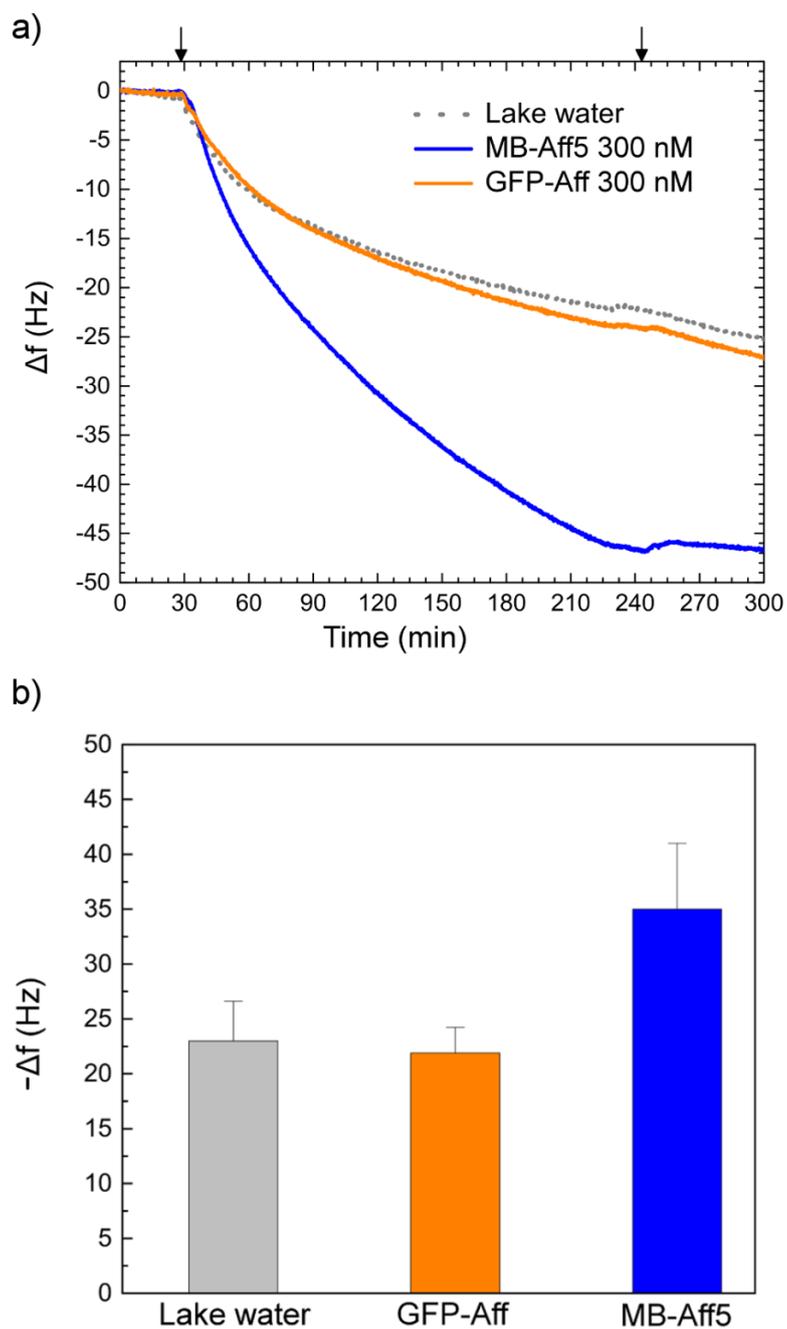
Figure 4.19: a) Real-time QCM-D and b) bar charts of shifts in the resonant frequency (third harmonic, F3) of MB:OH SAM-functionalised sensors during introduction of 300 nM MB-Aff5 in limnetic water samples. Unspiked limnetic samples (lake water is graphs) were used as blank, and 300 nM GFP-Aff in the same matrix was used as a control. It should be noted that the limnetic water samples were syringe-filtered through a 0.2 μM filter unit.

For environmental monitoring it is necessary that Affimers show high selectivity, that is, the ability to recognise their target among the interferences in a complex matrix, such as surface water samples. The selectivity of MB−Aff5 was studied using limnetic samples as the running solvent in

QCM-D measurements. Here, following filtration through 0.2 μM, the limnetic samples were spiked with MB-Aff5 (or GFP-Aff as a control) and injected to MB:OH SAM-functionalised sensors. As shown in Figure 4.19, a significant decrease in frequency was observed following exposure of the MB:OH SAM-functionalised QCM-D sensor surface to the limnetic sample spiked with MB-Aff5. The shift in frequency was 1.5 times greater than that observed following exposure of the same SAM to a blank limnetic sample (i.e., unspiked). This difference suggests that, despite the potentially interfering components in the sample, the MB−Aff5 binders were still able to effectively bind to MB. This was further supported by the QCM-D response of a limnetic sample spiked with the GFP-Aff control binders. Here, the frequency shift observed for the GFP-Aff was similar to that of the blank sample, indicating that the MB-Aff5 indeed binds to the surface-immobilised MB rather than to the interfering components of the background.

4.5.4 MB-Aff5 competition assay (QCM-D)

Competition assay formats are usually the most appropriate for small-sized targets (Section 2.2.1). The potential of MB-Aff5 binders for analyte detection in competition format was thus assessed using QCM-D. A mixture of 1:100 MB-Aff5:MB in PB 7 was injected over a mixed MB:OH SAM. A second MB:OH SAM-functionalised sensor was treated with a solution containing only MB-Aff5 in order to compare the two signals and investigate the degree of competition between surface-bound MB and free MB for MB-Aff5 binding sites. As seen in Figure 4.20, the QCM-D response from the MB-Aff5:MB mixture was 7 times lower than that of the MB-Aff5 baseline, revealing considerable interactions of MB-Aff5 with free MB which competed with that of the surface-bound MB. Notably, the injection of a solution of MB at 30 μM in the same buffer yielded no response, showing the absence of nonspecific interactions between the monolayer and free MB.
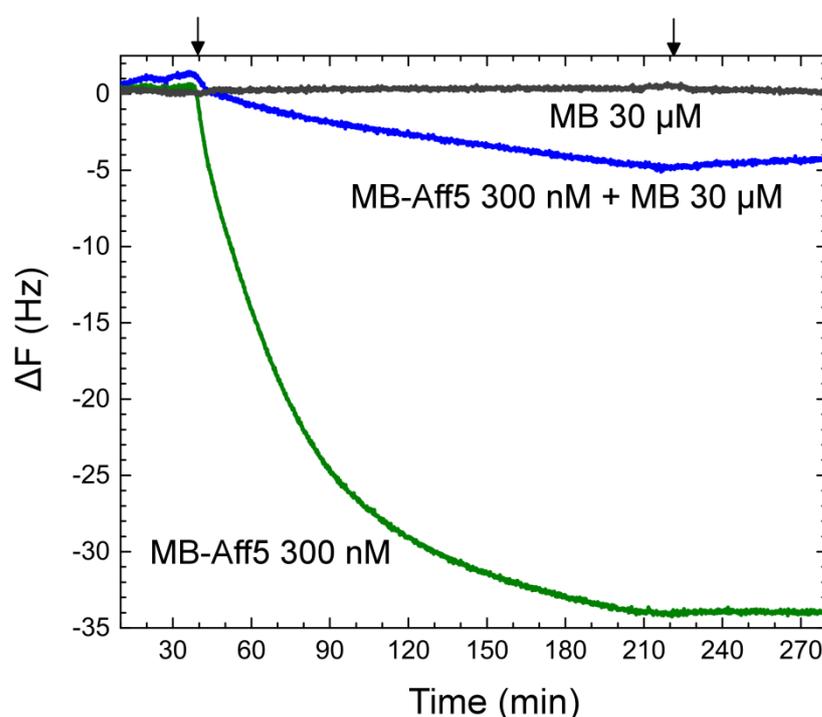
Figure 4.20: Comparison of QCM-D response (third harmonic, F3) between a MB-Aff5 solution and a 1:100 mixture of MB-Aff5 and MB injected over MB:OH SAM-functionalised sensors. As a control, the QCM-D response to a 30 μM MB solution was measured.
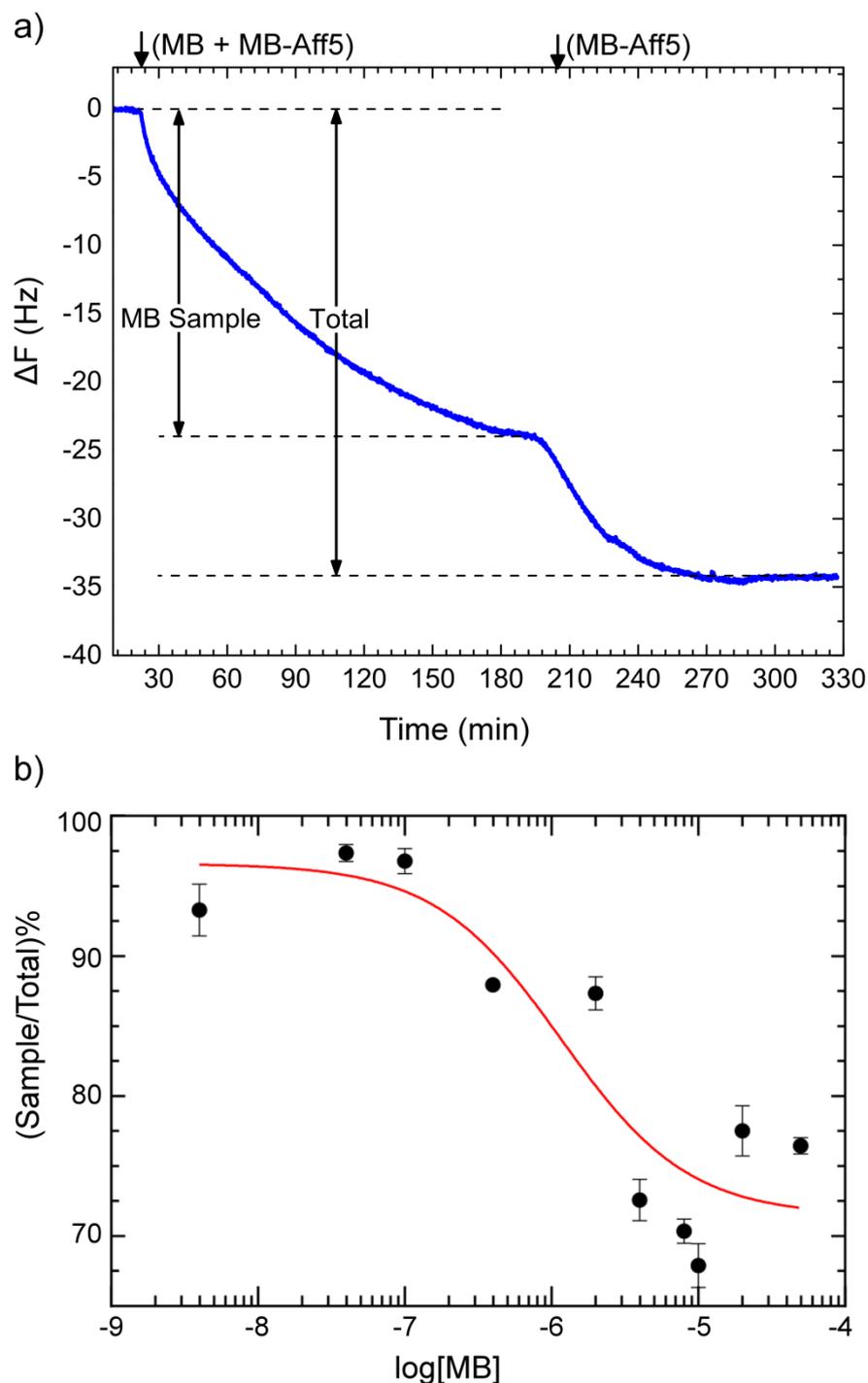
Figure 4.21: a) MB-Aff5 competition assay format showing QCM-D response (third harmonic, F3) during injection of MB-Aff5 and MB mixture, followed by injection of MB−Aff5 (400 nM) until saturation; b) Calibration curve of MB−Aff5 competition QCM-D assay. For each measurement, the first plateau (MB Sample) was normalised to the second plateau (Total) so that (sample/total)% was plotted as a function of MB concentration.

For the construction of a calibration curve, the degree of competition at different MB concentrations was measured through a two-step QCM-D experiment (Figure 4.21a). First, a pre-mixed sample of MB and MB-Aff5 was injected over a mixed 1:3 MB:OH SAM-functionalised

sensor. The sample was allowed to flow over the surface until the resonant frequency reached a plateau, at which point a solution containing only MB-Aff5 at the same concentration as in the mixture was introduced until a second plateau was reached, corresponding to a surface fully saturated with MB-Aff5. The first plateau (Sample) was then normalised to the second (Total, i.e. saturated). The process was repeated for a range of different MB concentrations in order to construct a standard curve (Figure 4.21b). Here, (Sample/Total)% was plotted as a function of MB concentration and fitted using a four parameter logistic (4PL) curve, typical for concentration-response data in competition assays (Equation 4.5):

$$Y = bottom + \frac{(top-bottom)}{(1+10^{((\log(IC_{50}-X)^{slope}})}$$ (4.5)

where, X is the competitor (MB) concentration, Y is the response, *bottom* is the response at infinite competitor concentration (lower plateau), *top* is the response in the absence of competitor (upper plateau), *slope* refers to the steepness of the curve (here, assuming one-site specific binding, the slope was set to a constant value of -1). IC_{50} (inhibitory concentration) is the concentration of competitor causing 50% inhibition of binding (i.e. 50% inhibition of MB-Aff5 binding to MB SAM due to free MB in solution) [48] [184] [185], and was found to be 1.17 μM. Finally, the detection limit (here, estimated from the lowest point of the linear range of the curve [186] was found to be 360 nM. Both the IC_{50} and the detection limit are higher than those reported in the literature regarding competition assays for detection of small molecules [48] [181] [187].

4.6 Conclusions

In this chapter, the potential of Affimers for detection of small organic molecules was evaluated using MB, a redox-active dye as a target compound. Detection of small-sized targets through immunoassays typically requires surface immobilisation. For this purpose, MB-terminated LCAT-OEGs were synthesised and used to form SAMs on the gold surfaces of sensors. The potential effects of labelling and surface immobilisation on the redox properties of MB were elucidated using CV and QCM-D, which demonstrated that MB retained its redox activity in the SAM, following the expected $2e^-$, $1H^+$ process. The immobilisation protocol was optimised by forming mixed SAMs with an appropriate dilutant (LCAT-OEG-OH), so as to reduce non-specific binding, increase order and dense packing of the monolayer and improve exposure of MB groups for Affimer binding. The mixed MB:OH SAMs were compared with pure MB SAMs using PM-IRRAS, CV and EIS, which showed that SAM dilution enabled surface immobilisation through a dense, well-ordered monolayer where the target was efficiently presented for biomolecular interactions with Affimers, and thus this immobilisation approach was selected for binding studies with MB Affimers.

The binding affinity of Aff1 and Aff5 was investigated via QCM-D measurements of MB:OH SAM-functionalised sensors. The dissociation constant, K_D, was estimated through saturation binding measurements and was found in the upper nanomolar region for both MB-Aff1 and MB-Aff5. Additionally, the K_D was estimated by studying the kinetics of the binding reaction in the QCM-D and was in the lower nanomolar region. These K_D values are comparable with those of high affinity antibodies [188] [189]. Notably, control QCM-D measurements (using either MB Affimers on OH SAMs or GFP-Affimers on MB:OH SAMs) ruled out non-specific binding. Critically, for environmental applications it is important to assess the performance of Affimers in the complexity of surface water samples; QCM-D measurements using Affimer-spiked limnetic samples revealed that MB-Aff5 showed very good selectivity for MB despite the complex matrix.

Competition formats are typically used for detection of small-sized targets in immunoassays. The potential for an Affimer-based competition assay was demonstrated using QMC-D. Here, the QCM-D response of MB-Affimer and MB mixtures was compared to that of MB-Affimer samples only, and considerable competition from solution-MB with surface-MB was observed. It is worth mentioning that the fact that the MB in solution competed with the surface-bound MB reveals that although the Affimers were selected using carboxypropyl-MB, the Affimer binding sites recognised the target, i.e. MB.

Finally, the degree of competition by different MB concentrations was measured in order to construct a calibration curve. The limit of detection (360 nM; 128 μg/L) was in the upper nanomolar region. While this is higher than the environmentally relevant concentrations (ng/L to μg/L) detected by antibody-based ELISAs for small molecules [48] [181] it should be noted that sensitivity in the QCM-D is limited at low concentrations [145] and that the presented assay is preliminary and unoptimised, aiming to demonstrate the potential of Affimers for competition assays. For the development of an Affimer-based assay or biosensor, other techniques and transduction methods should be considered, such as ELISA, SPR, reflectometric, impedimetric, etc., that are more amenable to miniaturisation. Moreover, further study would be required to improve performance, looking, for instance, at altering the length of the LCAT-OEG linkers or ratio of the LCAT-OEG-MB and LCAT-OEG-OH dilutant, working out the optimal concentrations of Affimer and surface-immobilised target or investigating sample pre-concentration approaches.

Although preliminary and unoptimised, these results from QCM-D measurements clearly demonstrate that the *in vitro* selected, small and robust Affimers can bind to small-sized, non-immunogenic targets as strongly as antibodies (Section 4.5.2) and with high selectivity (Section 4.5.3). Using MB as a proof-of-principle target, these findings showcase the high potential of Affimer technology to contribute in faster and cost-efficient assay development for applications across the breadth of diagnostics and environmental monitoring.

Chapter 5

Investigating Affimer Interactions with Diclofenac

5.1 Overview

In Chapter 4, the ability of Affimers to bind to small, organic molecules was demonstrated using methylene blue as a model target compound. This chapter is focused on Affimers selected against an emerging environmental contaminant, diclofenac (DCF), and their potential as bioreceptors in Affimer-based assays.

Interactions between DCF and the DCF-Affimers were studied initially using QCM-D. Here, immobilisation of the DCF target on gold-coated, QCM-D sensors was achieved via a SAM of DCF-terminated LCAT-OEG (LCAT-OEG-DCF), similar to the LCAT-OEG-MB SAMs used in Chapter 4. Prior to QCM-D measurements, the LCAT-OEG-DCF monolayers (also referred to as DCF SAMs) were characterised by EIS and PM-IRRAS.

Affimer binding was also assessed using an ELISA protocol developed by BSTG. Here, biotinylated-DCF (Appendix A) was immobilised on streptavidin-coated surfaces and the binding of DCF-Affimers was detected using an anti-His tag antibody conjugated with horseradish peroxidase (HRP). This ELISA was used to estimate the affinity constant, K_D, of DCF-Affimers through saturation binding measurements. Finally, the ELISA protocol was adapted in order to evaluate the potential of DCF-Affimers for use in competition assay formats.

5.2 Characterisation of LCAT-OEG-DCF SAMs (EIS, PM-IRRAS)

5.2.1 Materials

LCAT-OEG-DCF was synthesised by PhD student Jacob Hauser, School of Chemistry, University of Leeds, by adapting the solid-phase synthesis protocol described in Murray et al. [119]. An overview of the synthesis of LCAT-OEG-DCF is provided below (Figure 5.1). The product was stored in ethanol at 1 mM concentration (-18 $^{\circ}$C). Diclofenac sodium and 1-dodecanethiol 98% were purchased from Sigma-Aldrich (Gillingham, UK). 29-mercapto-3,6,9,12,15,18-hexaoxanonacosan-1-ol, referred to here as LCAT-OEG-OH (Figure 4.1d), was purchased from Prochimia Surfaces (Gdansk, Poland). All buffers and solutions were prepared using ultrapure water (18.2 MΩ·cm, Milli-Q systems, Millipore) and the pH was measured using a pH meter (Mettler-Toledo, Switzerland).
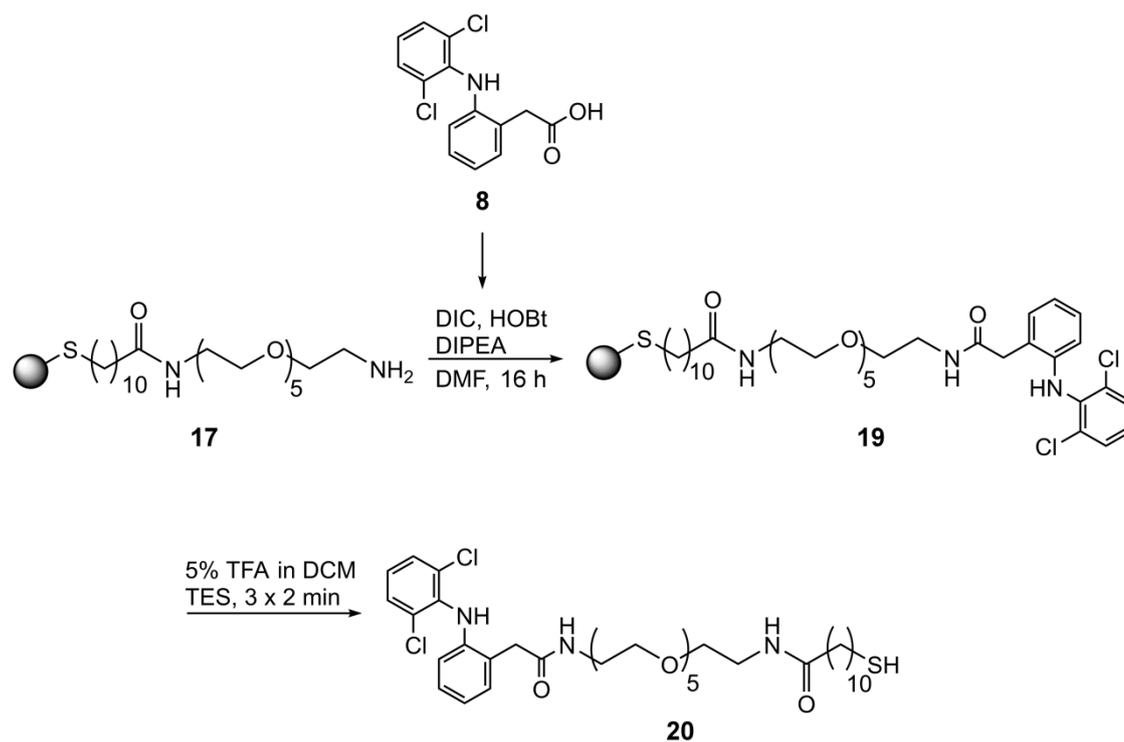
Figure 5.1: Schematic of the solid-phase synthesis of the LCAT-OEG-DCF SAM (20) used to produce a SAM. The synthetic protocol is an adaptation from Murray et al. [119] for LCAT-OEG-MB synthesis (Section 4.2.1 and Appendix B).

5.2.2 Target immobilisation on Au-coated substrates

Planar gold surfaces, fabricated by electron beam evaporation of 25 nm Ti/100 nm Au onto a cleaned Si wafer (IDB technologies, Wiltshire, UK), were functionalised with single-species or mixed LCAT-OEG monolayers. Prior to functionalisation, the wafers were cleaved to approximately 10 by 20 mm and cleaned by immersion in piranha solution (H_2SO_4:H_2O_2 70:30) for 10 min, followed by sonication in water, then ethanol for 10 min each and finally, dried with N_2 gas. (Note: Extreme caution must be taken when handling piranha solution, since it is strongly acidic and a strong oxidiser).

Pure LCAT-OEG SAMs were formed by immersion in a 0.1 mM ethanolic solution of the corresponding compound for 48 hours. Mixed DCF:OH SAMs were prepared using a mixture of 0.1 mM LCAT-OEG-DCF (20) and 0.1 mM LCAT-OEG-OH in ethanol in either a 1:1 or 1:2 ratio (v/v). Pure LCAT-OEG-OH (Figure 4.1d) and 1-dodecanethiol (Figure 4.1e) SAMs (referred to as OH SAM and C_{12} SAM respectively) were formed following the same approach and were used as reference in PM-IRRAS. After incubation, the functionalised substrates were rinsed gently with ethanol and dried with N_2 gas.

5.2.3 Electrochemical impedance spectroscopy

The SAM-functionalised, gold-coated substrates were used as the working electrode in a three-electrode electrochemical cell that included a Pt counter electrode and a Ag/AgCl (saturated KCl) reference electrode. Contact to the working electrode was achieved using a spring loaded pin connector. A Viton O-ring defined the surface area exposed to the electrolyte which was equal to 9.1 mm^2. EIS measurements were performed using a Bio Logic SP-300 potentiostat (Berkshire, UK). All measurements were performed in 100 mM sodium phosphate buffer pH 7 (PB 7). The impedance and phase angle of each SAM-modified electrode were measured over the frequency range of 200 kHz to 0.1 Hz at a 10 mV DC potential *vs* reference electrode Ag/AgCl and an AC potential of 10 mV.

5.2.4 Polarisation modulated - infrared reflection absorption spectroscopy

For PM-IRRAS measurements, Au-coated Si wafers were cleaved to 20 by 30 mm and functionalised with SAMs analogously to Section 4.2.2. Infrared spectra of the LCAT-OEG SAMs assembled on the gold surfaces were acquired using a Bruker Vertex70 spectrometer coupled with

a PMA50 polarisation modulation unit (Bruker UK Ltd, Coventry, UK). The incident angle was set at 80° with a 4 cm^{-1} spectral resolution, while the PEM controller operated at 1000 cm^{-1}. Average measurement time was 15 min, corresponding to a total of 1000 scans. C$_{12}$ SAMs were prepared using the same immobilisation approach as for LCAT-OEG SAMs and were used as a reference SAM.

5.2.5 Results

The effect of diluting the LCAT-OEG-DCF with LCAT-OEG-OH to form mixed SAMs was investigated through EIS, by comparing the impedance and phase angle of a pure DCF SAM and that of a mixed DCF:OH SAM (1:2 ratio). As seen in the Bode plots of Figure 5.2, the slope of log|Z| vs log(frequency) at low frequencies is close to -1 for each SAM (DCF: -0.905, R^2=0.999; DCF:OH: -0.925, R^2=0.999), suggesting that both SAMs are well-packed and approach ideal capacitor behaviour [174]. At 0.1 Hz, the phase angle of the DCF SAM is -68.5°; however, the phase angle of the DCF:OH SAM is considerably lower, at -81.8°, indicating that the mixed SAM forms more dense and insulating monolayers [126]. This observation suggests that dilution of the functionalised component of the SAM improves the packing of the monolayer.
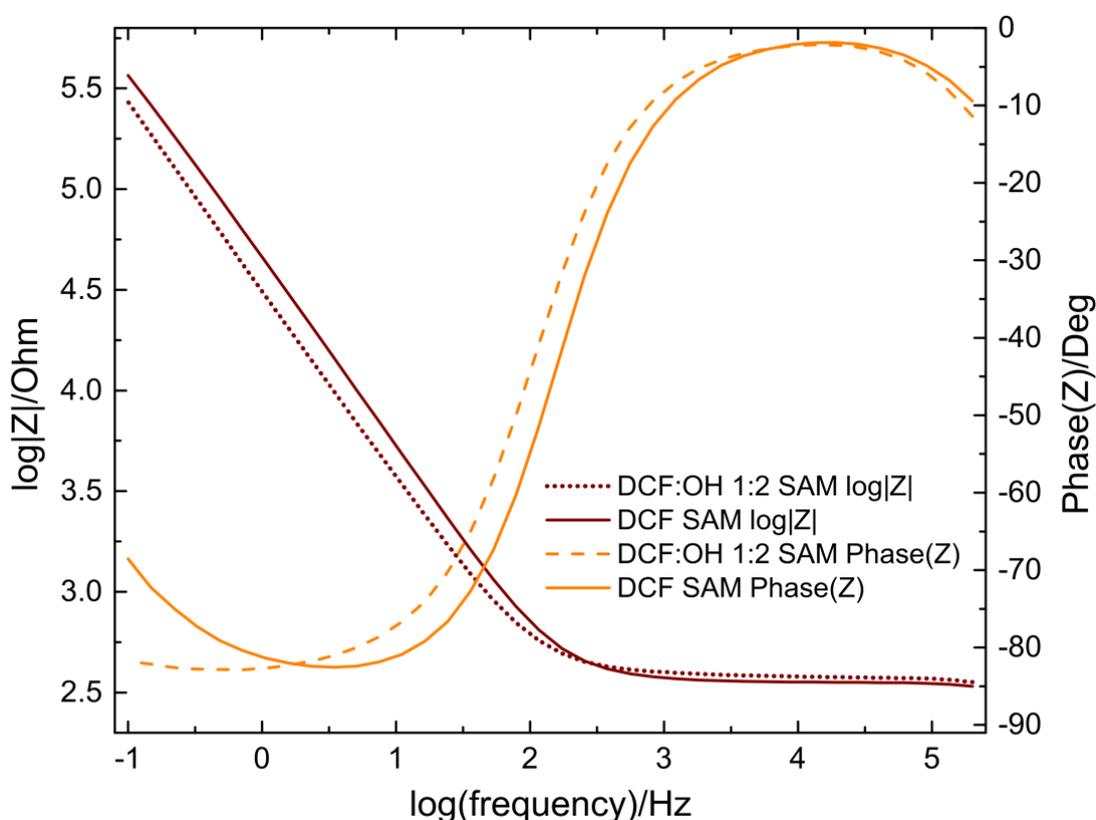
Figure 5.2: Bode impedance of DCF and mixed DCF:OH 1:2 SAMs in PB 7

The effect of diluting the DCF-SAM component on the conformation of the monolayer was also investigated by PM-IRRAS. Here, the pure DCF SAM was compared with mixed DCF:OH SAMs prepared using 1:1 and 1:2 ratios. A pure OH SAM and a C_{12} SAM were also measured for reference. As seen in Figure 5.3a, the C_{12} SAM showed sharp and intense IR absorption peaks at 2919 cm^{-1}, 2850 cm^{-1}, 2963 cm^{-1} and CH$_3$ 2877 cm^{-1}. These are attributed to the CH$_3$ and CH$_2$ symmetric (v_s) and asymmetric stretch (v_a) bands and correspond to a densely-packed, highly

crystalline alkanethiol SAM with all-trans alkyl chains and very little gauche defects (v_a CH$_2$ 2917-2919 cm^{-1} , v_s CH$_2$ 2851 cm^{-1}, v_a CH$_3$ 2963 cm^{-1}, v_s CH$_3$ 2877 cm^{-1}) [127] [175] [176]. The v_a CH$_2$ stretch in particular, is an indicator of the crystallinity of the molecular film [175-178]. This characteristic absorption peak (at 2919 cm^{-1}) was also observed for all LCAT-OEG SAMs, indicating the formation of a well-packed, all trans LCAT phase under the OEG layer. This is in agreement with the high insulating properties of the DCF and DCF:OH SAMs, shown by EIS (Figure 6.2).
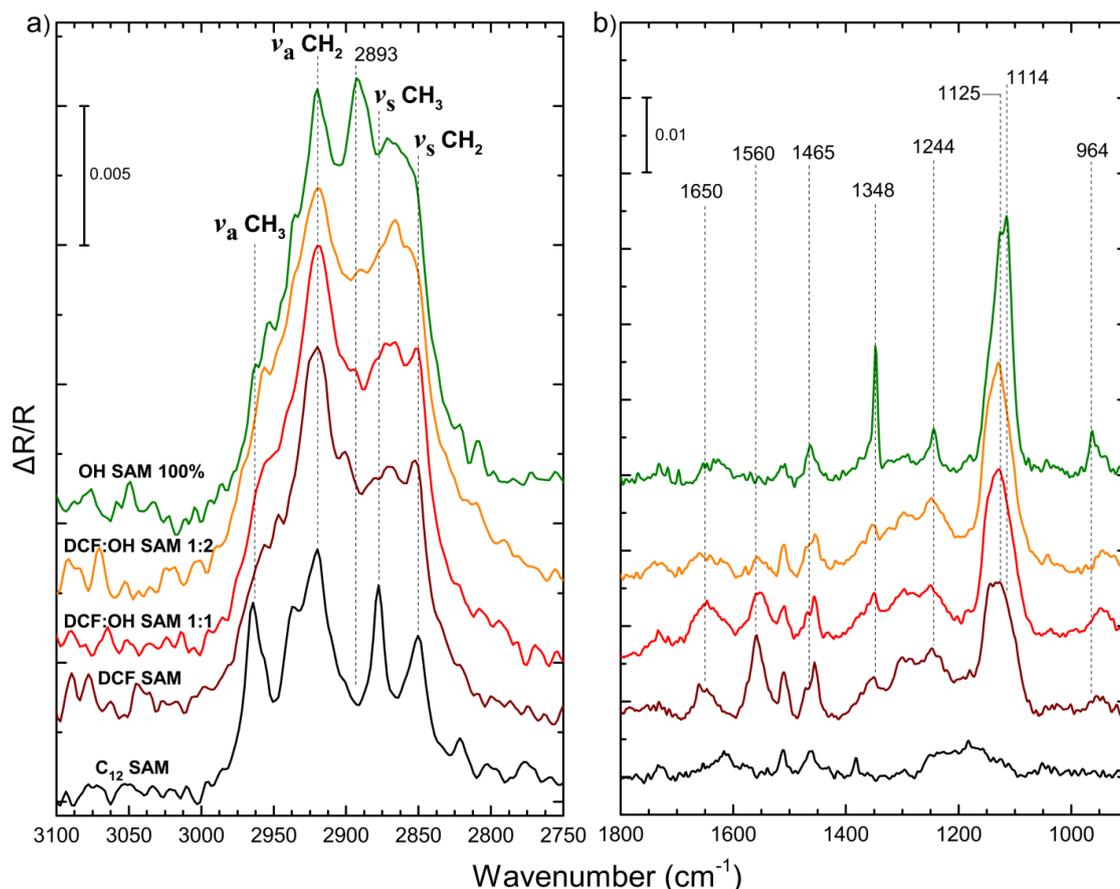
Figure 5.3: PM-IRRAS spectra of LCAT-OEG SAMs (OH SAM, DCF-SAM, DCF:OH 1:1 SAM, DCF:OH 1:2 SAM) and alkanethiol SAMs (C$_{12}$ SAM) on gold, showing a) the CH stretch region (2750-3100 cm^{-1}) and b) the fingerprint region (900-1800 cm^{-1}).). The spectra have been presented with the y-axis expanded, to make it easier to see the relevant peaks.

The fingerprint region between 900-1800 cm^{-1} (Figure 5.3b) contains the IR absorption peaks associated with the conformational characteristics of the OEG component of the SAM. Absorption peaks at 1348, 1244, 1114 and 964 cm^{-1} are distinctive and characteristic of a helical conformation of the OEG chains [176], and were observed as sharp, well-defined peaks for the OH SAM. The peak at 1114 cm^{-1}, characteristic of asymmetric C-O-C stretching of helical OEGs, was particularly intense and sharp for the OH SAM, revealing the high degree of crystallinity of the OEG layer, indicating that the OEG helices are orientated almost parallel to the surface normal [178] [127].

The smaller shoulder at 1125 cm^{-1} corresponds to the asymmetric C-O-C stretching of a less-ordered, amorphous-like OEG layer [178] [190]. The helical OEG peak at 1114 cm^{-1} was also observed for the DCF and mixed DCF:OH SAMs, but, as the amount of DCF in the SAM increased, the intensity of this peak decreased, while the 1125 cm^{-1} peak of amorphous OEG chains became increasingly dominant. The contrast between the helical and highly crystalline character of the OEG layer of pure OH SAM and the amorphous nature of the DCF-terminated SAMs was further supported by the presence of a strong and sharp IR absorption peak at 2893 cm^{-1} for the OH SAM (attributed to the CH$_2$ symmetric stretch of helical OEG chains) and its absence in the IR spectra of all other SAMs [127]. These observations indicate that, although all DCF-terminated LCAT-OEG SAMs (pure or mixed) contain regions of ordered, helical OEG layers, they are primarily dominated by disordered, amorphous OEG regions, and that this behaviour increases with the amount of DCF terminal groups in the SAM. The amorphousness of the OEG regions is attributed to steric hindrance between neighbouring DCF terminal groups which push the adjacent chains apart, preventing close packing and disrupting the helical conformation of the OEG chains.

The amorphous conformation of the OEG layer of the DCF-terminated SAMs was further evidenced by the reduced intensity of the 1348 cm^{-1} bands corresponding to the CH$_2$ wagging mode of a helical OEG, as well as by the absence of the 964 cm^{-1} peak of the helical, CH$_2$ rocking mode [127] [176]. In addition, the CH$_2$ scissoring mode of helical OEG at 1465 cm^{-1} [178] was present in the OH SAM, but for all SAMs containing a DCF-terminated molecule, the IR absorption peak of this vibrational mode appeared at slightly lower frequencies, around 1457 cm^{-1}, which corresponds to less ordered OEG layers [178] [191].

Finally, it is worth noting the amide II band (C-N-H bending mode) at 1560 cm^{-1}, which is present in the spectra of all DCF-terminated SAMs, and more intensely in those of the pure DCF SAM, whilst is absent in the spectrum of OH SAM. This absorption peak is the combination of the N-H in plane bending and the C-N stretching vibrational modes [192]. The presence of this peak in the spectra of the DCF-terminated SAMs can be attributed to two sources: (i) the amide bond connecting the LCAT with the OEG component (no amide II band is observed for the LCAT-OEG-OH SAM as here the LCAT is not connected to the OEG component through an amide bond) and (ii) the secondary amine of diclofenac. Finally, the amide I mode (C=O stretch at 1650 cm^{-1}) associated with the carboxylic acid group of DCF is only observed in the DCF-terminated SAMs as a short and broad peak [176] [178] [179]. These observations show that the LCAT-OEG-DCF molecules successfully form SAMs on the gold surfaces, which is important for studying DCF-Affimer interactions (here, using QCM-D), and the presence of the amide I and amide II mode bands in the IR spectra of the DCF-terminated SAMs demonstrates that the target has been successfully immobilised on the surface either as pure DCF SAMs or as mixed DCF:OH SAMs.

These findings show that a pure DCF SAM, although consisting of a densely packed LCAT region, exhibits a high degree of disorder in the OEG component. Critically, this disorder can be reduced by dilution of the LCAT-OEG-DCF in the SAM with LCAT-OEG-OH, which leads to an increase in the amount of helical OEG the SAM can accommodate, effectively improving the crystallinity and packing of the entire monolayer.

5.3 QCM-D Monitoring of DCF-Affimer Interactions with Surface-immobilised DCF

5.3.1 Materials and methods

Gold coated QCM-D sensors (QSX 301, Biolin Scientific, Stockholm, Sweden) were cleaned by sonication in a 2% Hellmanex III solution (Hellma Analytics, Müllheim, Germany) and thorough rinsing in ultrapure water, followed by UV-ozone treatment (30 min) and immersion in EtOH (30 min). Cleaned sensors were functionalised with LCAT-OEG SAMs (mixed DCF:OH 1:2 ratio or OH SAM as control) by immersion in 0.1 mM ethanolic solutions for 48 hours.

Following fuctionalisation, the sensors were rinsed in EtOH, dried with N_2 gas and loaded into the QCM-D flow modules (QSense E4, QFM 401, Biolin Scientific, Stockholm, Sweden). The surface area exposed to solution was equal to 0.95 cm^2 as defined by a Viton O-ring. Resonant frequency (F) and dissipation (D) were monitored while ultrapure water was passed over the sensors using a peristaltic pump at a flow rate of 20 μL/min, until a steady baseline was achieved (defined by a frequency shift of less than 1 Hz over 10 minutes), followed by injection of PBST to establish a running buffer baseline. Next, DCF-Affimer (DCF-Aff) solutions in PBST were introduced at a flow rate of 20 μL/min until the frequency saturated. Affimers raised against green fluorescent protein (GFP-Aff) were used as non-specific binding controls. Finally, the sensors were washed with PBST. PBST was prepared by adding 0.1% Tween-20 (Sigma-Aldrich, Gillingham, UK) in phosphate buffered saline (PBS: 137 mM NaCl; 10 mM phosphate; 2.7 mM KCl; pH 7.4).

5.3.2 Results

Figure 5.4 shows real-time QCM-D data during the exposure of a DCF:OH 1:2 SAM-functionalised sensor to a 5 μg/mL DCF-Aff solution (corresponding to a concentration of 400 nM) in PBST. The interaction of DCF-Aff with DCF caused a sharp decrease in the resonant frequency of the quartz sensor, owing to the increase in the mass deposited on the surface (the third harmonic (F3) is shown here). The frequency shift due to DCF-Aff binding was −11.61 Hz, which, according to the Sauerbrey model (Equation 3.14, Section 3.4), corresponds to an estimated deposited mass of 60.85 ng/cm^2 (for a 5 MHz crystal with C = -17.7 ng/Hz·cm^2). This corresponds to a surface coverage of 3.3×10^{12} molecules/cm^2 for a 12.4 kDa Affimer (Equation 3.16, Section 3.4). Notably, as DCF-Aff was introduced to the sensor, a brief increase in dissipation was observed ($\sim 0.8 \times 10^{-6}$); however, it gradually returned to baseline values. This initial increase in dissipation suggests that in the beginning of the interaction with DCF, the bound Affimers formed a disordered and viscoelastic molecular film above the monolayer. Subsequently, as the deposited mass continued to increase, the Affimers became more densely packed and formed a rigid layer above the DCF:OH SAM; thus the dissipation dropped back to baseline values ($\sim 0.0 \times 10^{-6}$).
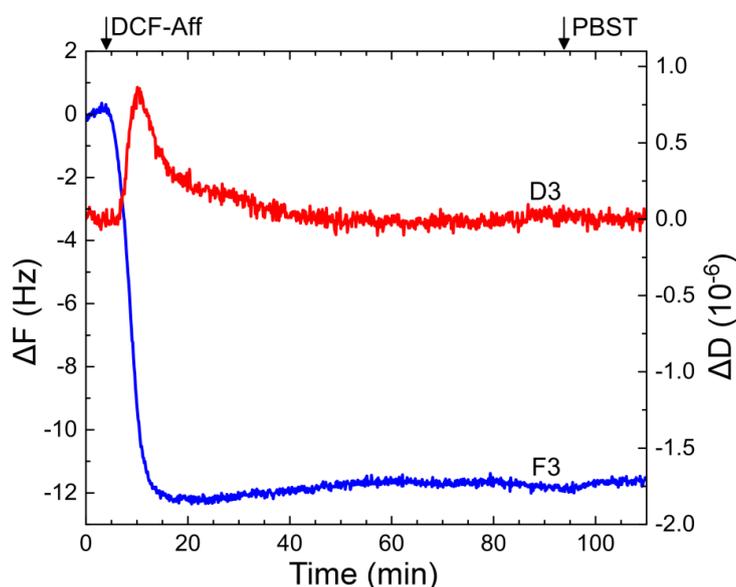
Figure 5.4: Real-time QCM-D showing changes in the resonant frequency (third harmonic, F3, blue) and dissipation (D3, red) as a function of time. Here, QCM-D sensors were functionalised with mixed DCF:OH 1:2 SAM and challenged with 5 μg/mL DCF−Aff (400 nM) in PBST.

As a control, DCF-OH 1:2 SAM-functionalised sensors were challenged with GFP-Aff (5 μg/mL in PBST), which would not be expected to bind to DCF. As shown in Figure 5.5a, the shifts in frequency and dissipation were insignificant compared to those observed between DCF-Aff and DCF (Figure 5.4), consistent with the lack of binding of GFP-Aff to DCF. Non-specific binding

was also investigated by challenging a 100% OH SAM-functionalised QCM-D sensor surface (i.e. no DCF) with 5 μg/mL DCF−Aff solution (Figure 5.5b). Again, both frequency and dissipation shifts were insignificant, indicating an absence of substantial non-specific binding between DCF-Aff and the LCAT-OEG SAM-functionalised QCM-D sensor surface, when DCF is not present.
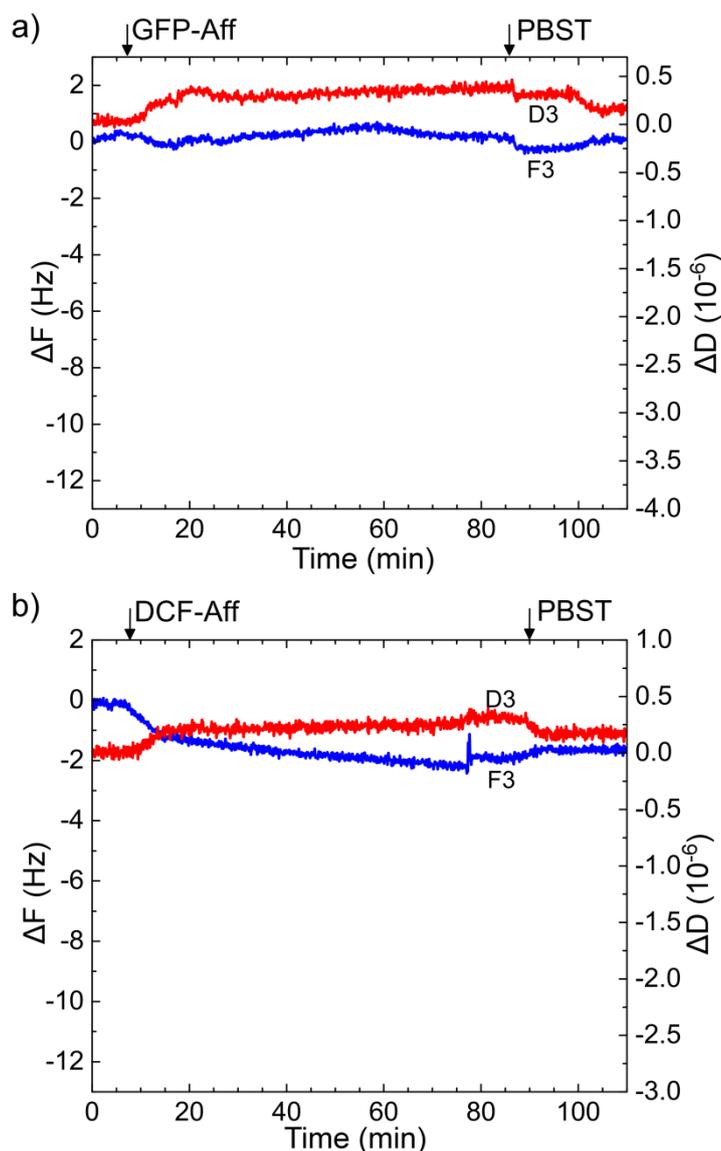
Figure 5.5: Real-time QCM-D showing changes in the resonant frequency (third harmonic, F3, blue) and dissipation (D3, red) as a function of time. QCM-D sensors were functionalised with a) mixed DCF:OH 1:2 SAM and challenged with 5 μg/mL control GFP−Aff in PBST or (b) 100% OH SAM and challenged with 5 μg/mL DCF−Aff in PBST.

The kinetics of the binding reaction were studied by injecting a DCF-Aff solution (5 μg/mL) over a DCF:OH 1:2 SAM at a slower flow rate of 10 μL/min (Figure 5.6). The rates of association (k_{on}) and dissociation (k_{off}) were estimated using Equations 4.3 and 4.4 and were found to be 1.04×10^5 M^{-1} min^{-1} and 7.3×10^{-3} min^{-1}, respectively, whilst B_{max} was 11.78 Hz. The dissociation constant,

K_D, calculated using the estimated association and dissociation rates ($K_D = k_{off}/k_{on}$) was found to be 73 nM ($R^2=0.985$). This is comparable with typical values for high affinity antibodies against small molecules [48] [181] [193].
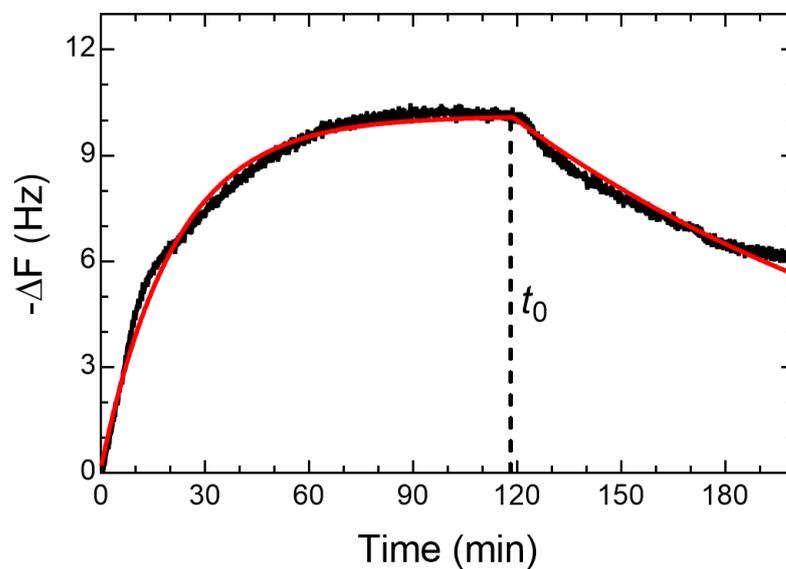
Figure 5.6: DCF-Aff binding kinetics: real-time QCM-D showing frequency shift (black line: third harmonic, F3) of DCF:OH 1:2 SAM-functionalised sensors during injection of 5 μg/mL (400 nM) DCF−Aff in PBST at 10 μL/min flow rate. Red line shows association−dissociation curve fit to the data and t_0 indicates time at which dissociation was initiated.

5.4 DCF-Affimer ELISA

5.4.1 Materials and methods

An ELISA protocol developed by the BSTG [194] was adapted in order to further characterise the binding reaction of DCF-Affimers to DCF and investigate the potential of diclofenac detection by an Affimer-based competition ELISA. ELISAs were performed in polystyrene 96-well ELISA microtiter plates (Maxisorp Nunc-Immuno Plate, ThermoFisher Scientific, Loughborough, UK) coated with streptavidin (Invitrogen, Paisley, UK) in PBS (137 mM NaCl; 10 mM phosphate; 2.7 mM KCl; pH 7.4). Triplicates were used for each sample and three controls were carried out; a negative control (no immobilised target, i.e. no DCF), an Affimer blank (no DCF-Aff) and a specificity control (GFP-Aff). PBST (0.1% Tween-20 in PBS) was used as a washing buffer, whilst 10x casein blocking buffer (Sigma-Aldrich, Gillingham, UK) was diluted to 2x in PBST and used as running buffer or blocking reagent. Anti-6x His Tag® antibody[9] conjugated with horseradish peroxidase (HRP) was purchased from antibodies-online (Aachen, Germany) and 3,3',5,5'-tetramethylbenzidine (TMB) with hydrogen peroxide (H_2O_2) was used as the substrate for colour development (Sigma-Aldrich). The intensity of the blue coloured product was measured using a VersaMax ELISA Microplate Reader spectrophotometer (Molecular Devices, Berkshire, UK).

First, 50 μL of 5 μg/mL of streptavidin were added to each well of the ELISA plate and incubated overnight at 4 °C. The following day, 2x blocking buffer was added to the streptavidin-coated wells (200 μL per well), incubated overnight at 37 °C and then washed with 300 μL per well of PBST. Biotinylated diclofenac (Appendix A) diluted in 2x blocking buffer to 5 (or 10) μg/mL, was next aliquoted at 50 μL per well onto the streptavidin-coated plate and incubated for 1 hour at room temperature (50 μL per well of 2x blocking buffer were added to the negative control wells). After 1 hour, the plate wells were washed 3 times with 300 μL per well of PBST. Then, 5 (or 10) μg/mL of DCF-Aff in 2x blocking buffer (or GFP-Aff to the specificity control wells) were added to each well (50 μL/well), incubated for 1 hour (50 μL/well of 2x blocking buffer were added to the blank control wells) and were washed 3 times with 300 μL of PBST per well. Subsequently, HRP-conjugated anti-6x His tag antibody (1 μg/mL in 2x blocking buffer) was added (50 μL/well) and incubated for 1 hour. Following incubation, the plate wells were washed 5 times with 300 μL per well of PBST. TMB and H_2O_2 were mixed in equal volumes and 50 μL added to each well and left

---

[9] Engineered proteins, including Affimers, are often designed to carry a string of histidine residues to their N- or C-terminus (here, a 6xHis string), which is used as a tag for detection of purification purposes [195]. Here, an anti-6xHis tag antibody is used to detect 6xHis-tagged Affimers.

to react for 5 minutes. Finally, the intensity of absorbance of the blue colour reaction product was measured at 620 nm using a microplate reader.

For competition ELISAs, solutions of different concentrations of DCF (not biotinylated) in PBST were prepared from a 10 mM stock solution of diclofenac sodium (Sigma-Aldrich, Gillingham, UK) in methanol (final concentration of methanol did not exceed 0.4% v/v in all mixtures of DCF with DCF-Aff). The DCF solutions were mixed with DCF-Aff (0.5 μg/mL in PBST) and incubated for 30 min. Then, 50 μL per well of each Affimer:DCF mixture were added into the plate wells (previously coated with biotinylated DCF) and incubated for 1 hour, before addition of HRP-labelled antibody.

5.4.2 Results

The concentrations of DCF and DCF-Aff were varied in order to identify the optimum amount of target (biotinylated DCF) and receptor (DCF-Aff) which yielded the strongest absorbance signal. Figure 5.7 shows the average absorbance intensity of the TMB reaction product in each sample (N=6, i.e. two ELISA experiments of three replicates per sample) 5 min after substrate addition. Although no significant differences between the absorbance readings for the different concentrations were found, the combination with highest signal intensity and minimum amounts of reagents was 5 μg/mL of DCF-Aff with 5 μg/mL biotinylated DCF and so this combination was selected for all subsequent ELISA experiments.
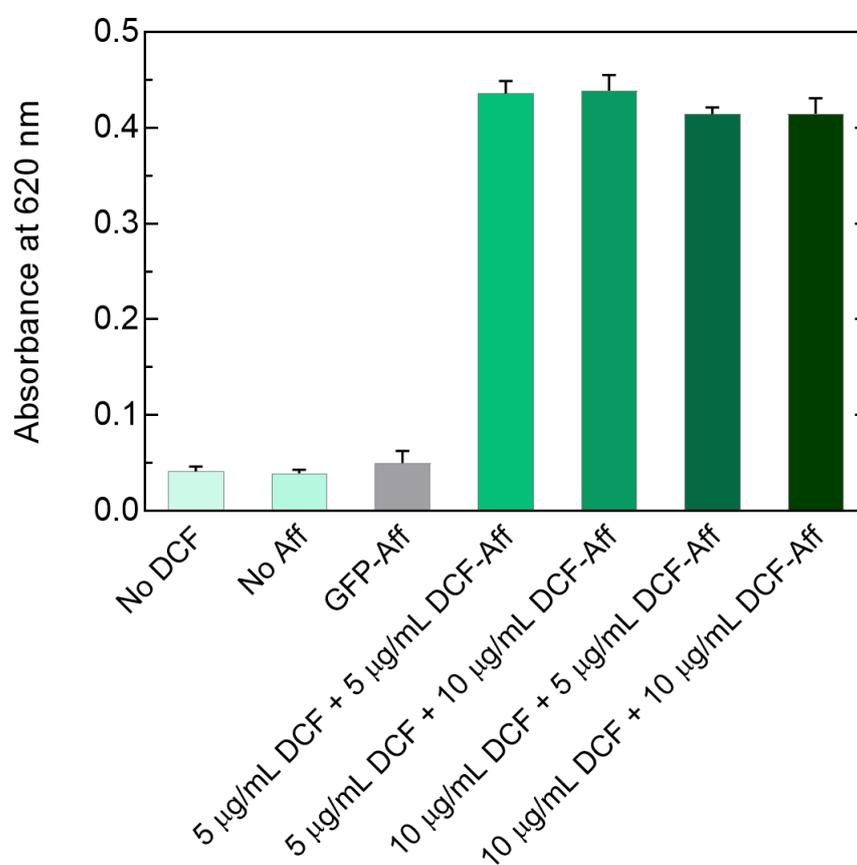
Figure 5.7: Results of DCF-Aff ELISA showing the TMB product absorbance measured by a microplate reader at 620 nm 5 min after substrate addition. The binding of DCF-Aff to surface-immobilised diclofenac was detected using an HRP-conjugated anti-His tag antibody. A negative control ('No DCF'), a blank ('No Aff') and a non-DCF Affimer ('GFP-Aff') were used as controls to investigate the degree of non-specific interactions. Four different combinations of concentrations of DCF-Aff and immobilised DCF were investigated in order to identify conditions that yielded the strongest signal.

The degree of non-specific binding was assessed using three controls: a negative control (i.e. no biotinylated DCF on the surface of the wells), a blank (no addition of DCF-Aff on DCF-coated plate wells) and a specificity control (addition of GFP-Aff on DCF-coated plate wells). As seen in

Figure 5.7, all controls yielded very weak signals (~0.04 absorbance units) compared to the DCF-Aff samples (~0.4). These results are consistent with the specificity of DCF-Aff binding to surface-immobilised DCF using QCM-D.

Next, the affinity of DCF-Aff was estimated through saturation binding measurements using the ELISA format described above, by adding increasing concentrations of DCF-Aff onto DCF-coated plate wells. As seen in Figure 5.8a, the colour intensity of the TMB reaction product increased with increasing DCF-Aff concentration, which ranged from 0.005 to 10 μg/mL (0.4 to 800 nM for a 12.4 KDa Affimer). The absorbance intensity was plotted as a function of DCF-Aff concentration (Figure 5.8b) and the data points were fitted to a Langmuir isotherm.

$$Y = \frac{B_{max} \cdot C}{K_D + C} \tag{5.1}$$

Here, B_{max} is the maximum response, C is the Affimer concentration (nM) and K_D is the dissociation constant [180] [183].

The calculated K_D was 37.87 nM ($R^2 = 0.978$), while the B_{max} was found to be 0.56 absorbance units. Here, the fitting of the Langmuir isotherm is very good and the estimated K_D reveals very high binding affinity. The Langmuir model, however, assumes one-site specific binding. The Affimer scaffold holds two randomised peptide loops for target binding, thus, to investigate the possibility of dimeric (cooperative) binding, the Hill (or Hill-Langmuir) model (Equation 5.2) was also used to determine the number of binding sites, so as to ensure the fitness of the Langmuir isotherm for analysing the saturation binding curve of DCF-Aff to DCF.

$$Y = \frac{B_{max} \cdot C^h}{K_D^h + C^h} \tag{5.2}$$

Here, h refers to the Hill slope or Hill coefficient. Provided that the binding reaction has reached equilibrium, an estimated Hill slope value of 1 suggests monomeric (one-site) binding (whilst h≈2 suggests dimeric binding) [180] [183]. Here, as seen in Figure 5.8b, the Hill fit to the DCF-Aff ELISA data was very good ($R^2 = 0.982$), displaying a smooth, hyperbolic curve, while the Hill slope was found to be 1.25. The proximity of the estimated Hill slope to 1 suggests that the DCF-Affimers exhibit one-site binding to DCF. The K_D was found to be 34.56 nM, which is very close to that estimated by the Langmuir equation. Consequently, the simpler model of the Langmuir isotherm can be indeed used for describing and analysing the saturation binding curve of DCF-Aff

to DCF. The estimate K_D is in the same range as that for high affinity antibodies [188] [189], which once again demonstrates that Affimers can bind very strongly to a small molecule like diclofenac.
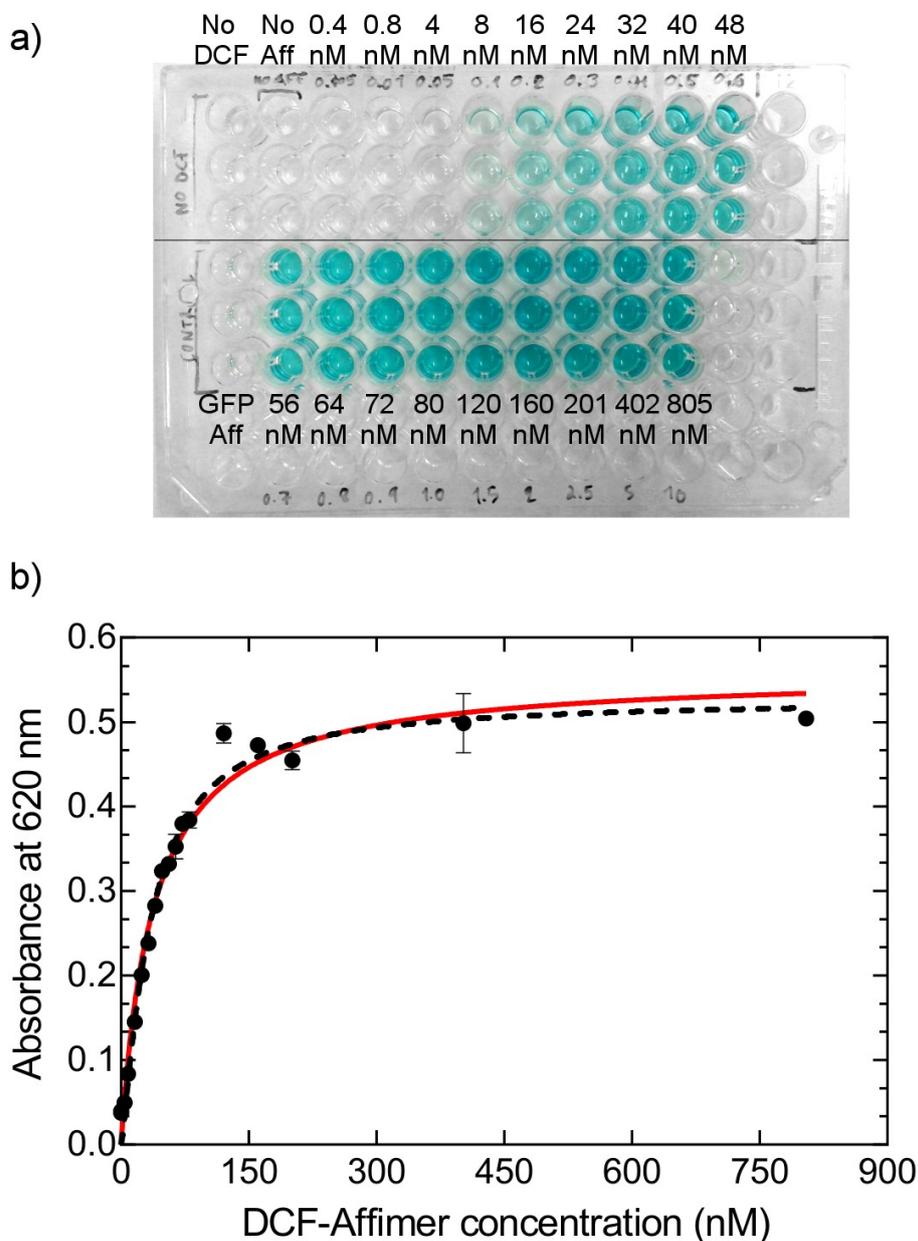
Figure 5.8: Saturation binding DCF-Aff ELISA: a) ELISA plate showing the TMB product (each triplicate of wells corresponds to different concentration of DCF-Aff on DCF-coated wells, including a blank, negative and specificity control); b) measured absorbance at 620 nm plotted as a function of DCF-Aff concentration (red line: Langmuir fitting, dotted line: Hill fitting).

Having characterised the affinity of DCF Affimers, the ELISA protocol was adapted to a competition format. In a competition assay, free-DCF competes with the immobilised DCF (surface-DCF) for Affimer binding. The number of Affimers bound to surface-DCF thus decreases with increasing concentration of free-DCF. Following washing, only those Affimers bound to

surface-DCF remain in the plate wells to be detected by the HRP-conjugated antibody. Consequently, the absorbance signal reduces as the concentration of free-DCF is increased.
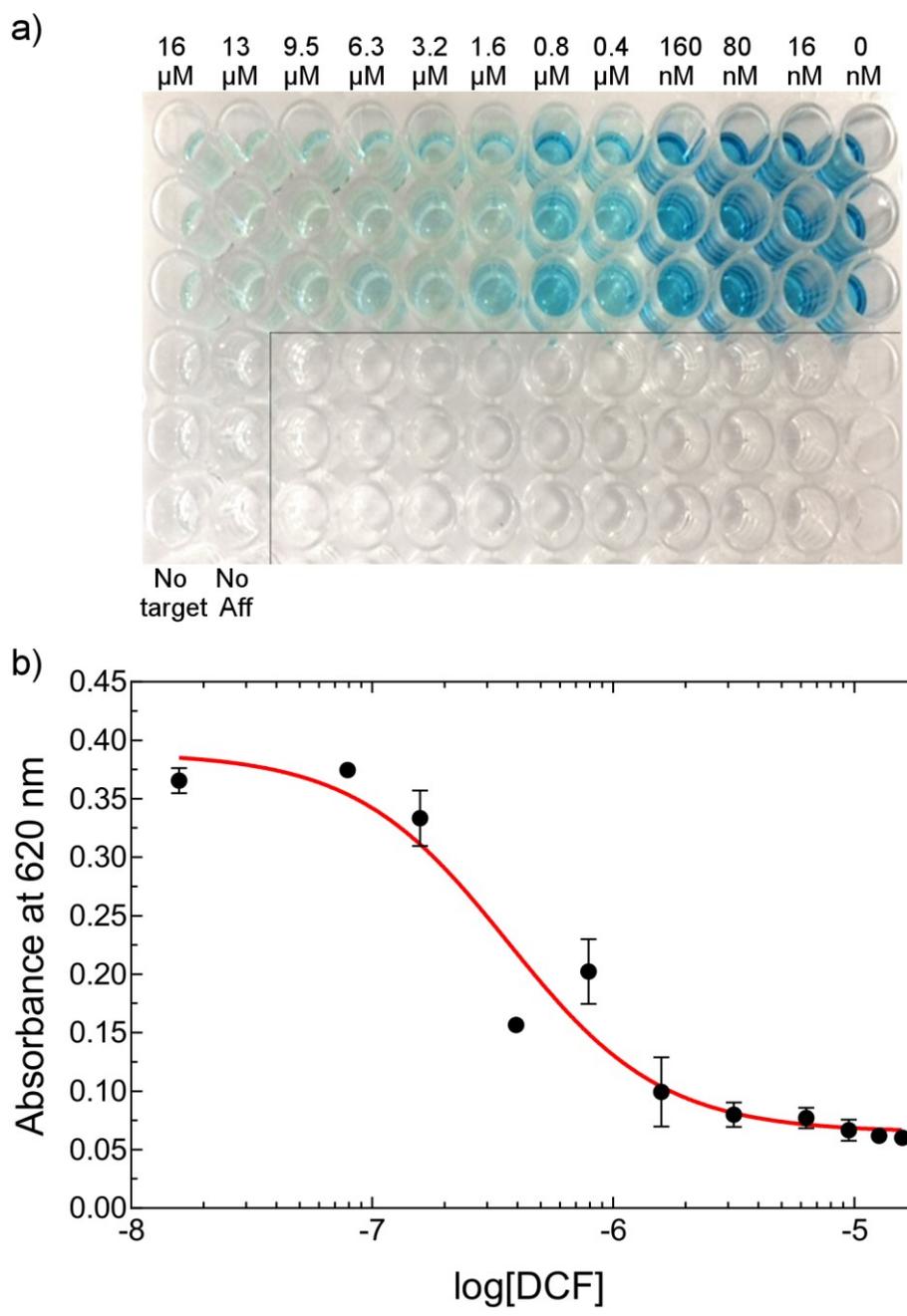
Figure 5.9: Competition DCF-Aff ELISA: a) ELISA plate wells showing the TMB colour product (each triplicate of wells corresponds to different concentration of free-DCF, including a blank and negative control); b) measured absorbance at 620 nm plotted as a function of the logarithm of DCF concentration (red line shows 4PL curve fitting).

The competition ELISA well plate and associated calibration curve is shown in Figure 5.9. The DCF-Aff competition ELISA was performed in collaboration with PhD student, Lia De Faveri, at the BSTG, University of Leeds. Here, the DCF-Aff concentration was 0.2 μg/mL (equivalent to

15.8 nM), while the free-DCF solution concentrations ranged from 16 nM to 16 μM. All materials were the same as described above (Section 5.4.1), save the TMB substrate (SeramunBlau® fast, Seramun Diagnostica GmbH, Heidesee, Germany). The data were fitted using a four parameter logistic (4PL) curve, Equation 5.3, which is used typically for concentration-response data in competition assays:

$$Y = bottom + \frac{(top-bottom)}{(1+10^{((\log(IC_{50}-X)^{slope}})}$$
(5.3)

Here, X is the competitor (free-DCF) concentration, Y is the response, *bottom* is the response at infinite competitor concentration (lower plateau), *top* is the response in the absence of competitor (upper plateau), *slope* refers to the steepness of the curve. IC_{50} (inhibitory concentration) is the concentration of competitor causing 50% inhibition of binding (i.e. 50% inhibition of DCF-Aff binding to surface-DCF due to free-DCF) [48] [184] [185].

As seen in Figure 5.9a, at high DCF concentrations the measured absorbance signal was evidently decreased, showing that the free-DCF exhibited considerable competition with surface-DCF. The response was plotted against the logarithm of DCF concentration and the resulting calibration curve, shown in Figure 5.9b, showed a clear decreasing trend with increasing concentration, typical of a competition ELISA. The 4PL curve (Equation 5.3) was found to be a good model of the experimental data (R^2 = 0.941) and yielded a value of IC_{50} = 0.36 μM. The IC_{50} is a measure of the binding inhibition potency of the free-DCF in the competition ELISA [184]. The value estimated here is higher than those reported from others in studies of antibody-based competition ELISAs for diclofenac detection [48] [187]. Finally, the detection limit for this competition assay (estimated as the blank signal + three standard deviations [196] was calculated to be 75 nM (106 μg/L), which is also higher that the values reported in the literature.

5.5 Conclusions

The work presented in this chapter aimed to evaluate the potential of DCF-Affimers as bioreceptors for Affimer-based immunoassays. The DCF-Aff to DCF binding reaction was investigated using QCM-D, where DCF was immobilised on the gold coated QCM-D sensors via LCAT-OEG-DCF SAMs. Prior to QCM-D, EIS and PM-IRRAS showed that dilution of the LCAT-OEG-DCF component of the SAM with LCAT-OEG-OH improved the order and quality of the monolayer conformation. A mixed (1:2 ratio) DCF:OH SAM was thus selected for QCM-D experiments. DCF-Aff showed considerable interactions with surface-immobilised DCF in the QCM-D, with minimum non-specific binding, as demonstrated using control measurements. Analysis of the kinetics of the binding reaction revealed a dissociation constant in the nanomolar region (73 nM), which compares well with that of high affinity antibodies [188] [189].

DCF-Aff interactions were also investigated using an ELISA. In agreement with QCM-D measurements, DCF-Aff exhibited significant affinity for DCF-coated wells, with negligible non-specific binding observed in control samples. The dissociation constant, K_D, estimated by saturation binding measurements, was the same order of magnitude as that found through kinetic analysis in QCM-D. Although picomolar affinities have been reported for antibodies against diclofenac [48], the value of K_D found here for DCF-Aff (37.87 nM) compares well with those for many high affinity antibodies against small molecules [181] [182] [187] [193].

While direct ELISAs are well suited for basic studies of molecular interactions, competition ELISAs are typically used for the detection of small molecules in the field. The potential of DCF-Affimers to be used in the competition assay format was thus evaluated. Results showed considerable competition between free-DCF and surface-DCF and a calibration curve was constructed, showing a clear decreasing trend with increasing free-DCF concentration. Although the detection limit (75 nM) was not low enough for the environmentally relevant concentrations of diclofenac (typically low picomolar range), these results are very promising, encouraging future optimisation of the assay to bring it into the necessary range. The competition ELISA data presented here are preliminary results reported with the purpose of demonstrating for the first time the potential of Affimers for the detection of small molecules in such competition assays, rather than to develop and validate an optimised Affimer-based ELISA. While additional research is required in order to optimise the ELISA protocol, the findings presented here are sufficiently encouraging to stimulate further research into Affimer-based assays for the detection of small-sized molecules, such as diclofenac.

Chapter 6

Conclusions

Current and emerging pollution issues demand increased monitoring of the presence of contaminants in the environment, so as to regulate their levels and apply efficient and well-informed mitigation plans. For example, many emerging contaminants such as pharmaceuticals, personal care products, cleaning agents, microplastics and engineered nanoparticles, are currently being freely discharged to the environment without regulation. There is an urgent need for additional monitoring in order to map the spatial and temporal distribution of these contaminants and to understand their impact on human and ecosystem health. Current analytical techniques (mainly LC- or GC-MS) provide accurate, robust and highly reliable approaches for detecting emerging contaminants in environmental samples, even at very low concentrations. However, these approaches are faced with several limitations (Section 1.2) that greatly impede the wide-spread adoption of a time- and cost-efficient environmental monitoring scheme. Immunoassays are an attractive alternative to standard analytical approaches, enabling high speed and low-cost monitoring in a scheme that can be integrated into a biosensor format to enable rapid, real-time, field measurements. Conventional immunoassays rely on antibodies to detect a target compound with very high affinity, specificity and selectivity and have found widespread application as important bioanalytical tools across a vast range of fields (Section 2.2). However, the use of antibodies for the detection of small-sized, non-immunogenic targets, such as many environmental contaminants, presents a number of challenges (Section 2.6). These challenges can potentially be addressed by Affimers (Section 2.8), which are protein engineered binders that mimic the high affinity and specificity associated with antibodies, but with reduced batch-to-batch variability, high stability, and *in vitro* selection that ensures rapid discovery of binders against a wide range of targets, including small, non-immunogenic targets. In recent years, many reports have showcased the remarkable potential of Affimers as antibody alternatives, but have focussed mainly on protein targets, which are large-sized molecules with several epitopes. However, the majority of environmental contaminants are small-sized targets. Considering the many advantages of Affimers over conventional antibodies, as well as the increasing need to optimise pollution monitoring approaches, this project aimed to investigate the potential of Affimers as alternative bioreceptors in bioassays for the detection of small-sized compounds, focusing on environmental contaminants.

Here, Affimers against two targets were selected: MB, which was selected as a proof-of-principle target due to its redox properties, and DCF, an important emerging contaminant with well-established evidence of its ecotoxicological impacts. The aims of this project were to a) demonstrate that the developed Affimers can bind to the selected small-molecule targets with very high affinity, b) assess their performance in the complexity of environmental water samples (selectivity), and c) develop an Affimer-based immunoassay for small molecule detection.

Biosensors for detecting small-sized targets are typically operated in a competition assay format, which requires the immobilisation of the target molecule on the sensing surface. It was thus necessary to develop and evaluate an appropriate approach to small molecule immobilisation. Here, an approach based on a biotin-OEG_8 linker on streptavidin coated surfaces or LCAT-OEG-MB and LCAT-OEG-DCF SAMs on gold was demonstrated. QCM-D and CV measurements of MB SAMs confirmed that MB retained its redox activity when immobilised on a gold sensor surface (Section 4.3). in addition, through CV, EIS and PM-IRRAS, it was shown that mixed MB:OH SAMs exhibited improved packing order over pure MB SAMs (Section 4.3.3). This immobilisation approach was subsequently adopted for studying target-Affimer interactions.

QCM-D studies showed that MB-Affimers bind strongly and specifically to surface-immobilised MB (Sections 4.5.1 and 4.5.2), and can demonstrate considerable selectivity in complex matrices, such as limnetic water samples (Section 4.5.3). The binding affinity estimated by saturation binding and kinetic analysis was found to be in the nanomolar region (K_D=13.7 nM for MB-Aff5). This is comparable with that of high affinity antibodies [188] [189]. In addition, an Affimer-based competition assay for MB detection was demonstrated using QCM-D (Section 4.5.4); the detection limit was found to be 360 nM (128 μg/L). This is higher than the environmentally relevant concentrations (ng/L to μg/L) [10] and the detection limits reported in the literature for antibody-based ELISAs for small molecules [48] [181] [193]. However, it should be noted that sensitivity of QCM-D is limited at low concentrations [145] and that the assay was presented as a proof-of-principle and was not optimised. Nonetheless, using MB as a proof-of-concept target, these findings demonstrated the ability of Affimers to bind strongly to small-sized compounds and the potential to use Affimers in bioassays to detect such targets.

Using the knowledge and experimental approaches developed through the MB-Affimer study, the performance of DCF-Affimers was evaluated (Chapter 5). Kinetic analysis of DCF-Affimer binding to DCF using QCM-D revealed a low dissociation constant (K_D=73 nM) that was within the same range as that estimated for MB-Affimers and compared well with that of high affinity antibodies [188] [189]. DCF-Aff interactions were also investigated using an ELISA. Here, saturation binding measurements yielded a dissociation constant of 37.87 nM, which is consistent

with the K_D estimated using QCM-D. Although picomolar affinities have been reported for antibodies against DCF, the K_D values found here for DCF-Affimers using QCM-D and ELISA compare well with those for many high affinity antibodies against small molecules [48] [181] [182] [193]. Finally, an Affimer-based competition ELISA for DCF detection was demonstrated with a detection limit of 75 nM.

The competition assays presented in this work are preliminary results with the purpose of demonstrating the potential of Affimers as bioreceptors in bioassays for the detection of small molecules. This study has confirmed that 1) *in vitro* selected, small and robust Affimers can bind to small-sized, non-immunogenic targets as strongly as antibodies, even in complex matrices and 2) Affimers can be successfully incorporated in conventional immunoassay approaches, such as competition ELISAs, to detect such targets. The importance of these findings is significant for bioanalytical applications, where there is a need for robust and cost-efficient alternatives to antibodies, particularly for environmental monitoring where raising antibodies against targets that are typically small-sized, non-immunogenic or toxic compounds can be challenging. Furthermore, detection of small molecules by Affimers can be important for healthcare applications, such as quantifying the concentration of pharmaceuticals in a patient sample.

Although not optimised, the results presented here are encouraging and support further research on Affimer-based bioassays for the detection of small-sized targets. Underpinned by the competition ELISA demonstrated in Chapter 5, future research may focus on optimising the assay performance in terms of increasing sensitivity (i.e. the slope of the calibration curve), reducing the detection and quantification limits of the assay and assessing the accuracy and intra-/inter-assay precision. Optimisation of each component of the assay will be required, namely; 1) reagent concentrations (i.e. Affimers, immobilised targets, buffers, enzyme-labelled detection antibody, substrate); 2) Composition of buffers, including blocking and washing buffers; 3) Selection of detection antibody, enzymatic label and substrate; 4) immobilisation approach (e.g. ELISA plate, adjustment of length of the biotin linker or possible alternatives to the biotin-streptavidin system); 5) Incubation times and number of washing steps. Furthermore, sample preconcentration approaches, such as affinity chromatographic columns, can be considered.

Besides assay optimisation, sensitivity can be improved through further development of the binding element. For instance, the affinity of strong-binding Affimers can be increased through *in vitro* affinity maturation. This can be achieved by site-directed or randomised mutagenesis of the amino acid residues within the antigen-binding sequences of the variable peptide loops, followed by increased phage display selection rounds to identify high affinity binders [197] [198]. Another approach to increase sensitivity would be the combination of Affimer reagents to create a bivalent

or polyvalent binder and thus introduce avidity to the target-binder interaction, mimicking the multivalent binding of immunoglobulins.

Critically, the matrix effects from environmental, clinical or other type of samples on the performance of the assay must be also examined. In addition, it is important to evaluate the cross-reactivity of the assay, that is the degree to which Affimers may bind to structurally similar molecules or compounds of the same class as the target, focusing on those that are expected to be in a particular type of sample (e.g. clinical or environmental). For instance, for the detection of DCF in surface water samples, potential cross-reactants may be DCF metabolites, structurally similar compounds like meclofenamic or tolfenamic acid or other NSAIDs like ibuprofen or ketoprofen [48].

Future considerations for the application of Affimers in environmental monitoring can be identified in the biosensor design and approaches. An Affimer-based assay can be combined with established lateral flow approaches to enable a low-cost, portable assay in a dipstick format. Furthermore, several biosensing techniques, such as optical (e.g. SPR, reflectometric, photonic/electrophotonic) or electrochemical (e.g. impedimetric, field-effect transistors) can be combined with novel micro- and nanofabrication technologies to develop highly sensitive lab-on-chip sensors for rapid target detection. In addition, the fact that Affimers can be designed for efficient immobilisation on sensor surfaces enables the development of microarrays for multiplexed detection of contaminants.

Preliminary applications of Affimers are increasingly reported by several studies, demonstrating the potential of Affimers as versatile bioreceptors in bioassays. The findings of this work contribute to this literature and are encouraging for the future development of biosensors for the detection of small molecules, thus introducing a novel, alternative technology for rapid, on-site monitoring of contaminants in the environment or for point-of-care clinical diagnostics.

Appendix A

Affimer selection against MB and DCF

This section presents the *in vitro* selection of Affimers against MB and DCF. Initially, both targets were coupled to a linker derivatised with biotin. This biotin linker enabled immobilisation on streptavidin coated surfaces for Affimer screening of a phage display library. Affimer selection, phage ELISA and expression was performed at the BSTG group (University of Leeds), by Dr. Christian Tiede, Anna Tang and PhD student Lia de Faveri and was supervised by Dr. Darren Tomlinson. A brief overview of the synthesis of the biotin labelled targets, Affimer selection processes and results are presented in the following sections.

Biotinylation of MB and DCF
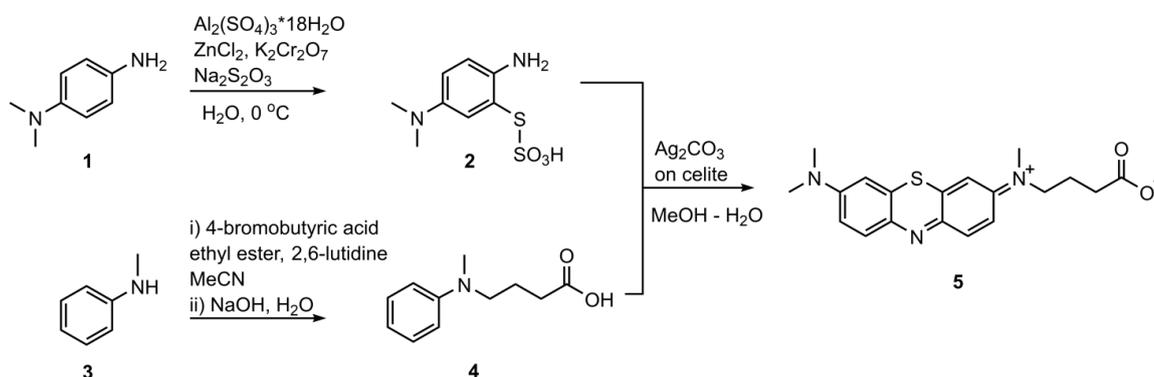
Figure A.1: Schematic overview of the synthetic protocol of N-(carboxypropyl) methylene blue (5), as described in Murray et al. [119], 2014.

A biotin linker with an amine moiety was used for NHS/EDC crosslinking with MB and DCF. This reaction links two molecules through an amide bond that is formed between an amine group on one molecule and a carboxylic acid on the other molecule. DCF has a single carboxylic acid group available for the crosslinking reaction. In contrast, MB does not contain a carboxylic acid and a modified version of MB was thus synthesised. For this purpose, N-(carboxypropyl) methylene blue was synthesised as described in Murray et al. [119], following a procedure adapted from Pheeney and Barton [166]. A schematic overview of the chemical synthesis steps and of the structure of N-

(carboxypropyl) methylene blue (MB-COOH) is shown in Figure A.1. Next, both MB-COOH and DCF were coupled to biotin, following a NHS/EDC coupling reaction [199].

2-Amino-5-(dimethylamino)phenylthiosulfonic acid (2)
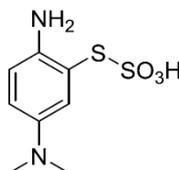
Aluminium sulfate octahydrate (45.0 g, 65 mmol), sodium thiosulfate (22.0 g 140 mmol), and zinc(II) chloride (8.8 g, 63 mmol) were dissolved separately into 100 mL, 80 mL and 12 mL of water, respectively. The solutions were then added to a flask containing **N,N-dimethylphenylenediamine (2)** (10.0 g, 73 mmol) and the mixture cooled to 0 °C under continuous stirring. A solution of potassium dichromate (5.0 g, 17 mmol) in water (30 mL) was added dropwise for 30 min, and the reaction mixture was stirred at 0 °C for 2 h and then was left to warm to room temperature. The precipitate was isolated by filtration; the solid was washed with water, acetone, then ether to afford the title compound as a lilac solid (8.3 g, 47%).

N-Methyl-*N*-(carboxypropyl) aniline (4)
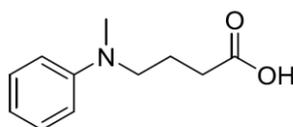
N-Methylaniline (3) (10.1 mL, 93 mmol), 2, 6-lutidine (11.3 mL, 100 mmol) and 4-bromobutyric acid ethyl ester (15.0 mL, 100 mmol) were refluxed in MeCN for 16 h. The MeCN was removed *in vacuo* to leave an indigo residue, which was dissolved in EtOAc (50 mL) and washed with water (2 × 20 mL). The organic layer was dried (Na$_2$SO$_4$) and concentrated to yield an indigo oil which was subjected to flash chromatography (SiO$_2$; EtOAc:Petrol 1:20). The effluent was acidified with HCl, washed with Et$_2$O, neutralised with solid NaHCO$_3$ and extracted with EtOAc. The extract was then hydrolysed with NaOH (2.5 M, 10 mL) at reflux for 2 h. The mixture was allowed to cool, washed with Et$_2$O, acidifed to pH 5 (conc. HCl), then extracted with EtOAc (3 × 30 mL) and dried (Na$_2$SO$_4$). Concentration *in vacuo* gave the title compound as a colourless oil (1.255 g) **ESI-LC-MS:** Calcd. for C$_{11}$H$_{16}$NO$_2$: *m/z* 194.1181 [M+H]$^+$; found 194.0. t$_R$ = 0.79 min (Figure A.2)
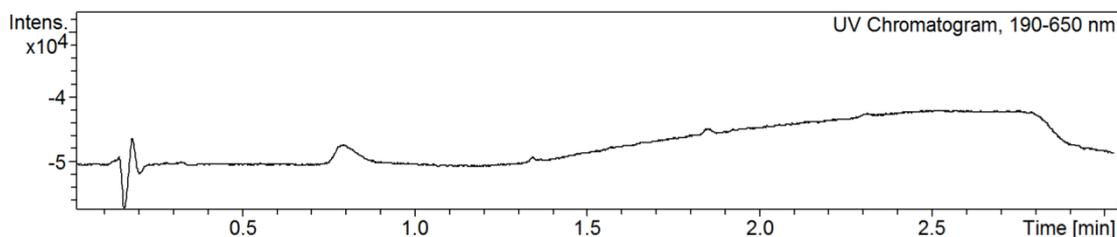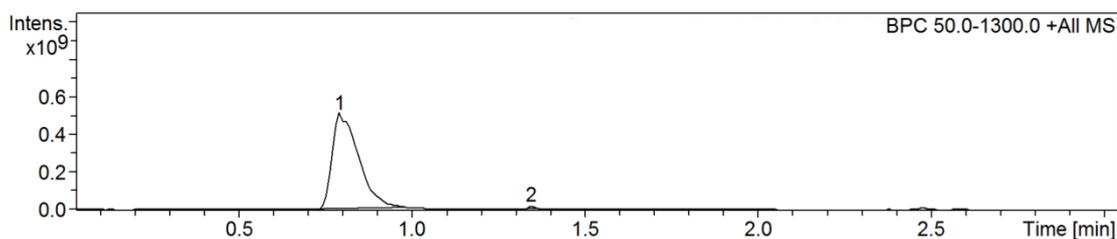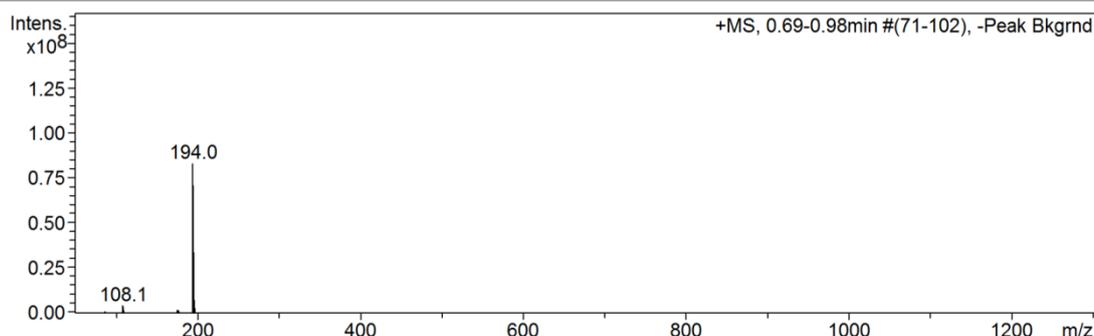
Figure A.2: ESI-LC-MS of *N*-Methyl-N-(carboxypropyl) aniline (4) (obtained on a Bruker HCT Ulltra mass spectrometer, School of Chemistry, University of Leeds)

N-(carboxypropyl) methylene blue (5)
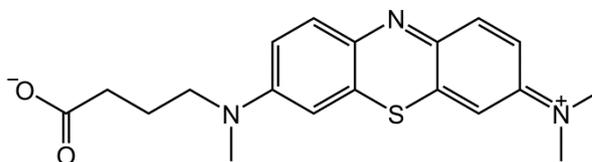
Compounds **1** (1.2 g, 4.9 mmol) and **2** (0.95 g, 4.9 mmol) were dissolved in a mixture of MeOH–H$_2$O (200:80 mL). The mixture was heated to ~50 °C and Fétizon's reagent (Ag$_2$CO$_3$ on celite; 5.7 g, 9.5 mmol) was added portion wise over 15 min. The mixture was then heated at reflux for 2 h. The Fétizon's reagent was removed by filtration and the filtrate was concentrated *in vacuo* to yield a dark blue residue, which was purified on a short SiO$_2$ column. The impurities were eluted with

EtOAc, after which the target compound was eluted with DCM-MeOH (9:1) to afford the target compound as an indigo-violet glassy solid (0.458 g, 26%). **ESI-LC-MS:** Calcd. for $C_{19}H_{22}N_3O_2S$ *m/z* 356.1 [M+H]+; found 356.1; t_R = 1.50 min (Figure A.3).

#	Cmpd. Label	RT [min]	Range [min]	Max. m/z	Area	Area %	Area Frac. %
1	Cmpd 1, 1.50 min	1.50	1.40 - 1.73	356.1	1050553439	100.0	100.0

Cmpd 1, 1.50 min
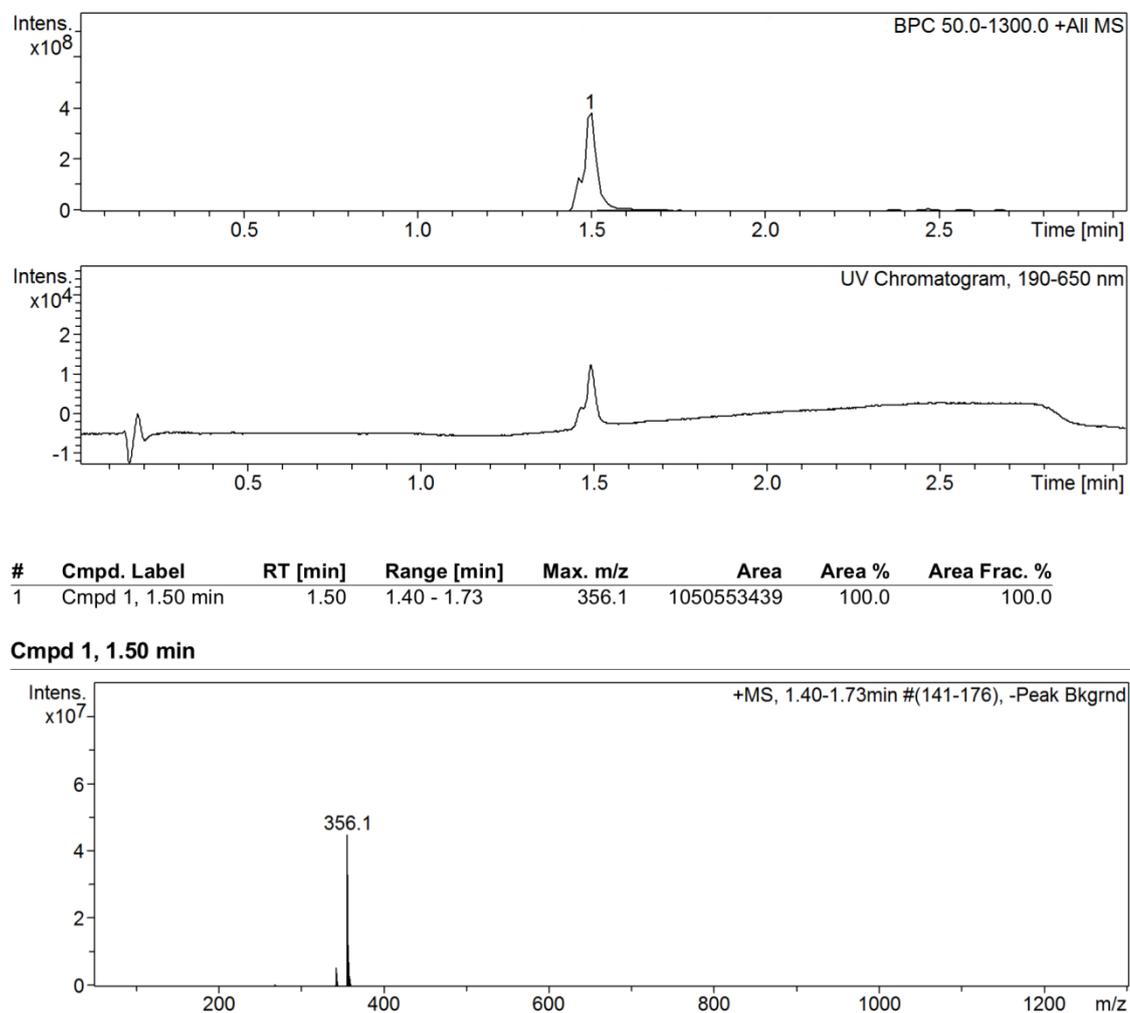
Figure A.3: ESI-LC-MS of N-(carboxypropyl) methylene blue (5) (obtained on a Bruker HCT Ulltra mass spectrometer, School of Chemistry, University of Leeds)

Biotinylation of N-(carboxypropyl) methylene blue
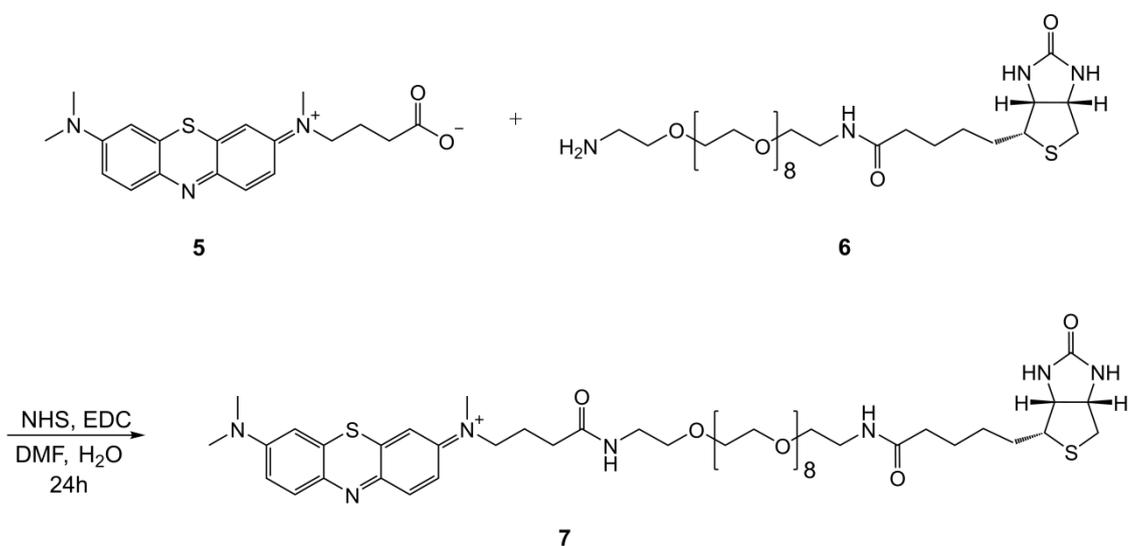
Figure A.4: Overview of the NHS/EDC coupling of N-(carboxypropyl) methylene (5) to biotin-PEG$_{(8)}$-NH$_2$ (6)

Unless noted otherwise, all reagents were purchased from Sigma-Aldrich (Gillingham, UK). A mixture of N-hydroxysuccinimide (NHS) solution (0.37 mg, 3.22 μmol) in 100 μL DMF and ethyl-(dimethylaminopropyl)-carbodiimide (EDC) solution (0.68mg, 3.22 μmol) in 100 μL DMF was prepared and a solution of **N-(carboxypropyl) methylene (5)** (1.14 mg, 3.22 μmol) in100 μL DMF was added and stirred for 5 min. Next, a solution of **biotin-PEG$_{(8)}$-NH$_2$ (6)** (1 mg, 1.46 μmol) in 100 μL of water was added dropwise and the reaction mixture was left to stir overnight. The purity of the product was examined by ESI-LC-MS (HCT Ultra; Bruker, Bremen, Germany) where only a small amount of impurities were detected The reaction mixture was diluted with water up to 1 mL to afford the product as a ~1 mg/ mL solution in 30% aqueous DMF. ESI-LC-MS: Calcd. for C$_{49}$H$_{78}$N$_7$O$_{12}$S$_2$ *m/z* 1020.508 [M+H]$^+$; found 1020.5; Calcd. for C$_{49}$H$_{79}$N$_7$O$_{12}$S$_2$ *m/z* 510.758 [M+2H]$^{2+}$; observed 510.8; t$_R$: 1.53 min (Figure A.5).
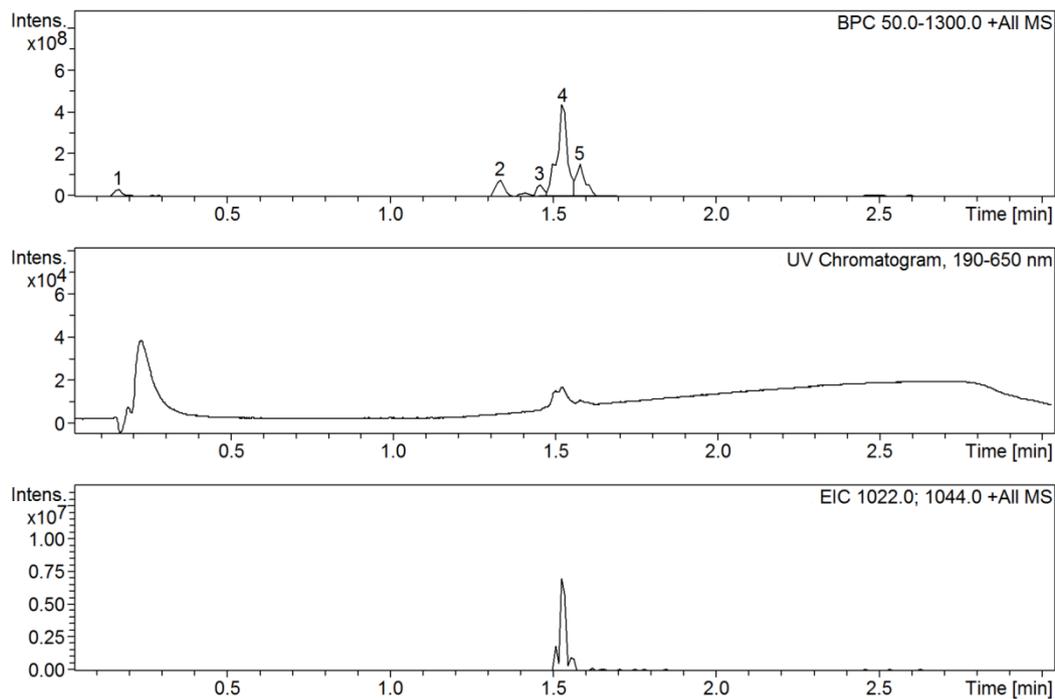
#	Cmpd. Label	RT [min]	Range [min]	Max. m/z	Area	Area %	Area Frac. %
1	Cmpd 1, 0.17 min	0.17	0.14 - 0.19	174.1	51701522	5.3	3.3
2	Cmpd 2, 1.34 min	1.34	1.26 - 1.39	683.4	150065504	15.4	9.5
3	Cmpd 3, 1.46 min	1.46	1.43 - 1.48	429.8	89043993	9.1	5.6
4	Cmpd 4, 1.53 min	1.53	1.48 - 1.56	510.8	974045486	100.0	61.6
5	Cmpd 5, 1.58 min	1.58	1.56 - 1.69	453.1	315787195	32.4	20.0

Cmpd 4, 1.53 min
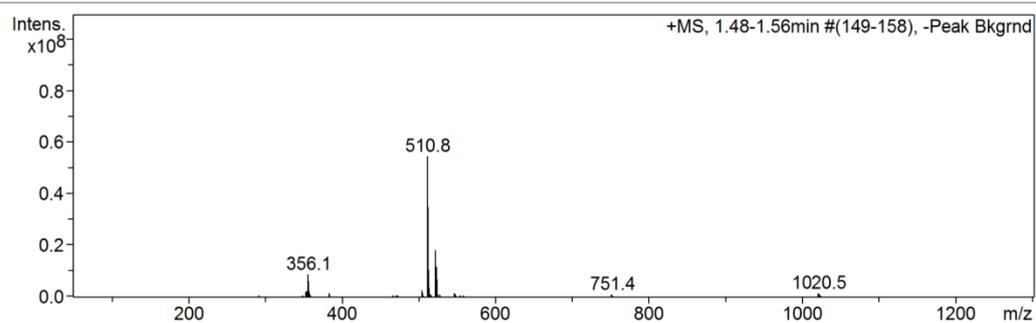
Figure A.5: ESI-LC-MS of biotinylated methylene blue (7) (obtained on a Bruker HCT Ulltra mass spectrometer, School of Chemistry, University of Leeds).

Biotinylation of DCF

Figure A.6: Overview of the NHS/EDC coupling of DCF (8) to biotin-PEG$_{(8)}$-NH$_2$ (6)

A mixture of *N*-hydroxysuccinimide (NHS) solution (7.4 mg, 0.0645 mmol) in 0.5 mL DMF and ethyl-(dimethylaminopropyl)-carbodiimide (EDC) solution (12.4 mg, 0.0645 mmol) in 1.0 mL DMF was prepared and a solution of diclofenac **(8)** (20.4 mg, 0.0645 mmol) in 1 mL DMF was added and stirred for 5 min. Next, a solution of biotin-PEG$_{(8)}$-amine **(6)** (20 mg, 0.0293 mmol) in 2.0 mL of water was added dropwise and the reaction mixture was left to stir overnight. After 24 h, DMF was removed under ultra-high vacuum (assisted by a warm water bath). The product was purified by preparative HPLC. The fractions with the purest product were collected, evaporated and freeze-dried to yield an off white solid (5.9 mg). Again, the purity of the product was confirmed by ESI-LC-MS (Calcd. for $C_{44}H_{68}Cl_2N_5O_{12}S$ *m/z* 480.1985 $[M+2H]^{2+}$; observed *m/z* 480.1; Calcd. for $C_{44}H_{66}Cl_2N_5NaO_{12}S$ *m/z* 981.281 $[M+Na]^+$; found 981.8); t_R=1.85 min (Figure A.7).

#	Cmpd. Label	RT [min]	Range [min]	Max. m/z	Area	Area %	Area Frac. %
1	Cmpd 1, 1.78 min	1.78	1.76 - 1.82	515.7	301277013	25.9	20.2
2	Cmpd 2, 1.85 min	1.85	1.82 - 1.90	480.1	1161891930	100.0	78.0
3	Cmpd 3, 2.00 min	2.00	1.97 - 2.02	295.4	25994272	2.2	1.7

Cmpd 2, 1.85 min
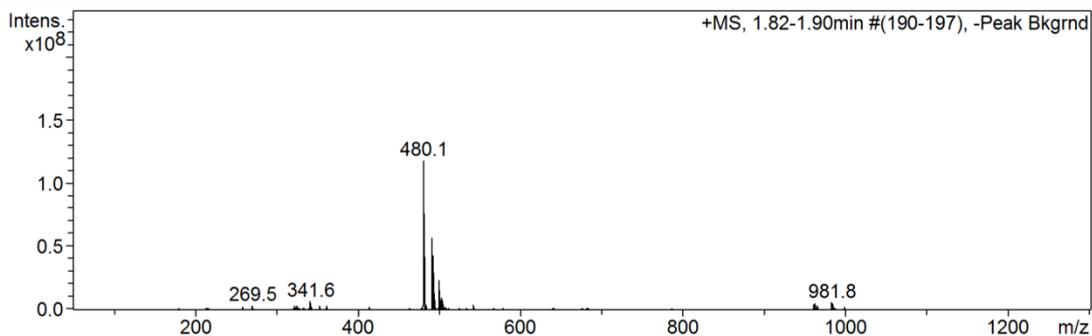
Figure A.7: ESI-LC-MS of biotinylated diclofenac (9) (obtained on a Bruker HCT Ulltra mass spectrometer, School of Chemistry, University of Leeds).

Affimer selection

Using a large Affimer phage display library, Affimers that bind to methylene blue and diclofenac were selected following the procedure described in Tiede et al. [27]. Due to the small size of the targets, five panning rounds were required for Affimer selection. In each round, the library of Affimer-carrying phages were screened against the immobilised, biotinylated target. The phages isolated from the final panning round were then analysed by a phage ELISA to identify those that bind to the target. Finally, the phage binders were sequenced in order to identify unique Affimer reagents. Selection and phage ELISA were performed by the BSTG, University of Leeds. Below is a brief description of the selection process and the phage ELISA performed by Dr. Christian Tiede, Anna Tang (MB-Affimers) and Lia De Faveri (DCF-Affimers). The processes were the same for MB and DCF Affimer; thus in the following section, unless noted otherwise, MB and DCF will be referred to as 'target'.

Phage display

For the first panning round, the biotinylated target was bound to streptavidin-coated wells (Pierce, Loughborough, UK) for 1 hour, then 10^{12} cfu pre-panned phages (phages screened against wells containing only the biotin linker, i.e. no target) were added for 2.5 hours with shaking. Panning wells were washed 10 times with PBST and eluted with 50 mM glycine for 10 min (pH 2.2, neutralised with Tris-HCl pH 9.1), then 100 mM triethylamine for 6 min (neutralised with Tris-HCl pH 7). The collected eluates were used to infect ER2738 cells (1 hour at 37 $^{\circ}$C with shaking), followed by plating onto LB agar plates with 100 µg/mL carbenicillin and grown overnight. Colonies were scraped, inoculated in 25 ml of 2XYT with carbenicillin and infected with ca. 1 x 10^9 M13K07 helper phages. After 16 hours the phage supernatant was incubated with biotinylated target bound to streptavidin magnetic beads (Invitrogen, Paisley, UK) and eluted and amplified as above, for the second pan. The third panning round was performed on neutravidin high binding capacity wells (Pierce, Loughborough, UK) and eluted as above. The fourth and five panning rounds were performed on streptavidin and neutravidin coated plates as described above.

Phage ELISA

Individual ER2738 colonies were grown in 100 µL of 2XTY with 100 µg/mL of carbenicillin in a 96-deep well plate at 37 °C (900 rpm) for 6 hours. A 25 µL aliquot of the culture was added to 200 µL of 2XYT containing carbenicillin and grown at 37 °C (900 rpm) for 1 hour. Helper phages (10

µL of 10^{11}/mL) were added, followed by kanamycin to 25 µg/mL overnight and incubated at 25 °C (450 rpm). Streptavidin-coated plates were blocked with 2X casein blocking buffer (Sigma-Aldrich, Gillingham, UK) overnight at 37 °C. The plates were incubated with biotinylated target for 1 hour, and 45 µL of growth medium containing the phages was added and incubated for 1 hour. Following washing, phage binding was detected by adding a 1 : 1000 dilution of HRP-conjugated anti-phage antibody (Seramun, Heideesee, Germany) for 1 hour and visualised with 3,3′,5,5′-tetramethylbenzidine (TMB) (Seramun, Heidesee, Germany) and measured at 620 nm.

MB-Affimers

Following five panning rounds, 24 individual colonies (each carrying one Affimer binder) were isolated. Those that bound to MB were identified by a phage ELISA (Figure A.8). 23 out of 24 reagents showed binding to MB and following sequencing, three unique sequences were identified: MB-Affimer 1, MB-Affimer 2 and MB-Affimer 5, referred to as MB-Aff1, MB-Aff2 and MB-Aff5, respectively (Table A.1). MB-Aff1 and MB-Aff5 were the most commonly occurring sequences and showed sequence homology in both loops, thus were taken forward for characterisation (Chapter 4). Notably, MB-Aff5 showed higher expression levels than MB-Aff1 (2.3 mg/mL and 0.6 mg/mL, respectively) and was selected for in-depth analysis of Affimer binding and assay development.
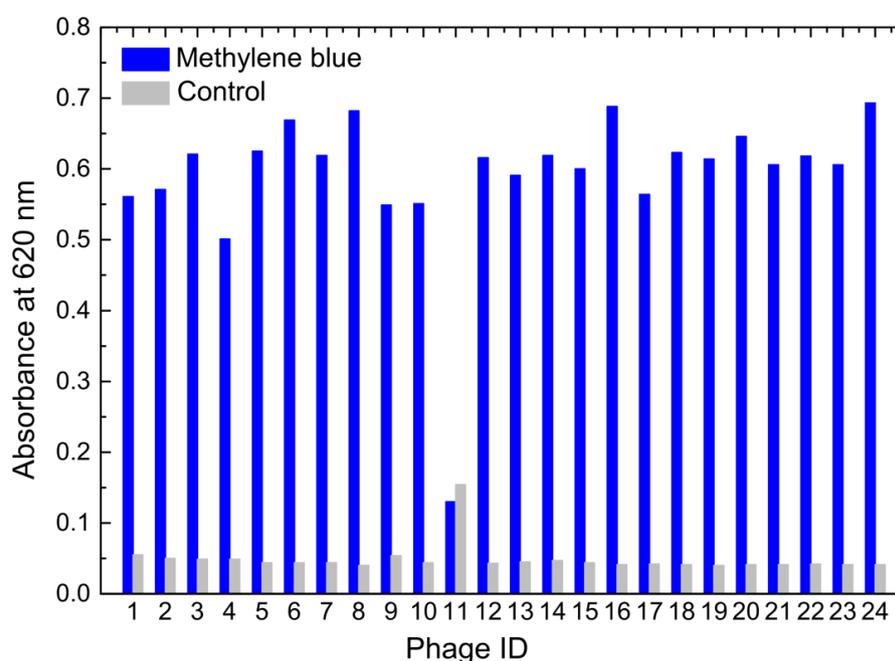
Figure A.8: Phage ELISA of Affimers from 24 clones incubated in streptavidin-coated wells previously treated with biotinylated MB (blue), showing the TMB product absorbance (620 nm). Controls (grey) are streptavidin-coated wells with no biotinylated MB (data provided by Christian Tiede and Anna Tang, BSTG).

Affimer	Loop sequence 1	Loop sequence 2
MB-Aff1	WGWVYTMGD	FNSTPPWNV
MB-Aff2	YKHQWGYW	WAHDDAGFF
MB-Aff5	WGYQEKKVY	FDESMPWPM

Table A.1: Peptide sequences of MB-Affimers binding loops (data provided by Dr Christian Tiede, BSTG). The entire Affimer sequence (scaffold and binding loops) can be found in Tiede et al. [27].

DCF-Affimers

Following five panning rounds, 48 individual colonies (each carrying one Affimer binder) were isolated. All binders demonstrated binding to DCF, as shown by phage ELISA (Figure A.9). Out of 48 binders, one unique sequence was identified (Table A.2), and the expressed DCF-Affimer (1.39 mg/mL) was taken forward for affinity characterisation and assay development (Chapter 5).
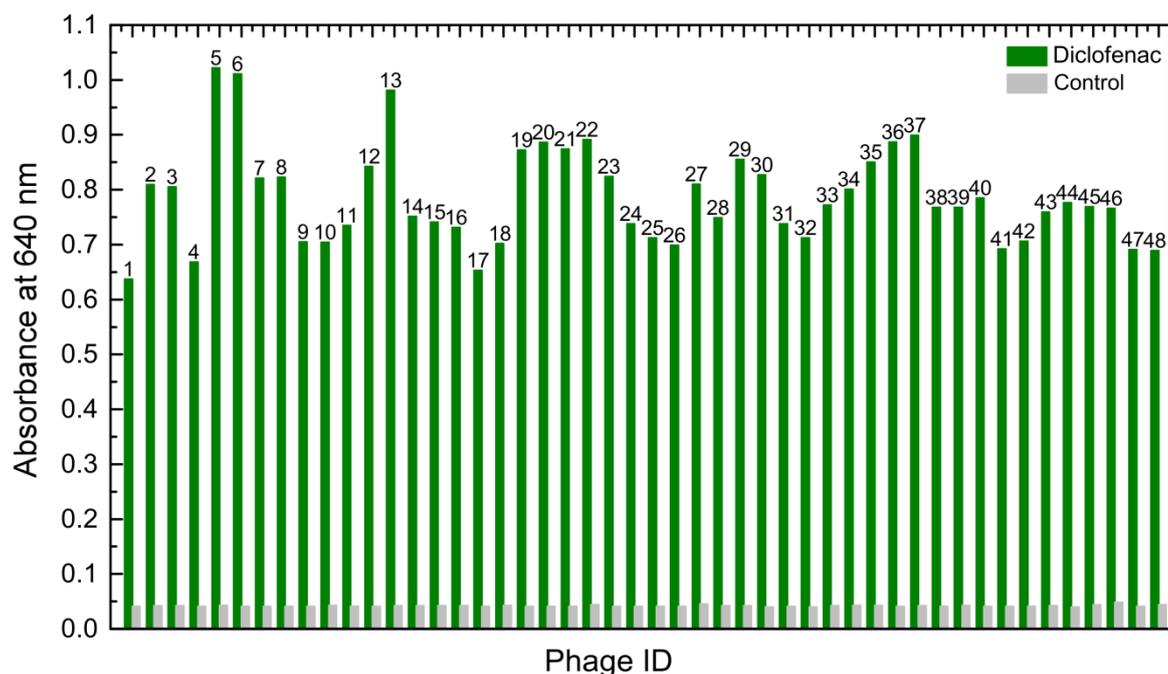
Figure A.9: Phage ELISA of Affimers from 48 clones incubated in streptavidin-coated wells previously treated with biotinylated DCF (green), showing the TMB product absorbance (620 nm). Controls (grey) are streptavidin-coated wells with no biotinylated DCF (data provided by Lia De Faveri, BSTG).

Affimer	Loop sequence 1	Loop sequence 2
DCF-Aff	TSMAYMQWG	QPAHINCFF

Table A.2: Peptide sequences of DCF-Affimers binding loops (data provided by Lia De Faveri, BSTG). The entire Affimer sequence (scaffold and binding loops) can be found in Tiede et al. [27].

Appendix B

LCAT-OEG-MB (18) synthesis

Materials

LCAT-OEG-MB was synthesised by adapting the solid phase synthesis procedure described by Murray et al. [119] (Figure 4.2). All chemicals and coupling reagents were purchased from major chemical suppliers. 2-Chlorotrityl chloride resin was purchased from VWR International. All non-aqueous solution phase reactions were carried out under a N_2 atmosphere, using solvents from a solvent purification system (Innovative Technology Inc. PureSolv®). Solid phase reactions were performed in fritted solid phase extraction tubes (Grace™, Fisher Scientific, Loughborough, UK) and agitated on a Stuart rotator. Lyophilisation of compounds was performed using a Virtis Benchtop K freeze dryer.

17-hydroxy-3,6,9,12,15-pentaoxaheptadecyl 4-methylbenzenesulfonate (11)
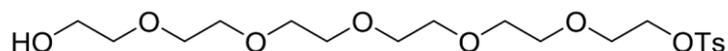
Silver (I) oxide (1.9 g, 8.3 mmol), and potassium iodide (176 mg, 1.06 mmol) were added to a stirred solution of **hexaethylene glycol (10)** (1.57 g, 5.31 mmol) in DCM (40 mL) at 0 °C. A solution of 4-toluenesulfonyl chloride (1.11 g, 5.84 mmol) in DCM (10 mL) was then added drop-wise and the reaction mixture was stirred at 0 °C until all starting material had been consumed (monitored using LC-MS). The reaction was quenched by filtering through a silica pad using EtOAc:MeOH 95:5 (125 mL) and the solvents were removed (rotary evaporator). The crude tosylate product was subjected to flash chromatography (SiO$_2$; EtOAc–MeOH 95:5) to afford the title compound as a colourless oil (1.64 g, 56%). **ESI-LC-MS:** Calcd. for $C_{19}H_{33}O_9S$: *m/z* 437.1 [M+H]$^+$; found 437.2; t_R = 1.68 min (Figure B.1).

#	Cmpd. Label	RT [min]	Range [min]	Max. m/z	Area	Area %	Area Frac. %
1	Cmpd 1, 1.39 min	1.39	1.37 - 1.43	323.1	65250270	1.3	1.1
2	Cmpd 2, 1.68 min	1.68	1.61 - 1.91	437.2	5125614162	100.0	89.6
3	Cmpd 3, 2.08 min	2.08	2.04 - 2.11	613.2	531892782	10.4	9.3

Cmpd 2, 1.68 min
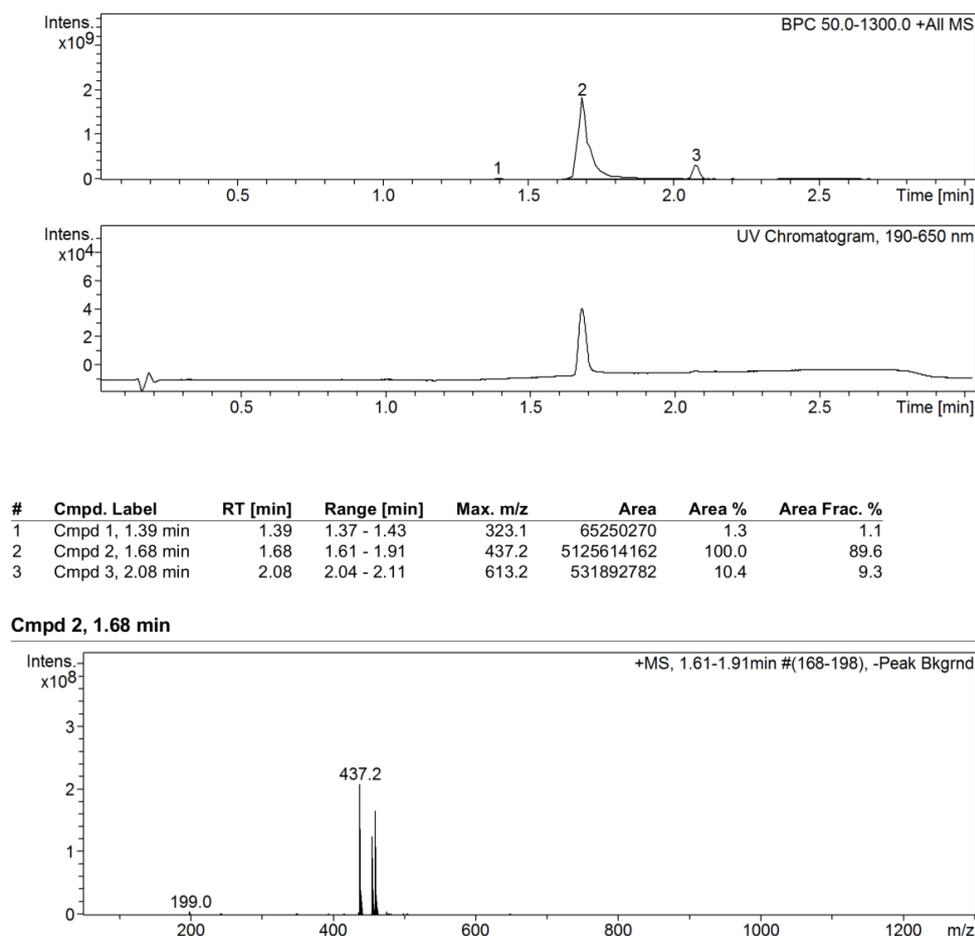
Figure B.1: ESI-LC-MS of 17-hydroxy-3,6,9,12,15-pentaoxaheptadecyl 4-methylbenzenesulfonate (11) (obtained on a Bruker HCT Ulltra mass spectrometer, School of Chemistry, University of Leeds).

17-amino-3,6,9,12,15-pentaoxaheptadecan-1-ol (12)
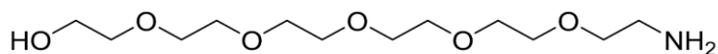
A solution of **(11)** (1.64 g, 3.76 mmol) in anhydrous DMF was added to a flask containing sodium azide (0.37 g, 5.7 mmol. The mixture was stirred and heated to 50 °C for 16 h, then left to cool to room temperature. The DMF was removed by co-evaporation with toluene at 50 °C, the residue re-suspended in EtOAc and filtered over a pad of SiO_2. The EtOAc was removed under reduced pressure to afford the product as a colourless oil (0.56, 47%). Next, the product was dissolved in THF (30 mL) and triphenylphosphine (0.54 g, 2.068 mmol) was added while stirring at 0 °C. The reaction mixture was stirred at 0 °C for 16 h, diluted into water (5 mL) and washed with toluene (2

× 3 mL); the aqueous layer was concentrated *in vacuo* to yield a colourless oil (0.41 g, 86%); **ESI-LC-MS:** Calcd. for $C_{12}H_{28}NO_6$, *m/z* 282.1 $[M+H]^+$: found 282.1; $t_R = 0.13$ min (Figure B.2).

#	Cmpd. Label	RT [min]	Range [min]	Max. m/z	Area	Area %	Area Frac. %
1	Cmpd 1, 0.13 min	0.13	0.08 - 0.16	282.1	4325742115	100.0	56.2
2	Cmpd 2, 0.18 min	0.18	0.16 - 0.56	330.1	3304494481	76.4	42.9
3	Cmpd 3, 1.40 min	1.40	1.35 - 1.43	330.1	64966634	1.5	0.8

Cmpd 1, 0.13 min
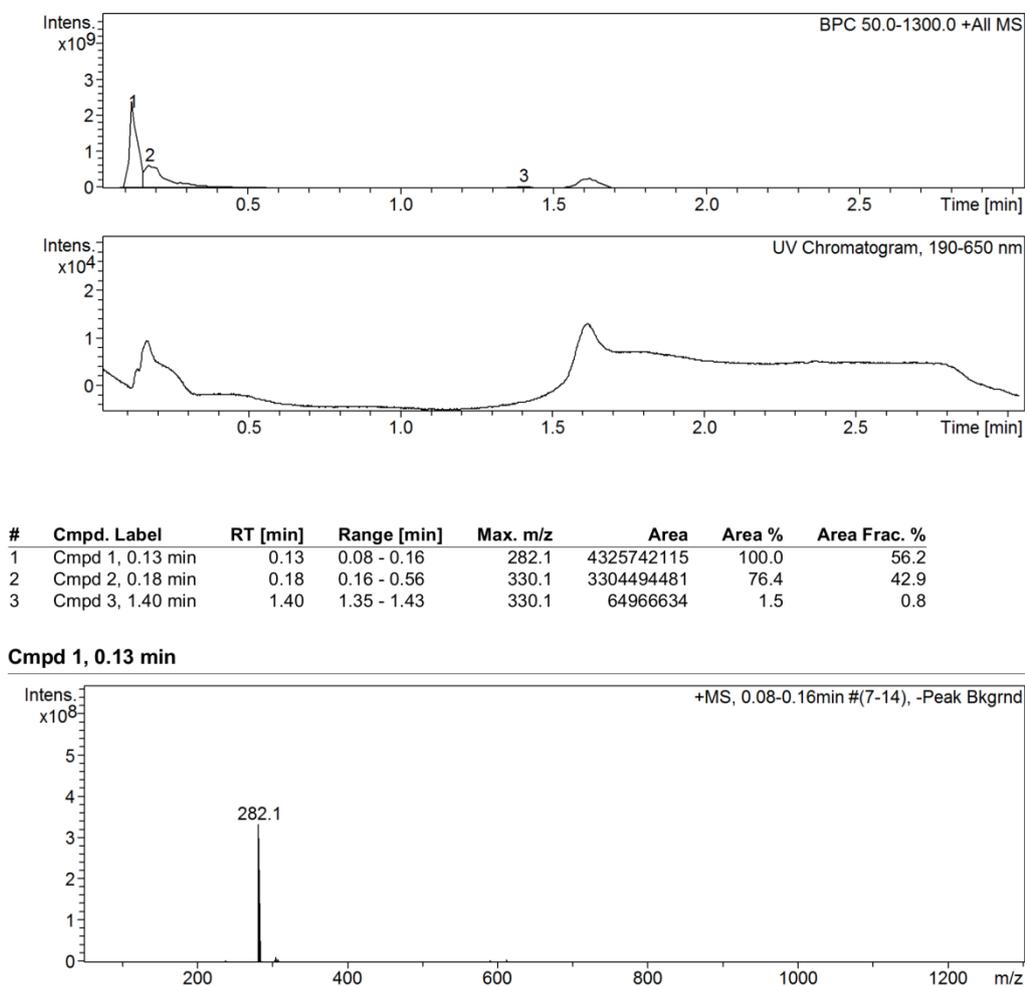
Figure B.2: ESI-LC-MS of 17-amino-3,6,9,12,15-pentaoxaheptadecan-1-ol (12) (obtained on a Bruker HCT Ulltra mass spectrometer, School of Chemistry, University of Leeds)

Reagent cocktails for solid phase chemistry:

Capping cocktail A for inactivation of 2-chlorotrityl chloride residues: MeOH (10% v/v) and DIPEA (1% v/v) in DCM.

Cleavage cocktail B for cleavage of LCAT-OEG-MB derivative **(18)**: TFA (5% v/v) and TES (2% v/v) in DCM.

N – 18 – (N' – (carboxypropyl) methylene blue) – 3, 6, 9, 11, 15 – pentaoxaheptadecyl – 11 – mercaptounadecamide (18)
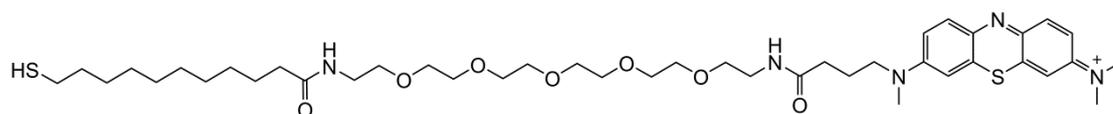
2-Chlorotrityl chloride resin (100 mg, 0.12 mmol) was placed in an empty solid phase extraction (SPE) tube and was swelled in DCM for 15 min; then the solvent was drained. A solution of **11-mercaptounadecanoic acid (11)** (56 mg, 0.24) in DCM (1.5 mL) was added to the resin and allowed to stir for 16 h (tube rotator). The resin was washed with DCM (3 × 1.5 mL), after which the remaining, unreacted, 2-chlorotrityl chloride groups were inactivated using capping cocktail A (1 mL, 2 × 2 min). The resin was washed with DCM (3 x 1.5 mL) and DMF (3 x 1.5 mL).

A solution of **(12)**, (85 mg, 0.36 mmol), HOBt (49 mg, 0.36 mmol), DIC (56 μL, 0.36 mmol) and DIPEA (70 μL, 0.36 mmol) was preincubated for five minutes in DMF (1.5 mL), then added to the resin and the reaction mixture stirred for 16 h. The resin was then washed with DMF (3 × 1.5 mL) and DCM (3 × 1.5 mL).

A solution of 4-toluenesulfonyl chloride (228 mg, 1.2 mmol), DMAP (29 mg, 0.24 mmol) and triethylamine (167 μL, 1.2 mmol) in DCM (1.5 mL) was added to the resin, and the reaction mixture was left to react overnight. The following day, the resin was drained, washed with DCM (3 × 1.5 mL) and treated with a freshly prepared tosylation solution and allowed to react overnight again. Then, the resin was washed with DCM (3 × 1.5 mL) and thoroughly with DMF (5 × 1.5 mL) to remove all traces of DCM.

Next, a suspension of sodium azide (78 mg, 1.2 mmol) in DMF (1.5 mL) was added to the resin and the reaction mixture stirred for 72 h. The excess sodium azide was removed by washing with

DMF-H$_2$O (5 × 1.5 mL) and the remaining water was washed out with DMF (5 × 1.5 mL). The resin was then washed with DCM (3 × 1.5 mL).

The resin bound azide **(16)** was washed with THF (3 × 1.5 mL), dried under vacuum and transferred to a Schlenk vessel. Then, a solution of anhydrous SnCl$_2$ (157 mg, 0.83 mmol) in THF (4 mL) was added to the vessel. The vessel was fitted with a charcoal scrubber and thiophenol (246 μL, 3.32 mmol) was added followed by DIPEA (786 μL, 4.15 mmol). The solution was stirred gently for 1 h. The reaction was quenched by filtering the resin, and the filtrate was collected in a bleach bath (10% in H$_2$O). The resin was washed with THF-H$_2$O (2:1, 3 × 10 mL), then THF (3 × 10 mL), and finally with DCM (3 × 10 mL). The resin-bound amine was transferred back to an SPE tube, washed with diethyl ether (1 × 1.5 mL), dried under high vacuum for 2 h and was then swelled in DMF.

A solution of *N*-(carboxypropyl) methylene blue **(5)** (128 mg, 0.36 mmol), DIC (56 μL, 0.36 mmol), HOBt (49 mg, 0.36 mmol) and collidine (54μL, 0.36 mmol) was dissolved in DMF and then added to the resin bound amine **(17)**. The reaction mixture was protected from light (by wrapping the SPE tube in aluminium foil) and stirred overnight. The solution was drained and the resin was washed with DMF (3 × 1.5 mL) and DCM (3 × 1.5 mL).

Next, the resin was washed with diethyl ether (1 × 1.5 mL), dried under high vacuum for 2 h and then treated with washes of cleavage cocktail B (1.5 mL, 3 × 2 min). The combined washes were concentrated to approx. 0.5 mL and precipitated into cold diethyl ether (25 mL; −20 °C) and left in a freezer overnight (-18 °C). The precipitate was collected by centrifugation (2 min, 40,000 rpm) and subjected to reverse phase chromatography, starting at 100% H$_2$O (+0.1% TFA) and moving to 100% MeOH (+0.1% TFA) in 5% increments, collecting each solvent mixture as a separate 10 mL fraction. Each fraction was analysed by TLC and the purity of the most intensely blue spots were assessed by LC-MS. All fractions containing the pure target compound were combined and the solvent removed *in vacuo* to yield MB-LCAT-OEG as a dark blue solid (11.1 mg). **ESI-LC-MS:** Calcd. for C$_{42}$H$_{68}$N$_5$O$_7$S$_2$ *m/z* 818.4 [M+H]$^+$; found 818.5; t$_R$ = 1.83 min (Figure B.3). The product was dissolved in ethanol and stored at 4 °C.
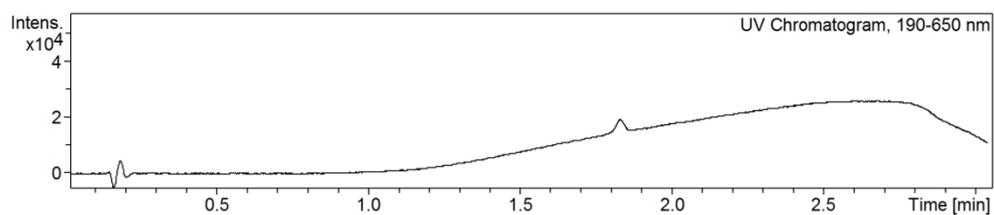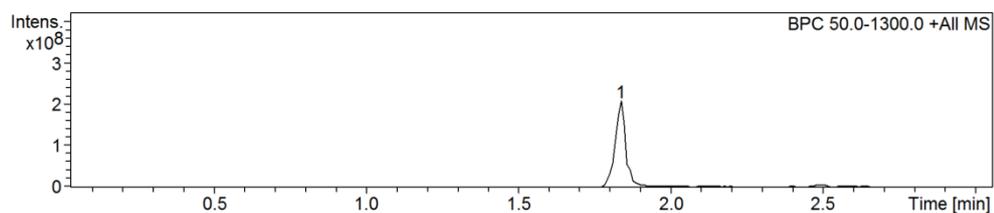
#	Cmpd. Label	RT [min]	Range [min]	Max. m/z	Area	Area %	Area Frac. %
1	Cmpd 1, 1.83 min	1.83	1.73 - 2.02	818.5	533624907	100.0	100.0

Cmpd 1, 1.83 min
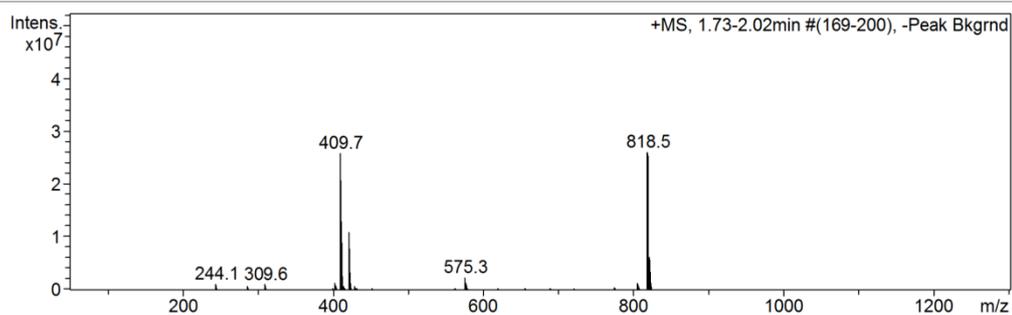
Figure B.3: ESI-LC-MS of LCAT-OEG-MB (18) (obtained on a Bruker HCT Ulltra mass spectrometer, School of Chemistry, University of Leeds)

Abbreviations

Ab	antibody
AC	alternating current
Ag	silver
AgCl	silver chloride
AM	antibody mimetic
AR	ankyrin repeat
Au	gold
AWACSS	automated water analyser computer supported system
BAW	bulk acoustic wave
BEWS	biological early warning systems
BSTG	BioScreening Technology Group
CDK	Cyclin-dependent kinase
CDR	complementarity determining region
cfu	colony-forming unit
Co	cobalt
Cr	chromium
CV	cyclic voltammetry
DARPins	designed ankyrin repeat proteins
DC	direct current
DCF	diclofenac
DCM	dichloromethane
DIC	diisopropylcarbodiimide
DIPEA	N,N-Diisopropylethylamine
TFA	trifluoroacetic acid
TES	triethylsilane
DMAP	4-dimethylaminopyridine
DMF	dimethylformamide
DNA	deoxyribonucleic acid
EC	emerging contaminant
EDC	ethyl-(dimethylaminopropyl)-carbodiimide
EDCs	endocrine disruptors
EIS	electrochemical impedance spectroscopy
ELISA	enzyme-linked immunosorbent assay

ENP	engineered nanoparticle
Et₂O	diethyl ether
EtOAc	ethyl acetate
FDA	(US) Food and Drug Administration
Fe	iron
FR	framework region
FT	Fourier transform
FWHM	full-width half maximum
GC	gas chromatography
GFP	green fluorescent protein
hCG	human chorionic gonadotropin
HER2	human epidermal growth factor
Hg	mercury
HOBt	hydroxybenzotriazole
HPLC	high performance liquid chromatography
HPV16	human papillomavirus 16
HRGC	high resolution gas chromatography
HRMS	high resolution mass spectrometry
HRP	horseradish peroxidase
IC$_{50}$	inhibitory concentration (causing 50% inhibition of binding)
IHP	inner Helmholtz plane
IPE	ideal polarised electrode
IR	infrared
IUPAC	International Union of Pure and Applied Chemistry
LB	lysogeny broth
LC	liquid chromatography
LCAT	long-chained alkanethiols
LOD	limit of detection
MB	methylene blue
MCT	mercury-cadmium-telluride
EtOH	ethanol
MeCN	acetonitrile
MeOH	methanol
MIP	molecularly imprinted polymer
MIR	mid-infrared region
MRM	multiple reaction monitoring
MS	mass spectrometry

MUA	11-mercaptoundecanoic acid
MZI	Mach-Zehnder interferometry
NHS	N-hydroxysuccinimide
NS1	non-structural protein 1
NSAID	non-steroidal anti-inflammatory drug
OEG	oligoethylene glycol
OHP	outer Helmholtz plane
Os	osmium
PAH	polycyclic aromatic hydrocarbons
PB 7	(sodium) phosphate buffer (pH 7)
PCET	proton-coupled electron transfer
PCP	personal care product
PCR	polymerase chain reaction
Pd	palladium
PDB	protein data bank
PEM	photoelastic modulator
PM-IRRAS	Polarisation modulation-infrared reflection-absorption spectroscopy
POCIS	polar organic chemical integrative sampler
Pt	platinum
PZET	piezoelectric transducer
QCM-D	quartz crystal microbalance with dissipation monitoring
RIANA	River ANAlyser
RIfS	reflectometric interference spectroscopy
RNA	ribonucleic acid
Ru	ruthenium
SAM	self-assembled monolayer
SAW	surface acoustic wave
scFv	single chain variable fragments
SELEX	systematic evolution of ligands by exponential enrichment
SiC	silicon carbide
SiO$_2$	silicon dioxide
SPE	solid phase extraction
SPR	surface plasmon resonance
SQT	Stefin A quadruple mutant-Tracy
ssDNA	single-stranded DNA
SteA	human cystatin Stefin A
STM	stefin A triple mutant scaffold

SUMO	small-ubiquitin-like modifier
Taq	*Thermus aquaticus*
THF	tetrahydrofuran
Ti	titanium
TLC	thin-layer chromatography
TMB	3,3',5,5'-tetramethylbenzidine
t_R	retention time
TrxA	thioredoxin
TWA	time-weighted average
US-EPA	US Environmental Protection Agency
UV	ultraviolet
v/v	volume/volume
ZnSe	zinc selenide

References

[1]   N. B. Grimm, S. Faeth, N. Golubiewski, C. Redman, J. Wu, X. Bai and J. Briggs, 'Global Change and the Ecology of Cities', *Science*, vol. 319, no. 5864, pp. 756-760, 2008.

[2]   G. Anderson and P. Hussey, 'Population aging: a comparison among industrialized countries', *Health Affairs*, vol. 19, no. 3, pp. 191-203, 2000.

[3]   C. Redshaw, W. Stahl-Timmins, L. Fleming, I. Davidson and M. Depledge, 'Potential Changes in Disease Patterns and Pharmaceutical Use in Response to Climate Change', *J. Toxicol. Environ. Health, Part B*, vol. 16, no. 5, pp. 285-320, 2013.

[4]   F. Stanczyk, D. Archer and B. Bhavnani, 'Ethinyl estradiol and 17β-estradiol in combined oral contraceptives: pharmacokinetics, pharmacodynamics and risk assessment', *Contraception*, vol. 87, no. 6, pp. 706-727, 2013.

[5]   I. Falconer, H. Chapman, M. Moore and G. Ranmuthugala, 'Endocrine-disrupting compounds: A review of their challenge to sustainable and safe water supply and water reuse', *Environ. Toxicol.*, vol. 21, no. 2, pp. 181-191, 2006.

[6]   A. Boxall, M. Rudd, B. Brooks, D. Caldwell, K. Choi, S. Hickmann, E. Innes, K. Ostapyk, J. Staveley, T. Verslycke, G. Ankley, K. Beazley, S. Belanger, J. Berninger, P. Carriquiriborde, A. Coors, P. DeLeo, S. Dyer, J. Ericson, F. Gagné, J. Giesy, T. Gouin, L. Hallstrom, M. Karlsson, D. Larsson, J. Lazorchak, F. Mastrocco, A. McLaughlin, M. McMaster, R. Meyerhoff, R. Moore, J. Parrott, J. Snape, R. Murray-Smith, M. Servos, P. Sibley, J. Straub, N. Szabo, E. Topp, G. Tetreault, V. Trudeau and G. Van Der Kraak, 'Pharmaceuticals and Personal Care Products in the Environment: What Are the Big Questions?', *Environ. Health. Perspect.*, vol. 120, no. 9, pp. 1221-1229, 2012.

[7]   A. Johnson, E. Dumont, R. Williams, R. Oldenkamp, I. Cisowska and J. Sumpter, 'Do Concentrations of Ethinylestradiol, Estradiol, and Diclofenac in European Rivers Exceed Proposed EU Environmental Quality Standards?', *Environ. Sci. Technol.*, vol. 47, no. 21, pp. 12297-12304, 2013.

[8]   G. Swan, V. Naidoo, R. Cuthbert, R. Green, D. Pain, D. Swarup, V. Prakash, M. Taggart, L. Bekker, D. Das, J. Diekmann, M. Diekmann, E. Killian, A. Meharg, R. Patra, M. Saini and K. Wolter, 'Removing the Threat of Diclofenac to Critically Endangered Asian Vultures', *Plos. Biol.*, vol. 4, no. 3, p. e66, 2006.

[9]   M. Saini, M. Taggart, D. Knopp, S. Upreti, D. Swarup, A. Das, P. Gupta, R. Niessner, V. Prakash, R. Mateo and R. Cuthbert, 'Detecting diclofenac in livestock carcasses in India with

an ELISA: A tool to prevent widespread vulture poisoning', *Environ. Pollut.*, vol. 160, pp. 11-16, 2012.

[10]   A. Boxall, *New and Emerging Water Pollutants arising from Agriculture*, 1st ed. OECD, 2012.

[11]   J. McMurry, *Organic chemistry*, 7th ed., Pacific Grove, CA: Brooks/Cole Pub., 2007.

[12]   R. Smith, *Understanding mass spectra*. Hoboken, N.J.: Wiley Interscience, 2004.

[13]   US EPA, 'Method 1694: Pharmaceuticals and Personal Care Products in Water, Soil, Sediment, and Biosolids by HPLC/MS/MS', US EPA, Washington, DC; 2007. Available: https://www.epa.gov/sites/production/files/2015-10/documents/method_1694_2007.pdf. [Accessed 19 June 2017].

[14]   US EPA, 'Method 1698: Steroids and Hormones in Water, Soil, Sediment, and Biosolids by HRGC/HRMS', US EPA, Washington, DC; 2007. Available: https://www.epa.gov/sites/production/files/2015-10/documents/method_1698_2007.pdf. [Accessed 19 June 2017].

[15]   R. Loos, 'Analytical methods relevant to the European Commission's 2012 proposal on priority substances under the Water Framework Directive', Publications Office of the European Union, Ispra, Italy, 2012.

[16]   E.T Furlong, M. C. Noriega, C.J. Kanagy, L. K. Kanagy, L. J. Coffey, and M. R. Burkhardt., 'Determination of human-use pharmaceuticals in filtered water by direct aqueous injection– high-performance liquid chromatography/ tandem mass spectrometry', U.S. Geological Survey Techniques and Methods, book 5, chap. B10, p. 49, 2014. Available: http://pubs.usgs.gov/tm/5b10/pdf/tm10-b5.pdf. [Accessed 19 June 2017].

[17]   I. Allan, 'A "toolbox" for biological and chemical monitoring requirements for the European Union's Water Framework Directive', *Talanta*, vol. 69, pp. 302-322, 2006.

[18]   I. Allan, J. Knutsson, N. Guigues, G. Mills, A. Fouillac and R. Greenwood, 'Chemcatcher® and DGT passive sampling devices for regulatory monitoring of trace metals in surface water', *J. Environ. Monit.*, vol. 10, no. 7, p. 821, 2008.

[19]   I. Allan, K. Booij, A. Paschke, B. Vrana, G. Mills and R. Greenwood, 'Field Performance of Seven Passive Sampling Devices for Monitoring of Hydrophobic Substances', *Environ. Sci. Technol.*, vol. 43, no. 14, pp. 5383-5390, 2009.

[20]   X. Jiang, 'Immunosensors for detection of pesticide residues', *Biosens. Bioelectron.*, vol. 23, no. 11, pp. 1577–1587, 2008.

[21]   A. Kumar and C. Lee, 'Synthesis and Biomedical Applications of Graphene: Present and Future Trends' in *Advances in Graphene Science*, 1st ed., M. Aliofkhazraei, InTech. 2013. Available: https://www.intechopen.com/books/advances-in-graphene-science/synthesis-and-biomedical-applications-of-graphene-present-and-future-trends. [Accessed 19 June 2017]

[22] S. Rodriguez-Mozaz, M. J. Lopez de Alda and D. Barcelo, 'Achievements of the RIANA and AWACSS EU Projects: Immunosensors for the Determination of Pesticides, Endocrine Disrupting Chemicals and Pharmaceuticals', in *Biosensors for Environmental Monitoring of Aquatic Systems*, D. Barceló and P. D. Hansen, Springer-Verlag Berlin Heidelberg, 2009, pp. 33-46.

[23] A. Lesk, *Introduction to protein architecture*. Oxford: Oxford University Press, 2001.

[24] M. Arugula and A. Simonian, 'Novel trends in affinity biosensors: current challenges and perspectives', *Meas. Sci. Technol.*, vol. 25, no. 3, p. 032001, 2014.

[25] K. Song, S. Lee and C. Ban, 'Aptamers and Their Biological Applications', *Sensors*, vol. 12, no. 12, pp. 612-631, 2012.

[26] V. Ruigrok, M. Levisson, M. Eppink, H. Smidt and J. van der Oost, 'Alternative affinity tools: more attractive than antibodies?', *Biochem. J.*, vol. 436, no. 1, pp. 1-13, 2011.

[27] C. Tiede, A. Tang, S. Deacon, U. Mandal, J. Nettleship, R. Owen, S. George, D. Harrison, R. Owens, D. Tomlinson and M. McPherson, 'Adhiron: a stable and versatile peptide display scaffold for molecular recognition applications', *Protein. Eng. Des. Sel.*, vol. 27, no. 5, pp. 145-155, 2014.

[28] A. Rawlings, J. Bramble, A. Tang, L. Somner, A. Monnington, D. Cooke, M. McPherson, D. Tomlinson and S. Staniland, 'Phage display selected magnetite interacting Adhirons for shape controlled nanoparticle synthesis', *Chem. Sci.*, vol. 6, no. 10, pp. 5586-5594, 2015.

[29] H. Kyle, K. Wickson, J. Stott, G. Burslem, A. Breeze, C. Tiede, D. Tomlinson, S. Warriner, A. Nelson, A. Wilson and T. Edwards, 'Exploration of the HIF-1α/p300 interface using peptide and Adhiron phage display technologies', *Mol. BioSyst.*, vol. 11, no. 10, pp. 2738-2749, 2015.

[30] M. Raina, R. Sharma, S. Deacon, C. Tiede, D. Tomlinson, A. Davies, M. McPherson and C. Wälti, 'Antibody mimetic receptor proteins for label-free biosensors', *Analyst*, vol. 140, no. 3, pp. 803-810, 2015.

[31] R. Sharma, S. Deacon, D. Nowak, S. George, M. Szymonik, A. Tang, D. Tomlinson, A. Davies, M. McPherson and C. Wälti, 'Label-free electrochemical impedance biosensor to detect human interleukin-8 in serum with sub-pg/ml sensitivity', *Biosens. Bioelectron.*, vol. 80, pp. 607-613, 2016.

[32] G. Muthuraman, T. Teng, C. Leh and I. Norli, 'Extraction and recovery of methylene blue from industrial wastewater using benzoic acid as an extractant', *J. Hazard. Mater.*, vol. 163, no. 1, pp. 363-369, 2009.

[33] B. Coulibaly, A. Zoungrana, F. Mockenhaupt, R. Schirmer, C. Klose, U. Mansmann, P. Meissner and O. Müller, 'Strong Gametocytocidal Effect of Methylene Blue-Based Combination Therapy against Falciparum Malaria: A Randomised Controlled Trial', *PLoS ONE*, vol. 4, no. 5, p. e5318, 2009.

[34] A. Hulanicki and S. Głąb, *Redox indicators. Characteristics and applications*. Great Britain: Pergamon Press Ltd., 1978, pp. pp. 463-498.

[35] *Dictionary.com*, 2017. [Online] Available: http://www.dictionary.com/browse/limnetic. [Accessed 19 June 2017].

[36] D. Skoog, F. Holler and T. Nieman, *Principles of instrumental analysis*. Philadelphia: Saunders College Pub., 1998.

[37] D. Wild, *The immunoassay handbook*, 4th ed. Oxford: Elsevier, 2013.

[38] S. Liu, Z. Zheng and X. Li, 'Advances in pesticide biosensors: current status, challenges, and future perspectives', *Anal. Bioanal. Chem.*, vol. 405, no. 1, pp. 63-90, 2012.

[39] Abnova.com, 'ELISA Pairs Kits - Resources - Support - Abnova', 2015. [Online]. Available: http://www.abnova.com/support/resources.asp?switchfunctionid={70196CA1-59B1-40D0-8394-19F533EB108F}. [Accessed 19 June 2017].

[40] V. Morozova, A. Levashova and S. Eremin, 'Determination of pesticides by enzyme immunoassay', *J. Anal. Chem.*, vol. 60, no. 3, pp. 202-217, 2005.

[41] N. Lisitsyn, A. Chernyi, I. Nikitina, V. Karpov and S. Beresten, 'Methods of protein immunoanalysis', *Mol. Biol.*, vol. 48, no. 5, pp. 624-633, 2014.

[42] J. Gabaldón, A. Maquieira and R. Puchades, 'Current Trends in Immunoassay-Based Kits for Pesticide Analysis', *Crit. Rev. Food Sci. Nutr.*, vol. 39, no. 6, pp. 519-538, 1999.

[43] M. Pomes, E. Thurman, D. Aga and D. Goolsby, 'Evaluation of Microtiter-Plate Enzyme-Linked Immunosorbent Assay for the Analysis of Triazine and Chloroacetanilide Herbicides in Rainfall', *Environ. Sci. Technol.*, vol. 32, no. 1, pp. 163-168, 1998.

[44] T. Giersch, 'A new monoclonal antibody for the sensitive detection of atrazine with immunoassay in microtiter plate and dipstick format', *J. Agric. Food Chem.*, vol. 41, no. 6, pp. 1006-1011, 1993.

[45] E. Thurman, M. Meyer, M. Pomes, C. Perry and A. Schwab, 'Enzyme-linked immunosorbent assay compared with gas chromatography/mass spectrometry for the determination of triazine herbicides in water', *Anal. Chem.*, vol. 62, no. 18, pp. 2043-2048, 1990.

[46] A. Deng, M. Himmelsbach, Q. Zhu, S. Frey, M. Sengl, W. Buchberger, R. Niessner and D. Knopp, 'Residue Analysis of the Pharmaceutical Diclofenac in Different Water Types Using ELISA and GC−MS', *Environ. Sci. Technol.*, vol. 37, no. 15, pp. 3422-3429, 2003.

[47] European Commission, 'Proposal for a directive of the European Parliament and of the Council amending Directives 2000/60/EC and 2008/105/EC as regards priority substances in the field of water policy', OJ, Brussels, 2012.

[48] M. Huebner, E. Weber, R. Niessner, S. Boujday and D. Knopp, 'Rapid analysis of diclofenac in freshwater and wastewater by a monoclonal antibody-based highly sensitive ELISA', *Anal. Bioanal. Chem.*, vol. 407, no. 29, pp. 8873-8882, 2015.

[49] 'Anti-Diclofenac Antibody Products', *Biocompare.com*, 2017. [Online]. Available: http://www.biocompare.com/pfu/110447/soids/343034/Antibodies/Diclofenac. [Accessed 19 June 2017].

[50] V. Perumal and U. Hashim, 'Advances in biosensors: Principle, architecture and applications', *J. Appl. Biomed.*, vol. 12, no. 1, pp. 1-15, 2014.

[51] R.S. Lowe , 'Overview of biosensor and bioarray technologies', in *Handbook of Biosensors and Biochips*, R.S. Marks, C.R. Lowe, D. C. Cullen, H. H. Weetall and I. Karube , Wiley, Weinheim, 2007.

[52] B. Leca-Bouvier and L. Blum, 'Enzyme for Biosensing Applications', in *Recognition Receptors in Biosensors*, 1st ed., M. Zourob, New York: Springer, 2010, pp. 177-220.

[53] A. Deng and H. Yang, 'A multichannel electrochemical detector coupled with an ELISA microtiter plate for the immunoassay of 2,4-dichlorophenoxyacetic acid', *Sens. Actuators, B*, vol. 124, no. 1, pp. 202-208, 2007.

[54] J. Homola, 'Present and future of surface plasmon resonance biosensors', *Anal. Bioanal. Chem.*, vol. 377, no. 3, pp. 528-539, 2003.

[55] D. Shankaran, K. Gobi And N. Miura, 'Recent advancements in surface plasmon resonance immunosensors for detection of small molecules of biomedical, food and environmental interest', *Sens. Actuators B*, vol. 121, no. 1, pp. 158-177, 2007.

[56] E. Mauriz, A. Calle, L. Lechuga, J. Quintana, A. Montoya and J. Manclús, 'Real-time detection of chlorpyrifos at part per trillion levels in ground, surface and drinking water samples by a portable surface plasmon resonance immunosensor', *Anal.Chim. Acta*, vol. 561, no. 1-2, pp. 40-47, 2006.

[57] V. Hodnik and G. Anderluh, 'Toxin Detection by Surface Plasmon Resonance', *Sensors*, vol. 9, no. 3, pp. 1339-1354, 2009.

[58] 'How Does Surface Plasmon Resonance Work?', *BionsensingUSA* [Online]. Available: http://biosensingusa.com/zh/technologies/surface-plasmon-resonance/surface-plasmon-resonance-work/. [Accessed 19 June 2017].

[59] J. Kirschner, 'Surface Acoustic Wave Sensors (SAWS): Design for Application', in *Microelectromechanical Systems*, 2010. Available: https://www.semanticscholar.org/paper/Surface-Acoustic-Wave-Sensors-SAWS-Design-for-Appl-Kirschner/0bbf94e76cb2f3b9f9c411ed57cab9f73c786e61. [Accessed 19 June 2017].

[60] 'QCM-D Technology - Biolin Scientific', *Biolin Scientific* [Online]. Available: http://www.biolinscientific.com/technology/qcm-d-technology/. [Accessed 19 June 2017].

[61] M. Dixon, 'Quartz Crystal Microbalance with Dissipation Monitoring: Enabling Real-Time Characterization of Biological Materials and Their Interactions', *J. Biomol. Tech.*, vol. 19, no. 3, pp. 151-158, 2008.

[62]   J. Přibyl, M. Hepel, J. Halámek and P. Skládal, 'Development of piezoelectric immunosensors for competitive and direct determination of atrazine', *Sens. Actuators B*, vol. 91, no. 1-3, pp. 333-341, 2003.

[63]   E. Gizeli, M. Thompson and D. Johannsmann, 'Special issue on acoustic wave sensor technology for biophysical and bioanalytical studies', *Sens Biosensing Res.*, vol. 11, p. 59, 2016.

[64]   K. Mitsakakis and E. Gizeli, 'Multi-sample acoustic biosensing microsystem for protein interaction analysis', *Biosens. Bioelectron.*, vol. 26, no. 11, pp. 4579-4584, 2011.

[65]   G. Papadakis, J. Friedt, M. Eck, D. Rabus, G. Jobst and E. Gizeli, 'Optimized acoustic biochip integrated with microfluidics for biomarkers detection in molecular diagnostics', *Biomed. Microdevices*, vol. 19, no. 3, 2017.

[66]   J. Berg, J. Tymoczko, L. Stryer and L. Stryer, *Biochemistry*. New York: W.H. Freeman, 2002.

[67]   I. Roitt, J. Brostoff and D. Male, *Immunology*, 7th ed. London: Mosby, 2006.

[68]   R. Goldsby, T. Kindt, B. Osborne and J. Kuby, *Immunology*, 5th ed. New York: W.H. Freeman, 2003

[69]   D. Nelson and M. Cox, *Lehninger principles of biochemistry*, 5th ed. New York: W.H. Freeman, 2008.

[70]   C. A Janeway, Jr, P. Travers, M. Walport and M. Shlomchik, *Immunobiology*, New York: Garland Science, 2001. Available: https://www.ncbi.nlm.nih.gov/books/NBK10757/. [Accessed 19 June 2017].

[71]   C. Kleanthous, *Protein-protein recognition*. Oxford: Oxford University Press, 2000.

[72]   P. Atkins and J. De Paula, *Atkins' Physical chemistry*, 9th ed. Oxford: Oxford University Press, 2009.

[73]   S. Reverdatto, D. Burz and A. Shekhtman, 'Peptide Aptamers: Development and Applications', *Curr. Top. Med. Chem.*, vol. 15, no. 12, pp. 1082-1101, 2015.

[74]   A. Nelson, 'Antibody fragments', *mAbs*, vol. 2, no. 1, pp. 77-83, 2010.

[75]   B. Zhang, Q. Mao, X. Zhang, T. Jiang, M. Chen, F. Yu and W. Fu, 'A novel piezoelectric quartz micro-array immunosensor based on self-assembled monolayer for determination of human chorionic gonadotropin', *Biosens. Bioelectron.*, vol. 19, no. 7, pp. 711-720, 2004.

[76]   J. Wackerlig and R. Schirhagl, 'Applications of Molecularly Imprinted Polymer Nanoparticles and Their Advances toward Industrial Use: A Review', *Anal. Chem.*, vol. 88, no. 1, pp. 250-261, 2016.

[77]   G. Vlatakis, L. Andersson, R. Müller and K. Mosbach, 'Drug assay using antibody mimics made by molecular imprinting', *Nature*, vol. 361, no. 6413, pp. 645-647, 1993.

[78]   I. Chianella, A. Guerreiro, E. Moczko, J. Caygill, E. Piletska, I. De Vargas Sansalvador, M. Whitcombe and S. Piletsky, 'Direct Replacement of Antibodies with Molecularly Imprinted

Polymer Nanoparticles in ELISA - Development of a Novel Assay for Vancomycin', *Anal. Chem.*, vol. 85, no. 17, pp. 8462-8468, 2013.

[79] J. Wackerlig and P. Lieberzeit, 'Molecularly imprinted polymer nanoparticles in chemical sensing - Synthesis, characterisation and application', *Sens. Actuators, B*, vol. 207, pp. 144-157, 2015.

[80] T. Schütze, B. Wilhelm, N. Greiner, H. Braun, F. Peter, M. Mörl, V. Erdmann, H. Lehrach, Z. Konthur, M. Menger, P. Arndt and J. Glökler, 'Probing the SELEX Process with Next-Generation Sequencing', *PLoS ONE*, vol. 6, no. 12, p. e29604, 2011.

[81] A. Ellington and J. Szostak, 'In vitro selection of RNA molecules that bind specific ligands', *Nature*, vol. 346, no. 6287, pp. 818-822, 1990.

[82] L. Krumpe and T. Mori, 'The Use of Phage-Displayed Peptide Libraries to Develop Tumor-Targeting Drugs', *Int. J. Pept. Res. Ther.*, vol. 12, no. 1, pp. 79-91, 2006.

[83] A. Johnson, Q. Song, P. Ko Ferrigno, P. Bueno and J. Davis, 'Sensitive Affimer and Antibody Based Impedimetric Label-Free Assays for C-Reactive Protein', *Anal. Chem.*, vol. 84, no. 15, pp. 6553-6560, 2012.

[84] J. McLeod and P. Ko Ferrigno, 'Antibody Alternatives', *The Scientist*, vol. 20, February 2016. Available: http://www.the-scientist.com/?articles.view/articleNo/45134/title/Antibody-Alternatives/. [Accessed 19 June 2017].

[85] 'An Affimer is not an aptamer', *Avacta.com* [Online].
Available: https://www.avacta.com/blogs/affimer-not-aptamer. [Accessed 19 June 2017].

[86] B. Geering and M. Fussenegger, 'Synthetic immunology: modulating the human immune system', *Trends Biotechnol.*, vol. 33, no. 2, pp. 65-79, 2015.

[87] C. Grönwall and S. Ståhl, 'Engineered affinity proteins - Generation and applications', *J. Biotechnol.*, vol. 140, no. 3-4, pp. 254-269, 2009.

[88] J. Löfblom, F. Frejd and S. Ståhl, 'Non-immunoglobulin based protein scaffolds', *Curr. Opin. Biotechnol.*, vol. 22, no. 6, pp. 843-848, 2011.

[89] K. Škrlec, B. Štrukelj and A. Berlec, 'Non-immunoglobulin scaffolds: a focus on their targets', *Trends Biotechnol.*, vol. 33, no. 7, pp. 408-418, 2015.

[90] M. Mascini, I. Palchetti and S. Tombelli, 'Nucleic Acid and Peptide Aptamers: Fundamentals and Bioanalytical Aspects', *Angew. Chem. Int. Ed.*, vol. 51, no. 6, pp. 1316-1332, 2012.

[91] P. Colas, B. Cohen, T. Jessen, I. Grishina, J. McCoy and R. Brent, 'Genetic selection of peptide aptamers that recognize and inhibit cyclin-dependent kinase 2', *Nature*, vol. 380, no. 6574, pp. 548-550, 1996.

[92] M. Gebauer and A. Skerra, 'Engineered protein scaffolds as next-generation antibody therapeutics', *Curr. Opin. Chem. Biol.*, vol. 13, no. 3, pp. 245-255, 2009.

[93]   'PRS-080: Pieris Pharmaceuticals, Inc. (PIRS)', *Pieris.com* [Online]. Available: http://www.pieris.com/pipeline/anemia-and-other-disease-areas/prs-080. [Accessed 19 June 2017].

[94]   'How KALBITOR® Works', *Kalbitor.com* [Online].
Available: https://www.kalbitor.com/how-kalbitor-works. [Accessed 19 June 2017].

[95]   J. Löfblom, J. Feldwisch, V. Tolmachev, J. Carlsson, S. Ståhl and F. Frejd, 'Affibody molecules: Engineered proteins for therapeutic, diagnostic and biotechnological applications', *FEBS Lett.*, vol. 584, no. 12, pp. 2670-2680, 2010.

[96]   J. Schilling, J. Schöppe and A. Plückthun, 'From DARPins to LoopDARPins: Novel LoopDARPin Design Allows the Selection of Low Picomolar Binders in a Single Round of Ribosome Display', *J. Mol. Biol.*, vol. 426, no. 3, pp. 691-721, 2014.

[97]   'Our Products - Molecular Partners', *Molecular Partners* [Online]. Available: https://www.molecularpartners.com/our-products/. [Accessed 19 June 2017].

[98]   E. Brient-Litzler, A. Pluckthun and H. Bedouelle, 'Knowledge-based design of reagentless fluorescent biosensors from a designed ankyrin repeat protein', *Protein Eng., Des. Sel.*, vol. 23, no. 4, pp. 229-241, 2009.

[99]   R. Woodman, J. Yeh, S. Laurenson and P. Ferrigno, 'Design and Validation of a Neutral Protein Scaffold for the Presentation of Peptide Aptamers', *J. Mol. Biol.*, vol. 352, no. 5, pp. 1118-1133, 2005.

[100] J. Davis, J. Tkac, S. Laurenson and P. Ferrigno, 'Peptide Aptamers in Label-Free Protein Detection: 1. Characterization of the Immobilized Scaffold', *Anal. Chem.*, vol. 79, no. 3, pp. 1089-1096, 2007.

[101] D. Evans, S. Johnson, S. Laurenson, G. Davies, P. Ko Ferrigno and C. Walti, 'Electrical protein detection in cell lysates using high-density peptide-aptamer microarrays', *J. Biol.*, vol. 7, no. 1, p. 3, 2008.

[102] P. Estrela, D. Paul, P. Li, S. Keighley, P. Migliorato, S. Laurenson and P. Ferrigno, 'Label-Free Detection of Protein interactions with peptide aptamers by open circuit potential measurement', *Electrochim. Acta*, vol. 53, no. 22, pp. 6489-6496, 2008.

[103] P. Estrela, D. Paul, Q. Song, L. Stadler, L. Wang, E. Huq, J. Davis, P. Ferrigno and P. Migliorato, 'Label-Free Sub-picomolar Protein Detection with Field-Effect Transistors', *Anal. Chem.*, vol. 82, no. 9, pp. 3531-3536, 2010.

[104] J. Davis, J. Tkac, R. Humphreys, A. Buxton, T. Lee and P. Ko Ferrigno, 'Peptide Aptamers in Label-Free Protein Detection: 2. Chemical Optimization and Detection of Distinct Protein Isoforms', *Anal. Chem.*, vol. 81, no. 9, pp. 3314-3320, 2009.

[105] S. Johnson, D. Evans, S. Laurenson, D. Paul, A. Davies, P. Ko Ferrigno and C. Wälti, 'Surface-Immobilized Peptide Aptamers as Probe Molecules for Protein Detection', *Anal. Chem.*, vol. 80, no. 4, pp. 978-983, 2008.

[106] W. Shu, S. Laurenson, T. Knowles, P. Ko Ferrigno and A. Seshia, 'Highly specific label-free protein detection from lysed cells using internally referenced microcantilever sensors', *Biosens. Bioelectron.*, vol. 24, no. 2, pp. 233-237, 2008.

[107] S. Straw, P. Ferrigno, Q. Song, D. Tomlinson and F. Galdo, 'Proof of concept study to identify candidate biomarkers of fibrosis using high throughput peptide aptamer microarray and validate by enzyme linked immunosorbant assay', *J. Biomed. Sci. Eng.*, vol. 06, no. 08, pp. 32-42, 2013.

[108] S. Laurenson, M. Pett, K. Hoppe-Seyler, C. Denk, F. Hoppe-Seyler, N. Coleman and P. Ko Ferrigno, 'Development of peptide aptamer microarrays for detection of HPV16 oncoproteins in cell extracts', *Anal. Biochem.*, vol. 410, no. 2, pp. 161-170, 2011.

[109] L. Stadler, T. Hoffmann, D. Tomlinson, Q. Song, T. Lee, M. Busby, Y. Nyathi, E. Gendra, C. Tiede, K. Flanagan, S. Cockell, A. Wipat, C. Harwood, S. Wagner, M. Knowles, J. Davis, N. Keegan and P. Ko Ferrigno, 'Structure−function studies of an engineered scaffold protein derived from Stefin A. II: Development and applications of the SQT variant', *Protein Eng., Des. Sel.*, vol. 24, no. 9, pp. 751-763, 2011.

[110] B. Porebski and A. Buckle, 'Consensus protein design', *Protein Eng., Des. Sel.*, vol. 29, no. 7, pp. 245-251, 2016.

[111] P. Carter, 'Introduction to current and future protein therapeutics: A protein engineering perspective', *Exp. Cell. Res.*, vol. 317, no. 9, pp. 1261-1269, 2011.

[112] R. Spruijt, C. Wolfs and M. Hemminga, 'M13 phage', in *Encyclopedia of Molecular Biology*, T. Creighton, New York: John Wiley & Sons, Inc., 1999.

[113] G. Smith and V. Petrenko, 'Phage Display', *Chem. Rev.*, vol. 97, no. 2, pp. 391-410, 1997.

[114] G. Løset, N. Roos, B. Bogen and I. Sandlie, 'Expanding the Versatility of Phage Display II: Improved Affinity Selection of Folded Domains on Protein VII and IX of the Filamentous Phage', *PLoS ONE*, vol. 6, no. 2, p. e17433, 2011.

[115] R. King, C. Tiede, K. Simmons, C. Fishwick, D. Tomlinson and R. Ajjan, 'Inhibition of complement C3 and fibrinogen interaction: a potential novel therapeutic target to reduce cardiovascular disease in diabetes', *The Lancet*, vol. 385, p. S57, 2015.

[116] C. Aldinger, D. Fernandez de Landa, B. Gomes, H. Kyle, L. McMorran, M. Johnson and P. Ko Ferrigno, 'Highly-specific Affimer® Binders to the NS1 protein of Zika virus with potential utility in diagnostics', *Avacta.com*, 2016. Available: https://www.avacta.com/sites/life_sciences/files/resource/ZikaPoster_0.pdf. [Accessed 19 June 2017].

[117] L. Dicker, R. Ford, L. McMorran, C. Räuber, A. Tang, C. Tiede, A. Maqbool, D. Williamson, F. Esteves, F. Kampmeier, M. McPherson, P. Ko Ferrigno, D. Tomlinson and M. Johnson, 'Affimer Technology - Next Generation Affinity Reagents', *Avacta.com*, 2014.

Available: https://www.avacta.com/resources/affimer-technology-next-generation-affinity-reagents. [Accessed 19 June 2017].

[118] V. Silin, H. Weetall and D. Vanderah, 'SPR Studies of the Nonspecific Adsorption Kinetics of Human IgG and BSA on Gold Surfaces Modified by Self-Assembled Monolayers (SAMs)', *J. Colloid Interface Sci.*, vol. 185, no. 1, pp. 94-103, 1997.

[119] J. Murray, D. Nowak, L. Pukenas, R. Azhar, M. Guillorit, C. Wälti, K. Critchley, S. Johnson and R. Bon, 'Solid phase synthesis of functionalised SAM-forming alkanethiol–oligoethyleneglycols', *J. Mater. Chem. B*, vol. 2, no. 24, p. 3741, 2014.

[120] J. Love, L. Estroff, J. Kriebel, R. Nuzzo and G. Whitesides, 'Self-Assembled Monolayers of Thiolates on Metals as a Form of Nanotechnology', *Chem. Rev.*, vol. 105, no. 4, pp. 1103-1170, 2005.

[121] F. Schreiber, 'Structure and growth of self-assembling monolayers', *Prog. Surf. Sci.*, vol. 65, no. 5-8, pp. 151-257, 2000.

[122] D. Mandler and S. Kraus-Ophir, 'Self-assembled monolayers (SAMs) for electrochemical sensing', *Journal of Solid State Electrochemistry*, vol. 15, no. 7-8, pp. 1535-1558, 2011.

[123] P. Atkins and J. De Paula, *Elements of physical chemistry*, 5th ed. Oxford: Oxford University Press, 2009.

[124] C. Vericat, M. Vela, G. Benitez, P. Carro and R. Salvarezza, 'Self-assembled monolayers of thiols and dithiols on gold: new challenges for a well-known system', *Chem. Soc. Rev.*, vol. 39, no. 5, p. 1805, 2010.

[125] M. Ho, P. Li, P. Estrela, S. Goodchild and P. Migliorato, 'Detection of Molecular Interactions with Modified Ferrocene Self-Assembled Monolayers', *J. Phys. Chem. B*, vol. 114, no. 32, pp. 10661-10665, 2010.

[126] A. Eckermann, D. Feld, J. Shaw and T. Meade, 'Electrochemistry of redox-active self-assembled monolayers', *Coord. Chem. Rev.*, vol. 254, no. 15-16, pp. 1769-1802, 2010.

[127] P. Harder, M. Grunze, R. Dahint, G. Whitesides and P. Laibinis, 'Molecular Conformation in Oligo(ethylene glycol)-Terminated Self-Assembled Monolayers on Gold and Silver Surfaces Determines Their Ability To Resist Protein Adsorption', *J. Phys. Chem. B*, vol. 102, no. 2, pp. 426-436, 1998.

[128] A. Bard and L. Faulkner, *Electrochemical methods*, 2nd ed. New York: Wiley, 2001.

[129] 'IUPAC Gold Book - inner Helmholtz plane (IHP)', Goldbook.iupac.org, Available: http://goldbook.iupac.org/I03048.html. [Accessed 19 June 2017].

[130] E. Barou, M. Bouvet, O. Heintz and R. Meunier-Prest, 'Electrochemistry of methylene blue at an alkanethiol modified electrode', *Electrochim. Acta*, vol. 75, pp. 387-392, 2012.

[131] 'Basics of EIS: Electrochemical Research-Impedance', *Gamry.com* Available: https://www.gamry.com/application-notes/EIS/basics-of-electrochemical-impedance-spectroscopy/. [Accessed 19 June 2017].

[132] S. Creager and T. Wooster, 'A New Way of Using ac Voltammetry To Study Redox Kinetics in Electroactive Monolayers', *Anal. Chem.*, vol. 70, no. 20, pp. 4257-4263, 1998.

[133] C. Lu and A. Czanderna, 'Applications of Piezoelectric Quartz Crystal Microbalances, Volume 7', in *Methods and Phenomena*, 1st ed., S. Wolsky and A. Czanderna, Denver, CO: Elsevier, 1984.

[134] 'Piezoelectric History', *Physical Chemistry Laboratory*. Available: http://www.tau.ac.il/~phchlab/experiments_new/QCM/piezoelectricity.html. [Accessed 19 June 2017].

[135] 'QCM Theoretical Background', *Physical Chemistry Laboratory*. Available: http://www.tau.ac.il/~phchlab/experiments_new/QCM/theory.html. [Accessed 19 June 2017].

[136] D. Buttry and M. Ward, 'Measurement of interfacial processes at electrode surfaces with the electrochemical quartz crystal microbalance', *Chem. Rev.*, vol. 92, no. 6, pp. 1355-1379, 1992.

[137] 'The piezoelectric effect in ceramic materials', *Morgan Technical Ceramics*. Available: http://www.morgantechnicalceramics.com/media/4126/chapter2.pdf. [Accessed 19 June 2017].

[138] K. Marx, 'Quartz Crystal Microbalance: A Useful Tool for Studying Thin Polymer Films and Complex Biomolecular Systems at the Solution−Surface Interface', *Biomacromolecules*, vol. 4, no. 5, pp. 1099-1120, 2003.

[139] E. Sengpiel, 'Harmonics, overtones and the fundamental', *Sengpielaudio.com*. Available: http://www.sengpielaudio.com/calculator-harmonics.htm. [Accessed 19 June 2017].

[140] 'Q-Sense: Your world on a sensor', *Biolin Scientific*. Available: http://www.biolinscientific.com/zafepress.php?url=%2Fpdf%2FQ-Sense%2FProducts%2FSensor%20%26%20Modules%2FQ-Sensors%20web.pdf. [Accessed 19 June 2017].

[141] M. Rodahl, F. Höök, A. Krozer, P. Brzezinski and B. Kasemo, 'Quartz crystal microbalance setup for frequency and Q‐factor measurements in gaseous and liquid environments', *Rev. Sci. Instrum.*, vol. 66, no. 7, pp. 3924‐3930, 1995.

[142] E. Casero, L. Vázquez, A. Parra-Alfambra and E. Lorenzo, 'AFM, SECM and QCM as useful analytical tools in the characterization of enzyme-based bioanalytical platforms', *The Analyst*, vol. 135, no. 8, p. 1878, 2010.

[143] A. Wu and M. Syu, 'Synthesis of bilirubin imprinted polymer thin film for the continuous detection of bilirubin in an MIP/QCM/FIA system', *Biosens. Bioelectron.*, vol. 21, no. 12, pp. 2345-2353, 2006.

[144] C. O'Sullivan and G. Guilbault, 'Commercial quartz crystal microbalances – theory and applications', *Biosens. Bioelectron.*, vol. 14, no. 8-9, pp. 663-670, 1999.

[145] 'Q-Sense Services - Biolin Scientific - QCM-D FAQ', *Biolin Scientific*. Available: http://www.biolinscientific.com/q-sense/services/?category=QCM-D+FAQ. [Accessed 19 June 2017].

[146] M. Thompson, A. Kipling, W. Duncan-Hewitt, L. Rajaković and B. Čavić-Vlasak, 'Thickness-shear-mode acoustic wave sensors in the liquid phase. A review', *The Analyst*, vol. 116, no. 9, pp. 881-890, 1991.

[147] K. Kanazawa and J. Gordon, 'Frequency of a quartz microbalance in contact with liquid', *Anal. Chem.*, vol. 57, no. 8, pp. 1770-1771, 1985.

[148] N. Cho, K. Kanazawa, J. Glenn and C. Frank, 'Employing Two Different Quartz Crystal Microbalance Models To Study Changes in Viscoelastic Behavior upon Transformation of Lipid Vesicles to a Bilayer on a Gold Surface', *Anal. Chem.*, vol. 79, no. 18, pp. 7027-7035, 2007.

[149] N. Cho, C. Frank, B. Kasemo and F. Höök, 'Quartz crystal microbalance with dissipation monitoring of supported lipid bilayers on various substrates', *Nature Protocols*, vol. 5, no. 6, pp. 1096-1106, 2010.

[150] S. Hauck, S. Drost, E. Prohaska, H. Wolf and S. Dübel, 'Analysis of Protein Interactions Using a Quartz Crystal Microbalance Biosensor', in *Protein-protein interactions : a molecular cloning manual*, E. Golemis, Ed. Cold Spring Harbor, NY: Cold Spring Harbor Laboratory Press, 2002, pp. 273-283.

[151] M. Rodahl, F. Höök, C. Fredriksson, C. Keller, A. Krozer, P. Brzezinski, M. Voinova and B. Kasemo, 'Simultaneous frequency and dissipation factor QCM measurements of biomolecular adsorption and cell adhesion', *Faraday Discuss.*, vol. 107, pp. 229-246, 1997.

[152] 'Insplorion Acoulyte', *Insplorion*,
Available: https://www.insplorion.com/en/instruments/products/insplorion-acoulyte/.
[Accessed 19 June 2017].

[153] 'Q-Sense Modules and Sensors', *Biolin Scientific*. Available:
http://www.biolinscientific.com/zafepress.php?url=%2Fpdf%2FQ-
Sense%2FProducts%2FSensor%20%26%20Modules%2FQS_P_Modules-and-
Sensors%20Brochure.pdf. [Accessed 19 June 2017].

[154] 'Electrochemistry and QCM-D on the same surface', *Biolin Scientific*. Available:
http://www.biolinscientific.com/zafepress.php?url=%2Fpdf%2FQ-
Sense%2FTechnology%20Notes%2FQS-TN-02-Electrochemistry-QCM-D.pdf. [Accessed 19 June 2017].

[155] D. Pavia, G. Lampman and G. Kriz, *Introduction to spectroscopy*. Belmont, CA: Brooks/Cole, Thomson Learning, 2001.

[156] '4.3: Infrared spectroscopy', *Chemistry LibreTexts*. Available:
https://chem.libretexts.org/Textbook_Maps/Organic_Chemistry_Textbook_Maps/Map%3A_

Organic_Chemistry_With_a_Biological_Emphasis_(Soderberg)/Chapter_04%3A_Structure_Determination_I/4.3%3A__Infrared_spectroscopy. [Accessed 19 June 2017].

[157] 'How an FTIR Spectrometer Operates', *Chemistry LibreTexts*, Available: https://chem.libretexts.org/Core/Physical_and_Theoretical_Chemistry/Spectroscopy/Vibratio nal_Spectroscopy/Infrared_Spectroscopy/How_an_FTIR_Spectrometer_Operates. [Accessed 19 June 2017].

[158] P. Griffiths and J. De Haseth, *Fourier Transform Infrared Spectrometry*. Hoboken, NJ: Wiley, 2007.

[159] 'Introduction to Modern FT-IR Spectroscopy', *Department of Chemistry, Aarhus University*. Available: http://old.chem.au.dk/~orgsurf/PM-IRRAS.pdf. [Accessed 19 June 2017].

[160] B. Frey, R. Corn and S. Weibel, 'Polarization-Modulation Approaches to Reflection–Absorption Spectroscopy', in *Handbook of Vibrational Spectroscopy*, P. Griffiths and J. Chalmers, Ed. Chichester: John Wiley & Sons Ltd, 2002.

[161] 'Light Reflectance Definition', *Performativedesign.com*. Available: http://performativedesign.com/definition/light-reflectance/. [Accessed 19 June 2017].

[162] C. Stapleton (Bruker Optics), 'IRRAS / PM-IRRAS - Investigation of ultrathin layers on metals', University of York, 2016.

[163] 'Polarization Primer - Hinds Instruments', *Hindsinstruments.com*. Available: http://www.hindsinstruments.com/knowledge-center/technology-primer/pem-100photoelastic-modulation/polarization-primer/. [Accessed 19 June 2017].

[164] T. McIlvaine, 'A buffer solution for colorimetric comparison', *J. Biol. Chem.*, vol. 49, pp. 183-186, 1921.

[165] H. Britton and R. Robinson, 'CXCVIII - Universal buffer solutions and the dissociation constant of veronal', *J. Chem. Soc. (Resumed)*, p. 1456, 1931.

[166] C. Pheeney and J. Barton, 'DNA Electrochemistry with Tethered Methylene Blue', *Langmuir*, vol. 28, no. 17, pp. 7063-7070, 2012.

[167] M. Góes, H. Rahman, J. Ryall, J. Davis and P. Bueno, 'A Dielectric Model of Self-Assembled Monolayer Interfaces by Capacitive Spectroscopy', *Langmuir*, vol. 28, no. 25, pp. 9689-9699, 2012.

[168] M. Rampi, O. Schueller and G. Whitesides, 'Alkanethiol self-assembled monolayers as the dielectric of capacitors with nanoscale thickness', *Appl. Phys. Lett.*, vol. 72, no. 14, pp. 1781-1783, 1998.

[169] K. Weber, L. Hockett and S. Creager, 'Long-Range Electronic Coupling between Ferrocene and Gold in Alkanethiolate-based Monolayers on Electrodes', *J. Phys. Chem. B*, vol. 101, no. 41, pp. 8286-8291, 1997.

[170] M. Contineanu, C. Bercu, I. Contineanu and A. Neacsu, 'A Chemical And Photochemical Study Of Radicalic Species Formed In Methylene Blue Acidic And Basic Aqueous Solutions', *An. Univ. Bucuresti. Chimie*, vol. 18, no. 2, pp. 29-37, 2009.

[171] D. Weinberg, C. Gagliardi, J. Hull, C. Murphy, C. Kent, B. Westlake, A. Paul, D. Ess, D. McCafferty and T. Meyer, "Proton-Coupled Electron Transfer", *Chemical Reviews*, vol. 112, no. 7, pp. 4016-4093, 2012.

[172] H. Finklea, 'Consequences of a potential-dependent transfer coefficient in ac voltammetry and in coupled electron–proton transfer for attached redox couples', *J. Electroanal. Chem.*, vol. 495, no. 2, pp. 79-86, 2001.

[173] E. Ostuni, L. Yan and G. Whitesides, 'The interaction of proteins and cells with self-assembled monolayers of alkanethiolates on gold and silver', *Colloids Surf., B*, vol. 15, no. 1, pp. 3-30, 1999.

[174] S. Campuzano, M. Pedrero, C. Montemayor, E. Fatás and J. Pingarrón, 'Characterization of alkanethiol-self-assembled monolayers-modified gold electrodes by electrochemical impedance spectroscopy', *J. Electroanal. Chem.*, vol. 586, no. 1, pp. 112-121, 2006.

[175] S. Lee, Y. Shon, R. Colorado, R. Guenard, T. Lee and S. Perry, 'The Influence of Packing Densities and Surface Order on the Frictional Properties of Alkanethiol Self-Assembled Monolayers (SAMs) on Gold: A Comparison of SAMs Derived from Normal and Spiroalkanedithiols', *Langmuir*, vol. 16, no. 5, pp. 2220-2224, 2000.

[176] R. Valiokas, L. Malysheva, A. Onipko, H. Lee, Ž. Ruželė, S. Svedhem, S. Svensson, U. Gelius and B. Liedberg, 'On the quality and structural characteristics of oligo(ethylene glycol) assemblies on gold: An experimental and theoretical study', *J. Electron Spectrosc. Relat. Phenom.*, vol. 172, no. 1-3, pp. 9-20, 2009.

[177] L. Kankate, U. Werner, A. Turchanin, A. Gölzhäuser, H. Großmann and R. Tampé, 'Protein resistant oligo(ethylene glycol) terminated self-assembled monolayers of thiols on gold by vapor deposition in vacuum', *Biointerphases*, vol. 5, no. 2, p. 30, 2010.

[178] R. Valiokas, S. Svedhem, M. Östblom, S. Svensson and B. Liedberg, 'Influence of Specific Intermolecular Interactions on the Self-Assembly and Phase Behavior of Oligo(Ethylene Glycol)-Terminated Alkanethiolates on Gold', *J. Phys. Chem. B*, vol. 105, no. 23, pp. 5459-5469, 2001.

[179] T. Hayashi and S. Mukamel, 'Vibrational−Exciton Couplings for the Amide I, II, III, and A Modes of Peptides', *J. Phys. Chem. B*, vol. 111, no. 37, pp. 11032-11046, 2007.

[180] E. Hulme and M. Trevethick, 'Ligand binding assays at equilibrium: validation and interpretation', *Br. J. Pharmacol.*, vol. 161, no. 6, pp. 1219-1237, 2010.

[181] G. Marchesini, E. Meulenberg, W. Haasnoot and H. Irth, 'Biosensor immunoassays for the detection of bisphenol A', *Anal. Chim. Acta*, vol. 528, no. 1, pp. 37-45, 2005.

[182] R. Rich, L. Hoth, K. Geoghegan, T. Brown, P. LeMotte, S. Simons, P. Hensley and D. Myszka, 'Kinetic analysis of estrogen receptor/ligand interactions', *Proc. Natl. Acad. Sci. U. S. A.*, vol. 99, no. 13, pp. 8562-8567, 2002.

[183] H. Motulsky, 'The GraphPad Guide to Analyzing Radioligand Binding Data', *GraphPad Prism*, 1995. Available: http://www3.uah.es/farmamol/Public/GraphPad/radiolig.htm. [Accessed 19 June 2017].

[184] K. Cox, V. Devanarayan, A. Kriauciunas, J. Manetta, C. Montrose and S. Sittampalam, 'Immunoassay Methods', 2012, in *Assay Guidance Manual*, [Online] S. Sittampalam, N. Coussens and K. Brimacombe et al., Bethesda, MD: Eli Lilly & Company and the National Center for Advancing Translational Sciences; 2004-. Available: https://www.ncbi.nlm.nih.gov/books/NBK92434/. [Accessed 19 June 2017].

[185] R. Campbell, J. Dymshitz, B. Eastwood, R. Emkey, D. Greenen, J. Heerding, D. Johnson, T. Large, T. Littlejohn, C. Montrose, S. Nutter, B. Sawyer, S. Sigmund, M. Smith, J. Weidner and R. Zink, 'Data Standardization for Results Management' 2012, in *Assay Guidance Manual*, [Online] S. Sittampalam, N. Coussens and K. Brimacombe et al., Bethesda, MD: Eli Lilly & Company and the National Center for Advancing Translational Sciences; 2004-. Available: https://www.ncbi.nlm.nih.gov/books/NBK91993/. [Accessed 19 June 2017].

[186] C. Kifude, H. Rajasekariah, D. Sullivan, V. Stewart, E. Angov, S. Martin, C. Diggs and J. Waitumbi, 'Enzyme-Linked Immunosorbent Assay for Detection of Plasmodium falciparum Histidine-Rich Protein 2 in Blood, Plasma, and Serum', *Clin. Vaccine Immunol.*, vol. 15, no. 6, pp. 1012-1018, 2008.

[187] S. Rau, U. Hilbig and G. Gauglitz, 'Label-free optical biosensor for detection and quantification of the non-steroidal anti-inflammatory drug diclofenac in milk without any sample pretreatment', *Anal. Bioanal. Chem.*, vol. 406, no. 14, pp. 3377-3386, 2014.

[188] 'KD value: a quantitative measurement of antibody affinity', *Abcam.com*. Available: http://www.abcam.com/primary-antibodies/kd-value-a-quantitive-measurement-of-antibody-affinity. [Accessed 19 June 2017].

[189] H. Zhang, P. Williams, M. Zborowski and J. Chalmers, 'Binding affinities/avidities of antibody–antigen interactions: Quantification and scale-up implications', *Biotechnol. Bioeng.*, vol. 95, no. 5, pp. 812-829, 2006.

[190] L. Malysheva, A. Onipko, R. Valiokas and B. Liedberg, 'First-principles modeling of oligo(ethylene glycol)-terminated and amide group containing alkanethiolates', *Appl. Surf. Sci.*, vol. 246, no. 4, pp. 372-376, 2005.

[191] L. Malysheva, Y. Klymenko, A. Onipko, R. Valiokas and B. Liedberg, 'Ab initio calculations of equilibrium geometries and vibrational excitations of helical ethylene-glycol oligomers: application to modeling of monolayer infrared spectra', *Chem. Phys. Lett.*, vol. 370, no. 3-4, pp. 451-459, 2003.

[192] F. Mallamace, C. Corsaro, D. Mallamace, S. Vasi, C. Vasi and G. Dugo, 'The role of water in protein's behavior: The two dynamical crossovers studied by NMR and FTIR techniques', *Comput. Struct. Biotechnol. J.*, vol. 13, pp. 33-37, 2015.

[193] B. Hock, M. Seifert and K. Kramer, 'Engineering receptors and antibodies for biosensors', *Biosens. Bioelectron.*, vol. 17, no. 3, pp. 239-249, 2002.

[194] L. De Faveri, (2016, April 14) 'RE: Diclofenac ELISA results and method', Personal email.

[195] 'His-tagged Proteins–Production and Purification', *Thermo Fisher Scientific*. Available: http://www.thermofisher.com/uk/en/home/life-science/protein-biology/protein-biology-learning-center/protein-biology-resource-library/pierce-protein-methods/his-tagged-proteins-production-purification.html. [Accessed 19 June 2017].

[196] A. Shrivastava and V. Gupta, 'Methods for the determination of limit of detection and limit of quantitation of the analytical methods', *Chron. Young Sci.*, vol. 2, no. 1, p. 21, 2011.

[197] F. Hoppe-Seyler, I. Crnkovic-Mertens, C. Denk, B. Fitscher, B. Klevenz, E. Tomai and K. Butz, "Peptide aptamers: new tools to study protein interactions", *J. Steroid Biochem. Mol. Biol.*, vol. 78, no. 2, pp. 105-111, 2001.

[198] 'Antibody Affinity Maturation - Creative Biolabs', *Creative-biolabs.com*, Available: http://www.creative-biolabs.com/antibody-affinity-maturation.html. [Accessed 26 September 2017].

[199] G. Hermanson, *Bioconjugate techniques*, 2nd ed. Rockford, IL: Elsevier, 2008.